Quantum noise limited light interferometry with cold trapped atoms

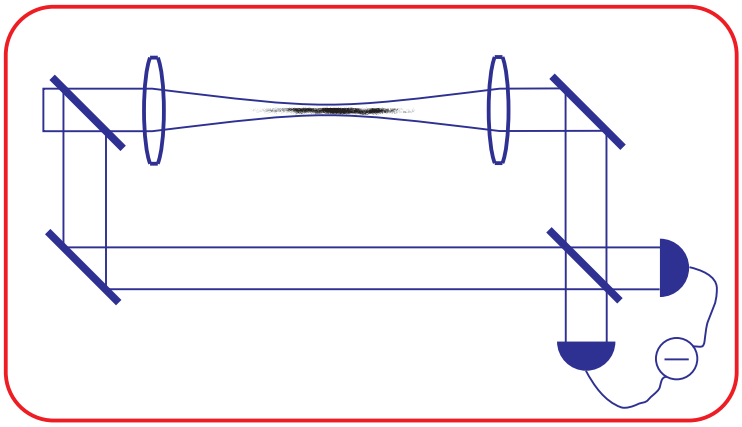

Plamen Petrov

QUANTOP - Danish National Research
Foundation for Quantum Optics
Niels Bohr Institute
University of Copenhagen

PhD Thesis

· 2006 ·

Quantum noise limited light interferometry with cold trapped atoms

Plamen Petrov

QUANTOP - Danish National Research
Foundation for Quantum Optics
Niels Bohr Institute
University of Copenhagen

PhD Thesis

· 2006 ·

Academic advisor: Prof. Eugene Polzik

Abstract

We present a method of nondestructive characterization of cold and trapped caesium atomic samples which relies on optical phase-shift measurement in a shot-noise-limited Mach-Zehnder white-light interferometer. The phase shift imposed on an off-resonant light due to dispersive interaction with atoms is monitored via a pulsed homodyne detection scheme, allowing for fast and nondestructive characterization of atomic samples. The estimated rate of real transition for a single probe pulse is found to be as low as 0.038. The population fluctuation of the upper hyperfine level in the caesium electronic ground state is measured to scale linearly with the number of atoms, which is an evidence that the experimental apparatus has the sensitivity to track the projection noise of a coherent superposition state.

Contents

Preface

The results presented in this thesis are obtained in about four years of experimental work under the supervision of Prof. Eugene Polzik. I joined the Quantum Optics Laboratory in January 2002, which at that time was situated at the Institute of Physics and Astronomy, Aarhus University. During that time I was fortunate to work with Jens Mikkelsen and Anton Vershovski in setting up together the first magneto-optical trap in my life. I am also grateful to Jens Lykke Sorensen and Wolfgang Tittel who were helping me a lot as a beginner in the field of optics when my patience was at the limit.

In February 2003 the whole lab moved to the Niels Bohr Institute, and together with Daniel Oblak and Carlos Alzar we started rebuilding the setup. I want to give my gratitude to these two guys, who have been patient with my Balkan temper, and to thank them for the help during the long hours in the laboratory. I also want to thank to Carlos for his fast and fruitful comments on the thesis and to Niels Kjaergaard contributing to part of the results. Here I should not forget mentioning Joerg Muller and his yes and no-s in lots of discussion we had, and moreover for giving me good advises for finding a way out of the vacuum problems.

During these years I also had the pleasure to discuss different matters with Christian Schori, Brian Julsgaard, Andrew Hilliard, Jacob Sherson, Jonas Neergard-Nielsen, Christian Hettich, Christina Olausson, Rasmus Olson and Bo Nielsen, and Sebastian R. de Echaniz and Marcin Kubasik from the Institute of Photonics -ICFO in Barcelona. I would also like to thank the Niels K. Lindegaard, Erik G. Jacobsen, Jens E. Sorensen and Ejner Petersen from the mechanical workshop at the Blegdamsvej 17 for the fast and excellent work they have done, to Ole B. Rasmusen from the electronic workshop, to Bjorn Nilson and Jimmy Hansen for the software assistance.

Finally, I would like to thank to my scientific advisor Prof. Eugene Polzik who has given me the opportunity to enter in the amazing field of cold atoms and quantum optics, as well as for his patience, support and guidance.

At the end I want to tank to my lovely wife Valentina for her huge patience and moral help in difficult moments, and to my little daughter Lora who has not forgotten his father during the hours of absence from home.

The project was supported by the European Research Training Network CAUAC (Cold atoms and ultra-precise atomic clocks) funded via the contract N:HPRN-CT-2000-00165 and the Danmarks Grundforsknings fond.

Plamen Petrov, February 2006

List of Publications

Journal Papers

1. D. Oblak, P.G. Petrov, C.L. Garrido Alzar, W. Tittel, A.K. Vershovski, J.K. Mikkelsen, J.L. Sørensen, and E.S. Polzik, "Quantum noise limited interferometric measurement of atomic noise: towards spin squeezing on the Cs clock transition", *Phys. Rev. A*, **71**, 043807, (2005).

2. J.H. Mueller, P. Petrov, D. Oblak, C.L. Garrido Alzar, S.R. de Echaniz, E.S. Polzik, "Diffraction effects on light-atomic ensemble quantum interface", *Phys. Rev. A*, **71**, 033803, (2005).

3. P.G. Petrov, D. Oblak, C.L. Garrido Alzar, Niels Kjærgaard, and E.S. Polzik, "Non-destructive interferometric characterization of an optical dipole trap", to be submitted to *Phys. Rev. A*.

Contribution to Conferences

1. P.G. Petrov, D. Oblak, C.L. Garrido Alzar, N. Kjaergaard, E.S. Polzik, "Nondestructive characterization of an optical dipole trap" *ICOLS'05*, 19-24th June 2005, Aviemore, Scotland, (poster).

2. P.G. Petrov, J.H. Mueller, D. Oblak, C.L. Garrido Alzar, S.R. de Echaniz, E.S. Polzik, "Diffraction effects on light-atomic ensemble quantum interface," *CAUAC European Network Meeting*, 24-27th April 2004, Porquerolles, France, (talk).

3. P.G. Petrov, C.L. G. Alzar, D. Oblak, J. K. Mikkelsen, J. L. Sørensen, W. Tittel, A.K. Vershovski, and E.S. Polzik, "Quantum noise limited interferometric measurement of atomic noise," *CAUAC European Network Meeting*, 9-12th October 2003, Braunschweig, Germany, (talk).

4. P. Petrov, C.L.G. Alzar, D. Oblak, J. K. Mikkelsen, J. L. Sørensen, W. Tittel, A.K. Vershovski, and E.S. Polzik, "Probing the atomic population in Mach-Zender type interferometric setup" *Young Atomic Optician Conference (YAO 2003)*, 3rd-8th June 2003, Amsterdam, The Netherlands, (poster)

5. P.G. Petrov, J.K. Mikkelsen, J.L.Sørensen, W. Tittel, A.K. Vershovski, and E.S.Polzik "Squeezing the population number difference of cold Cs atomic ensemble by using non-demolition measurement", *34th Conference of European Group of Atomic Spectroscopy (EGAS 34)*, 9-12th July 2002, Sofia, Bulgaria (poster).

Chapter 1

Introduction

The quantum nature of atom light interaction has been studied for many decades, but only in the recent 30 years it has entered the unique field of the cold atoms and ultra-precise spectroscopy. The use of cold atoms in atomic clocks has improved the frequency measurement accuracy and nowadays this measurement is limited by the quantum projection noise of an ensemble of uncorrelated particles [1].

It has been shown that for correlated atomic ensembles employed in the Ramsey interrogation cycle the uncertainty of frequency determination can be reduced below the fundamental quantum projection noise level [2]. A correlated atomic state has been recognized as a state for which the ensemble wavefunction cannot be factorized over the wavefunction of different parties [3]. The preparation of a correlated atomic state involves generation of spin-squeezed state [4]. There are different schemes to generate squeezed states. The Quantum Non-Demolition (QND) measurement has been identified as an efficient method for production of spin-squeezed states [5]. Squeezed state generated through Faraday polarization rotation has been produced for ensemble of room temperature atoms [6]. Transfer of the quantum state of non-classical light beam to an ensemble of cold atoms has been found to produce correlated atomic ensembles [7]. The generation of spin-squeezing via continuous quantum feedback has been proposed in [8] and experimentally implemented by Geremia et al. [9] for a sample of cold caesium atoms.

The advantages of using cold atoms to generate squeezed states has been pointed out in [6], as a way to increase the interaction time by a factor of at least thousand. The high optical densities of cold atomic samples allow for increasing of the interaction strength and in the same time to reduce the decoherence due to absorption by increasing the detuning of the probe light. Inserting the atomic sample into optical cavity has also been recognized [10] as a tool to increase the interaction strength.

All of the above experiments are implemented with atoms in a coherent state, and the detection is done in a polarization interferometer, where the circularly polarized components of a linearly polarized probe experience different index of refraction due to coupling to atomic levels with different projections of the total angular momentum. The power of the probe light ranges from 1 mW [6] to 250 nW [10].

The current thesis includes experimental and theoretical results on light-matter interaction, which are a step toward generation of a spin-squeezing on the caesium clock transition [11] via a QND measurement of atomic population number difference by monitoring the phase shift of an off-resonant light, imposed by interaction with cold atomic sample, in a Mach-Zehnder interferometer. Compared to the above experiments our proposal for spin-squeezing on the clock transition involves QND measurement on a superposition i.e.

clock state. The pulsed probe light and the low power in the probe beam in a combination with high detuning, allows for pulse integrated rate of spontaneous emission lower than one. The evidence for the nondestructive character of our interferometric measurement is the experimental data presented in this thesis on the characterization of a magneto-optical and dipole traps.

The thesis is organized as follows. The chapters 2 to 5 are the theoretical part of the thesis. In *Chapter 2* we introduce the atomic and light variables and describe the interaction of an ensemble of two level atoms with a coherent light field. The corresponding phase shift and absorption are derived from the complex index of refraction. *Chapter 3* includes basic theory of cold atomic sample preparation in a magneto-optical-trap (MOT) and loading it in a single focused beam dipole trap. *Chapter 4* is dedicated to description of the main experimental tool - the Mach-Zehnder interferometer, including the noise sources influencing the experimental signal. *Chapter 5* presents a simple model to include diffraction effects in the problem of light-matter quantum interface, i.e. to derive simple scaling laws for the signal to noise ratio of the interaction in different sample geometries. In *Chapter 6* we start with the experimental part of the thesis and describe the experimental setup for laser cooling and trapping of caesium atoms in a MOT, along with the characterization of trap atom number, density and temperature using the fluorescence detection method. *Chapter 7* describes the dipole trap setup and presents results on a fluorescence imaging of the atomic cloud with a triggerable camera. The experimental setup of the Mach-Zehnder interferometer is presented in *Chapter 8* together with experimental results on the interferometer noise. Finally in *Chapter 9* we present results on the non-destructive quantum-noise limited characterization of cold atoms prepared in a MOT and trapped in a dipole trap. In *Chapter 10* we make a summary of the thesis and discuss future research plans towards spin-squeezing on the caesium clock transition.

Chapter 2

Atom-light interaction

In the basis of the current work underlies the interaction of an atomic sample with coherent light. The chapter presents the basic quantum mechanical properties of that interaction.

We start with introduction of the operators used to describe the atomic system and light in quantum mechanics. The state of a two level atom is represented by operators and the collective behavior of the atoms is described by its density operator. An alternative view of the collective problem is presented by the use of the atomic collective angular momentum formalism allowing a pictorial illustration of the state evolution using the Bloch sphere representation. The electromagnetic field is quantized using the harmonic oscillator annihilation and creation operators. The phase of the real light beam is described by inclusion of a coherent state formalism.

In the second part of this chapter we construct the atom-field dipole interaction hamiltonian and solve the equations of motion for the system. We derive expressions for the phase shift and absorption of light and introduce the off-resonant interaction hamiltonian.

2.1 Atomic States

2.1.1 Atomic operator

In the atom light combined quantum mechanical system the atomic energy is described by the use of the atomic operator. The definition of the atomic operator can be found elsewhere in the textbooks [12, 13]. Let's us assume that an atom can occupy a set of energy levels and let us choose two of them i.e. state $|i\rangle$ and state $|j\rangle$. Then the atomic operator is defined as:

$$\hat{\sigma}_{ij} = |i\rangle\langle j| \tag{2.1}$$

We can distinguish between to type of atomic operators. For $i = j$ the operator is called population operator, and when $i \neq j$ we refer the corresponding operator as coherence or projection operator. In the atomic operator representation the states $|i\rangle$ and $|j\rangle$ are eigenstates of the population operator with eigenvalues of $\hbar\omega_i$ and we have the usual orthogonal relation of $\langle i|j\rangle = \delta_{ij}$ and unity operator defined in the space of the eigenstates as $\sum_i |i\rangle\langle i| = \mathbf{1}$. Every atomic state vector Ψ can be expressed as a superposition of the eigenstates of the atomic operator i.e. $\Psi = \sum_i c_i|i\rangle$. The mean values of the diagonal elements of the atomic matrix representation $\sigma = ||i\rangle\langle j||$ are the probabilities of the atom to occupy a state with index i i.e. $\langle\hat{\sigma}_{ii}\rangle = |c_i|^2$.

When acting with the operator in Eq.(2.1) on a given atomic state $|j\rangle$ we get that

$\hat{\sigma}_{ij}|j\rangle = |i\rangle$. Hence the operator $\hat{\sigma}_{ij}$ acting on a state $|j\rangle$ changes the internal atomic state to $|i\rangle$. For an ensemble of many atoms the collective operator will be defined as a sum over the number of atoms N_{at}.

$$\hat{\sigma}_{ij} = \sum_{k}^{N_{at}} \hat{\sigma}_{i,j}^{(k)} = \sum_{k}^{N_{at}} |i\rangle\langle j|^{(k)} \tag{2.2}$$

The Hamiltonian of the atomic system in quantized form is expressed as a sum over all possible atomic states which can be excited by interaction with light. Then the atomic hamiltonian $\hat{H}_A$ is obtained by summation over the number of atoms in the ensemble

$$\hat{H}_A = \sum_{k}^{N_{at}} \sum_{i} \hbar\omega_i |i\rangle\langle i|^{(k)} \tag{2.3}$$

2.1.2 Dipole operator

In practice, atoms interact with light and change their internal state. In the dipole approximation the internal atomic state is described by the position of the valence electron w.r.t. the nuclei. In classical terms one can think of an atomic dipole with the negatively charged electron and positively charged nuclei. In quantum mechanics to describe the position of the electron we use the position operator $\hat{r}$. The dipole operator is then expressed as the product of the electron charge e and the electron position operator $\hat{r}$. Using the definition for the atomic operator in Eq.2.1 we get to:

$$\hat{d}^{(k)} = e\hat{r}^{(k)} = e\sum_{i,j} |i\rangle\langle i|\hat{r}^{(k)}|j\rangle\langle j| = \sum_{i\neq j} \hat{d}_{ij}^{(k)} \hat{\sigma}_{ij}^{(k)} \tag{2.4}$$

Note that all terms with $i = j$ vanish since they involve diagonal matrix elements of the odd-parity operator $\hat{d}$. The index k in the above equation refers to a k-th atom from an ensemble of N atoms. The above expressions consider a collection of atoms in the discrete case.

In most of the experimental cases a continuous variable treatment of the problem is necessary. For that reason we must define an atomic number operator as $\hat{N} = \sum_i \hat{\sigma}_{ii}$ which has a mean value of $\langle\hat{N}\rangle = N/(\mathcal{N}(x,y,z)dxdydz)$ with an atomic number density being $\mathcal{N}$. Then the mean value of an operator $\hat{O}$ is defined as

$$\langle\hat{O}\rangle = \int_V \mathcal{N}(x,y,z)\hat{O}(x,y,z)dxdydz \tag{2.5}$$

The three dimensional integration can be simplified by assuming different atomic sample geometries.

2.1.3 Density operator. Mixed and pure states.

In the following, we consider the state of a collection of uncorrelated atoms which is described by a statistical density operator $\hat{\rho}$ [13]. The density operator first introduced by J. von Neumann in 1927, quantitatively describes the state of an ensemble of identically prepared particles. That is to say that all particles are in a state with a state vector $|\Psi\rangle$ referred as pure state. If an ensemble contains particles prepared in different uncorrelated

states, we say that the state is mixed. The density operator of a mixed state is defined as follows:

$$\hat{\rho} = \sum_i \alpha_i |\Psi_i\rangle\langle\Psi_i| \tag{2.6}$$

where the sum runs over the all sub-ensembles with state vectors $|\Psi_i\rangle$ and α_i is the probability of the ensemble to be in the state with $|\Psi_i\rangle$. From the above expression it follows that for a pure state only one α probability will be different from zero, which means that all particles are in the same state and the density operator becomes:

$$\hat{\rho} = |\Psi\rangle\langle\Psi| \tag{2.7}$$

The last two equations depict that every mixed state can be expanded in a superposition of pure states. If a measurement of observable A is performed on a mixed ensemble the value obtained is the ensemble average and is defined as:

$$\left[\hat{A}\right] = \mathrm{Tr}(\hat{\rho}\hat{A}) \tag{2.8}$$

$$[\hat{\sigma}_{ij}] = \mathrm{Tr}(\hat{\rho}\hat{\sigma}_{ij}) = \rho_{ij} \tag{2.9}$$

where $\hat{A}$ is the operator associated with the observable A. The result is invariant to any basis of states since the trace operation is independent of representation [13]. Using this relation we can calculate the ensemble average of the atomic operator $\hat{\sigma}_{ij}$ as shown above.

2.1.4 Atomic collective angular momentum

Another useful representation of the state of an ensemble of two-level atoms is the pseudo-spin formalism. According to that every atom is represented by an angular momentum or spin [14, 15]. The state of an atom which can occupy either ground state $|3\rangle$ or excited state $|4\rangle$ is described by the following system of pseudo-spin operators expressed as the components of the atomic operator. The choice of the levels is in accordance with the ground state hyperfine structure of caesium Sec.3.1.

$$\begin{aligned} \hat{\jmath}_x^k &= \frac{1}{2}(\hat{\sigma}_{43}^k + \hat{\sigma}_{34}^k), \\ \hat{\jmath}_y^k &= \frac{-i}{2}(\hat{\sigma}_{43}^k - \hat{\sigma}_{34}^k), \\ \hat{\jmath}_z^k &= \frac{1}{2}(\hat{\sigma}_{44}^k - \hat{\sigma}_{33}^k), \end{aligned} \tag{2.10}$$

where $\hat{\jmath}_x^k$, $\hat{\jmath}_y^k$ and $\hat{\jmath}_z^k$ are the projections of the angular momentum operator $\hat{\jmath}^k$ on the x, y, and z axes, respectively. These operators fulfil the angular momentum commutation relation $[\hat{\jmath}_i, \hat{\jmath}_j] = i\varepsilon_{ijl}\hat{\jmath}_l$, where ε_{ijl} is the Levi-Civita tensor. For an ensemble of N_{at} atoms, we define the collective angular momentum operators by $\hat{J}_x = \sum_k \hat{\jmath}_x^k$, for the x component, and similarly for the other.

The atomic ensemble state can be pictorially illustrated by the use of the Bloch sphere representation [16]. According to that the mean value of the operators in Eq.(2.10) are coordinates of a vector along x, y and z, which length is $\langle\hat{J}\rangle^2 = \langle\hat{J}_x\rangle^2 + \langle\hat{J}_y\rangle^2 + \langle\hat{J}_z\rangle^2$ and it should stay constant under rotation of the pseudo-spin vector if the number of atoms in the ensemble does not change. The values of the projections can change but the length of the vector $\hat{J}$ is constant. Then the evolution of the ensemble state is represented by

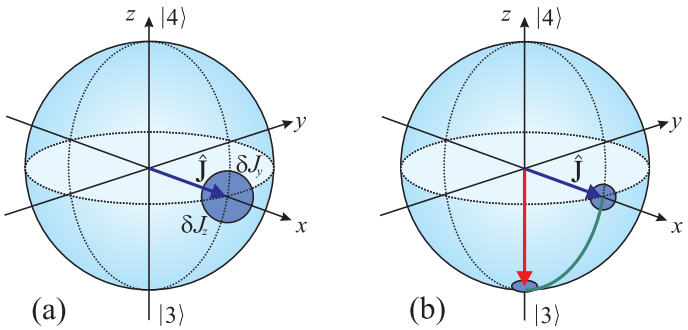

Figure 2.1: *Bloch sphere representation of the collective atomic pseudo-spin (a). An example of trajectory over the sphere surface with initial state having all atoms in* $|3\rangle$ *and after a* $\pi/2$ *pulse of radiation is applied the new state becomes a superposition state (see text for details)(b).*

a trajectory over the surface of the Bloch sphere [see Fig.2.1]. The population difference between the two atomic levels is then given by the projection of $\hat{J}$ on the polar axis ($\hat{J}_z$), whereas the projections ($\hat{J}_x$) and ($\hat{J}_y$) in the sphere's equatorial plane give information about the atomic coherences. Let us consider a coherent superposition state where the probability to find the atoms in the ground state is equal to that of finding them in the excited one. Then the state vector can be written in the form:

$$|\Psi\rangle = \frac{1}{\sqrt{2}}\left(|3\rangle + |4\rangle\right) \tag{2.11}$$

This state is a very important one for atomic clocks [2, 17]. For that state the density operator has the form given by Eq.(2.7).

Then the ensemble average of the components of the collective spin are calculated from the single atom state Eq.(2.11) and the spin projections in Eq.(2.10) using Eq.(2.8) and multiplication by N_{at}.

$$\langle \hat{J}_x \rangle = N_{at},\ \langle \hat{J}_y \rangle = \langle \hat{J}_z \rangle = 0, \tag{2.12}$$

$$\delta \hat{J}_x = 0,\ \delta \hat{J}_y = \delta \hat{J}_z = \frac{1}{2}\sqrt{N_{at}}, \tag{2.13}$$

$$\delta \hat{J}_y \delta \hat{J}_z \geq \frac{N_{at}}{4} \tag{2.14}$$

When performing a measurement on $\hat{J}_z$ the outcome of the measurement will be distributed around the mean value with uncertainty $\delta \hat{J}_z$, which obeys the Heisenberg uncertainty relation [Eq.(2.12)]. In the Bloch sphere representation the uncertainties are illustrated as a sphere with a radius equivalent to the uncertainty of the minimum uncertainty state satisfying the equality in the uncertainty relation. The square of the uncertainty, i.e. the noise of that state is the so called *quantum projection noise* [17], which is discussed in detail in Ch.4.

We must note that if the N_{at} is reduced during the measurement, the state is no longer pure since the atoms which have been removed from the sample will form another sub-ensemble leading to transformation of the overall ensemble state into a mixed state.

Let us now look at a mixed state with half of the atoms in the ground and half in the excited state. The density matrix of such state will be a sum of two terms $|3\rangle\langle 3|$ and

$|4\rangle\langle 4|$ as depicted in Eq.(2.6). Using the density matrix and Eq.(2.8) we find the following relations between the operators in Eq.(2.10).

$$\langle \hat{J}_x \rangle = \langle \hat{J}_y \rangle = \langle \hat{J}_z \rangle = 0, \tag{2.15}$$

$$\delta \hat{J}_x = \delta \hat{J}_y = \delta \hat{J}_z = \frac{1}{2}\sqrt{N_{at}}, \tag{2.16}$$

Note that this state has the same uncertainty as that of a coherent superposition state but the length of the macroscopic pseudo-spin vector is zero which indicates that the ensemble is not oriented or polarized, whereas in the case of pure or *coherent* atomic state is polarized giving rise to a macroscopic atomic orientation. The mixed collective spin state can be represented as a sphere with radius of $\delta \hat{J}_z = \frac{1}{2}\sqrt{N_{at}}$ in the center of the coordinate system.

As we have mentioned above the evolution of the spin state can be represented by rotations around different axes having the tip of the spin vector fictionally drawing a trajectory on the Bloch sphere as in Fig.2.1(b). The rotation can be caused by a pulse of electromagnetic radiation and according to the detuning and the phase of that radiation the atom performs different rotations [2]. The plotted trajectory is a rotation of the atomic spin by an angle of $\theta_y = \pi/2$ under coherent excitation with a pulse of a microwave radiation with duration of $\tau_{\pi/2} = \frac{\theta_y}{\Omega_\mu}$ with Ω_μ being the Rabi frequency of the field [2]. Here we have assumed that the states in concern are the two hyperfine levels of the ground state in Cs as shown in Fig.3.1(a). After application of the $\pi/2$ pulse a superposition state is created where the spin vector lies in the equatorial plane of the Bloch sphere.

2.2 Light States

In this section we introduce the quantum states of light which are to be used throughout the discussion of light matter interaction. A detailed derivation of the quantum mechanical representation of the electromagnetic field is made in Appendix A. In the classical description [18] the electromagnetic field is described by its electric field vector given by the following expression:

$$\mathbf{E}(\mathbf{r},t) = \frac{1}{\sqrt{2}}(\epsilon \mathcal{E}(t) e^{i(\mathbf{k}\cdot\mathbf{r}-\omega t)} + \epsilon^* \mathcal{E}(t)^* e^{-i(\mathbf{k}\cdot\mathbf{r}-\omega t)}) \tag{2.17}$$

where $\omega = |\mathbf{k}|c$ is the frequency of the wave with $\mathbf{k}$ being the wave vector. The quantity $\mathcal{E}$, which caries the dimension, is the field amplitude and generally has slow time dependance compared with the field oscillation at ω. The intensity of the field is calculated as $I = \frac{c\varepsilon_0}{2}|\mathcal{E}(t)|^2$.

In quantum mechanics the light variables are described by operators. To describe the electromagnetic field quantum-mechanically we use the annihilation $\hat{a}$ and creation $\hat{a}^\dagger$ operator of the harmonic oscillator formalism. For a field with k modes of p polarizations we have:

$$\hat{\mathbf{E}}(\mathbf{r},t) = i\sum_{k,p}\sqrt{\frac{\hbar\omega_k}{2\varepsilon_0 V}}(\epsilon \hat{a}_{kp} e^{i(\mathbf{k}\cdot\mathbf{r}-\omega_k t)} - \epsilon^* \hat{a}^\dagger_{kp} e^{-i(\mathbf{k}\cdot\mathbf{r}-\omega_k t)}) \tag{2.18}$$

where the sum is done over all modes and polarizations in a quantization volume V. The Hamilton operator of the electromagnetic field describes the total field energy and is a

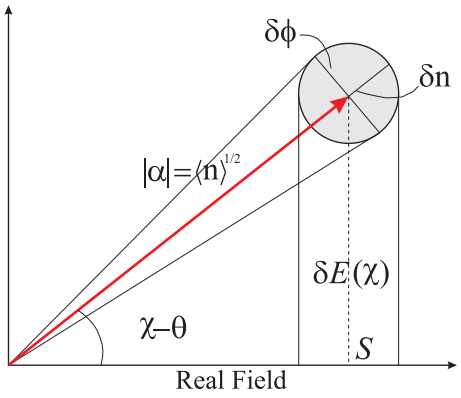

Figure 2.2: *Scheme of a coherent state with the uncertainties in the phase and photon number. The horizontal axis is the mean value of the electric field with and its deviation.*

sum of the electric and magnetic field contribution integrated over the volume:

$$\hat{H} = \sum_{k,p} \hbar\omega_k \left(\hat{a}^\dagger_{kp} \hat{a}_{kp} + \frac{1}{2} \right) \tag{2.19}$$

The hamiltonian contains the inherent feature of the quantum description of the radiation field i.e. the zero point energy $\hbar\omega_k/2$ when there are no photons in the field. The energy is similar to the energy of the quantum mechanical harmonic oscillator. The product $\hat{a}^\dagger_{kp}\hat{a}_{kp}$ is called photon number operator $\hat{n}_{kp}$. Its eigenstates are the so called Fock or number states [19]. The eigenvalues of $\hat{n}_{kp}$ give the number of photons in the k-th mode with polarization p as well as the mean value of $\langle \hat{n}_{kp} \rangle = n_{kp}$. For simplicity, we now consider a single mode case having only one member of the sum in Eq.(2.18) and omit the index kp. When acting on a number state $|n\rangle$ with the annihilation operator $\hat{a}$ a photon is destroyed $|n-1\rangle$, and when acting with the creation operator a photon is created in the mode $|n+1\rangle$. Using these relations we can obtain the state $|n\rangle$ by successive applications of the creation operator on the vacuum state $|0\rangle$. According to discussion above we have:

$$\begin{aligned} \hat{n}|n\rangle &= n|n\rangle, \\ \hat{a}|n\rangle &= \sqrt{n}|n-1\rangle \\ \hat{a}^\dagger|n\rangle &= \sqrt{n+1}|n+1\rangle \\ |n\rangle &= \frac{\left(\hat{a}^\dagger\right)^n}{\sqrt{n!}}|0\rangle. \end{aligned} \tag{2.20}$$

The number states are useful for description of a low photon number light sources, but they fail in representing the real optical fields, where the total number of photons is large. The phase of a well defined photon number state $|n\rangle$ is completely random [12]. However, the phase of the light in real beams is a very important physical quantity and a good description of it is required. The most commonly used for that purpose state is the coherent light state introduced by Roy Glauber in [20] which is a linear superposition of number states.

$$|\alpha\rangle = \exp\left(-\frac{1}{2}|\alpha|^2\right) \sum_{n=0}^{\infty} \frac{\alpha^n}{\sqrt{n!}} |n\rangle \tag{2.21}$$

where α is the eigenvalue of the photon annihilation operator $\hat{a}|\alpha\rangle = \alpha|\alpha\rangle$. The mean value of the photon number operator for the coherent state is $\langle\hat{n}\rangle = |\alpha|^2$. The probability of finding n photons in the field is given by Poisson distribution

$$P(n) = |\langle n|\alpha\rangle|^2 = e^{-\langle n\rangle}\frac{\langle n\rangle^n}{n!} \tag{2.22}$$

To illustrate the importance of the coherent state for the phase of a real light field containing large number of photons, we introduce the hermitian operators:

$$\hat{X} = \frac{1}{2}\left(\hat{a}^\dagger + \hat{a}\right),\ \hat{Y} = \frac{i}{2}\left(\hat{a}^\dagger - \hat{a}\right). \tag{2.23}$$

The operators are also known as amplitude $\hat{X}$ and phase $\hat{Y}$ quadrature operators of the electromagnetic field and can be found in any quantum optics textbooks [12]. Then the electromagnetic field Eq.(2.18) for a single mode can be expressed in terms of these operators as:

$$\hat{\mathbf{E}}(\chi) = \sqrt{\frac{\hbar\omega_k}{2\varepsilon_0 V}}\left(\hat{X}\cos\chi + \hat{Y}\sin\chi\right) \tag{2.24}$$

with $\chi = \omega t - \mathbf{k}\cdot\mathbf{r} - \pi/2$. The coherent state expectation value of the field operator and its varince can be calculated from Eq.(2.23) and Eq.(2.24) and using the properties of the coherent states:

$$\mathrm{S} = \langle\alpha|\hat{\mathbf{E}}(\chi)|\alpha\rangle = |\alpha|\cos(\chi-\theta),\ \mathrm{N} = (\delta\hat{\mathbf{E}}(\chi))^2 = \frac{1}{4}. \tag{2.25}$$

In the last equations the field is expressed in the units of the pre-factor below the square-root and the complex value of α is $\alpha = |\alpha|e^{i\theta}$.

A schematic representation of coherent state is shown in Fig.2.2. The mean amplitude associated with the coherent state is shown as an arrow with length $|\alpha| = \sqrt{\langle\hat{n}\rangle}$ inclined by an angle of $\chi - \theta$ as also described in [12]. The projection on to the real field axis gives the expectation value S of the real field with its standard deviation $\mathrm{N}^{1/2} = 1/2$. The uncertainty in the photon number $\delta n = \sqrt{\langle n\rangle}$ and phase $\delta\phi = 1/(2\sqrt{\langle n\rangle})$, represented by mutually orthogonal directions in the uncertainty disk, are found to obey the product $\delta n\delta\phi \geq 1/2$.

The last conclusion is only a qualitative example, since it is not a consequence of a commutation relation between number and phase operators. Nevertheless, it correctly describes the trade off between amplitude and phase uncertainties of the electric field operator associated with the coherent state. The fractional uncertainty in the photon number $\frac{\delta n}{\langle n\rangle} = \frac{1}{\sqrt{\langle n\rangle}}$ and in the phase $\delta\phi$ both improve with increasing the photon number. The higher the photon number the better the amplitude and phase of the real field are defined.

2.3 Atom-light interaction

In this section we briefly discuss the interaction of a two level atom with an electromagnetic field and derive general expression for the phase shift and absorption expressions in the case of caesium D_2 line.

2.3.1 Interaction Hamiltonian

The section describes the interaction Hamiltonian, which is to be used further in the context of the interaction of an off-resonant beam with a sample of cold atoms. In our experiment we use an optical transition to probe the atomic population of a sample of cold atoms. The coupling of atomic dipole moment with the electric vector of the light field rules the evolution of the atomic state. In this interaction the light field and atomic system are described quantum-mechanically. In the rotating wave approximation (RWA) the interaction Hamiltonian is given by:

$$\hat{H}_i = \hbar \left(g\hat{\sigma}_{eg}\hat{a} + g^*\hat{\sigma}_{ge}\hat{a}^\dagger \right) \tag{2.26}$$

$$g = \frac{i\omega\epsilon \cdot \hat{d}_{ge}}{\sqrt{2\hbar V \omega \epsilon_0}} \tag{2.27}$$

where g is a coupling constant with ω being the frequency of the driving field, $\hat{d}_{eg} = \hat{d}^*_{ge}$ is the introduced in previous chapter dipole matrix element of the transition between two levels $|g\rangle$ ground and $|e\rangle$ excited, and $\hat{\sigma}_{ge}$ and $\hat{\sigma}_{eg}$ are the atomic operators also described in Ch.2. An alternative representation is the use of the so called rising and lowering operators with the property $\hat{\sigma}_+|g\rangle = |e\rangle$ and $\hat{\sigma}_-|e\rangle = |g\rangle$ in analogy with annihilation and creation operator of the EM field. Then the interaction Hamiltonian is expressed as:

$$\hat{H}_i = \hbar \left(g\hat{\sigma}_+\hat{a} + g^*\hat{\sigma}_-\hat{a}^\dagger \right) \tag{2.28}$$

The first term in the above equation describes the absorption of photon from the field i.e. the atom is excited and a photon is annihilated. The second term corresponds to stimulated emission of a photon meaning that an atom relaxes to the ground state and a photon is created.

2.3.2 Equations of motion.

The total Hamiltonian of the system is a sum of the different contributions - atoms, light and interaction Hamiltonians. Using equations Eq.(2.3), Eq.(2.19), and Eq.(2.28) we get:

$$\hat{H}_{tot} = \frac{1}{2}\hbar\omega_0\hat{\sigma}_z + \hbar\omega\hat{a}^\dagger\hat{a} + \hbar \left(g\hat{\sigma}_+\hat{a} + g^*\hat{\sigma}_-\hat{a}^\dagger \right). \tag{2.29}$$

In the last equation the reference level for the atomic state energies is taken right between the two states ground and excited. The operator $\hat{\sigma}_z = \hat{\sigma}_{ee} - \hat{\sigma}_{gg}$ and the vacuum energy is neglected for a light field with large photon numbers. In the Heisenberg picture the time evolution of the operators is governed by the equation of motion

$$\frac{d\hat{O}}{dt} = -\frac{i}{\hbar}[\hat{O}, \hat{H}_{tot}] \tag{2.30}$$

In our case the operators of interest are the lowering and the field annihilation operator. Using the Eq.(2.30) and substituting $g = i|g|$ we can derive the following system of differential equations.

$$\dot{\hat{a}} = -i\omega\hat{a} - |g|\hat{\sigma}_- \tag{2.31}$$

$$\dot{\hat{\sigma}}_- = -i\omega_0\hat{\sigma}_- - |g|\hat{\sigma}_z\hat{a} \tag{2.32}$$

$$\dot{\hat{\sigma}}_+ = i\omega_0\hat{\sigma}_+ + |g|\hat{\sigma}_z\hat{a} \tag{2.33}$$

The above set of equations describe the evolution of a system which does not have any spontaneous decay. Lets assume that via spontaneous emission the atom decays to the ground state with a rate of γ. A master equation analysis of the spontaneous decay of atomic coherence operator $\hat{\sigma}_z$ is presented for example in [21]. To correct for the spontaneous decay we rewrite Eq.(2.31), Eq.(2.32), Eq.(2.33) in the form:

$$\dot{\hat{a}} = -i\omega\hat{a} - |g|\hat{\sigma}_- \tag{2.34}$$

$$\dot{\hat{\sigma}}_- = -\left(\frac{\gamma}{2} + i\omega_0\right)\hat{\sigma}_- - |g|\hat{\sigma}_z\hat{a} \tag{2.35}$$

$$\dot{\hat{\sigma}}_+ = -\left(\frac{\gamma}{2} - i\omega_0\right)\hat{\sigma}_+ + |g|\hat{\sigma}_z\hat{a} \tag{2.36}$$

The derivation of the equations is extensively done in [22]. Here we only give the results for the light annihilation operator and the lowering operator, in order to solve the Heisenberg equation of motion for $\hat{a}$. The equations for the slowly varying operators $\hat{a}' = \hat{a}\exp i\omega t$ and $\hat{\sigma}'_- = \hat{\sigma}_-\exp i\omega t$ are obtained by substituting the $\hat{a}_-$, and $\hat{\sigma}_-$ operators in Eq.(2.34).

$$\dot{\hat{a}}' = -\hat{a}'|g|^2\frac{-i\Delta + \frac{\gamma}{2}}{\Delta^2 + \left(\frac{\gamma}{2}\right)^2}\hat{\sigma}_z \tag{2.37}$$

$$\dot{\hat{\sigma}}'_- = \left(-\frac{\gamma}{2} + i\Delta\right)\hat{\sigma}'_- - |g|\hat{a}'\hat{\sigma}_z \tag{2.38}$$

$$\dot{\hat{\sigma}}'_+ = \left(-\frac{\gamma}{2} - i\Delta\right)\hat{\sigma}'_+ + |g|\hat{a}'\hat{\sigma}_z \tag{2.39}$$

In the last equation we have inserted the detuning of the light field from the atomic transition $\Delta = \omega - \omega_0$.

2.3.3 Phase shift and absorption.

In this section we will discuss the imprint of the atomic variable onto the light variable and derive the main characteristics of the light-atom interaction.

The Eq.(2.37) concerns a single atom, since in the Eq.(2.29) enters the single atom Hamiltonian. For an ensemble of atoms one must replace the expression in the exponent with a sum over all atoms or integrate over the density profile of the sample. Assuming that the atomic population does not change much for the time the light passes through the entire atomic sample of length l, we can solve Eq.(2.37)

$$\hat{a}'(t) = \hat{a}'(0)\exp\left(-|g|^2\frac{-i\Delta + \frac{\gamma}{2}}{\Delta^2 + \left(\frac{\gamma}{2}\right)^2}\hat{\sigma}_z\frac{l}{c}\right) \tag{2.40}$$

Then the $\hat{\sigma}_z$ will represent the inversion of the atomic sample. The imaginary part of

the exponent in Eq.(2.40) depends on $1/\Delta$ and the real part is decreasing as $1/\Delta^2$. The imaginary part is proportional to the *phase shift* of the light, resulting from coherent elastic scattering of probe light photons, whereas the real part is responsible for the *absorption* of photons. Hence, the last equation suggests that the interaction can be both dispersive and absorptive.

The discussion so far was concentrated on a two-level atomic system. However, in practice the atoms have many levels and some of them can contribute to the phase shift and absorption, depending on the detuning of the light with respect to the corresponding atomic transitions involving these levels. The net effect of the interaction is modification of the light's phase and intensity.

The macroscopic variable, which characterizes the ability of the atomic medium to change the light phase and intensity is the complex index of refraction n_Δ. In the case of alkali metal D line $J \rightarrow J'$ transition, between states having total electronic angular momentum of J and J', the n_Δ is given by [23]

$$n_\Delta - 1 = \frac{\lambda^3}{8\pi^2}(2J+1) \times \sum_{F,F'} \mathcal{N}_F S_{FF'} \frac{\gamma}{2} \frac{\Delta_{FF'} + i\left(\frac{\gamma}{2}\right)}{\Delta_{FF'}^2 + \left(\frac{\gamma}{2}\right)^2}, \tag{2.41}$$

where $S_{FF'}$ are the hyperfine transition $F \rightarrow F'$ strength factors, explained in Appendix B, $\Delta_{FF'} = \omega - \omega_{FF'}$ is the detuning of the probe laser with respect to the hyperfine transition, $\mathcal{N}_F$ is the number density of the atoms in the ground hyperfine state with total angular momentum of F, λ is the common wavelength for the transitions in the current D line. The above equation is valid for a polarized probe light interacting with unpolarized atomic sample. The population of all magnetic sublevels $|F, m_F\rangle$ is assumed to be the same i.e $\mathcal{N}_{F,m_F} = \mathcal{N}_F/(2F+1)$. In the case of Cs D_2 line $J = 1/2 \rightarrow J' = 3/2$, the values for F and F' run in the limits $F = 3, 4$ and $F' = 2, 3, 4, 5$ [see Sec.3.1].

The real part of the refractive index $\phi = k_0 l \Re\left(n_\Delta - 1\right)$ is the phase shift imposed on the light field by the dispersive interaction with atomic sample. It can be written in the following form

$$\phi_\Delta = \frac{\lambda^2}{2\pi A} \sum_{F,F'} N_F S_{FF'} \frac{\Delta_{FF'} \frac{\gamma}{2}}{\Delta_{FF'}^2 + \left(\frac{\gamma}{2}\right)^2} \tag{2.42}$$

At the same time there is an absorptive interaction which reduces the real part of the exponent in Eq.(2.40). Expressing this quantity with the imaginary part of the refraction index $\alpha = k_0 l \Im\left(n_\Delta - 1\right)$ gives the absorption which is connected with loss of photons from the field.

$$\alpha_\Delta = \frac{\lambda^2}{2\pi A} \sum_{F,F'} N_F S_{FF'} \frac{\left(\frac{\gamma}{2}\right)^2}{\Delta_{FF'}^2 + \left(\frac{\gamma}{2}\right)^2} \tag{2.43}$$

The absorption α_Δ is inversely proportional to the square of the light detuning and this property can be used to reduce the rate of absorption using large detuning of the probe light. In the last two equations we have substituted the density $\mathcal{N}_F = N_F/Al$, with A being the sample cross section, N_F the number of atoms on state with angular momentum F and $J = 1/2$ for the case of the Cs electronic ground state.

A pictorial representation of the detuning dependance of both absorption and phase shift is shown in Fig.2.3 for the case of atoms on the two ground states of caesium. The

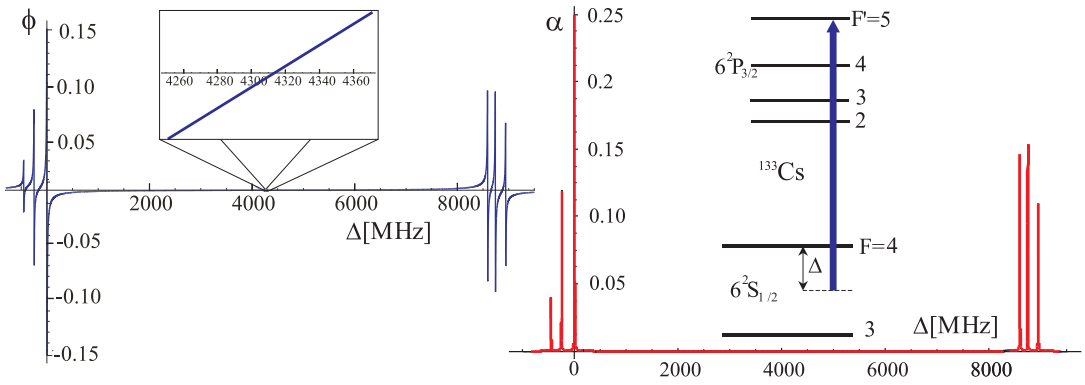

Figure 2.3: *Theoretical phase shift ϕ_Δ for equal populations of the two ground states. The phase shift is zero at a detuning of $\Delta_0 = 4312$ MHz (a); and absorption α_Δ (b) for the case of caesium atom interacting with light field detuned as shown in the levels scheme.*

probe field is detuned by Δ from the D_2 line cycling transition and the two ground states are equally populated. The light field intensity is assumed to be low enough, so that the populations are not perturbed.

To this end we have considered that the population does not change during the interaction time τ i.e. the time the light passes through the atomic sample. For an atomic sample of 3 mm the time it takes the light to pass is 10^{-2} ns. However, for a time equal to the probe pulse duration τ_p, typically several microseconds, the population could change. Then the $\hat{\sigma}_z$ operator will depend on the time and has to be averaged over the pulse duration $\bar{\hat{\sigma}}_z = \frac{1}{\tau_p}\int_0^{\tau_p} \hat{\sigma}_z(t')dt'$ over the pulse duration.

An additional complication arises from spatial dependance of the light field intensity and the spatial density distribution of the atomic sample. For example, we can take the Gaussian beam, where we have both radial and axial dependance. Then the phase shift have to be sampled over the spatial profile of the light beam. Effectively, this can be done by replacing the gaussian profile with an equivalent top hat profile with an area of $A = \pi w_0^2/2$ like it is often done in the characterization of spatially non-uniform light beams [24].

In the case of a non-uniform atom number distribution in the atomic sample an additional sampling has to be done over the important spatial coordinates. The coupling of an inhomogeneous light beams to a non-uniform atomic samples is extensively discussed in [25] and a general overview of that is done in Ch.5. The atomic samples investigated in this work exhibit rotational symmetry in the direction of light field propagation z. For experiments on the MOT we can assume that the density is almost constant along the transverse direction, whereas in the case of dipole trapped sample it is not.

Taking into account the above considerations we can express the phase shift and absorption of an ensemble of multilevel atoms with an inversion operator of $\hat{\sigma}_z^{(FF')} = \hat{\sigma}_{FF} - \hat{\sigma}_{F'F'}$ using Eq.(2.40), Eq.(2.42), and Eq.(2.43) as:

$$\phi_\Delta = \frac{\phi_0}{l}\sum_{F,F'} S_{FF'}\frac{\frac{\gamma}{2}\Delta_{FF'}}{\Delta_{FF'}^2 + \left(\frac{\gamma}{2}\right)^2}\int_0^l \hat{\sigma}_z^{(FF')}(\tau_p)dz \tag{2.44}$$

$$\alpha_\Delta = \frac{\phi_0}{l}\sum_{F,F'} S_{FF'}\frac{\left(\frac{\gamma}{2}\right)^2}{\Delta_{FF'}^2+\left(\frac{\gamma}{2}\right)^2}\int_0^l \hat{\sigma}_z^{(FF')}(\tau_p)dz \tag{2.45}$$

To obtain the last equations we have also substituted the value of the coupling constant $|g|^2$ for the case of the alkali D line transitions as it is shown in Appendix B [Eq.(B.8)].

$$|g_{FF'}|^2 = (2J+1)\frac{c}{l}\frac{\lambda^2}{4\pi A}\frac{\gamma}{2}S_{FF'} \tag{2.46}$$

When calculating the mean values of $\langle\phi_\Delta\rangle$ and $\langle\alpha_\Delta\rangle$ in Eq.(2.44,2.45) the integral gives l and we factor out a dimensionless factor ϕ_0 expressed through atomic sample and light parameters:

$$\phi_0 = \frac{\lambda^2 l\mathcal{N}}{2\pi} = \frac{|g_{FF'}|^2 l}{\frac{\gamma}{2}c}N_{at} \tag{2.47}$$

The phase shift grows as the atomic density grows. In practise, it is often preferable to have large detuning of the probe light in order to keep the rate of absorption low. Hence, at a fixed detuning, the higher the density of the atomic sample the bigger the phase shift.

2.3.4 Off-resonant interaction

In the following lines we will describe a case of an interaction that weakly couples the ground and excited state via an optical field that is detuned by an amount bigger then the hyperfine splitting of the excited state. The analysis is based on the alkali metal level structure and in particular the atomic Cs.

The interaction hamiltonian in Eq.(2.28) can be rewritten in the case of slowly varying amplitude approximation with the help of the Eq.(2.38) and Eq.(2.39).

$$\hat{H}_i = -\hbar\left[\sum_{F'=2}^{4}\frac{|g_{3F'}|^2\Delta_{3F'}\hat{a}^\dagger\hat{a}}{\Delta_{3F'}^2+\left(\frac{\gamma}{2}\right)^2}\left(\hat{\sigma}_{33}-\hat{\sigma}_{F'F'}\right)+\sum_{F'=3}^{5}\frac{|g_{4F'}|^2\Delta_{4F'}\hat{a}^\dagger\hat{a}}{\Delta_{4F'}^2+\left(\frac{\gamma}{2}\right)^2}\left(\hat{\sigma}_{44}-\hat{\sigma}_{F'F'}\right)\right] \tag{2.48}$$

Now it is convenient to express the inversion operators with the operator of number of atoms and the $\hat{J}_z$ projection of the collective atomic angular momentum from Sec.2.1.4 as $\hat{\sigma}_{33} = \frac{\hat{N}_{tot}}{2} - \hat{J}_z$ and $\hat{\sigma}_{44} = \frac{\hat{N}_{tot}}{2} + \hat{J}_z$. This in a sense mean that the population of the ground hyperfine states is expressed as the sum of half of the total population and the population number difference.

In the off-resonant case the excited state is little populated, thus we can replace the $\hat{\sigma}_{F'F'}$ with zero. Then the population operators $\hat{\sigma}_{33}$ and $\hat{\sigma}_{44}$ can be pulled out of the sum. Further, it is possible to chose a detuning Δ_0 at which the two sums in Eq.(2.48) are equal and have opposite sign [see also Fig.2.3(a)]. Hence, at that particular detuning the mean phase shift in Eq.(2.42) will vanish for equal populations of the two ground state hyperfine levels. Then the interaction Hamiltonian becomes:

$$\hat{H}_i = \hbar\tilde{\kappa}\left(\frac{\hat{n}}{2}+\hat{S}_z\right)\hat{J}_z \tag{2.49}$$

In the last equation we have made a step forward to describe the light field interacting with atoms as propagating in an interferometer with two arms, probe arm which contains the atoms and a reference arm. Then the photon number operator $\hat{a}^\dagger\hat{a}$ in Eq.(2.48) is the one which describes the photon flux in the probe arm. We express it as half of the input photon

number $\hat{n}$ plus an operator $\hat{S}_z$ describing the difference between the photon numbers in the two arms i.e. $\hat{S}_z = \frac{1}{2}(\hat{a}^\dagger_{pr}\hat{a}_{pr} - \hat{a}^\dagger_{ref}\hat{a}_{ref})$. The last operator is equivalent to the Stock's operators for the light polarization in polarization rotation experiments [5,7,26,27] or the operator of the difference in the number of photons between the two arms of the separated arm interferometer as described in [28]. Additional information of $\hat{S}$ is provided in Ch.4 in the context of light interferometers.

The interaction strength depends on the value of the coupling constant at a detuning Δ_0. The last is is given by:

$$\tilde{\kappa} = \sum_{F'=2}^{5} \frac{|g_{3F'}|^2 \Delta_0}{\Delta_0^2 + \left(\frac{\gamma}{2}\right)^2}. \tag{2.50}$$

The physical meaning of the coupling constant will be also discussed in the scope of the collective light atom coupling in Ch.5 and in the Outlook. For now we will only restrict to noting that the hamiltonian in Eq.(2.49) in the off-resonant limit describes a quantum non-demolition measurement (QND) [5] that generates non-classical spin states [2,4].

The imprint of the atomic variable on the light phase via the interaction Hamiltonian in Eq.(2.49) can be also interpreted in terms of light phase change, by rewriting the phase shift from Eq.(2.42) in the form presented in [11]:

$$\phi_\Delta = \frac{\phi_0}{2}\left[(1+\beta)\sum_{F'=3}^{5} S_{4F'}\frac{\frac{\gamma}{2}\Delta_{4F'}}{\Delta_{4F'}^2 + \left(\frac{\gamma}{2}\right)^2} + (1-\beta)\sum_{F'=2}^{4} S_{3F'}\frac{\frac{\gamma}{2}\Delta_{3F'}}{\Delta_{3F'}^2 + \left(\frac{\gamma}{2}\right)^2}\right] \tag{2.51}$$

$$\beta = \frac{\mathcal{N}_{F=4} - \mathcal{N}_{F=3}}{\mathcal{N}_{at}} = \frac{\langle \hat{J}_z \rangle}{\langle \hat{J} \rangle} \tag{2.52}$$

where β is the population number difference connected with the $\hat{J}_z$ component of the collective pseudo-spin operator.

Let us now suppose that $\beta = 0$ and the probe light is detuned by Δ_0 from the cycling transition as shown in Fig.2.3. Then the coherent probe field will acquire a phase shifts from the two equally populated ground hyperfine levels separately, which would have the same absolute value and opposite signs, thus giving a zero overall phase shift. Then any excursion of the population number difference $\hat{J}_z$ will reflect in a non-zero phase shift.

Chapter 3

Atomic sample preparation

This chapter describes spectroscopy properties of atomic caesium, basic theory on laser cooling in a Magneto-Optical Trap (MOT) and optical trapping using an Far-Off Resonant optical Dipole Trap (FORT). The discussion follows the experimental procedure of atomic sample preparation. The use of the cold atoms is justified due to the longer interaction times and negligible Doppler broadening of the atomic transition at lower temperatures. The loading of the cold sample into an optical trap enables higher atom number density and allows for efficient coupling of an inhomogeneous light beams to a cigar-shaped atomic samples.

3.1 Caesium level diagram

Cesium is an alkali metal with a mass of $M = 133$a.u. and a periodic table number $Z = 55$. As an alkali metal it has only one valence electron which can have either $S = 1/2$ or $S = -1/2$ spin angular momentum. Then via the L-S coupling the total electronic angular momentum becomes $J = 1/2$ and $J = 3/2$ thus giving rise to two fine structure components $6P_{1/2}$ and $6P_{3/2}$ of the first excited state with $L = 1$. The separation of these two states from the ground state $6S_{1/2}$ in wavelength units is 894.592 nm and 852.347 nm, respectively (see Fig.3.1(a)). In the atomic spectroscopy literature they are known as doublet lines, and often called as D_1 and D_2 lines. The coupling of the total electronic angular momentum J with the nuclear spin $I = 7/2$ results in a total atomic angular momentum of $F = J + I$. This so called hyperfine interaction splits the electronic states to two $F = 3, 4$ hyperfine levels in the ground state with a separation in frequency units of 9.19263 GHz. The microwave transition between these levels is used as an international atomic frequency standard worldwide. Going back to the first excited state we get values for the total atomic angular momentum of $F' = 3, 4$ and $F' = 2, 3, 4, 5$ for the $6P_{1/2}$ and $6P_{3/2}$, respectively. The energy separations between the hyperfine states of the two excited electronic states are 1.16768 GHz and 151 MHz, 201 MHz, and 251 MHz for $6P_{1/2}$ and $6P_{3/2}$ manifolds, respectively. The hyperfine transitions of the D_2 line are worldwide used for laser cooling of the alkalis. The natural linewidth of the D_2 line is $\gamma = \Gamma/2\pi = 5.2$ MHz. In the case of ^{133}Cs the cooling transition is the so-called cycling transition $6\mathrm{S}_{1/2}(\mathrm{F} = 4) \rightarrow 6\mathrm{P}_{3/2}(\mathrm{F}' = 5)$. The name cycling comes from the fact that the transition to the lower ground state hyperfine level $F = 3$ is dipole forbidden, since the excited state is $F' = 5$. This would mean that the atom can perform many absorption cycles before being pumped to the lower hyperfine ground state. The mechanism of that

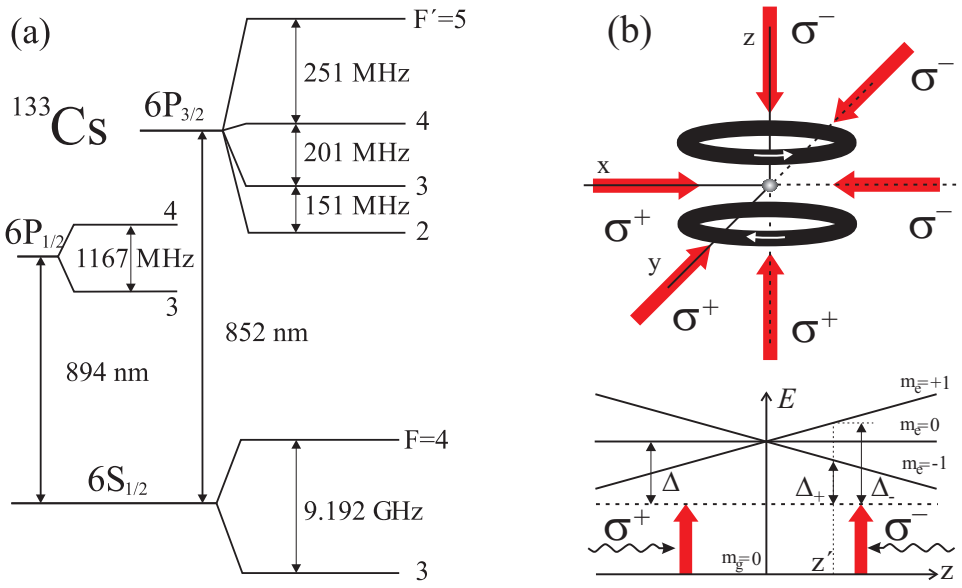

Figure 3.1: *Caesium levels diagram (a). Schematic description of MOT (b).*

depumping is via populating the lower laying $F' = 4$ state. Unfortunately, the probability of that process to happen is high enough to overcome the cooling effect on the cycling transition. To bring back the atom into the cooling cycle an additional "hyperfine repump" laser couples the ground state $F = 3$ to the excited state $F' = 4$ via the transition $6S_{1/2}(F = 3) \rightarrow 6P_{3/2}(F' = 4)$.

3.2 Laser cooling of neutral atoms

The idea that the light can exert pressure has been explored for many centuries. However the first experimental evidence has been observed in 1933 by R. Frisch [29]. In 1970 Ashkin has showed that an optical transitions in alkali metal atoms can produce a force that can be used for atom trapping [30]. The ability of the light force to guide macroscopic particles has been proved in [31]. In 1975 Hänsch and Schawlow [32] has proposed that the light could exert substantial force to be potentially used for cooling of atoms. Since that time directionally cold atomic beams have been created giving rise to a possibility of using the light absorption to slow an atomic vapor. The combination of both laser light and spatially varying magnetic fields has proven to be an efficient way to slow an atomic beams [33]. Later, it has been realized [34] that using three dimensional optical molasses one can reduce the atomic kinetic energy thus cooling the atomic vapor to low temperatures. However, in most of the cases the lifetime of the molasses is limited in some milliseconds thus preventing of long interaction with light fields for the sake of spectroscopy. Then the implementation of spontaneous force trap [35] which combines the light scattering force with a quadrupole magnetic field has made it possible to open a new branch of the atomic spectroscopy known as laser cooling and trapping. The spontaneous force trap has also been named as magneto-optical trap or shortly MOT. The theory of atom cooling using light in a MOT is described elsewhere [36, 37] and in the following few pages we make a brief introduction to laser cooling and trapping techniques.

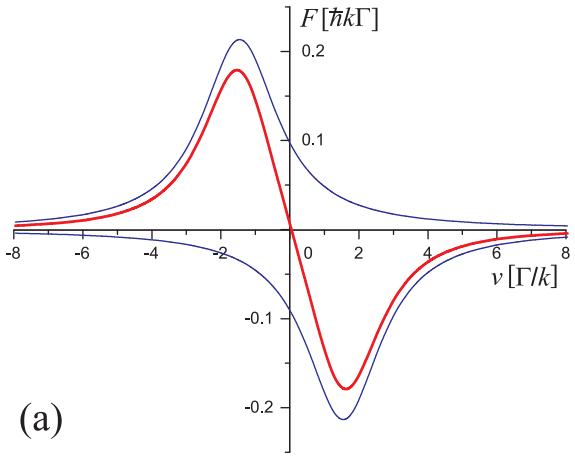

Figure 3.2: The force on an atom in the case of optical molasses (a)

3.2.1 Magneto-optical trap

The magneto-optical trap consists of spatially varying magnetic field $B(z) = bz$ created by gradient coils with opposing currents of the same value and a cooling laser light detuned slightly below the atomic resonance Fig.3.1(b). Since the magnetic field drops linearly towards the center of the trap this would mean that the atomic transition frequency will change in the same manner due to the position dependent Zeeman shift. Let us consider the case of transition $J_g = 0 \rightarrow J_e = 1$. The ground state does not shift in an external field $m_g = 0$, while the excited state has magnetic sublevels with $m_e = -1, 0, +1$. The process of cooling can be explained with an optical pumping between the magnetic sublevels of the ground and excited states for a slowly moving atom. Suppose that an atom is at a position z' in Fig.3.1(b). At that position the magnetic field of the trap shifts the sublevel $m_e = -1$ of the excited state closer to resonance with the circularly polarized beam σ^-. Thus the atom initially in $m_e = -1$ state will scatter more photons from the beam counteracting its motion than the co-propagating beam. Hence the light scattering force will push the atom towards the center of the trap. Oppositely, an atom moving to the left and initially in $m_e = +1$ state at a position $-z'$ will predominantly scatter photons from the σ^+ beam and hence will be pushed toward the trap center. During these cycles of absorption and subsequent spontaneous emission the atom loses kinetic energy due to the recoil momentum transfer of the oppositely propagating photons. As a results the atoms are accumulated around the trap center and stored for long times. According to discussion above we can extend the 1D case to 3D having counterpropagating beams for all three coordinate axes. The scheme can also be applied with the same success to the general case of $J_g \rightarrow J_e = J_g + 1$.

The force acting on an atom is a result of two forces from the σ^- and σ^+ beams. Let's denote these two forces as F_- and F_+. They depend on the cooling light parameters: $s_0 = I/I_s$ the saturation parameter on resonance and $I_s = \pi\hbar\nu\gamma/3$ is the saturation intensity, the detunings $\Delta_\pm$, and photon momentum $\hbar\mathbf{k}$.

$$\mathbf{F}_\pm = \pm\frac{\hbar\gamma\mathbf{k}}{2}\frac{s_0}{1 + s_0 + (2\Delta\pm/\gamma)^2} \tag{3.1}$$

The detunings $\Delta_\pm$ for each of the laser beams depend on atom velocity and magnetic field.

$$\Delta_\pm = \Delta \mp \mathbf{k}\cdot\mathbf{v} \pm \frac{(g_e m_e - g_g m_g)\,\mu_B B}{\hbar} \tag{3.2}$$

The second term in Eq.(3.2) denotes the doppler shift of the atomic transition due to the atomic velocity $\mathbf{v}$. The third term is the Zeeman shift of the atomic transition frequency, proportional to the magnetic field B.

Then the resulting force on an atom is $\mathbf{F} = \mathbf{F}_+ + \mathbf{F}_-$. Note that the forces in Eq.(3.1) are position dependent since the magnetic field depends linearly on the distance to the trap center i.e. $B(z) = bz$ where b denotes the magnetic field gradient. If we fix the position the force $\mathbf{F}$ will look exactly as the one in the case of optical molasses [see Fig.3.2(a)] as a function of atom velocity.

In the limit of small Doppler and Zeeman shifts the force on an atom can be approximated to an expression which looks exactly like a damped oscillator equation in the classical mechanics.

$$\mathbf{F} = -\beta\mathbf{v} - \kappa\mathbf{r} \tag{3.3}$$

where the damping coefficient β and the spring constant κ are given by the following relations [36]:

$$\beta = \frac{8\hbar k^2 s_0 \frac{\Delta}{\gamma}}{\left[1 + s_0 + \left(\frac{2\Delta}{\gamma}\right)^2\right]^2}, \qquad \kappa = \frac{(g_e m_e - g_g m_g)\,\mu_B b}{\hbar k}\beta \tag{3.4}$$

In the last set of equations the value of $k = |\mathbf{k}|$ is the modulo of the light propagation vector and in Eq.(3.3) the magnetic field is represented as a vector $\mathbf{B} = b\mathbf{r}$, where b denotes the magnetic field gradient.

Once the force is known the equation of motion for an atom can be found using the second Newton's principle. The differential equation governing the motion of an atom in the MOT is then:

$$\ddot{\mathbf{r}} + \Gamma_{MOT}\dot{\mathbf{r}} + \omega_{MOT}^2\mathbf{r} = 0. \tag{3.5}$$

It is straightforward that the above equation describes damped harmonic motion of an atom in the trap as expected from the origin of the force in Eq.(3.1). The damping rate of the motion is defined as $\Gamma_{MOT} = \beta/M$ and the oscillations in the trap are given by $\omega_{MOT} = \sqrt{\kappa/M}$. For a magnetic field gradient of 10 G/cm the oscillation frequency is typically few kHz and the damping rate is of the order of few hundred kHz. Then the motion is overdamped with characteristic restoring time of $2\Gamma_{MOT}/\omega_{MOT}^2$.

The temperature of the atoms in the MOT is expected to be comparable with that of a 3D optical molasses. In the early days it was believed that the Doppler limit is the lower temperature that can be achieved with laser cooling. The limiting Doppler temperature for low light intensity is found to be proportional to the detuning of laser light [38]:

$$k_B T_D = \frac{\hbar\gamma}{4}\frac{1 + (2\Delta/\gamma)^2}{2|\Delta|/\gamma}. \tag{3.6}$$

Setting the red detuning to $\Delta = \gamma/2$ gives minimum value for the Doppler temperature of $T_D = \frac{\hbar\gamma}{2k_B}$. For atomic caesium the value is 124 μK. However, later much lower temperatures have been measured for sodium atoms released from 3D optical molasses [38]. This

on the other hand stimulated the development of the sub-Doppler cooling theory [39, 40] in order to explain these lower temperatures. We will give short theoretical description of these sub-Doppler cooling techniques in the following section.

3.2.2 Sub-Doppler cooling techniques

When two light beams with orthogonal linear polarization are counterpropagating the resulting light field exhibits spatially dependent polarization as shown in Fig.3.3(a). This is the so called polarization gradient. The two light fields $\mathbf{E}_1(\mathbf{x}, z, t) = E_0\mathbf{x}\cos(\omega t + kz)$ and $\mathbf{E}_2(\mathbf{y}, z, t) = E_0\mathbf{y}\cos(\omega t - kz)$ will superpose and the resulting field is expressed by:

$$\mathbf{E}(z) = E_0\left[(\mathbf{x}+\mathbf{y})\cos(\omega t)\cos(kz) + (\mathbf{x}-\mathbf{y})\sin(\omega t)\sin(kz)\right] \quad (3.7)$$

$$\mathbf{E}(z) = 2E_0\cos\omega t\left[(\mathbf{x})\cos(kz) + (\mathbf{y})\sin(kz)\right] \quad (3.8)$$

where $\mathbf{x} = (1, 0, 0)$ and $\mathbf{y} = (0, 1, 0)$ are the polarization vectors of the light beams, $k = 2\pi/\lambda$ is the wavenumber, z is the distance along the propagation axis. It is seen that at z=0 the polarization is linear forming an angle w.r.t. the x-axis of $\pi/4$, further at $\lambda/8$ or $kz = \pi/4$ the polarization converts to σ_-. At a distance of quarter-wavelength the resulting field is again linear but with a polarization rotated at an angle of $-\pi/4$ along the x-axis and so forth. In the case of σ_+ σ_- beams another expression can be derived but this time the polarization only rotates at an angle of $\pi/2$ along the propagation axis at a distance of $\lambda/4$ [see Eq.(3.7)]. These two polarization configurations, however, lead to completely different sub-Doppler cooling schemes.

Suppose that the transition coupled by the molasses beams is $J_g = 1/2 \rightarrow J_e = 3/2$. In the case of linear polarizations the light shift changes along the propagation axis in accordance with polarization change from linear to circular and again to linear with a period of $\lambda/2$ [Fig.3.3(a)]. The shift of the $m_g = +1/2$ ground state is largest for σ_+ light, whereas the $m_g = -1/2$ state is maximally shifted for σ_-. The change is due to the different Clebsh-Gordan coefficients for the different polarization of the coupling light. In the case of the σ_+ σ_- polarized beams the sublevels of the ground state are equally shifted and the energy shift does not depend on the position along the propagation axis, since the polarization is always linear [Fig.3.3(b)].

Assume that an atom is moving along z axis in a 1D molasses beams as in Fig.3.3(a). At the position of $\lambda/8$ the atom initially in $m_g = -1/2$ will remain in that state if the velocity of the atom is such that it travels a distance of $\lambda/4$ before being optically pumped to the $m_g = +1/2$ state i.e. to the bottom of the next potential valley at $z = 3\lambda/8$. During this travel the atom "climbs" a potential hill and reduces its kinetic energy. Thus on average an atom will remain on the same magnetic sublevel climbing the potential hill-Sisyphus effect. The equilibrium temperature in this cooling configuration according to Dalibard et al. [39] is found to be of the order of the light shift of the ground state:

$$k_B T_{eq} = \frac{\hbar\Omega^2}{8|\Delta|} \quad (3.9)$$

where Ω is the Rabi frequency per molasses beam. Since the calculation in [39] is in the semiclassical approach the limiting temperature in optical molasses will always be higher

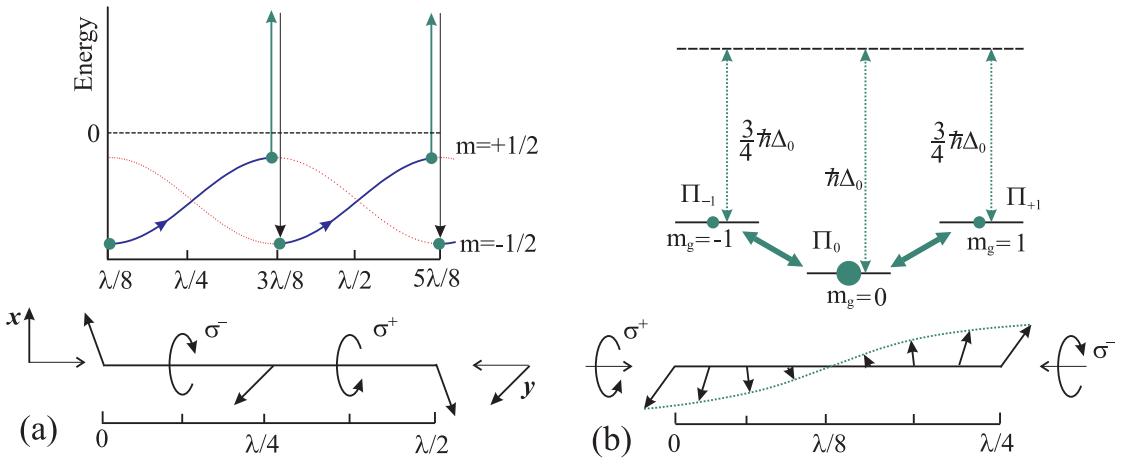

Figure 3.3: *Polarization gradients in* lin⊥lin *and Sisyphus effect on a slowly moving atom in* lin⊥lin *optical molasses (a). Polarization gradients in* σ_+ σ_- *configuration and equilibrium population of the ground state sublevels (b).*

than the recoil temperature given by the kinetic energy associated with one photon recoil:

$$k_B T_R = \frac{\hbar^2 k^2}{2M} \tag{3.10}$$

In σ_+ σ_- optical molasses the damping force has different origin. It arises from unbalanced radiation pressures due to different absorption of the two counter-propagating beams. However, the force is not due to the Doppler effect but results from the different population of the magnetic sublevels $m_g = -1$ and $m_g = +1$ of the ground $J_g = 1$ state. If an atom with velocity v is moving towards $z > 0$ it will absorb more photons from the σ_- beam than from the co-propagating σ_+. In the atomic rest frame which rotates with angular velocity of kv the polarization of light is always parallel to the quantization axis, thus allowing only for π transitions to be produced. Then the interaction hamiltonian contains a term which results from the rotation of the light polarization and is equal to $\mathbf{V}_{rot} = kv\mathbf{J_z}$ according to [39]. The mean value of $\langle \mathbf{J_z} \rangle$ is proportional to the population number difference between the levels $m_g = -1$ and $m_g = +1$. The population difference between these levels changes in accordance with the angle of rotation of the linear polarization along the propagation axis [Fig.3.3(b)].

$$\Pi_{+1} - \Pi_{-1} = \frac{40}{17}\frac{kv}{\Delta_0} \tag{3.11}$$

where Δ_0 is the light shift of the $m_g = 0$ state in frequency units. If the atom is at rest the populations of the different sublevels have their steady state values of $\Pi_{-1} : \Pi_0 : \Pi_{+1} = 4/17 : 9/17 : 4/17$. If the atom is moving then non-adiabatic couplings between the Zeeman sublevels appear so that the equilibrium populations in Fig.3.3(b) changes in accordance with Eq.(3.11). In short, the motion induced atomic orientation in the ground state creates a friction or damping force due to the induced imbalance of the photon absorption rates of the two oppositely propagating molasses beams. The equilibrium temperature of this cooling method is calculated by the authors of [39] to be of the order of the one obtained

in the lin⊥lin configuration

$$k_B T_{eq} = \frac{\hbar\Omega^2}{10|\Delta|} \tag{3.12}$$

Note that for a ground state of $J_g = 1/2$ the second cooling mechanism does not work since in that state no alignment can exist. Despite of that in alkali metals when using transitions between hyperfine magnetic sublevels the $\sigma_+\sigma_-$ polarization gradient cooling can be applied since the total angular momentum of the ground states is always higher than 1/2.

3.2.3 Dark states

Another method of attaining low temperatures in laser cooling physics is the use of states that cannot be excite by light. These states are called dark states. The dark state have different origin. In the case of coherent quantum superposition states created by Raman coupling between ground state hyperfine components in the alkalis the excitation probability of the excited state vanishes and a coherent population transfer can be achieved, between the hyperfine components. These processes creating dark states are coherent population trapping (CPT) [41] and electromagnetically induced transparency (EIT) [42]. Other type of dark states are the ones that simply cannot be excited by light since the light is very far detuned and the excitation probability is negligible. For example in Cs atom the ground state hyperfine component $F = 3$ is a dark state for the cooling light, that couples the cycling transition $6\mathrm{S}_{1/2}(\mathrm{F} = 4) \rightarrow 6\mathrm{P}_{3/2}(\mathrm{F}' = 5)$. An atom on $F = 3$ cannot be excited by the cooling light to one of the $6P_{3/2}$ hyperfine states, because the light is about 9 GHz detuned with respect to any of the transitions $F = 3 \rightarrow F' = 2, 3, 4$. The lower hyperfine state of the alkalis plays an important role in reducing the light scattering force for the purpose of loading the cold atomic sample from a MOT into an optical dipole trap. The experimental sequence for loading an optical dipole trap is described in detail in the experimental part of the thesis [Ch.7].

3.3 Optical dipole trap

The section deals with theoretical concepts of the optical trapping of neutral atoms. The theory behind the optical trapping [43] is explained by the dressed state picture of the atom light interaction. Since the first demonstration of optical trapping by Chu et al. [44] the optical dipole traps have became an efficient tool for storing cold atomic samples. The first optical dipole trap had detuning of only -650 GHz, but nowadays traps are very far from resonance with a wavelength detuning ranging from several nm for the FORT to the extreme 10 μm in the case of quasi-electrostatic traps (QUEST) created by CO_2 lasers. This large detunings have allowed formation of all-optical Bose-Einstein Condensation (BEC) of alkali atoms [45,46] and Li_2 molecules [47]. Very tight dipole traps has been produced to trap a single atom [48]. The standing wave dipole traps allowed the manipulation of single atoms [49–51] in an optical conveyor belt [52] for the use in quantum information with neutral atoms [53]. Standing wave dipole traps has also opened the way two a very interesting field of cold atoms in optical latices [54, 55] for both cold atoms and ultra-cold quantum gasses as BEC [56]. The cancelation of the stark shift induced by the dipole trap laser on the intercombination transition in the alkali-earth atoms [57] has enabled the construction of optical lattice clocks [58]. High density large atomic clouds in red detuned dipole traps has been observed in both single beam focused trap and optical

lattice [59, 60]. An extensive analysis of the loading dynamics of optical dipole traps has been done in [61] and a review of dipole traps has been made in [62].

3.3.1 Classical Lorentz model

The dipole force on an atom can be explained with the classical Lorentz model of a driven induced dipole. Suppose that an electric field of the form $\mathbf{E}(\mathbf{r},t) = \frac{1}{2}\left[E(\mathbf{r})\exp\left(-i\omega t\right) + c.c.\right]$ induces a dipole moment of an atom $\mathbf{p} = \alpha(\omega)\mathbf{E} = -e\mathbf{r}$. The dipole potential associated with the induced dipole is given by:

$$U(\mathbf{r}) = -\frac{1}{2}\langle \mathbf{p}\cdot\mathbf{E}\rangle = -\frac{1}{2\epsilon_0 c}\Re(\alpha)I(\mathbf{r}) \tag{3.13}$$

where ϵ_0 is the electric permeability of the vacuum, c speed of light, $\alpha(\omega)$ is the induced complex atomic scalar polarizability, and $I(\mathbf{r})$ is the intensity of the light beam. It is seen that the dipole potential depends on the position $\mathbf{r}$. Hence, there will be a dipole force acting on an atom:

$$F = -\nabla U(\mathbf{r}) = \frac{1}{2\epsilon_0 c}\Re(\alpha)\nabla I(\mathbf{r}) \tag{3.14}$$

Along with this dispersive interaction proportional to the $\Re(\alpha)$, there is an absorption which scales as the $\Im(\alpha)$. The power dissipated by the atomic dipole is characterized by the scattering rate or absorption rate Γ_{sc}:

$$\Gamma_{sc}(\mathbf{r}) = \frac{1}{\hbar\epsilon_0 c}\Im(\alpha)I(\mathbf{r}). \tag{3.15}$$

In the classical Lorentz model the motion of the electron around the nucleus induced by the light field is described by a driven oscillator equation and the atomic polarizability is expressed as a function of the driving field frequency:

$$\alpha(\omega) = -\frac{6\pi\epsilon_0 c^3\gamma}{\omega_0^2}\frac{1}{\omega^2-\omega_0^2+i(\omega^3/\omega_0^2)\gamma}. \tag{3.16}$$

where γ is the on-resonance damping rate and ω_0 is the atomic resonance frequency. Substituting equation Eq.(3.16) in equations Eq.(3.13) and Eq.(3.15) we arrive at the final expressions for the potential depth $U(\mathbf{r})$ and photon scattering rate in the classical Lorentz description of the dipole trap:

$$U(\mathbf{r}) = \frac{3\pi c^2}{2\omega_0^3}\frac{\gamma}{\Delta}I(\mathbf{r}). \tag{3.17}$$

$$\Gamma_{sc}(\mathbf{r}) = \frac{3\pi c^2}{2\hbar\omega_0^3}\left(\frac{\gamma}{\Delta}\right)^2 I(\mathbf{r}) \tag{3.18}$$

where $\Delta = \omega - \omega_0$ is the detuning of the trapping laser w.r.t the atomic resonance. In the last equation we have also assumed that the detining Δ is small compared to the optical frequencies ω and ω_0 thus having the ratio between them $\omega/\omega_0 \approx 1$.

The dipole potential depth is proportional to $1/\Delta$, whereas the scattering rate is proportional to $1/\Delta^2$. It is then clear from the above equations that the far off-resonant dipole trap has the advantage over the near resonant that the scattering rate of the FORT is much lower. Another consequence is that when the detuning is negative $\Delta < 0$ the trap

is called red detuned and atoms are collected at the maximum intensity. If the detuning is positive $\Delta > 0$ the trap is blue detuned and the atoms are repelled from the maximum of the light intensity towards its minimum.

The choice of the detuning demands different experimental realization of optical trapping. The red detuned traps are easily produced by focusing a gaussian light beam using a lens. The blue detuned traps require additional manipulation to create local minima of the light field. The main experimental configurations employ focused "donut" light beams [63], light sheets [64] or a rapidly rotating single focused beam [65].

3.3.2 Quantum description. Dressed states.

In this section we will give in short the quantum mechanical description of the calculation of the dipole trap potential and the associated scattering rate using the full quantum treatment of light interacting with a two level atom via the electric dipole interaction. An atom in the ground state $|g\rangle$ and a light field with $|n\rangle$ photons can be represented by the combined product state $|g,n\rangle = |g\rangle \otimes |n\rangle$. When the atom absorbs a photon from the field the state becomes $|e,n-1\rangle = |e\rangle \otimes |n-1\rangle$ which means that the atom is excited to state $|e\rangle$ and the number of photons in the field has decreased by one $|n-1\rangle$.

The system hamiltonian $\hat{H}$ is a sum of the atomic hamiltonian $\hat{H}_A$, the light hamiltonian $\hat{H}_L$, and the electric dipole interaction hamiltonian $\hat{H}_{ED}$. These three terms can be expressed, as it has already been done in Sec.2.3, in the following way:

$$\hat{H}_A = \hbar\omega_0 |e\rangle\langle e| \tag{3.19}$$

$$\hat{H}_L = \hbar\omega \left(\hat{a}^\dagger \hat{a} + \frac{1}{2}\right) \tag{3.20}$$

$$\hat{H}_{ED} = -\mathbf{d}\cdot\mathbf{E} = \frac{\hbar\Omega}{2}\left(|e\rangle\langle g|\hat{a}e^{-i\omega t} + |g\rangle\langle e|\hat{a}^\dagger e^{i\omega t}\right) \tag{3.21}$$

where ω_0 is the frequency of the atomic transition between the levels $|g\rangle$ and $|e\rangle$, ω is the frequency of the single mode field with annihilation operator $\hat{a}$, and Ω is the on-resonance Rabi frequency. It also must be noted that the atomic hamiltonian is referenced to the energy of the ground state which is taken to be zero, in contrast to Sec.2.3 where the reference is between the levels. The eigenvalues of the $\hat{H}$ in the field rotating frame are calculated in Appendix C. Here we only give the result:

$$E_\pm(n) = \hbar\left(-\frac{\Delta}{2} + \omega n \pm \frac{1}{2}\sqrt{\Delta^2 + \Omega^2 n}\right) \tag{3.22}$$

The corresponding eigenstates $|1n\rangle$ and $|2n\rangle$ to the eigenvalues of the Hamiltonian are the so-called "dressed" states [66] which are combined state of single mode electromagnetic field and a two-level atom and can be expressed in the basis of the product states $|g,n\rangle$ and $|e,n-1\rangle$ in the form:

$$|1n\rangle = \sin\theta|g,n\rangle + \cos\theta|e,n-1\rangle \tag{3.23}$$

$$|2n\rangle = \cos\theta|g,n\rangle - \sin\theta|e,n-1\rangle \tag{3.24}$$

where the mixing angle θ is defined as $\tan 2\theta = -\frac{\Omega\sqrt{n}}{\Delta}$. It can be noted that the dressed states depend on the number of photons in the field. A pictorial representation of the dressed state approach is shown in Fig.3.4. The combined light-atom states are separated

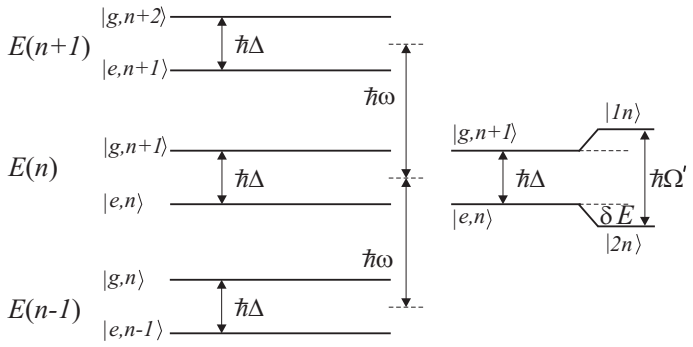

Figure 3.4: *Pictorial representation of the dressed state approach. Uncoupled combined states of atom and light (right) and dressed states (left).*

by the photon energy of the driving field $\hbar\omega$. The dressed states, on the other hand, are separated by the energy quanta associated with the generalized Rabi frequency $\hbar\Omega' = \hbar\sqrt{\Delta^2 + \Omega^2}$. The value of δE in the figure is the light shift of the state in presence of the radiation field with a very large detuning $\Delta \gg \Omega$ from the atomic resonance:

$$\delta E = \frac{\hbar\Omega^2}{4\Delta}. \tag{3.25}$$

Another interesting feature of the light shift in the dressed approach is that the ground state shifts differently depending on the sign of the detuning Δ. If the laser is red detuned $\Delta < 0$ the ground state is down-shifted w.r.t the unperturbed case, and for blue detuning $\Delta > 0$ the energy of the ground state is increased. The same applies for the excited state but with an opposite sign. In order to include the spatial dependance of the light shift we have to express the Rabi frequency in terms of the light intensity and the absorption linewidth. The absorption linewidth γ is expressed by the dipole operator matrix element [67] as:

$$\gamma = \frac{\omega_0^3 |\langle e|\mathbf{d}|g\rangle|^2}{3\pi\hbar\epsilon_0 c^3} \tag{3.26}$$

This equation along with the relation $\hbar\Omega = -E(\mathbf{r})|\langle e|\mathbf{d}|g\rangle|$ and inserting the light intensity via $I(r) = \frac{1}{2}c\epsilon_0 E(r)^2$ leads to the final expression for the light shift or equivalently the dipole potential

$$U(\mathbf{r}) = \delta E(\mathbf{r}) = \frac{3\pi c^2}{2\omega_0^3}\frac{\gamma}{\Delta} I(\mathbf{r}) \tag{3.27}$$

It is not surprising that the last result is the same as the one obtained from the classical model in Eq.(3.17). However in reality the atoms have many electronic levels and the model of a two level atom is not entirely accurate. These levels are coupled via dipole allowed transitions to the ground state, or to each other. Then in the presence of dipole trap field the resulting transitions will be driven with a strength, depending on the detuning and power of the driving laser (i.e. dipole laser), thus modifying the light shift or respectively the dipole potential. In order to apply Eq.(3.27) to a multilevel atom one has to know the dipole matrix elements $d_{ij} = \langle g_i|\mathbf{d}|e_j\rangle$, as defined in Ch.2, of the transitions from the ground states $|g_i\rangle$ to the excited states $|e_j\rangle$. The matrix element can be also written as the product of the reduced matrix element $||\mathbf{d}||$ and the Clebsch-Gordon coefficients C_{ij}

according to [23]. Whit this substitution the shift of the ground state $|g_i\rangle$ becomes:

$$\delta E_i(\mathbf{r}) = \frac{3\pi c^2}{2} \sum_j \frac{C_{ij}^2 \gamma_{ij}}{\omega_{ij}^3 \Delta_{ij}} I(\mathbf{r}) \tag{3.28}$$

The sum in the above equation is done over all excited states coupled to the ground state via the dipole allowed transition $|g_i\rangle \rightarrow |e_j\rangle$ with relevant detunings $\Delta_{ij} = \omega - \omega_{ij}$ where $\omega_{ij} = E_j - E_i$ the frequency of the earlier mentioned transition. The contribution of each excited state is determined by its transition strength factor C_{ij}^2. The last equation is valid for arbitrary detuning Δ_{ij}.

Now let us consider the case of alkali metal atoms. The level scheme of D line transitions are similar for all elements from the first group of the periodic table, thus we can use the level scheme of caesium in Fig.3.1 as an example to express our point. At detunings much larger than the fine structure splitting of the excited state $\Delta \gg \Delta'_{FS}$ both fine and hyperfine structure of the excited state are not resolved. Hence, we can pull the ω_{ij} out of the sum and use an effective natural linewidth γ. In this case we say that the trap is far-off-resonant and the hyperfine and fine structure do not necessarily has to be taken into account. In contrast to that in the case of detunings smaller than the fine splitting of the excited state the light shift depends on the polarization of the trapped light [62]. For linear polarization it still obeys Eq.3.28, whereas for $\sigma^{\pm}$ an additional term appears in the numerator [61].

In our experiment the dipole trap laser is far off resonant with a wavelength of 1030nm. Then the wavelength detunings from the $6P_{1/2}$ and $6P_{3/2}$ electronic states of Cs become 136 nm and 178 nm, whereas the fine structure splitting of the first electronic excited state is 42 nm. The light shift induced by this laser and consequently the optical trap potential can be calculated as:

$$U(\mathbf{r}) = \frac{\pi c^2}{2} \left(\frac{\gamma_{1/2}}{\omega_{1/2}^3 \Delta_{1/2}} + \frac{2\gamma_{3/2}}{\omega_{3/2}^3 \Delta_{3/2}} \right) I(\mathbf{r}) \tag{3.29}$$

where $\omega_{1/2}$ and $\omega_{3/2}$ are the detunings of the trap laser w.r.t. the transitions $6S_{1/2} \rightarrow 6P_{1/2}$ and $6S_{1/2} \rightarrow 6P_{3/2}$, with a natural linewidth of $\gamma_{1/2} = 4.56$ MHz and $\gamma_{3/2} = 5.22$ MHz, respectively.

3.3.3 Focused beam red-detuned dipole trap

This section is dedicated to the dipole trap realized in the present experiment. It is based on a single focused gaussian beam. Since the gaussian beam has a non-uniform intensity distribution it can be used to create a gradient of the electric field vector that translates into a dipole force caused by position dependent light shift or also called dynamical Stark shift. Generally speaking the dipole traps are result of the position dependent Stark shift of the atomic ground state as explained in the previous section. It is well known that focusing a gaussian beam of light leads to highest intensity at the waist position. Away from the waist it decreases quadratically with the position z and by a gaussian law in the direction r perpendicular to the beam propagation direction. The following system of equations describe the gaussian beam:

$$I(r) = \frac{c\epsilon_0 E^2}{2} \frac{w_0^2}{w(z)^2} \exp\left(-\frac{2r^2}{w(z)^2} \right) \tag{3.30}$$

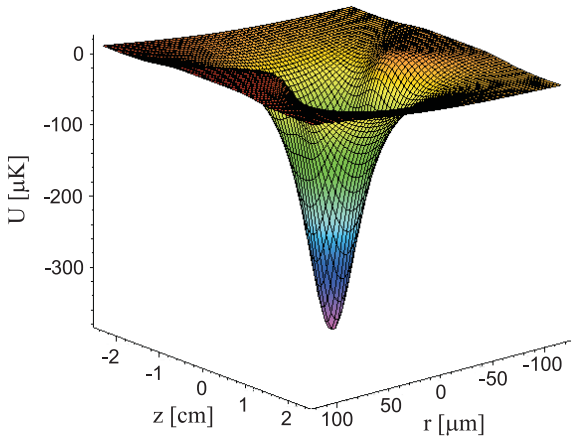

Figure 3.5: *Potential surface of the dipole trap*

$$w(z) = w_0\sqrt{1+\left(\frac{z}{z_R}\right)^2}, z_R = \frac{\pi w_0^2}{\lambda} \tag{3.31}$$

where w_0 is the waist radius, z_R the Rayleigh range and λ the light wavelength. Using the last equations we can transform the dipole potential $U(r)$ to:

$$U(r) = U_0\frac{w_0^2}{w(z)^2}\exp\left(-\frac{2r^2}{w(z)^2}\right) \tag{3.32}$$

$$U_0 = \frac{c^2 P}{w_0^2}\left(\frac{\gamma_{1/2}}{\omega_{1/2}^3\Delta_{1/2}} + \frac{2\gamma_{3/2}}{\omega_{3/2}^3\Delta_{3/2}}\right) \tag{3.33}$$

where the optical beam power $P = \frac{\pi c\epsilon_0}{4}E^2 w_0^2$ has been introduced. The above equations fully describe the spatial features of the optical trap and a sample potential surface is presented in Fig.3.5. It can be seen that due to the radial gaussian profile the confinement is much stronger in the radial direction. The radial scale is in micrometers, whereas the axial scale is in centimeters. The plotted surface is a result of a simulation which also takes into account the gravity potential $U_{Grav} = \frac{Mgr}{k_B}$. The resulting dipole potential will then be reduced by the $U_{Grav}(r)$. The optical trap in Fig.3.5 is created by a gaussian beam with a waist radius of $w_0 = 40$ μm and an optical power of 3.5 W at a laser wavelength of 1030 nm, which accounts to a potential depth of 380 μK. The rate at which an atom scatters the photons of the trapping field is easily expressed using the relation:

$$\hbar\Gamma_{sc} = \frac{\gamma_{1/2}}{\Delta_{1/2}}U_{1/2} + \frac{\gamma_{3/2}}{\Delta_{3/2}}U_{3/2} \tag{3.34}$$

with $U_{1/2}$ and with $U_{3/2}$ being the terms of the r.h.s. of Eq.(3.33). Finally, after substituting these terms in Eq.(3.34) we get:

$$\Gamma_{sc} = \frac{c^2 P}{\hbar w_0^2}\left(\frac{\gamma_{1/2}^2}{\omega_{1/2}^3\Delta_{1/2}^2} + \frac{2\gamma_{3/2}^2}{\omega_{3/2}^3\Delta_{3/2}^2}\right) \tag{3.35}$$

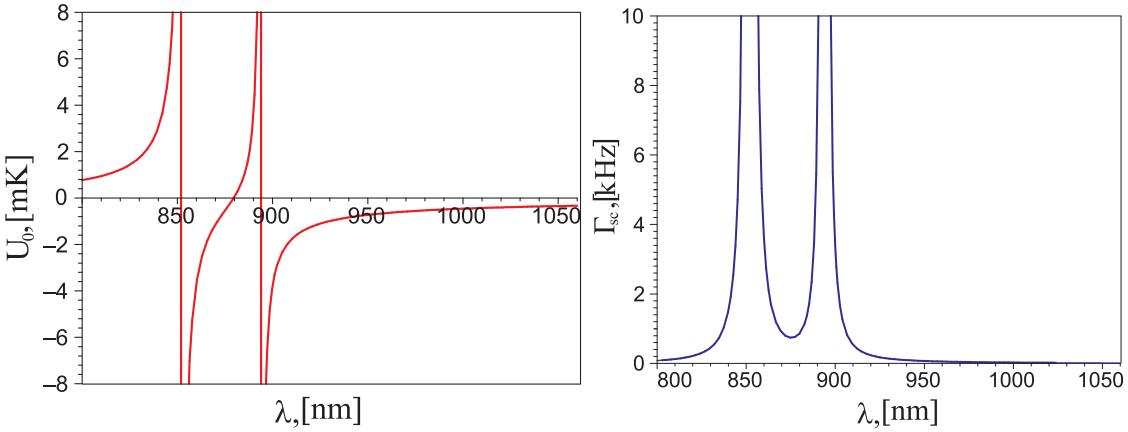

Figure 3.6: *Dipole potential (left) and scattering rate (right). Parameters listed in text.*

Again, as we have found in the classical calculation, the scattering rate Γ_{sc} scales as $1/\Delta^2$, whereas the dipole potential scales as $1/\Delta$.

The scattering rate and dipole potential curves are shown in Fig.3.6 for a trap with same parameters as in Fig.3.5 as a function of the dipole trap laser frequency. It is seen that the scattering rate for a dipole laser light at a wavelength of 1030 nm is very low. At the same time there is a reasonable trapping potential of 380 μK. The last value is more than enough to obtain a deep trap since the temperature of the atoms after the sub-Doppler cooling can be as low as several μK [59]. Note that for a wavelength of the laser of around 880 nm the light shifts of the two electronic states are opposite in sign and equal in absolute value, which practically means that no trapping effect can be observed for that wavelength.

The trap potential is also characterized by its oscillation frequencies. These are the frequencies at which trapped atoms oscillate inside the potential. From a classical point of view these oscillations are connected with a eigenfrequencies of a classical harmonic oscillator and are often used in experiments to characterize the trap potential [68]. The deeper the trap the higher the trap frequencies. A single beam focused trap has two eigenfrequencies i.e. radial ω_r and axial ω_{ax} defined as:

$$\omega_r = \sqrt{\frac{4U_0}{Mw_0^2}},\ \omega_{ax} = \sqrt{\frac{2U_0}{Mz_R^2}} \tag{3.36}$$

In the quantum mechanics case, if the trap depth is much higher than the temperature of the trapped atoms, we can assume that the potential is harmonic and the atoms will occupy different levels inside the trap with energies:

$$E_n = \hbar\omega_i \left(n + \frac{1}{2}\right) \tag{3.37}$$

where ω_i is the eigenfrequency of the trap which can be the radial or the axial one in Eq.(3.36) for a gaussian beam trap. It can also be seen that the trap frequencies differ significantly in the case of single focused beam trap due to the large difference between the w_0 and z_r.

Chapter 4

Mach-Zehnder Interferometer theory

This chapter gives an introduction to the interferometry used in the experiment to characterize the atomic sample by monitoring the phase shift of a coherent light beam. As it was mentioned in Ch.2.3 the off-resonant interaction is characterized by the phase shift of the light imposed by the atoms. In optics the light interferometry is the best way to measure optical phase. In the current experiment we use a Mach-Zehnder interferometer which has the atomic sample in one arm and the other is used as a reference.

We start the introduction with the quantum mechanical treatment of the light interferometer. Secondly we outline the main noise sources influencing the pulsed homodyne detection of the phase shift.

4.1 Interferometer calculations

The section introduces the operator method for the evolution of the light fields entering the interferometer [12, 69]. Let's assume we have a Mach-Zehnder interferometer which has in one arm an atomic sample inserted. The light with annihilation operator $\hat{a}$ enters the interferometer from the left as shown in Fig.4.1. The vacuum field is denoted by the annihilation operator with $\hat{b}$. The interferometer consists of two arms: an arm with atoms i.e. probe arm and a reference arm. The pathlength difference between the two arms is $(z_1 - z_2)$ with z_1 and z_2 being the optical lengths of the probe and reference arm, respectively. These lengths are measured between the first beamsplitter BS_1 and the second one BS_2.

4.1.1 Lossless interferometer

Firstly we will consider the case of a lossless interferometer, which would mean that the total number of photons entering the interferometer is conserved.

$$\hat{n}_{in} = \hat{a}^\dagger \hat{a} + \hat{b}^\dagger \hat{b} = \hat{d}_1^\dagger \hat{d}_1 + \hat{d}_2^\dagger \hat{d}_2 = \hat{n}_{out} = \hat{n} \tag{4.1}$$

The homodyne detection scheme works by subtraction of the number of photons emerging from the two outputs of the interferometer. This way the desired signal will be proportional

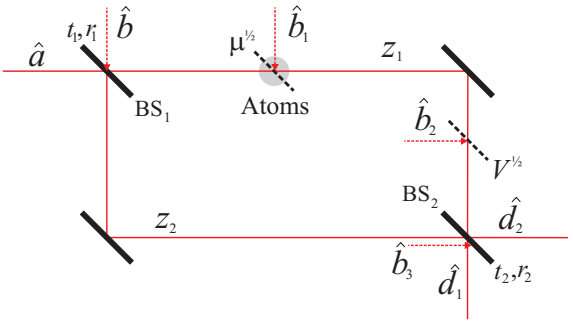

Figure 4.1: *A sketch of the interferometer operator model*

to the difference of the number of photons detected in each output port.

$$\hat{n}_- = \hat{d}_1^\dagger \hat{d}_1 - \hat{d}_2^\dagger \hat{d}_2 \tag{4.2}$$

The annihilation operators of the output fields $\hat{d}_1$ and $\hat{d}_2$ are expressed with the input fields annihilation operators $\hat{a}$ and $\hat{b}$ using the interferometer transformation matrix also called scattering matrix.

$$\begin{pmatrix} \hat{d}_1 \\ \hat{d}_2 \end{pmatrix} = \begin{pmatrix} S_{11} & S_{12} \\ S_{21} & S_{22} \end{pmatrix} \begin{pmatrix} \hat{a} \\ \hat{b} \end{pmatrix} \tag{4.3}$$

The scattering matrix $\mathbf{S}$ is a product of three matrices describing the transformation of the input operators after each beamsplitter $\mathbf{S}_{BS_2}$ and $\mathbf{S}_{BS_1}$ and a diagonal propagation matrix $\mathbf{S}_p$:

$$\mathbf{S} = \mathbf{S}_{BS_2}\mathbf{S}_p\mathbf{S}_{BS_1} = \begin{pmatrix} r_2 & it_2 \\ it_2 & r_2 \end{pmatrix} \begin{pmatrix} e^{ikz_1} & 0 \\ 0 & e^{ikz_2} \end{pmatrix} \begin{pmatrix} r_1 & it_1 \\ it_1 & r_1 \end{pmatrix} \tag{4.4}$$

In the last equation we have inserted the reflectivity and transmission of the two beamsplitters r_1, t_1 and r_2, t_2, respectively. After the transformation of the input operators the $\hat{n}_-$ operator is found to be:

$$\begin{aligned} \hat{n}_- = &\left(|S_{11}|^2 - |S_{21}|^2\right) \hat{a}^\dagger \hat{a} + \left(|S_{12}|^2 - |S_{22}|^2\right) \hat{b}^\dagger \hat{b} + \\ &+ \left(S_{11}S_{12}^* - S_{22}^* S_{21}\right) \hat{b}^\dagger \hat{a} + \left(S_{11}^* S_{12} - S_{22} S_{21}^*\right) \hat{a}^\dagger \hat{b} \end{aligned} \tag{4.5}$$

The initial light state is a coherent input in one channel and vacuum in the other $|\Psi\rangle = |\alpha\rangle_a \otimes |0\rangle_b$. Then the mean value of the $\hat{n}_-$ is:

$$\langle \hat{n}_- \rangle = \langle \Psi | \hat{n}_- | \Psi \rangle = \left[\left(r_1^2 - t_1^2\right)\left(r_2^2 - t_2^2\right) - 4r_1 r_2 t_1 t_2 \cos\left(k\Delta l\right)\right] \langle \hat{n} \rangle \tag{4.6}$$

In the last equation the only term which has a non-zero contribution to the mean is the one of the coherent input. The mean value of the vacuum field operator vanishes as well as the cross terms in Eq.(4.5). The new variable inserted in Eq.(4.6) is the pathlength difference between the two arms $\Delta l = z_1 - z_2$, which also includes the atomic contribution to the mean value of $\hat{n}_-$. The last equation has to be converted in terms of appropriate experimental variables. In the experiment, we use silicon photodiodes to detect the light. The photodiode does not conduct if there is no light incident on it. However, when light

is impinging on the photodiode the conductivity changes and the voltage drop across the semiconductor creates a photocurrent. The resulting photocurrent is proportional to the quantum efficiency of the detector ε, the elementary charge e, the mean photon number $\langle \hat{n}_- \rangle$ and inversely proportional to the duration of the interaction τ. Having these collected and inserting the value of the phase difference between the two arms as $\phi = k\Delta l$ we have:

$$\langle i_- \rangle = \frac{\varepsilon e \langle \hat{n} \rangle}{\tau} \left[\left(r_1^2 - t_1^2 \right) \left(r_2^2 - t_2^2 \right) - 4 r_1 r_2 t_1 t_2 \cos(\phi) \right] \tag{4.7}$$

In the case of symmetric interferometer with 50/50 beamsplitters we substitute the values of reflection and transmission coefficients with $r_1 = r_2 = t_1 = t_2 = 1/\sqrt{2}$. Then the first term in the square brackets of Eq.(4.7) vanishes. Calculating the coefficients in front of every term in Eq.(4.5) for a symmetric interferometer we obtain the following expression for the subtracted photon number operator as:

$$\hat{n}_- = \cos(\phi) \left(\hat{a}^\dagger \hat{a} - \hat{b}^\dagger \hat{b} \right) + \sin(\phi) \left(\hat{a}^\dagger \hat{b} + \hat{b}^\dagger \hat{a} \right) \tag{4.8}$$

The last equation can be compared to the result for a symmetric Mach-Zehnder interferometer characterized by unitary operations in the group SU(2) developed by Yurke et al [28]. According to this formalism the interferometer can be described by a set of Hermitian operators very similar to the projections of the atomic collective angular momentum operators introduced in Sec.2.1.4

$$\begin{aligned} \hat{S}_x &= \frac{1}{2}(\hat{a}^\dagger \hat{b} + \hat{b}^\dagger \hat{a}), \\ \hat{S}_y &= \frac{-i}{2}(\hat{a}^\dagger \hat{b} - \hat{b}^\dagger \hat{a}), \\ \hat{S}_z &= \frac{1}{2}(\hat{a}^\dagger \hat{a} - \hat{b}^\dagger \hat{b}), \end{aligned} \tag{4.9}$$

with a commutation relation $[\hat{S}_i, \hat{S}_j] = i\varepsilon_{ijk}\hat{S}_k$. The annihilation operators $\hat{a}$ and $\hat{b}$ represent the two fields entering or leaving a beamsplitter. When a measurement of the two outputs is performed the operator of interest is the $\hat{S}_z$, since it gives the photon's number difference between the two output channels. Using Eq.(4.9) we can express the detected photon number operator in Eq.(4.8) as:

$$\frac{\hat{n}_-}{2} = \cos(\phi)\hat{S}_z + \sin(\phi)\hat{S}_x \tag{4.10}$$

The vector operators $\hat{S}_i,\ i = x, y, z$ define a fictitious (S_x, S_y, S_z) space. The input interferometer state is a coherent one and can be described as a vector with a length of $\langle \hat{S}_z \rangle = \frac{\langle \hat{n} \rangle}{2}$ directed along the z axis. The output state then is rotated on an angle ϕ around the y axis as seen from Eq.(4.10).

This angular momentum formalism of the interferometer operation is useful for the description of the atom light interaction at the off-resonant limit.

4.1.2 Losses in the interferometer

The above calculations are made under assumption that the number of photons is preserved, which means that the equations do not account for absorption of photons or non-perfect mode overlap resulting in reduced visibility. To include these factors in the

problem we model the overlap and the losses due to absorption via mixing of the vacuum fields $\hat{b}_i$ on beamsplitters as shown in Fig.4.1. The beamsplitters have transmission of $\sqrt{\mu}$ and $\sqrt{V}$ with μ being the probe arm intensity transmission coefficient and V the coefficient describing the non-perfect mode overlap at the second beamsplitter.

The beamsplitters modify the scattering matrix of the interferometer and after the transformation of the operators, taking the expectation value of the photocurrent as described in Sec.4.1.1 and choosing 50/50 beamsplitters we arrive at:

$$\langle i_- \rangle = \frac{\varepsilon e \langle \hat{n} \rangle}{\tau} \sqrt{\mu V} \cos(\phi) \tag{4.11}$$

The last equation is a result of algebraic calculation of 5×5 matrix equation with column vectors having coordinates of $(\hat{a}, \hat{b}, \hat{b}_1, \hat{b}_2, \hat{b}_3)$. The general result is given in [11].

The value of μ lies between 0 and 1. At $\mu = 0$ trivially no interference will appear meaning that the light is lost in the probe arm and never reaches the detector. When $\eta = 1$ there aren't any losses and the interference have maximum visibility according to Eq.(4.12). The losses μ due to absorption are dominant when the light is near-resonant. These losses are connected with the absorption coefficient defined in Sec.2.3 via the exponential low $\eta = \exp(-\alpha_\Delta)$.

The V parameter is connected with the visibility of the interference pattern $\mathcal{V}$ as:

$$\mathcal{V} = \frac{\langle \hat{d}_1^\dagger \hat{d}_1 \rangle_{\phi=\pi} - \langle \hat{d}_1^\dagger \hat{d}_1 \rangle_{\phi=0}}{\langle \hat{d}_1^\dagger \hat{d}_1 \rangle_{\phi=\pi} + \langle \hat{d}_1^\dagger \hat{d}_1 \rangle_{\phi=0}} = \frac{2\sqrt{\mu V}}{1+\mu} \tag{4.12}$$

when the absorption is negligible $\mu \approx 1$ the visibility of the interference is $\mathcal{V} = \sqrt{V}$.

The phase difference ϕ between the two arms in the above equation can change due to change of the pathlengths difference, change in the refractive index and shift of the laser wavelength. If there are atoms present in the probe arm the light can also shift but this time due to the interaction with atoms. The last phase modification is the useful signal which caries information about the atomic sample, and the first three contribute to the noise. Hence the phase difference is a sum of two contributions:

$$\phi = \phi_N + \phi_\Delta \tag{4.13}$$

The atomic contribution to the light phase is denoted as ϕ_Δ as already discussed in Sec.2.3. The phase shift resulting from the noise sources is depicted with ϕ_N. It has to be mentioned that ϕ_N can also have a non-zero mean vale. In the next section we will see how the value of ϕ_N and its noise can be minimized.

4.2 Noise Sources

The section introduces the different noise contributions to the measured signal. In the experiment we measure the subtraction photocurrent i_- produced by the light impinging on the two detectors in the balanced detection scheme. The fluctuations in the photocurrent we denote as δi_- or with their variance $(\delta i_-)^2$.

In practice the photocurrent is a function of time and the same holds for its fluctuations. Then the photocurrent can be expressed as the sum of its mean value $\langle i_- \rangle$ which is independent of time and a time dependent fluctuations $\delta i_-(t)$ i.e. $i_-(t) = \langle i_- \rangle + \delta i_-(t)$.

The noise of the measured variable can be expressed via its spectral density $W(\omega) = \langle|(\delta i_-(\omega))^2|\rangle/2\pi$. The spectral density is a measure for the magnitude of the fluctuations at a given detection frequency ω.

$$\langle(\delta i_-(t))^2\rangle = \int_{-\infty}^{\infty} W(\omega)d\omega \tag{4.14}$$

The last formula will be used to characterize all the classical noise contributions to the photocurrent since they are frequency dependent. The shot noise of light is a *white noise*, and is independent of the detection frequency, which would mean that it is constant in time.

In practice the detectors have spectral response function $r(\omega)$, which defines the ability of the detector to react to external disturbance at the detection frequency. Then the bandwidth of the detection is expressed as:

$$B = \int_0^{\infty} |r(\omega)|^2 d\omega \tag{4.15}$$

With this consideration the noise of the detected photocurrent can be studied in the limits of the detection bandwidth:

$$\langle(\delta i_-(t))^2\rangle = \int_{-\infty}^{\infty} W(\omega)B(\omega)d\omega = \int_{-\infty}^{\infty} W(\omega)|r(\omega)|^2 d\omega \tag{4.16}$$

For a white noise spectrum the noise spectral density does not depend on the detection frequency and the W can be pulled out of the integral.

4.2.1 Shot noise

The fluctuations of the number of photons in a light beam $(\delta n)^2$ for a coherent light state will scale linearly with the mean value of the photon number. This has already been mentioned in the Sec.2.2 in the discussion of coherent state, and here we adopt it to the case of an interferometer. For a lossless interferometer we have derived an equation for the detected photon number $\hat{n}_-$ in Eq.(4.5). According to the definition for the operator variance we can write that:

$$\langle(\delta\hat{n}_-)^2\rangle = \langle\hat{n}_-^2\rangle - \langle\hat{n}_-\rangle^2 \tag{4.17}$$

When taking the square of $\hat{n}_-$ we get cross terms containing the annihilation and creation operators of the vacuum state, which expectation values are zero for a product state with a coherent state in one input and vacuum in the other. The only term with non-zero expectation value would be the one which contains the $(\hat{a}^\dagger\hat{a})^2$. It expectation value is easily calculated using the commutation relations of the creation and annihilation operators $[\hat{a}, \hat{a}^\dagger] = 1$ as shown in [12]. Then for a lossless symmetric interferometer we can write that:

$$\langle(\delta\hat{n}_-)^2\rangle = \langle\hat{n}\rangle \tag{4.18}$$

The last equation describes the physical nature of the shot noise. It scales linearly with the number of atoms and is an inherent feature of the coherent states as it has been described in the Sec.2.2.

For the case of interferometer with losses we expect that the shot noise reduces according to the loss of photons from the probe beam. Since the loss can be modeled to happen

only in one of the arms say probe arm. This way we can write that the noise is

$$\langle(\delta\hat{n}_-)^2\rangle = \left(T^2+1\right)\frac{\langle\hat{n}\rangle}{2} \tag{4.19}$$

where $T^2 = \mu V$ is the transmission through the probe arm. For a lossless interferometer the value of $T^2 = 1$.

Since the shot noise is a white noise, it is constant for all times and frequencies. Then for the variance of the detector photocurrent we obtain with the help of Eq.(4.11) and Eq.(4.16):

$$\langle(\delta i_-)^2_{SN}\rangle = \frac{B(\varepsilon e)^2\langle\hat{n}\rangle}{\tau_p}\frac{(T^2+1)}{2}. \tag{4.20}$$

4.2.2 Classical noise

In that section we will treat the problem of classical noise. As we have already mentioned the classical noise is frequency dependent in contrast to the shot noise. There are different kind of disturbances which give rise to a classical noise. The most important for our interferometric measurement are the amplitude and phase noise of the laser and the acoustic noise. In the following lines we give the general description of these noise contributions and an estimate of their influence on the detector photocurrent.

Amplitude noise

The field in one of the output ports of the interferometer can be expressed in classical terms as $E_{1,2} = \frac{E(t)\pm E(t-\Delta t)}{2}$, where Δt is a time delay associated with the pathlength difference Δl between the two arms. The E is the input field that enters the interferometer given by Eq.(2.17).

The photocurrent can be calculated using the intensity of the light beam and its cross section A as:

$$i_m = \varepsilon e\frac{c\epsilon_0 A}{2\hbar\omega}|E_m|^2,\ m = 1,2 \tag{4.21}$$

where m denotes which output of the interferometer is considered. The other quantities are already defined in previous chapters. Using the last two equations we can derive an expression for the subtracted photocurrent as

$$i_- = \varepsilon e\frac{c\epsilon_0 A}{2\hbar\omega}\left(|E_2|^2 - |E_1|^2\right) \tag{4.22}$$

At this point we can introduce a perturbation to the amplitude of the light field as $\mathcal{E}(t) = \mathcal{E}(1+\delta P(t))$, where $P(t)$ is a real function of time. Using this relation we arrive at:

$$i_- = -i_0 T\cos\phi\,(1+\delta P(t))\,(1+\delta P(t-\Delta t)) \tag{4.23}$$

The last expression is obtained using the interference term $E(t)E^*(t-\Delta t)$ by factoring out the $\mathcal{E}\mathcal{E}^*$ and introducing a quantity which carries the dimension of the photocurrent $i_0 = \varepsilon e\frac{2c\epsilon_0 A}{\hbar\omega}|\mathcal{E}|^2$. The value of the photocurrent is also modified by the probe arm transmission T as shown discussed in Sec.4.2.1. Omitting the cross term in the equation above we get that:

$$i_- = -i_0 T\cos\phi\,(1+\delta P(t)+\delta P(t-\Delta t)) \tag{4.24}$$

In the above equation the first term is the mean value and the second and the third are fluctuating terms. We can approximate the sum of the two noise terms with $2\delta P(t)$ since Δt is small compared to the coherence time of the laser light $t_c = l_c/c$, where l_c is coherence length. Then leaving out only the fluctuating term we can extract from the above equation information about the standard deviation and the noise

$$(\delta i_-(t))_a = 2i_0 T \cos\phi \delta P(t) \tag{4.25}$$

$$\langle(\delta i_-(t))^2\rangle_a = \left(2\varepsilon \frac{eT\cos\phi\langle\hat{n}\rangle}{\tau_p}\right)^2 \int_{-\infty}^{\infty} W_a(\omega)\delta\omega \tag{4.26}$$

It is interesting to note that the classical amplitude noise scales as $\langle\hat{n}\rangle^2$ and also depends on the interferometer residual phase shift when there are not atoms in the probe arm $\phi = \phi_N$. Thus setting the residual phase of the interferometer to $(m+1/2)\pi$ would cancel the amplitude noise. This can be done by employing an additional laser far detuned from the atomic transition to lock the interferometer to the side of the interference fringe. The wavelength of that laser is chosen to be several nanometers away from the probed atomic transition. Locking the interferometer at half fringe is also demanded by the possibility of detecting small phase shifts at large probe detunings.

The use of balanced homodyne detection is also imposed by the cancelation of the non-interference terms in Eq.(4.22). These terms have the same sign for the two outputs thus vanishing after subtraction. We must also note here that for the quantum amplitude noise the above does not hold, since it is uncorrelated and instead of vanishing it will add after the subtraction.

Phase noise

To describe the phase noise we introduce a perturbation $\delta\phi(t)$ to the phase of the light in the expression for the electric field $E(r,t) = \mathcal{E}\exp(i(\mathbf{k}\cdot\mathbf{r} - \omega t))$ in the following way:

$$\omega\Delta t = \langle\omega\rangle\Delta t + \delta\phi(t) \tag{4.27}$$

Inserting this equation in the exponent of the field and using the non-zero interference terms in Eq.(4.22) we find that the perturbation of the light phase is directly transferred onto the detection photocurrent as:

$$i_- = -i_0 T\cos\left(\phi + \delta\phi(t) - \delta\phi(t-\Delta t)\right) \tag{4.28}$$

The last equation includes a linearized phase inside the cosine argument. For $\Delta t \ll t_c$ the phase perturbation $\delta\phi(t,\Delta t) = \delta\phi(t) - \delta\phi(t-\Delta t) \ll \pi/2$, thus allowing for expansion of the cosine

$$i_- = -i_0 T\left(\cos\phi - \delta\phi(t,\Delta t)\sin\phi\right) \tag{4.29}$$

The above equation is also justified by the fact that the coherence length l_c of an extended cavity diode lasers is hundreds of meters which is much longer compared to the typical pathlength difference Δl of few milliliters. Than the condition of $\Delta t \ll t_c$ is readily satisfied in our experimental conditions. Next, taking only the fluctuating part and calculating its variance we get

$$\langle(\delta i_-(t))^2_{ph}\rangle = \left(2\varepsilon \frac{eT\sin\phi c\langle\hat{n}\rangle}{\tau_p}\right)^2 \int_{-\infty}^{\infty} W_{ph}(\omega')d\omega' \tag{4.30}$$

The phase noise spectral density $W_{ph}(\omega')$ in the above equation can be converted to frequency noise spectral density $W_\omega(\omega')$ using the relation given in [70].

$$W_{ph}(\omega') = W_\omega(\omega')\frac{\sin^2(\omega'\Delta t/2)}{(\omega'/2)^2}. \tag{4.31}$$

For a pathlength difference of less than a millimeter the time delay between the two arms is $\Delta t < 3$ps. Then the product $\omega'\Delta t < 0.01$ for detection frequencies less than 3GHz. Then the sin function in the above expression can be expanded to first order in $\omega'\Delta t/2$ and we get

$$\langle(\delta i_-(t))^2_{ph}\rangle = \left(2\varepsilon\frac{eT\sin\phi c\Delta t\langle\hat{n}\rangle}{\tau_p}\right)^2\int_{-\infty}^{\infty}W_\omega(\omega')d\omega'. \tag{4.32}$$

In Eq.(4.32) as well as in Eq.(4.30) we have substituted the value of i_0. We see that the phase Eq.(4.30) and frequency noise Eq.(4.32) again as a classical noise sources are proportional to $\langle\hat{n}\rangle^2$. In practice the phase noise of the diode laser translates into frequency noise having the 1/f content at low frequencies, followed by a white noise level for intermediate frequency ranging from around 100 kHz up to 10 MHz and relaxation oscillation in the GHz region.

We have already mentioned that we need to lock the interferometer to a half fringe to cancel the amplitude noise contribution and now a different method for phase noise cancelation is required since the phase noise depends on the sine function. The Eq.(4.30) contains the pathlength difference between the interferometer arms $c\Delta t$. Hence, if the the pathlength between the arms is set to zero, then the phase noise will vanish. This can be accomplished by aligning the interferometer in the so called *white light* position. This would mean that the two arms have equal optical pathlengths thus making possible an interference of incoherent light. Since in the practice we do not have a pure white light source, the condition for a white light alignment would translate to a pathlength difference smaller than the coherence length of the light source.

Acoustic noise

As acoustic noise we refer to any external disturbance that can perturb the path-length difference between the two interferometer arms. This type of noise is caused by mechanical vibration of mirrors, optical mounts, air fluxes etc. Lets assume that the pathlength is disturbed by a small perturbation $kc\delta(\Delta t) = \omega\delta(\Delta t)$. Then the photocurrent can be written in the form:

$$i(t) = i_0T\cos(\omega\langle\delta t\rangle + \omega\delta(\Delta t)(t)) \tag{4.33}$$

Taking the variance of the above equation and substituting the value of i_0.

$$\langle(\delta i(t))^2_{\Delta t}\rangle = (i_0T\omega\sin\phi)^2\langle\delta(\Delta t)^2\rangle = \left(\frac{e\varepsilon\langle\hat{n}\rangle\sin\phi T}{\tau_p}\right)^2\int_{-\infty}^{\infty}W(\omega')_{\Delta t}d\omega' \tag{4.34}$$

We have found difficult to characterize the acoustic noise spectral density $W_{\Delta t}$ and the adopted way of fighting the acoustic noise was to isolate the interferometer as it will be shown in the experimental part of the thesis. An extensive analysis of this type of noise is done in the thesis by Daniel Oblak [22].

4.2.3 Atomic noise

In the previous section we have shown that the interferometer phase shift can be influenced by variations in the phase and amplitude of the probe light. We have also marked these as noise contributions to the detected signal and found ways to surpass them.

However, as it was mentioned in Sec.4.1.2, the phase of the light can also change due to interaction with atoms. The noise imposed in that way we refer as *atomic noise* ϕ_Δ. Then the atomic noise can be also named as atom induced phase noise. Hence we can use Eq.(4.29) to calculate the induced noise in the detector photocurrent.

$$\langle(\delta i_-(t))^2\rangle_\Delta = \left(2\varepsilon\frac{eT\sin(\phi)\langle\hat{n}\rangle}{\tau_p}\right)^2\langle(\delta\phi_\Delta(t))^2\rangle \tag{4.35}$$

The atomic noise in the above equation is dependent on the atom number as seen from Eq.(2.44) and Eq.(2.47).

In the measurements presented in this thesis the experimentally observed phase shift is proportional to the atomic population of a particular atomic state of atoms prepared in a MOT or FORT as also seen from Eq.(2.42). This way if the population of that state fluctuates, then this will directly result in fluctuations in the measured phase shift. We will refer to this type of noise as *atom number fluctuations or population noise*.

Let's assume we have the following conditions. The collective state of Cs atoms is a coherent superposition as described in Ch.2, Eq.(2.11) in the case of a single atom. The probe light is off-resonant, and the detuning is set so that the light is equally sensitive to the populations of the two levels. The population of the excited state in these conditions is negligible. Then performing a measurement on the sample will *project* the ensemble state to one of the states $|3\rangle$ or $|4\rangle$. If the measurement is repeated many times, with a state preparation in between the consecutive measurements, the outcomes will show that the collective atomic state is projected to either of the state $|3\rangle$ or $|4\rangle$. Then the indeterminism on which state the projection happens is called *quantum projection noise*.

The phase shift of the interferometer in presence of atoms is a function of the probe light detuning with respect to the $F = 3$ and $F = 4$ hyperfine components of the ground $6S_{1/2}$ state and the atomic population of these levels. By the use of equations Eq.(2.48) and Eq.(2.51) we can express the phase shift with the operator of the total number of atoms $\hat{N}$ and the population number difference $\hat{J}_z$

$$\phi_\Delta = \frac{\phi_0}{Al\mathcal{N}}\left(D_+(\Delta)\frac{\hat{N}}{2} + D_-(\Delta)\hat{J}_z\right) \tag{4.36}$$

$$D_\pm(\Delta) = \sum_{F'=3}^{5} S_{4F'}\frac{\frac{\gamma}{2}\Delta_{4F'}}{\Delta_{4F'}^2 + \left(\frac{\gamma}{2}\right)^2} \pm \sum_{F'=2}^{4} S_{3F'}\frac{\frac{\gamma}{2}\Delta_{3F'}}{\Delta_{3F'}^2 + \left(\frac{\gamma}{2}\right)^2} \tag{4.37}$$

The Eq.(4.36) is valid only for expectation values or variances of the variables. Calculating the variance of ϕ_Δ gives

$$\langle(\delta\phi_\Delta)^2\rangle = \left(\frac{\phi_0}{Al\mathcal{N}}\right)^2\left(D_+^2(\Delta)\frac{\langle(\delta\hat{N})^2\rangle}{4} + D_-^2(\Delta)\langle(\delta\hat{J}_z)^2\rangle\right) \tag{4.38}$$

We see that the atomic noise can be divided to two main contributions i.e. the projection noise $(\delta\hat{J}_z)^2$ and the atom number fluctuations $(\delta\hat{N})^2$. In the following few lines we will

give some explanation of these two.

Projection noise

The second term in Eq.(4.38) is the quantum projection noise of a collective coherent superposition state. When this state is created the pseudospin vector $\hat{\mathbf{J}}$ lies in the equatorial plane of the Bloch sphere and the uncertainties of its projections $\hat{J}_z$ and $\hat{J}_y$ satisfy the Heisenberg uncertainty relation. Substituting the value of $(\delta\hat{J}_z)^2$ we get

$$\langle(\delta\phi_\Delta)^2_{\hat{J}_z}\rangle = \left(\frac{\lambda^2}{2\pi A}\right)^2 D_-^2(\Delta)\frac{N_{at}}{4}, \tag{4.39}$$

where we have inserted the value of ϕ_0. The last equation tells that the coherent superposition state has a variance of the population number difference proportional to the total number of atoms N_{at} in the ensemble, as expected from Eq.(2.11).

In many experiment it is necessary to characterize the atomic state by measuring the projection noise, being the fundamental quantum noise limit. To measure the projection noise of the sample prepared in a pure superposition state one needs to perform a measurement on a coherently prepared atomic samples. The measurement protocol should have the following sequence. First the atomic state is prepared in a superposition state. Second, an off-resonant pulse is applied that projects the ensemble state to one of the states creating the superposition. To have a good statistics we need to perform several measurements. However, to be in the same conditions, we need after every optical probing to prepare again the superposition state, since after the measurement has taken place the state of the ensemble is already projected. We have to also ensure that the measurement is performed with the same sensitivity for both ground state hyperfine levels.

Population noise

The noise measurements performed in our experiment involve a mixed ensemble state where atoms are distributed among the hyperfine levels $|3\rangle$ and $|4\rangle$ of the ground electronic state in caesium. This would mean that density matrix of the ensemble is $\rho = p_3|3\rangle\langle 3| + p_4|4\rangle\langle 4|$. Since during cooling process the repump laser prevents atoms to accumulate on the $|3\rangle$ the population of that level is much less than the population of $|4\rangle$. Moreover, in the experiment, the light probe we use, is far detuned from the transitions coupling the $|3\rangle$ state to the excited $6P_{3/2}$ state (around 9 GHz). Then the variance of $\hat{J}_z$ will be proportional to the number of atoms in $|4\rangle$ state i.e. we will observe population noise.

There are two type of population noise which can be measured by interferometric setup. First, one can choose to make a measurement of freshly prepared atomic samples in a consecutive MOT or FORT loading cycles. The variance of the equilibrium number of atoms loaded in the MOT or the FORT scales linearly with the loaded atom number since the different loading cycles are not correlated.

The second type of population fluctuations arises from the atomic motion in the cold cloud. Since the atoms have a finite kinetic energy associated with their mean velocity they will move in and out of the probing volume resulting in a population noise. To measure these fluctuations one needs to send consecutive pulses and perform measurement in a single trapping cycle. Hence, we need to send the pulses with a time separation longer than the time it takes an atom with average velocity to cross the probing beam cross-section. This way we will assure that when the second pulse arrives it will already see new

atoms.

To calculate the number of atoms which have been replaced by the thermal motion in the trap [71] we use a numerical analysis similar to the release and recapture experiments [72]. The number of atoms replaced N_{re} by new ones after waiting a time t is found to behave as

$$N_{re} = N_{at}\left(1 - e^{-\frac{t}{t_{re}}}\right) \tag{4.40}$$

with t_{re} the effective time at which N_{at}/e atoms have been replaced or refreshed. Choosing very short time separation between probe pulses will reflect in probing of atoms which state has already been measured by the first pulse. The above equation is valid for times much shorter than the atomic sample lifetime. The noise associated with the thermal motion is proportional to the number of atoms replaced after some time t as:

$$\langle(\delta\phi_\Delta)^2_{\hat{N}}\rangle = \left(\frac{\lambda^2}{2\pi A}\right)^2 D^2_+(\Delta)\frac{N_{re}}{4} \tag{4.41}$$

At the end of this section we want to collect all the noise contributions to the experimentally measured detector photocurrent.

$$\langle(\delta i)^2\rangle = \langle(\delta i)^2_e\rangle + \langle(\delta i)^2_{SN}\rangle + \langle(\delta i)^2_a\rangle + \langle(\delta i)^2_{ph}\rangle + \langle(\delta i)^2_{\delta t}\rangle + \langle(\delta i)^2_{\hat{J}_z}\rangle + \langle(\delta i)^2_{\hat{N}}\rangle \tag{4.42}$$

The variances in Eq.(4.42) are expressed through the measured phase-shift and the number of atoms using the equations from the previous sections. The new noise contribution added here is the electronic noise $\langle(\delta i)^2_e\rangle$. The shot noise $\langle(\delta i)^2_{SN}\rangle$ is given by Eq.(4.20). The amplitude noise is calculated from Eq.(4.25) and can be canceled by locking the interferometer at a half fringe. The phase noise Eq.(4.30) depends on the pathlength difference and is surpassed by aligning the interferometer in the white-light position. The acoustic noise is given by Eq.(4.34). The atom induced phase noise is separated to projection noise in Eq.(4.39) and the density or population noise in Eq.(4.41)

Chapter 5

Diffraction effects on light-matter quantum interface

The light atom interaction in the context of the collective variables couples atomic collective variable to a light variable. The importance of the interaction is connected with generation of spin-squeezed states, quantum mapping between atoms and light, quantum memory operations, creation of macroscopic entanglement, and teleportation of atomic states [5, 8, 73–78]. The efficiency or signal-to-noise ratio (SNR) of the interaction is a function of parameters as optical depth on resonance and absorption. In the experiment a collection of atoms in an atomic cloud interacts with a light beam. Often the light is off-resonant [6, 7, 26, 27] and the interaction is considered to be of the nondestructive [11] or QND type [6, 9]. The elastically scattered photons carry information about the atomic state. Since the interaction is non-dissipative the scattered waves are coherent and diffraction effects can occur thus in some cases reducing the SNR. To overcome the diffraction or at least to minimize it one needs to predefine the atomic sample geometry as well as the geometry of the light beam.

In most of the experimentally demonstrated interaction schemes the light beam is often large compared to the atomic sample [7,26] prepared in a MOT. In other experiments using room temperature atoms in a vapor cell [6, 27] the atomic density is constant along the entire sample. Coupling an inhomogeneous light beam to a cold atomic sample has been realized using a cavity [10] or a focused gaussian beams [11]. The choice of a cavity or a focused beam is dictated by the possibility to increase the photon density at the region of the atomic sample and to enhance the interaction using the cavity finesse. However, along with this positive effect the diffraction can influence the interaction especially when a dipole trapped atomic samples are used [79].

In this section we present a model to describe the effects of the diffraction on light atom coupling in terms of collective atomic and light variables [25]. Starting from a purely classical model of light atom elastic scattering we derive simple scaling geometrical parameters to describe the 3D problem and relate it to the already investigated 1D scattering.

5.1 Collective light-atom coupling

The effective hamiltonian in the off resonant limit Eq.(2.48) contains a coupling term $\hat{S}_z\hat{J}_z$, that describes the time-dependent interaction between a pulse of light and an ensemble of two-ground-states atoms in a sample with cross-sectional area A and length l. The atomic

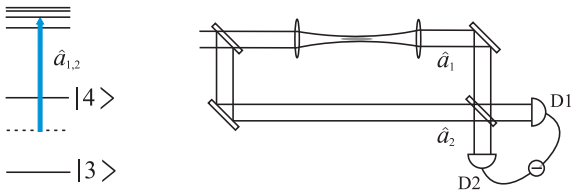

Figure 5.1: *Light-atom interaction in a Mach-Zehnder interferometer*

sample is placed in one of the arms of a Mach-Zehnder interferometer as shown in Fig.5.1.

$$\hat{H}_c = \hbar \frac{2\sigma_0}{Al\tau} \left(\frac{\gamma}{2\Delta}\right) \int_0^l \hat{s}_z(z,t)\hat{j}_z(z,t)\mathrm{d}z \tag{5.1}$$

The light is detuned by Δ from the atomic resonance, as shown in Fig.2.3, and $\sigma_0 = \lambda^2/2\pi$ is the on-resonance absorption cross-section. The integration of the $\hat{H}_c$ runs over the length of the atomic sample, with a coefficient in front of the integral describing the coupling strength of the interaction.

The z components of the collective angular momentum operators for atoms and light per unit length are defined as in Eq.(2.10) and Eq.(4.9). Here the difference is that the discrete sum over all atoms in the sample now runs in a slab with length δz

$$\hat{j}_z = \frac{1}{2\delta z} \sum_k^{N(z)} \left(\hat{\sigma}_{44}^{(k)}(t) - \hat{\sigma}_{33}^{(k)}(t)\right) \tag{5.2}$$

$$\hat{s}_z = \frac{1}{2\delta z} \sum_k^{n(z)} \left(\hat{a}_1^{\dagger(k)}\hat{a}_1^{(k)} - \hat{a}_2^{\dagger(k)}\hat{a}_2^{(k)}\right) \tag{5.3}$$

The annihilation operators for the probe and reference arm's light fields are $\hat{a}_1$ and $\hat{a}_2$, respectively. In expressing the atomic operators we have assumed that the levels of interest are the ground states of atomic caesium. The time evolution of the system is governed by the Heisenberg equation of motion Eq.(2.30) and the transformation of the input *in* operator projections at the output *out* is expressed by the following relations

$$\begin{aligned}
\delta\hat{J}_y^{out} &= \delta\hat{J}_y^{in} - \frac{2\sigma_0}{A}\frac{\gamma}{2\Delta} < \hat{J}_x > \delta\hat{S}_z^{in} \\
\delta\hat{J}_z^{out} &= \delta\hat{J}_z^{in} \\
\delta\hat{S}_y^{out} &= \delta\hat{S}_y^{in} - \frac{2\sigma_0}{A}\frac{\gamma}{2\Delta} < \hat{S}_x > \delta\hat{J}_z^{in} \\
\delta\hat{S}_z^{out} &= \delta\hat{S}_z^{in}
\end{aligned}$$

The operators with $\hat{J}_z$ and $\hat{S}_z$ have replaced the atomic and light operators in Eq.(5.2) after an integration along the sample length.

The z components of the atomic and light collective pseudospin are conserved, whereas the y components are transformed according to the above equations. Then a measurement on $\hat{S}_y$ would reveal an information about the population number difference $\hat{J}_z$. Assuming an initially prepared coherent state of the macroscopic atomic and light vectors, along the

x axis, a set of measurements of $\hat{S}_y$ with $\langle \hat{S}_y \rangle = 0$ will give a variance

$$(\delta \hat{S}_y^{out})^2 = \frac{n_{ph}}{4} + \left(\frac{2\sigma_0}{A} \frac{\gamma}{2\Delta} \frac{n_{ph}}{2} \right)^2 \frac{N_{at}}{4} \tag{5.4}$$

The first term on the right hand side is the shot noise of light and the second is the excess light noise due to atomic fluctuations amplified by the value of $\langle \hat{S}_x \rangle$. The first term is constant since it describes white noise as already discussed in previous chapter. The value of the atomic variable $\hat{J}_z^{in}$ can be deduced from the measurement with a signal to noise ratio (SNR) defined by

$$\left(\frac{S}{N} \right)_{1D}^2 = \frac{\sigma_0^2}{A^2} N_{at} n_{ph} \left(\frac{\gamma}{2\Delta} \right)^2 \tag{5.5}$$

The index 1D in Eq.(5.5) refers to the one dimensional problem.

In the experimental configuration employing the Mach-Zehnder interferometer, as in Fig.5.1 the detected by the homodyne detector signal is expressed as the photocurrent i_- in units of elementary charge integrated over the pulse duration τ

$$\begin{aligned} S_D &= \int_0^\tau \frac{i_-}{e} \mathrm{d}t \\ &= \varepsilon \frac{\tau}{\hbar\omega} \frac{c\varepsilon_0}{2} \left(2|E_{sc}||E_r| \int_{A_D} M_{sc} M_r \mathrm{d}A + 2|E_p||E_r| \int_{A_D} M_p M_r \mathrm{d}A \right). \end{aligned} \tag{5.6}$$

The indexes p, r, and sc refer to the probe, reference, and scattered wave propagating in the interferometer arms. The terms in the brackets describe the transverse overlap of the waves over the photodetector area A_D, with M being the mode functions. The last include the oscillatory dependance on the interferometer pathlength difference. Generally, we assume that the probe field E_p and scattered field E_{sc} do not share the same spatial mode and have different phases due to the atom light interaction generating the scattered waves.

The second term in Eq.(5.6) does not carry any information about the atomic variable and its fluctuations are the classical noise in amplitude and phase of the probe light. The first and the second term are nearly $\pi/2$ out of phase, which means that when the first term is maximum the second will vanish. Setting the pathlength of the interferometer to zero and the residual phase to $\pi/2$ makes the second term disappear as it was discussed in Sec.4.2.2. The value of the signal $S^2 = S_D S_D^*$ and the noise N^2 are then expressed as

$$\begin{aligned} S^2 &= 2\varepsilon^2 \left(\frac{\tau}{\hbar\omega} \right)^2 P_{sc} P_r \\ N^2 &= \frac{\varepsilon\tau}{\hbar\omega} 2P_r \end{aligned}$$

The signal depends on the product of the scattered power P_{sc} and the power of the reference light beam P_r. On the other hand the noise depends on P_r only. The last has a lower limit defined by the shot noise. The coupling strength κ^2 or SNR then obtains its general expression

$$\kappa^2 = \left(\frac{S}{N} \right)^2 = \varepsilon n_{ph}^{sc} \tag{5.7}$$

As it was expected the coupling strength is proportional to the detected fraction of the coherently scattered photons n_{ph}^{sc}. It is then straightforward that the scattered power can

be increased by increasing the input optical power to the interferometer. However, the detection saturation power and the requirement for low spontaneous emission rate set a limit to the input power.

The SNR can be expressed by using two additional parameters called integrated rate of spontaneous emission η and optical depth or optical column density α_0.

$$\eta = n_{ph}\frac{\sigma_0}{A}\left(\frac{\gamma}{2\Delta}\right)^2 \tag{5.8}$$

$$\alpha_0 = N_{at}\frac{\sigma_0}{A} \tag{5.9}$$

Then the strength of the interaction becomes:

$$\kappa^2 = \eta\alpha_0. \tag{5.10}$$

The last has also been recognized as a figure of merit for collective variable light-atom coupling [80].

5.2 Scattering model

In the discussion here we are mostly interested in maximizing the scattered power by choosing an optimal sample geometry. We develop a simple classical method to calculate the stationary diffracted field by an atomic sample regarded as an ensemble of fixed point scatterers with a certain density distribution. Since we are interested in cold atoms the doppler shift can be neglected. The time, for which a measurement takes place is short enough compared to the recoil time.

5.2.1 Description

To describe the scattering process we use the first Born approximation [81], neglecting the multiple scattering events. The scatterers are assumed to be independent, which is true for not too high atomic densities $n_{at} < k^3$. The scattering is coherent and happens mainly in the forward direction i.e. along the propagation direction of the probe field. The total scattered field is calculated as a sum over the scattered fields of independent scatterers.

The model parameter which characterizes the scattering event is the scattering amplitude f. In our calculation we assume s-wave scattering thus having f independent on the scattering angle Ω. Integrating $|f|^2$ over the solid angle renders the scattering cross-section at a given detuning Δ of the probe laser from the atomic resonance. For detunings large compared to the excited state hyperfine splitting the scattering cross-section for any of the sublevels of the ground state is approximately the same for linearly polarized light.

$$\begin{aligned}\int_{4\pi}|f|^2\mathrm{d}\Omega &= \sigma_0\frac{1}{1+\left(\frac{2\Delta}{\gamma}\right)^2}\\ f &= -\lambda\sqrt{\frac{3}{8\pi^2}}\frac{1+i\left(\frac{2\Delta}{\gamma}\right)}{1+\left(\frac{2\Delta}{\gamma}\right)^2}\end{aligned} \tag{5.11}$$

The total scattered wave is the sum of the waves scattered by individual scatterers j ($j = 1..N_{at}$) and can be expressed in terms of electromagnetic field vector in complex

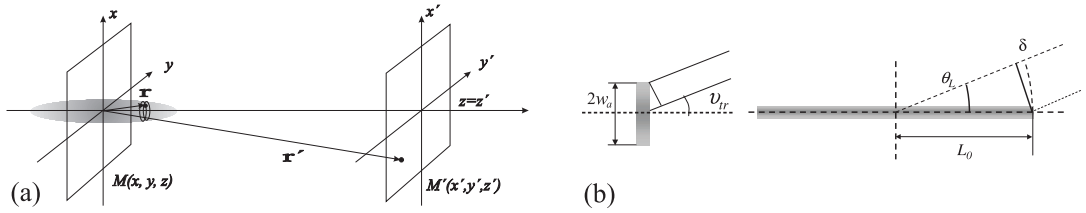

Figure 5.2: *Description of the scattering model (a). Diffraction limited scattering cones for transversally (left) and longitudinally extended atomic samples (b).*

notation as [Fig.5.2(a)]:

$$\vec{E}_{sc}(\vec{r'}) = \sum_{j=1}^{N_{at}} \vec{E}_p(\vec{r_j}) f \frac{\exp(-ik|\vec{r'} - \vec{r_j}|)}{|\vec{r'} - \vec{r_j}|} \tag{5.12}$$

Since atoms can occupy the two hyperfine states $|3\rangle$ and $|4\rangle$ they will contribute with opposite signs to the total scattered field. Then atomic density or density of the point scatterers can be written in the form:

$$\delta n(\vec{r}) = \sum_{j=1}^{N_4} \delta(\vec{r} - \vec{r_j}) - \sum_{k=1}^{N_3} \delta(\vec{r} - \vec{r_k}) \tag{5.13}$$

with normalization condition giving the population difference between the two levels

$$\delta N_{at} = \int_{\mathbb{R}^3} \mathrm{d}r^3 \delta n(\vec{r}). \tag{5.14}$$

Next, we use a continuous density distribution according to a smooth probability distribution to find a particle in a small volume element, again suitably normalized to the total number of particles. The scattered field at some observation point $\vec{r'}$ outside the sample in integral form becomes:

$$\vec{E}_{sc}(\vec{r'}) = \int_{\mathbb{R}^2} \mathrm{d}x\mathrm{d}y \int_{-L}^{L} \mathrm{d}z \vec{E}_p(\vec{r}) \delta n(\vec{r}) f \frac{\exp(-ik|\vec{r'} - \vec{r}|)}{|\vec{r'} - \vec{r}|} \tag{5.15}$$

At this point we need to make assumption of the scattering angle. We expect that constructive interference of the scattering amplitudes happens for small angles along the forward propagation direction. In the paraxial domain (small angles to the optical axis), we can approximate the spherical wave propagator in Eq.(5.15) by using a Fresnel expansion formula for the distance $|\vec{r'} - \vec{r}|$ [24, 81]. Then the kernel or propagator in the integral is transformed to

$$\begin{aligned} K(|\vec{r'} - \vec{r}|) \quad &\simeq \quad \frac{\exp(-ik(z' - z))}{(z' - z)} \exp\left\{ ik \frac{xx' + yy'}{z' - z} \right\} \\ &\quad \times \exp\left\{ -ik \frac{x^2 + y^2}{2(z' - z)} \right\} \exp\left\{ -ik \frac{x'^2 + y'^2}{2(z' - z)} \right\} \end{aligned}$$

We choose the incident probe beam not as a plane wave but rather as gaussian with parameters $w(z), R(z), \Phi(z)$ being the beam radius, wavefront radius and Guoy phase,

respectively:

$$\vec{E}_p(x,y,z) = \vec{E}_0 \frac{w(0)}{w(z)} \times \exp\left\{-i[kz - \Phi(z)] - \frac{x^2+y^2}{w^2(z)} - ik\frac{x^2+y^2}{2R(z)}\right\}$$

The density distribution is modeled as a Gaussian in the radial and longitudinal directions. This choice of density profile is also compatible with the density distribution of atoms inside a harmonic potential at thermal equilibrium. In the case of dipole trapped atomic sample when the kinetic energy of trapped particles is low enough w.r.t. the trap depth, the gaussian shape of the trap potential can be considered parabolic and the shape of atomic sample gaussian.

The atomic density distribution in the transverse direction has a radius w_a, which depends on z due to the weaker confinement by the dipole trap laser beam (wavelength λ_{dip}) away from its minimal beam waist. In the longitudinal direction (along the propagation axis of the probe beam) it is described by a $1/e$-length parameter L_0.

$$\begin{aligned} \delta n(x,y,z) &= \frac{\delta N_{at}}{\pi^{3/2} L_0 w_a^2(z)} \exp\left[-\frac{x^2+y^2}{w_a^2(z)} - \frac{z^2}{L_0^2}\right] \\ w_a(z) &= w_a \sqrt{1 + \left(\frac{z}{z_{dip}}\right)^2} \\ z_{dip} &= \frac{\pi w_a^2}{\lambda_{dip}} \end{aligned} \tag{5.16}$$

Finally, the scattered wave field can be evaluated by solving the integral

$$\vec{E}_{sc}(\vec{r'}) = \int_{\mathbb{R}^2} \mathrm{d}x\mathrm{d}y \int_{-L}^{L} \mathrm{d}z \vec{E}_{probe}(\vec{r}) n(\vec{r}) f K(|\vec{r'} - \vec{r}|) \tag{5.17}$$

Here the integration over z runs over the length effectively occupied by the sample. We evaluate the scattered field distribution in some distant observation plane (M' in Fig.5.2(a)) by carrying out the integration over the transverse coordinates of the sample analytically and integrating numerically over the length of the sample. Using standard software on a desktop PC a scattered field profile can be calculated in several seconds allowing for fast interactive optimization of parameters. Not surprisingly for our model assumptions and the choice of the density distribution, we find the scattered mode profile to be very close to Gaussian in all of the studied cases and we can extract parameters like width and radius of curvature by fitting to the corresponding mode profile. The scattering efficiency is evaluated by calculating the total scattered power in the observation plane.

5.2.2 Qualitative examples

Before presenting results from numerical calculation we wish to look closely to some examples of scattering by different sample geometries. The on-axis scattering intensity is essentially independent on the sample geometry at the far-field since all waves will interfere constructively in the forward direction. Thus the scattering efficiency is mainly determined by the opening angle of the scattering cone around the propagation axis. To demonstrate

these consideration we will consider two types of atomic samples i.e. transversally and longitudinally extended.

Let us first consider a short sample of width $2w_a$ as drawn in Fig.5.2(b) to the left. The limiting angle at which the interference ceases to be constructive can be found by dividing the sample into two parts. The pathlength difference between the waves scattered from the center and the end of a half has to be half wavelength in order to have complete cancelation. From that condition the maximum opening angle of scattering cone is

$$\nu_{tr} \approx \tan \nu_{tr} = \frac{\lambda}{\pi w_a} \tag{5.18}$$

A close look to ν_{tr} will discover analogy with the far field diffraction angle of the Gaussian beam. A narrow sample will scatter more than a wide sample since the corresponding diffraction angle will be greater. The scattering angle goes as $1/w_a$ and the scattered intensity as $1/w_a^2$.

Next we consider a pencil-shaped atomic sample, readily obtained in a single focused beam dipole trap. The sample length is much greater than the sample width $L_0 \gg w_a$ as shown in Fig.5.2(b) to the right. We apply the same procedure as before and find the limiting opening angle of the diffraction cone to be

$$\begin{aligned} \delta = L_0(1 - \cos\theta_L) \approx L_0 \frac{\theta_L^2}{2} &= \frac{\lambda}{2\pi} \\ \theta_L &= \left(\frac{\lambda}{\pi L_0}\right)^{1/2}. \end{aligned} \tag{5.19}$$

By equating the two angles we combine the effect of the sample length and width, and define a characteristic length of the atomic sample z_{ra}

$$z_{ra} = \frac{\pi w_a^2}{\lambda} \tag{5.20}$$

For atomic sample with length L_0 longer or comparable with z_{ra}, the scattered waves by different section along the propagation axis are mismatched in phase and consequently will interfere destructively, thus significantly reducing the scattered wave intensity with respect to a short sample with the same number of atoms.

An approximate formula for the scattered power can be derived by the help of the above considerations using the procedure described in [25], which combines the influence of the experimental parameters sample length, sample width and probe beam radius.

$$P_{sc} \simeq P_{probe} N_{at}^2 \frac{3\sigma\lambda^2}{4\pi^3 w_0^2 w_a^2} \frac{1}{1 + w_a^2/w_0^2} \frac{1}{\sqrt{1 + (L_0/\tilde{z}_{ra})^2}} \tag{5.21}$$

$$\theta_T^2 = \frac{\lambda^2(w_a^2 + w_0^2)}{\pi^2 w_0^2 w_a^2} \tag{5.22}$$

Here we introduced $\tilde{z}_{ra}$, the modified atomic Rayleigh range by using the definition of θ_T from the second equation in Eq.(5.21)and the relation $\tilde{z}_{ra} = \lambda/(\pi\theta_T^2)$. The above expression does not take into account the transverse change of the probe beam diameter along the sample length, or in other words, the probe beam is assumed to have a plane phase front curvature.

The last equation is an attempt to find a compact analytical expression to estimate

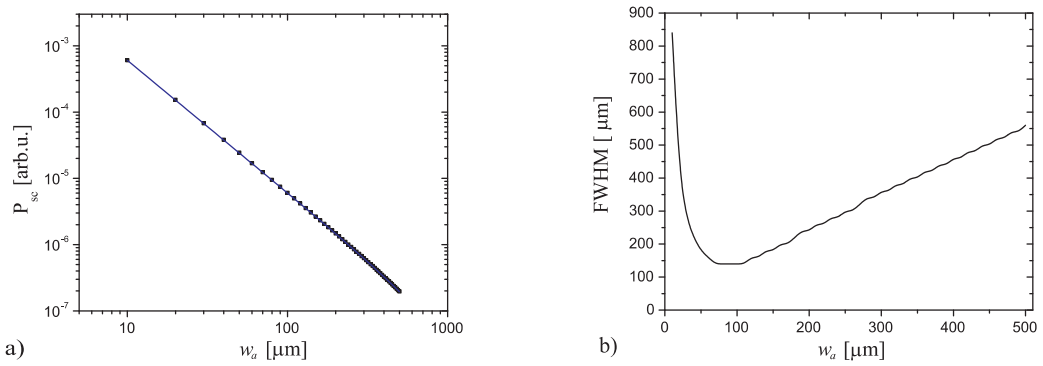

Figure 5.3: *(a) Power of the scattered wave (symbols) vs. the characteristic transverse radius of atomic sample of length $L_0 = 1\mu m$ for constant number of atoms and a wide probe beam $w_0 = 1000\mu m$ together with the analytic prediction from Eq.(5.21)(solid line). b) FWHM of the intensity distribution in the observation plane for the same parameters.*

the diffraction effects based on the qualitative consideration made for the different sample geometries. For more accurate results we must do the integration in Eq.(5.17) - the essence of the scattering model we have developed so far. Then comparing the analytical estimate in Eq.(5.21) and the output results of the scattering model will tell us how well the analytical prediction can be used for a quick estimation of the optimum sample geometry.

5.2.3 Numerical results

The section presents results from the scattering model in comparison with the analytical prediction of Eq.(5.21). Again, the data is calculated for the D_2 line of Cs. The probe detuning and power are fixed as well as the number of atoms in the sample for all results presented.

We start with the dependance of the scattered power on the sample transverse dimension. For a "hypothetically" short atomic sample with a width of 1 μm and a wide probe beam of $w_0 = 1000$ μm we would expect that as long as the width of the "pancake" shaped sample increases, the scattered power should decrease since the destructive interference in forward direction is appreciable for wide atomic samples. The result is shown in Fig.5.3(a). The scattering efficiency drops dramatically with increasing sample size. A comparison with the $(1/w_a^2)[1/(w_a^2 + w_0^2)]$ dependence from our analytical estimate shows perfect agreement. At a fixed position of the observation plane for different sample widths the condition for Fraunhofer diffraction is different. The full width at half maximum (FWHM) of the scattered wave transverse intensity distribution in the observation plane is shown in Fig.5.3(b). The observation plane does not appear in the far field for all the samples with different widths. Then the plotted dependance can be explained as the transverse span of a gaussian beams with a varying waist diameter and fixed position. Hence, one must be careful when choosing the position of the observation plane. Its position has to meet the requirement for propagation in the far field.

The dependance of the scattered optical power as a function of the sample length in units of z_{ra} is shown in Fig.5.4(a) in the case of wide probe beam and fixed sample width of $w_a = 20$ μm. The numerical solution is in a good agreement with the analytical estimate.

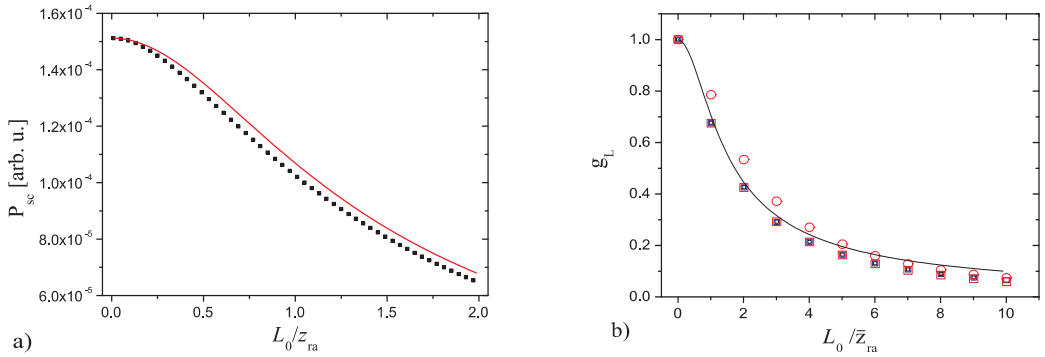

Figure 5.4: *(a) Scattered power vs. the characteristic length of the atomic sample with atomic waist radius $w_a = 20\mu m$ probed by a beam $w_0 = 1000\mu m$. Numerical data (symbols) and analytic prediction from Eq.(5.21) (solid line) are shown together. (b) Same as in (a) for sample width $w_a = 3, 5, 10, 20\mu m$ (squares) and for a narrow probe beam $w_0 = w_a = 20\mu m$ (circles) with the length scaled to $\tilde{z}_{ra}$.*

Note that the dependance does not include the effective Rayleigh length $\tilde{z}_{ra}$ - a product of the considerations we have made in Sec.5.2.2. We define the geometric factor g_L as the function describing universally the length dependence:

$$g_L = P_{sc}(L_0)/P_{sc}(0) \simeq \frac{1}{\sqrt{1 + (L_0/\tilde{z}_{ra})^2}} \tag{5.23}$$

The parameter g_L obtains a value of 1 for a sample of infinitesimally short length, and approaching zero for a infinitely long atomic samples. A check of that dependance is shown in Fig.5.4. For a wide beam the analytical estimate agrees well with the scattering model for scaled sample lengths up to $L_0/\tilde{z}_{ra} = 8$. The mismatch between the model and the analytical prediction is of the order of 20% for a sample with Fresnel number of 1/8. The Fresnel number of the sample is defined as $\tilde{z}_{ra}^{-1}$. In contrast, for the case of a matched with the sample size beam the analytical estimate fails to describe accurately the behavior of the longitudinal geometrical factor g_L, since Eq.(5.21) does not include transverse change of the probe beam geometry over the sample length. To include the effect of the changing beam geometry one must introduce an axial average of the of the incident intensity over the sample length as it is done in the Appendix of [25].

The third important parameter in the coupling problem which can be experimentally varied is the probe beam radius. A very large probe is not optimum. The sample is illuminated homogeneously but the intensity experienced by an atom is rather low. The scattering efficiency dependance on the decreasing probe diameter is a function on two parameters. Decreasing the probe beam size will increase the intensity an atom can see, but in the same time the number of atoms addressed by the probe beam will decrease. The result of the numerical calculations in the case of varying probe beam radius is shown in Fig.(5.5). Again for a very short sample the analytical estimate agrees well with the scattering model results. For long samples both the analytical formula and scattering model predict a finite probe beam diameter at which the scattering efficiency maximizes. For reasons already discussed in the context of Fig.5.4(b), the analytical estimate starts

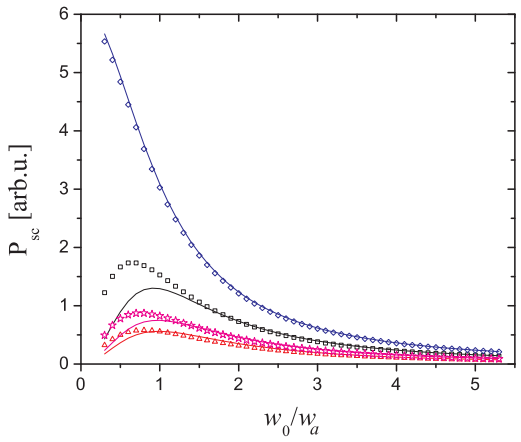

Figure 5.5: *Scattered power vs relative size of sample and probe beam for samples ($w_a = 10\mu m$) of length $L_0 = 1, 400, 738, 1000\mu m$ (diamonds, squares, stars, triangles)together with the analytic prediction from Eq.(5.21)(solid lines) in scaled units.*

to deviate from the numerical result for small probe beam radii. By dropping out the straightforward dependance on the probe intensity and the degree of transverse localization ($\propto w_0^{-2} \cdot w_a^{-2}$) we arrive at a new parameter that we refer to as transversal geometrical factor g_T

$$g_T = \frac{1}{1 + w_a^2/w_0^2} \tag{5.24}$$

The optimum value of g_T is higher for relatively short samples since the optimum probe beam size relative to the fixed width of atomic density distribution is smaller than one as seen in Fig.5.4(a). For long samples the transversal factor approximates 1/2.

5.3 Application to a dipole trapped sample

In the next lines we present numerical results for the case of dipole trapped sample. The sample is trapped in a single focused gaussian beam. In thermal equilibrium the sample geometry is determined by the trapping beam waist [62]. For the purpose of our experiment we consider a 1030 nm wavelength of trap laser at a constant depth of $U_0 = k_B \times 1$ mK. The temperature of trapped atoms is also fixed to 100 μK. Specifying the dipole trap laser power determines the waist needed to achieve the desired trap depth, thus also fixing the thermal radius w_a and the sample length L_0. In our calculation we fix the peak density of the sample to $n_{peak} = 10^{12}\text{cm}^{-3}$, which specifies the number of atoms N_{at}.

In Fig.5.5 we see that for long samples the probe beam size equal to the sample size is close to the optimum condition at which the scattered power is maximum. Next, we choose $n_{ph} = 10^8$ to interact with the sample, at a detuning in natural linewidth units of $\Delta/\gamma = 100$. Then we can numerically calculate the SNR using Eq.(5.7) by calculating the scattered power and convert it into number of coherently scattered photons, for unity quantum efficiency. The results are plotted in Fig.5.6(a). The increase of the dipole power is translated into increase of the number of atoms. This is a result of the above made assumptions for constant peak density. It can be seen that for bigger atomic samples the SNR saturates. Thus the benefit of having more atoms is reduced by the increasingly unfavorable elongated geometry.

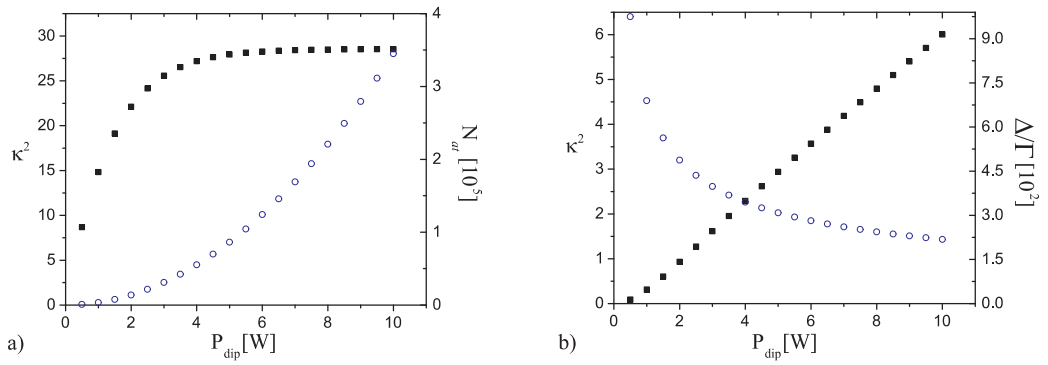

Figure 5.6: *(a) achievable coupling strength (filled symbols, left axis) and number of trapped atoms(open symbols, right axis) as a function of invested dipole trap power; (b) achievable coupling strength (filled symbols, left axis) and probe detuning (open symbols, right axis) needed to satisfy* $\eta = 0.1$ *(see text for details).*

In the real experiment along with the elastic scattering there is a spontaneous emission. The parameter we use to describe the spontaneous emission is the rate at which it happens. Every point in Fig.5.6(a) represents different transverse size of the atomic sample. Then the rate η will also change and has to be calculated for each point of the graph by calculating the number of spontaneously emitted photons per atom for an average incident intensity experienced by the atoms and integrating over the pulse duration time τ as done in [25]. To include the same non-destructive conditions, i.e. the same η for each point, we adjust the detuning so that the values of η become identical for all the points. The result of the numerical calculation of κ^2 with $\eta = 1$ and scaled detuning is shown in Fig.5.6(b). The advantage of the bigger samples over the samples with less atoms is again restored.

5.4 Coupling strength in the 3D model

In Sec.5.1 we have introduced the SNR or coupling strength of the light atom interaction at the off-resonant limit. We have shown that calculating the number of coherently scattered photons gives the κ^2 parameter. However in the real experiment we cannot distinguish between coherently scattered photons and incident photons. The signal we detect is the interference between these photons. To overcome this problem we need to express the power of the scattered wave with the incident power by inclusion of the geometrical corrections to it. The scattered power in Eq.5.21 can be rewritten using two new parameters the transverse beam area A_{ph} as πw_0^2 and the sample area A_{at} as πw_a^2

$$P_{sc} = \frac{3}{2} N_{at}^2 \frac{\sigma_0}{A_{ph}} \frac{\sigma_0}{A_{at}} \left(\frac{\gamma}{2\Delta}\right)^2 g_T g_L P_{inc}$$

Using eq.(5.7) we obtain the SNR assuming unit quantum efficiency detection and inserting the $(\delta N_{at})^2 = N_{at}/4$ as:

$$\kappa^2 = \left(\frac{S}{N}\right)^2_{3D} = \frac{1}{8} g_T g_L \frac{3\sigma_0^2}{A_{at} A_{ph}} N_{at} n_{ph} \left(\frac{\gamma}{2\Delta}\right)^2 \tag{5.25}$$

In the last equation we have substituted the value of the atom number fluctuations with the noise of an atomic sample prepared in a coherent superposition state of the kind introduced in Ch.2, Eq.(2.11). Comparing Eq.(5.25) to the expression Eq.(5.7), obtained from the 1-D model in Sec.5.1, we see that the coupling strength is modified by the diffraction effects encoded in the geometrical factors. The equations give the same results for samples with Fresnel numbers close to 1 and equal probe and sample diameter. For an elongated atomic samples with $L_0 \gg \tilde{z}_{ra}$ and size equal to the probe beam size we can expand the geometrical factors and obtain an expression for the coupling strength in the case of elongated samples as

$$\kappa^2 = \frac{\pi^{3/2}}{8}\left(\frac{\lambda}{2\pi}\right)^3 n_{peak} n_{ph}\left(\frac{\gamma}{2\Delta}\right)^2. \tag{5.26}$$

where n_{peak} is the peak atomic density.

At the end as a conclusion to this chapter we can summarize that we have found a simple analytical formula to include the diffraction effects in the light-matter quantum interface. The validity of the analytical prediction was tested using a numerical calculation of the scattering integral for atomic samples of different geometries. We found that the analytical estimate agrees with the numerical results at 20% level over a wide range of parameters.

The coupling strength of the interaction is modified by the geometry of the atomic sample through the geometrical factors describing the effect on the longitudinal and transverse extent of the sample.

Chapter 6

Magneto-Optical Trap

The magneto optical trap is a main ingredient in our experiment. In this chapter we give a detailed description of the magneto-optical traps used in the experiments performed at Århus University (AU) and Niels Bohr Institute (NBI). The MOT at Aarhus we refer to as a first generation MOT or AU MOT and the MOT at NBI we refer to as second generation MOT or NBI MOT.

The chapter start with description of the optical setup for laser cooling of Cs atoms in a MOT in Sec.6.1. The setup is the same for AU and NBI MOT's. Next, we describe the master lasers locked to a saturation spectroscopy resonances via a frequency modulation technique and the slave lasers. Third, in Sec.6.2, we describe the vacuum setups of the two experiments at AU and NBI. In Sec.6.3, we continue with the characterization of the quadrupole traps used in the two experiments, including a section devoted to compensation of eddy-current induced magnetic fields. In Sec.6.4 we present the main components of the imaging systems used in the first and second generation MOT. The last section presents results from fluorescence measurement of the density, number of atoms, size and temperature of the atoms in the AU MOT.

6.1 Optical setup

The laser cooling of atoms as it has been shown in the theoretical part require 6 opposing beams with polarization chosen to drive $\Delta m = \pm 1$ transition between magnetic sublevels of ground and excited states. The frequency of the laser must be smaller than the atomic transition frequency and has to be easily changed to allow for implementation of different sub-Doppler cooling schemes. The intensity in each beam has to be large enough to saturate the atomic transition. The bigger the beam radius the larger the trap volume, and the higher the number of atoms collected in the MOT.

To access the demands of the cooling process we chose firstly to stabilize two extended cavity diode lasers and then to inject their light into two additional powerful laser diodes [82], for the cooling and repumping light, respectively. We refer to the first as "master" lasers and to the second as "slave" lasers. The method is widely used in laser cooling experiments.

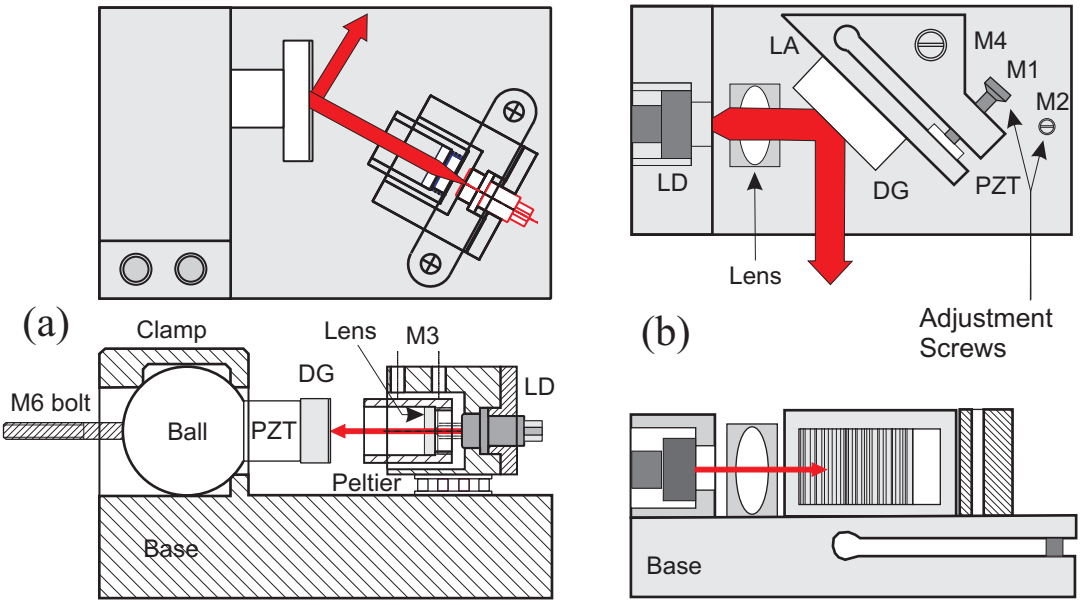

Figure 6.1: *Master lasers mechanical design. (a) Ball design top and side view, laser diode (LD), diffraction grating (DG), piezo-electric transducer (PZT). (b) Laser design adopted from Ricci et. al.*

6.1.1 Master lasers

The master lasers are based on two AR coated laser diodes[1] which emit up to 35 mW of optical power under a feedback from a grating[2] in Litrow configuration [83, 84]. The first diffraction order creates the feedback and the zero-th order is reflected as the laser output beam. We used two different mechanical mounts for the grating and laser diode. The schemes of these mounts are shown in Fig.6.1.

To the setup described in Fig.6.1(a) we refer as the "ball" design and the mechanical mount in Fig.6.1(b) is a worldwide famous mount first introduced by Ricci et al. [84].

In the ball design the laser diode is placed in a cooper cylindrical housing with outer radius of 12.5 mm, which is trimmed by one third of its radius. The laser diode is positioned in the housing in a prefabricated nest and tapped by a lid attached with M3 bolts. A small hole in the lid allows for inserting of a temperature sensor inside the nest. The laser collimation lens is placed in a small threaded-end tube with dimensions adapted to the standard size of collimation lens holders provided by Thorlabs[3]. The lens is attached to the diode laser housing by six M3 bolts placed in groups of two along the housing and separated radially by 120°.

Since the diode laser wavelength depends on the temperature the latter has to be stabilized actively on a mK range. The active element which provides the connection between the laser and the environment is an Peltier thermoelectric cooler. The Peltier element is based on a semiconductor material which creates a temperature difference when an electric current flows through it. Depending on the direction of the current the Peltier can cool or heat.

[1] Eagleyard ridge waveguide lasers
[2] holographic replica 1200 lines/mm Optometric Co.
[3] Achromatic diode laser collimator f=13.5mm, Thorlabs Inc.

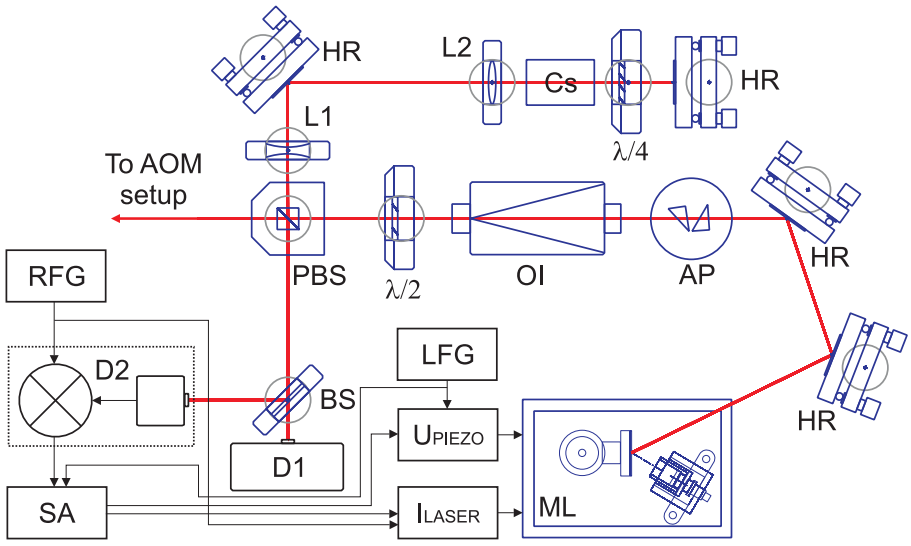

Figure 6.2: *Master laser setup: master laser (ML), anamorphic prism pair (AP), optical isolator (OI), polarizing beam-splitter cube (PBS), beamsplitter (BS), $f = -25$mm lens (L1), $f = 175$mm lens (L2), caesium cell (Cs), high-reflection mirror (HR), DC detector(D1), 5 MHz tuned detector (D2). Electronics setup also shown except temperature controller: current controller*(I_{LASER}), *high-voltage piezo-driver* (U_{PIEZO}), *sweep generator (LFG), radio-frequency generator (RFG), servo amplifier (SA) or PI controller.*

The change in the temperature inside the diode laser housing is monitored by a thermistor i.e. semiconductor material which changes its resistance when the temperature of the environment changes.

The whole construction of the laser diode housing is placed on the Peltier element and attached to a brass base by use of curved clamp and plastic screws. The upper surface of the Peltier is covered with heat-conductive paste in order to increase the thermal conductivity.

The grating is holographic replica with 1200 lines/mm and is glued to a high-voltage piezoelectric transducer (PZT). The latter is glued to a stainless steel ball with a welded M6 screw on it, used for alignment purposes. Finally the ball is clamped to the base using M6 screws. We usually use a micrometer translation stage to tune to the desired wavelength. The stage is adapted to the M6 screw on the ball.

Further, the whole base is placed on a second big Peltier element attached to an aluminum cylindrical holder with groove at the bottom to adapt a fork for clamping to the optical table. The setup has very good long term stability even though it looks a little bit strange. The wavelength at which the fluorescence can be observed in the atomic cell (look at the next section) is roughly tuned very easily, thus the mechanical design allows for very quick tuning.

The mechanical construction showed considerably good long term stability of up to 4-6 months without major adjustment. There was only one alignment pitfall. The fixing of the screws used to attach the ball to the base is difficult, because the ball can slip during the tightening.

The second mechanical design consist of a lever arm (LA), attached with a M4 screw to the base [see Fig.6.1(b)]. The opening of the lever is adjusted by pushing with a micrometric screw (M1). Between the screw and the lever a low-voltage PZT is attached.

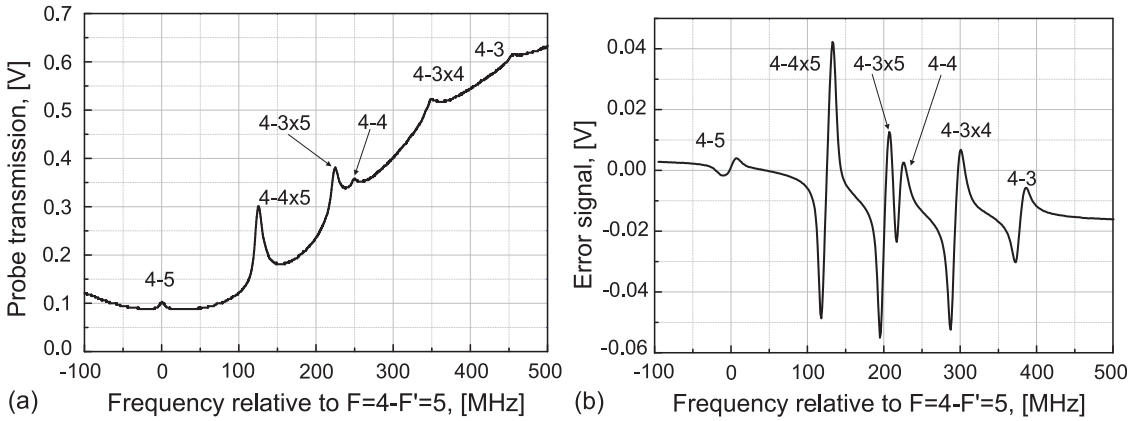

Figure 6.3: *Saturation absorption spectroscopy. (a) Saturation absorption profile for* $F = 4 \rightarrow F' = 3, 4, 5$. *(b) FM spectroscopy error signal for the relevant levels from (a).*

The diode is placed in a housing, and fixed to the base. The base is also slotted in the horizontal direction to form a lever, the position of which can be adjusted with another screw (M2). The diode laser collimation lens is placed in threaded housing.

The adjustment of the angle is done by the M4 screw coarsely and by the MM1 finely. The vertical direction is adjusted by MM2. The lens holder can be attached to a micrometric translation stage during the alignment process. After collimation of the laser beam the lens holder is fixed to the base using epoxy glue.

6.1.2 Saturation Absorption Spectroscopy

In our experiments we use an atomic resonance as a reference for stabilization of the diode lasers. This section will briefly introduce the concept of saturation absorption spectroscopy as a tool to produce narrow doppler-free absorption resonances.

The saturation absorption spectroscopy is investigated in detail [85, 86]. Briefly, it consists in the following. A powerful "pump" light beam interacts with a group of atoms having a certain velocity i.e. certain atomic velocity class. Atoms initially in the ground state absorb photons from the laser beam with a detuning that matches the Doppler shift of the resonance of an atom at rest. In other words, the pump beam burns a hole in the velocity distribution of the ground state. Then a weak counter-propagating probe beam is used to detect the resulting atomic velocity distribution. If the frequency of the pump and probe beams are the same then they interact with the same velocity class of atoms that has zero velocity component in the propagation direction. Thus the Doppler shift is canceled and a peak in the transmission profile of the probe beam is observed when the laser frequency is scanned across the resonance Fig 6.3(a). If the atomic excited state has hyperfine structure, then the individual hyperfine levels can be resolved using this method. An additional crossover resonances appear between the adjacent hyperfine levels due to the interaction with atoms with the same velocity but excited to a different hyperfine component.

In the experiment the output laser beam is directed to a pair of anamorphic prisms, one pair for each of the master lasers, to convert it from elliptical to a circular one [see Fig.6.2]. After the shaping the laser beam passes through an optical isolator[4] to ensure

[4]OFR, mod. IO-2.5D-852-VLP, transm. 86-90 % isol. 34-40 dB

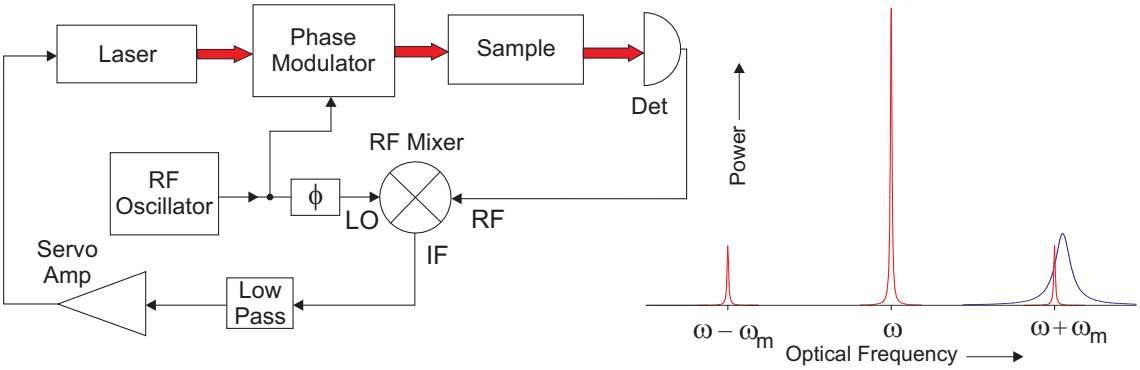

Figure 6.4: *Principle scheme of frequency modulation spectroscopy (left), and spectrum of the laser light after the phase modulation along with absorption resonance (right).*

that there is no optical feedback to the laser. With a PBS and half waveplate we can split and adjust the laser beam in two channels. One channel is used to prepare a seeding beam for injection-locking of the slave laser, and the other goes to the saturation spectroscopy stage containing the Cs atomic vapor filled in a low pressure glass cell[5]. The strong pump beam depletes the ground state. The reflected beam probes the created population in the atomic medium and is detected by a photodiode (D1).

The laser frequency is tuned via changing the cavity length by modulating the voltage applied to the PZT at a given rate and modulation depth. In our case the PZT voltage is modulated at 100 Hz with a triangular waveform from a low frequency generator[6]. The amplitude of the modulation signal is chosen to allow for a full scan of the hyperfine manifold of the excited state. The curve in Fig 6.3(a) represents the power of the transmitted probe beam as a function of the frequency separation between the adjacent excited states when the frequency of the cycling transition is chosen as a reference. We can clearly distinct the three hyperfine transitions $F = 4 \rightarrow F' = 5, 4, 3$ along with the crossover resonances $3 \times 4, 4 \times 4, 4 \times 5$, respectively. The transmission at the crossovers is higher and they are good candidates for use as a reference to lock the master lasers using an frequency modulation (FM) spectroscopy technique.

6.1.3 Frequency modulation spectroscopy

The long term stability of the lasers is of main importance in a laser cooling experiment. Thermal fluctuations and mechanical vibrations are among the worst influences that can destabilize the laser frequency. This generates laser frequency jitter i.e. laser frequency noise. The later is connected to the linewidth of the laser [87]. To prevent the detrimental effects of this noise onto laser radiation frequency one needs to stabilize i.e. "lock" the laser frequency to a stable frequency reference. The stabilization of the laser frequency leads to a reduction of the linewidth of the laser.

Stabilization of lasers is a vast laser physics field and we are not going to discuss it in much detail here. We will only present briefly our stabilization scheme. In general a reference for the laser stabilization can be either an atomic medium [86] or an optical cavity [88]. Another already stabilized laser or a beat-note of two lasers [89] can also be used as a reference for locking.

[5] 10^{-3}mbar

[6] Escort 2MHz frequency generator

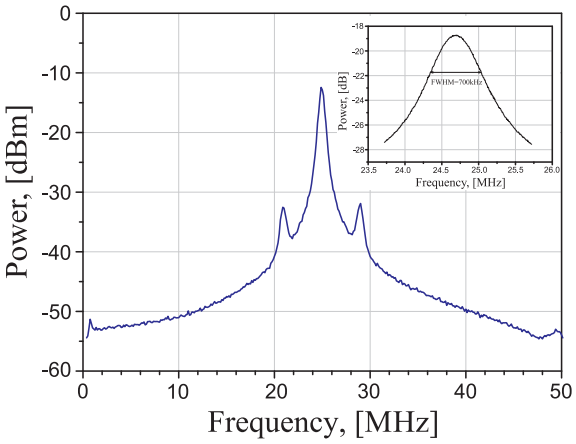

Figure 6.5: *Beat note of two extended cavity master diode lasers. The lasers are locked to* $F = 4 \rightarrow F' = 4$ *and* $F = 4 \rightarrow F' = 3 \times 5$ *transition. The sidebands at* 4 MHz *are due to the modulation of the diode laser injection currents. The onset shows the beat-note width of* 700 kHz.

The idea behind the stabilization of the laser frequency in general is the following. The output laser frequency is compared to the frequency of the reference, and the result is used in a feedback scheme to create correction of a controllable laser parameter, such that the difference between the laser frequency ω and the reference frequency ω_0 vanishes. To accomplish this the laser phase is modulated at a frequency ω_m with a modulation depth of M by a phase modulator using a radio-frequency (RF) oscillator. The phase modulation results in a frequency modulation (FM) [90–92] with a spectrum that contains, a carrier at the laser frequency $\omega_c = \omega$, and two sidebands with frequencies of $\omega \pm \omega_m$ as shown in Fig.6.4. The modulated laser light is sent through a sample that "contains" the spectral reference. If the spectral feature is not present the two sidebands have equal intensities and opposite phases, thus resulting in constant intensity at the detector (Det). However, when one of the sidebands interacts with the spectral feature its intensity is reduced and the amplitude of the detected signal changes. If the carrier frequency is scanned (in our case using the PZT of the diode laser) then the output signal exhibits an amplitude modulation (AM) depending on the frequency modulation. Thus the effect of the atomic sample is conversion of FM to AM. The produced photocurrent contains beat signals at the ω_m and is directed to a double balanced mixer, where it is demodulated via mixing with the local oscillator at ω_m. The result at the intermediate frequency (IF) of the mixer is a bipolar error signal proportional to the frequency offset $\omega_0 - \omega_c$. After a low-pass filtering the error signal is fed to a servo amplifier (ServoAmp) or proportional integral derivative (PID) controller to produce a time dependent correction for the controllable laser parameter.

In our experiment the reference is a saturation absorption resonance, created with the method already discussed in Sec.6.1.2. Usually we use a crossover peak from the signal plotted in Fig.6.3(a). The laser current is directly modulated using a sine waveform from a RFG[7] at a frequency of 4MHz [see Fig.6.2]. This results in sidebands separated from the main carrier at 4MHz. They are detected by a phase sensitive 4 MHz-tuned detector-mixer (D2) that generates an error signal Fig.6.3(b) via demodulation at 4 MHz. Further

[7]HAMEG 10MHz programable function generator

the error signal is sent to a proportional integrator circuit (SA) to produce slow and fast correction to the voltage and current of the piezo-driver and laser current controller, respectively.

With that procedure applied we lock the cooling master laser to the 3×4 crossover and the repump laser to the 2×3 crossover. Then the frequency is further shifted with acousto-optical modulators (AOM's) by an amount of 336 MHz and 276.5 MHz for the cooling and repump lasers, respectively. The AOM setup is explained in a next section.

As we mentioned above locking the laser to a reference will reduce its emission linewidth. Typically the extended cavity diode lasers have a linewidth of several 100 kHz. The estimation of the laser linewidth can be done in various experimental ways [93–95]. Here we look at the beat-note of two extended cavity diode lasers when they are combined on a 50/50 beamsplitter.

The beat-note contains two components: sum and difference of the frequencies of the two lasers. The first is filtered out due to the limited bandwidth of the fast photodiode[8] and the second one is detected and observed with an RF spectrum analyzer[9]. The detector is also used to measure the beat-note of the lasers with a frequency difference as large as the ground state hyperfine splitting (9.192 GHz) of Cs. The result from the beat-note measurement is shown in Fig.6.5. The difference between the laser frequencies is 25MHz and the sidebands are due to the modulation of the laser current with an RF signal of 4MHz explained earlier in this section. The width of the carrier is estimated to be around 700 kHz, indicating that at least one of the two lasers has a linewidth lower than 1 MHz.

6.1.4 Slave lasers

The two slave lasers are high power laser diodes[10] which provide up to 200 mW and 150 mW, respectively, of optical power at 852nm. They are injection-locked to the master lasers. Two experimental setups are made for the cooling and repump light, respectively. The slave laser setup is shown in Fig.6.6.

The seeding beam comes from the left and is denoted with an arrow. It is further split by a PBS1 and the reflected part is focused with a lens L1 in an AOM1[11] in a double pass configuration, to a waist 0.2mm inside the crystal. The overall shift of the AOM1 is 251 MHz for the cooling laser and 251 MHz and 191.5 MHz for the repump laser. The obtained diffraction efficiency is 80%. The AOM1 controls the detuning of the MOT cooling light and its RF drive frequency can be changed by varying the input voltage of the voltage-controlled oscillator (VCO) of the AOM driver.

The reflected from the curved mirror HCR beam propagates in the same path as the incoming beam. However, its polarization is orthogonal with respect to the incoming beam and thus it is transmitted through the PBS1. Further the seeding beam is transmitted through the PBS2 and subsequently through the lens system L2-L3 where its radius is reduced 5 times in order to match it with the slave laser beam. The weak slave laser beam reflected off the optical isolator's PBS [the dashed line in Fig.6.6] is used to align the overlap of the slave laser beam and the seeding beam, via the two high reflection mirrors HR1 and HR2. For a good alignment overlap the seeding and the weak reflected slave beam propagate almost along the same path. This eventually can induce instability in

[8] NewFocus Inc. 15GHz bandwidth, GaAs photodiode, model 1480-S
[9] Agilent HP 4411B, maximum frequency 1.5GHz
[10] JDS Uniphase SDL-5432, SDL-5422
[11] TeO_2 frequency shifter Brimrose Co.

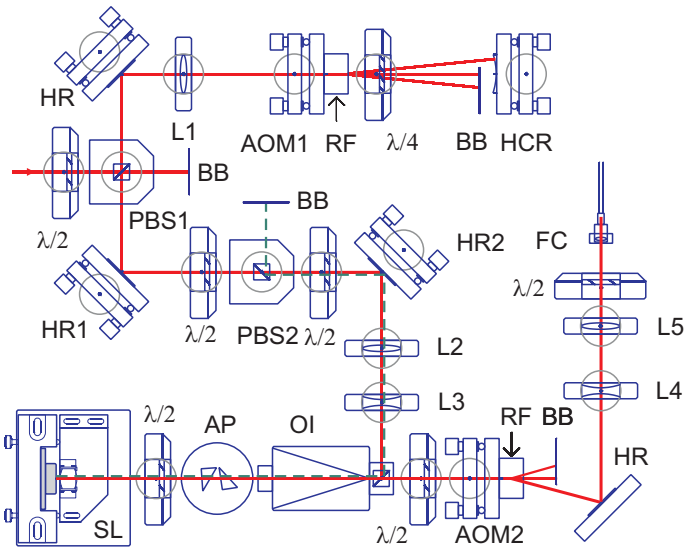

Figure 6.6: *Slave laser setup: slave laser (SL), anamorphic prism pair (AP), optical isolator (OI), polarizing beam-splitter cube (PBS), $f=$ 200mm lens (L1), $f=$ 125mm lens (L2), $f=-$25mm lens (L3), high-reflection mirror (HR), high-reflection curved mirror* R = 100mm *(HCR), acousto-optical modulators (AOM1) and (AOM2) with drive frequency* 125MHz and 85MHz*, beam blocks (BB), fiber coupler (FC).*

the master laser. For that reason a PBS and half-wave plate are inserted in the path of the seeding beam to reflect off the counter-propagating slave laser beam. Another thing to emphasize here is that the power of the seeding beam has to be as low as possible to prevent for master-laser-light-induced instabilities. The values of the seeding beam power typically is less than 1 mW.

The injection locked slave laser beam is sent through an AOM2 which is used as an intensity modulator with a fixed frequency shift of 85 MHz. Additionally, mechanical shutters are used to completely blocked the light of the two slave lasers, when it is needed. The maximum obtained diffraction efficiency is 81%, and 73% for the cooling and repump slave lasers, respectively. The first diffracted order of the AOM2 is sent to a telescope lens system to match the beam diameter with the diameter of the fiber eigenmode via the fiber connector FC.

Two independent saturation absorption spectroscopy stages are set up for both slaves in order to monitor their injection locking.

6.1.5 Trap optics

The MOT requires 6 beams to provide cooling in three dimensions. Two basic configurations of the light fields in MOT are known. The beams can be either three which are retro-reflected or six which are independent. In our setup we use six independent beams which are produced by splitting the cooling and repump beam. The beams are combined in advance on a PBS. Then the six beams are sent to six fiber couplers where they are coupled into six polarization maintaining fibers.

As we have shown in Ch.3, the MOT requires that the pairs of opposing beams must have σ_+ and σ_- polarization with respect to the direction of the magnetic field. This would mean that the beams in the horizontal plane must have polarization which is opposite to

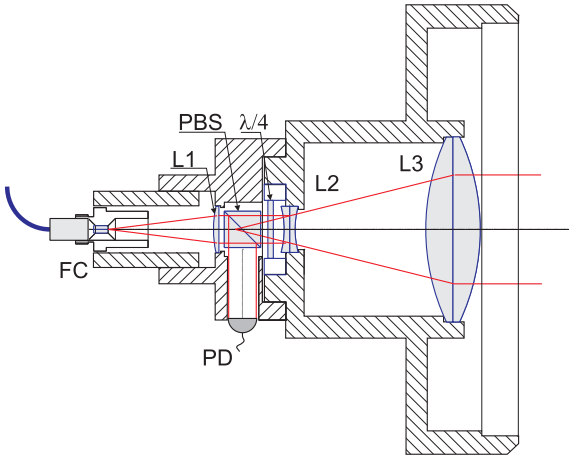

Figure 6.7: *Trap beam collimator. fiber connector (FC), collimating lens* $f = 30$mm *(L1), polarizing beam-splitter cube (PBS),* $f = -15$mm *lens (L2), 50mm dia.* $f = 60$mm *lens (L3), photodiode (PD).*

the polarization of the vertical beams. Since in the first generation MOT a Ti chamber have been used the trap optics was designed to meet the requirements of the chambers flange radius. Then we adopted this design to the second generation MOT which employs a quartz cell. The design of the beam collimator is shown in Fig.6.7.

The optical setup includes a collimating lens, polarizing beam cube quarter-wave plate to produce circular polarization and a 4x telescope. The resulting gaussian beam diameter is 2.5 cm. A photodiode is inserted in the reflected beam path for monitoring purposes. The fiber coupling varies on a monthly bases and has to be checked regularly using either the photodiode or a fiber optic powermeter. Nevertheless, the variation in the power is about 10% when monitored for approximately 30 days. The efficiency of light coupling in the fibers on average is around 50% per fiber. There is slight difference between the coupling efficiency of the two lasers due to the slightly different beam radii of the two beams - cooling and repump. The maximum power levels obtained for the six beams are 60 mW and 30 mW for the cooling and repump light respectively.

6.2 Vacuum setup

In this section we describe briefly the vacuum setup used in the experiments at Århus and NBI. The AU MOT was loaded in a Titanium chamber, whereas the NBI MOT employed a ultra-high vacuum (UHV) quartz cell. The vacuum setup builded for AU MOT was extended from an initial vacuum setup employing a quartz cell for application in a atomic fountain. The initial line of thought for this project was building an atomic fountain and testing possibilities for generation of squeezed states specifically addressed to the Cs fountain clock (see Sec.10.2.3). However, since the generation of this non-classical state is a fundamental quantum-mechanical problem it can also be studied separately and then applied to the atomic fountain. This second "line of thought", was completely adopted when we moved the laboratory to Copenhagen.

6.2.1 Århus vacuum setup

The chamber used in the experiment at Århus University was made out of Titanium by Kimbal Physics Corp[12]. A picture of the chamber is shown in Fig.6.8. Titanium is a good vacuum material [96] since it shows faster decrease of the degassing effect when heated compared to the stainless steel. The choice of Titanium is also favored by its non-magnetic properties. Stray magnetic fields and their gradients could cause population of magnetic sublevels with magnetic quantum number different from $m = 0$. This is crucial for Cs atomic clock, where the $0 \rightarrow 0$ transition in the ground state is required.

As it can be seen the chamber has 6 big viewports corresponding to the DN63CF flange and 8 small corresponding to DN16CF. The six big windows provide the inputs for the six MOT beams, and the small windows are used for both interferometric and fluorescence detection. The optical access of these viewports is 55mm and 13mm in diameter. The chamber uses titanium flanges attached to it by hex-head Titanium bolts. The chamber viewports[13] were also made out of Titanium and BK7 glass with an anti-reflective coating (AR) at 852nm 63mm diameter optical windows[14] and 14mm in diameter AR coated for both 852 and 1064nm.

The optical windows were glued to the Ti flanges using thermoplastic epoxy[15], which was cured at 100 deg. for 30 min. The epoxy is advertised as very-low-outgassing-rate material. The BK7 glass and Ti have similar thermal expansion coefficient (8.3μm/°C : 9.2μm/°C) but unfortunately different modulo of elasticity (60 GPa:116 GPa). As a consequence the BK7 window cracked during sealing with copper gaskets. The only choice to keep the windows intact was to use Viton gaskets[16] in order to prevent the mechanical stress over the viewports. Since some of the windows were already broken we needed to repair them by placing a thin layer of the same glue along the joint between the glass and Ti flange from the side "facing" the vacuum.

The crack on the windows and the Viton gaskets did not alow for efficient bake out of the apparatus. The maximum bake-out temperature for the chamber was not more than 130°C. The ion pump was baked up to 150°C with magnets in place. The pressure after the cool-down and starting the ion-pump was of the order of 2×10^{-8}mbar. Since we do not use gauge the estimation of the pressure inside the apparatus can be done either by the ion pump leak current or by the loss rate of the MOT.

The vacuum setup sketch is shown in Fig.6.9. We use a 20 l/s ion pump[17] to maintain the vacuum inside the apparatus. The chamber was supported by home-built aluminium holder and pumped out through thin 9.5cm long tube with a working aperture of 1.2cm in diameter. The calculated effective pumping speed of the apparatus is 1.65 l/s taking into account the overall length of about 60cm long tubing and the reduction due to the small orifice. The overall outgassing rate was calculated to be around 4.4×10^{-7} mbar.l/s, which with the calculated pumping speed gives the limiting pressure of 2.7×10^{-7} mbar. The real value of the pressure inside the experimental chamber was probably higher due to the leaks through the cracked windows, which have appeared after the baking.

The atomic source, 4mg of solid Cs, was placed in a small container and heated to

[12] Kimbal Physics Inc. Spherical cube
[13] MBE Components GmBH.
[14] EKSPLA Co.
[15] Epotek H74
[16] MDC vacuum Co.
[17] Varian Vacuum Inc. VacIon-20, Star Cell pump

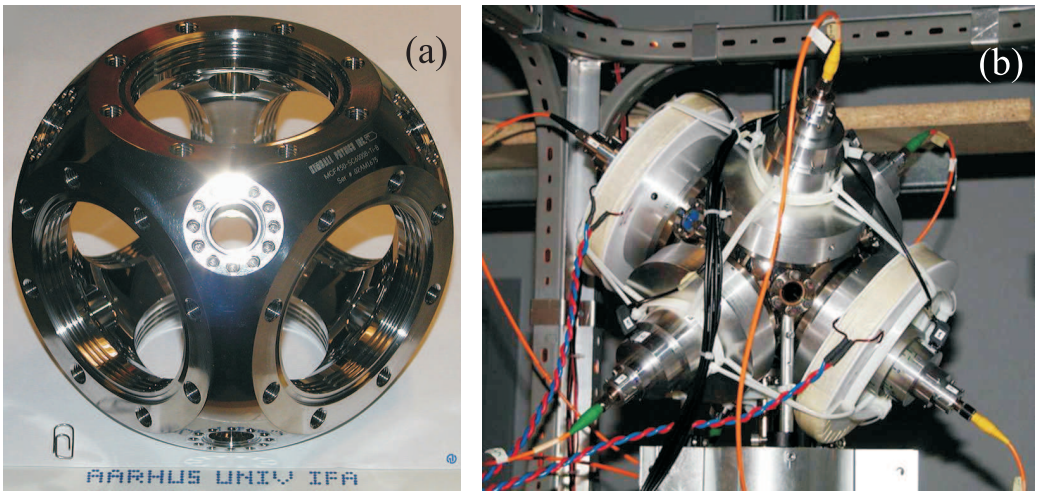

Figure 6.8: *Titanium chamber used in the AU MOT(a). Assembly of the AU MOT (b).*

evaporate certain amount. The container was attached to a right angle valve[18] with Viton seal. Two different attachment configurations of the Cs container were used. Firstly, the container was attached close to the ion pump. Due to the long distance to the chamber and the thin connecting tube the migration speed of the Cs vapor to the chamber was rather low. Moreover the gravity force is directed opposite to the mean velocity of the particles traveling upward. The other configuration was to place the source at the top so that atom will be helped by the gravity, but again the effect of the thin tube dominates. Nevertheless after a week the chamber was supplied with atoms.

6.2.2 NBI vacuum setup

After the moving at the Niels Bohr Institute we took the decision to rebuild the vacuum setup so to get rid of the cracked viewports and the Viton gaskets. It turned out that the windows can only be removed from the flanges by mechanical means i.e. machining them out. Then we switch to use a quartz cell[19]. The vacuum setup along with the orientation of the trap beams is shown in Fig.6.10.

This time the setup is a lot easier to assemble, maintain and use. The ion pump and its holder are the heaviest parts in the whole construction attached to an optical bredboard. The coils and the collimators are attached to a home-made aluminum plate with dimensions 750×580 mm. The plate is supported to the optical bredboard by using Strut aluminum profile[20].

The bake-out procedure this time went up to 180°C for the quartz cell and 200°C for the ion pump which had its magnets taken off. After baking for a week and subsequent cooling down we get to the level of 10^{-9}mbar with an effective pumping speed of 2.6 l/s. The pressure we estimated from the ion pump current which showed less then 6μA. The gauge at the turbo pump at the same time showed 8×10^{-10}mbar.

The old Cs container was replaced with four Cs dispensers[21] connected in series two by

[18] MDC Caburn, check number
[19] Starna Inc.
[20] Bosch-Rexroth Inc.
[21] SAES Getters CS/NF/17/50 FT10+10

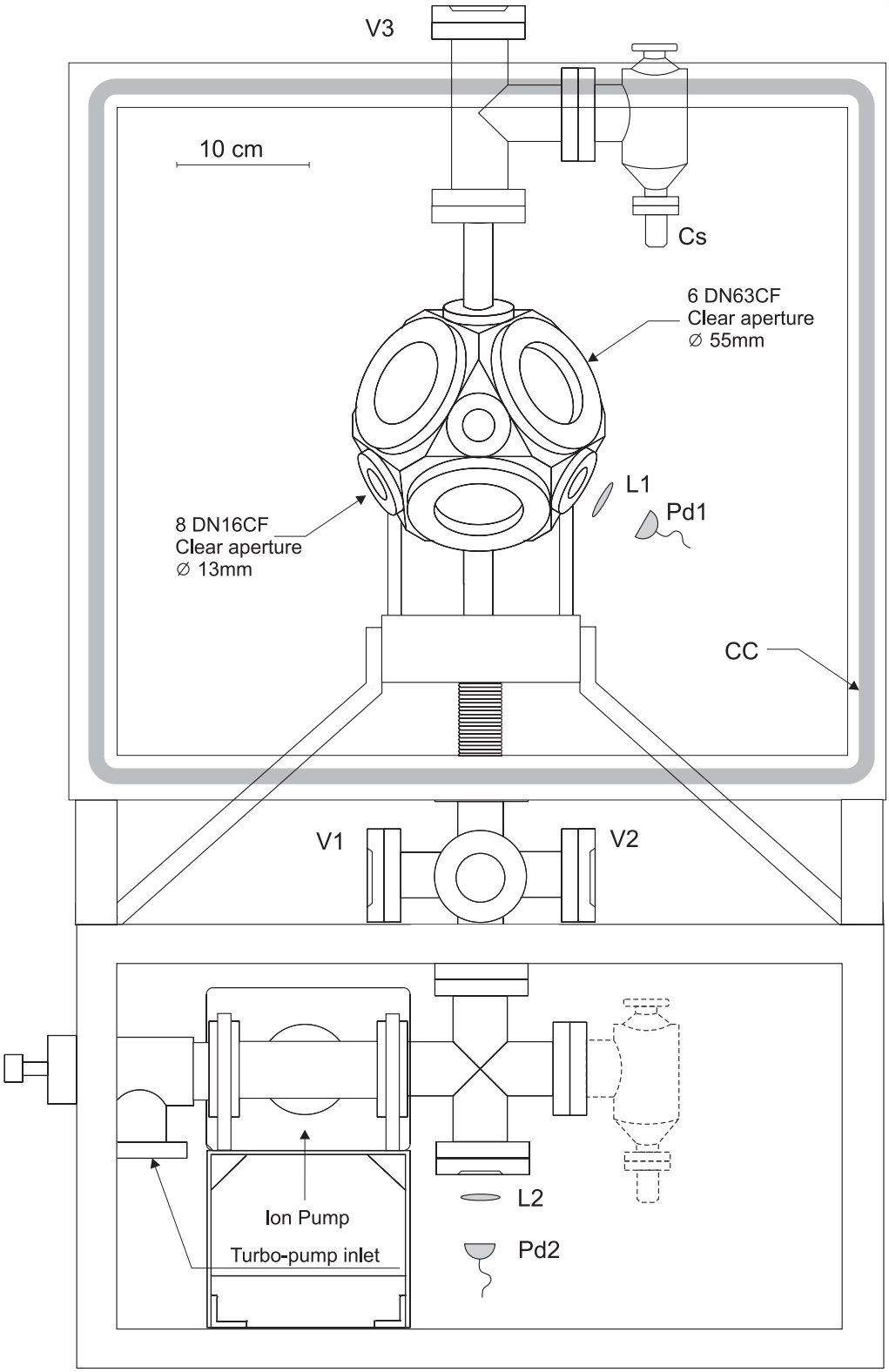

Figure 6.9: *Layout of the vacuum setup in Aarhus: non-magnetic viewports (V1,V2,V3), caesium container (Cs), compensating coils (CC), lenses (L1,L2), photodiodes (Pd1,Pd2).*

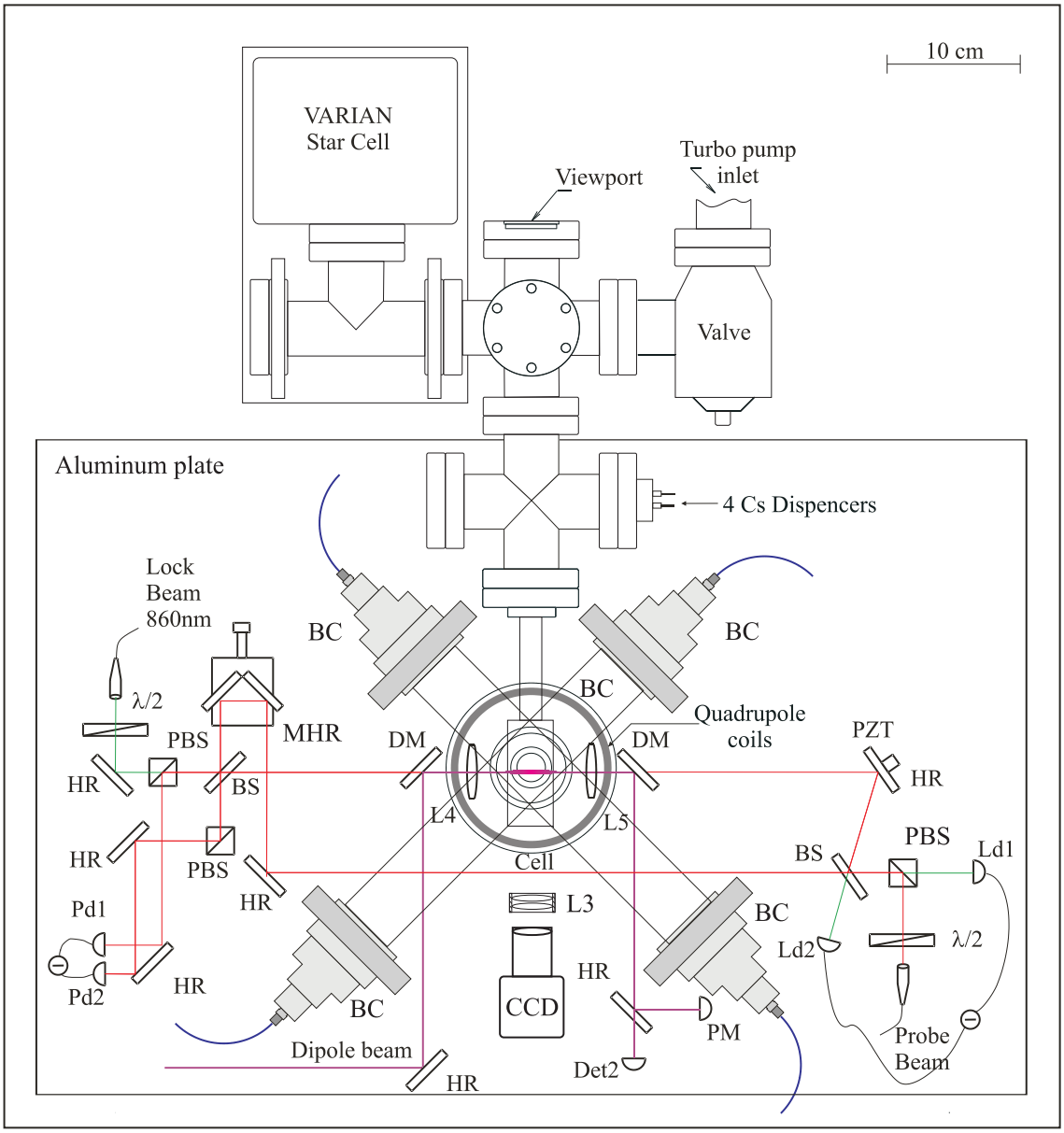

Figure 6.10: *Layout of the trap setup and interferometer in Copenhagen: beam collimators (BC), mounted achromatic lens pair (L3). The compensating coils not shown here. Interferometer components: high reflectors (HR), dichroic mirrors (DM), 50/50 beamsplitters (BS), polarizing beamsplitters (PBS), achromatic doublet lenses* f = 100 mm *(L4,L5), probe beam detectors (Pd1,Pd2), locking beam detectors (Ld1,Ld2), movable high reflectors (MHR), auxiliary detector (Det2), high-power powermeter (PM).*

two. The release of Cs from the dispenser is done by evaporation when an electrical current flows trough it. The maximum Cs content in a dispenser is 7.3 mg. The operating current used is in the range of $3.2 - 3.5$ A. The necessary amount of Cs in the cell is produced for a time interval of 3 hours to 3h − 20min depending on the value of the current.

6.3 Magnetic field and trap orientation

In this section we describe the geometry of the MOT including the quadrupole magnetic trap [97] and light beams. As before, here we also consider the two traps AU MOT and NBI MOT separately.

In the second part of this section we briefly present the switching characteristics of the quadrupole field in the NBI MOT. The switching was done using a home-built current driver to compensate the eddy-currents induced magnetic fields.

In both AU and NBI MOT the stray laboratory magnetic field were compensated by 3 pair of compensating coils. Each coil pair have the currents in every coil flowing in the same direction.

6.3.1 Århus trap

The trap at Århus University was created by a pair of coils with radius of 77mm separated 186mm apart and placed on the Ti flanges. The copper wire was wound on a teflon ring. The number of turns in each coil is 170 and with a current of 7.3A we get to field gradient of 10G/cm. The power dissipated from the coils was around 30W which leads to substantial heating of the coil. To prevent this we switched to a hollow copper tube, which can be water cooled. Due to the large cross-section of the tube the number of achievable turns was limited to only 24 thus leading to an increase of the current to 50A.

The switching time of the magnetic field was mainly determined by the coils inductance and the eddy current induced magnetic fields. The latter were almost the same for both coils due to the symmetry of the chamber (see Fig.6.8(b)). The magnetic transient decay time constant was estimated by measuring the decay of the MOT after switching of the magnetic field. The value deduced from the experimental data at 10G/cm is 10 ms. The presence of molasses cooling light during the detection could also contribute to the decay i.e. to increase its time constant.

6.3.2 NBI trap

The trap at Niels Bohr Institute has smaller coils with radius of 50mm but this time they are placed very close to each other. The distance between coils is 50mm and the number of turns 38 per coil. This value with a current of 7A gives 11.7G/cm magnetic field gradient. The power dissipated during continuous operation dropped down to 4W compared to the Århus coils and water cooling is not required. The magnetic field as a function of the distance between the coils is shown in Fig.6.11(a). The experimentally obtained value of the magnetic field gradient is 11.4G/cm, which agrees well with the theoretical one. In temperature units the maximum trap depth for that field gradient is around 64 mK at a distance of around 9 cm from the trap center. The switching of the coils in the second generation MOT is provided by a home-built current driver in order to compensate the eddy-current magnetic field and a brief description of that is given in the following chapter.

6.3.3 Compensation of magnetic field transients

The fast switching of magnetic field in a MOT depends solely on the eddy-currents induced magnetic field transients. The dynamics of these transient is governed by the well-known Lenz law. The time we have to perform a measurement on an atomic sample in most cases is limited by the interval which is required for the current flowing through the coil

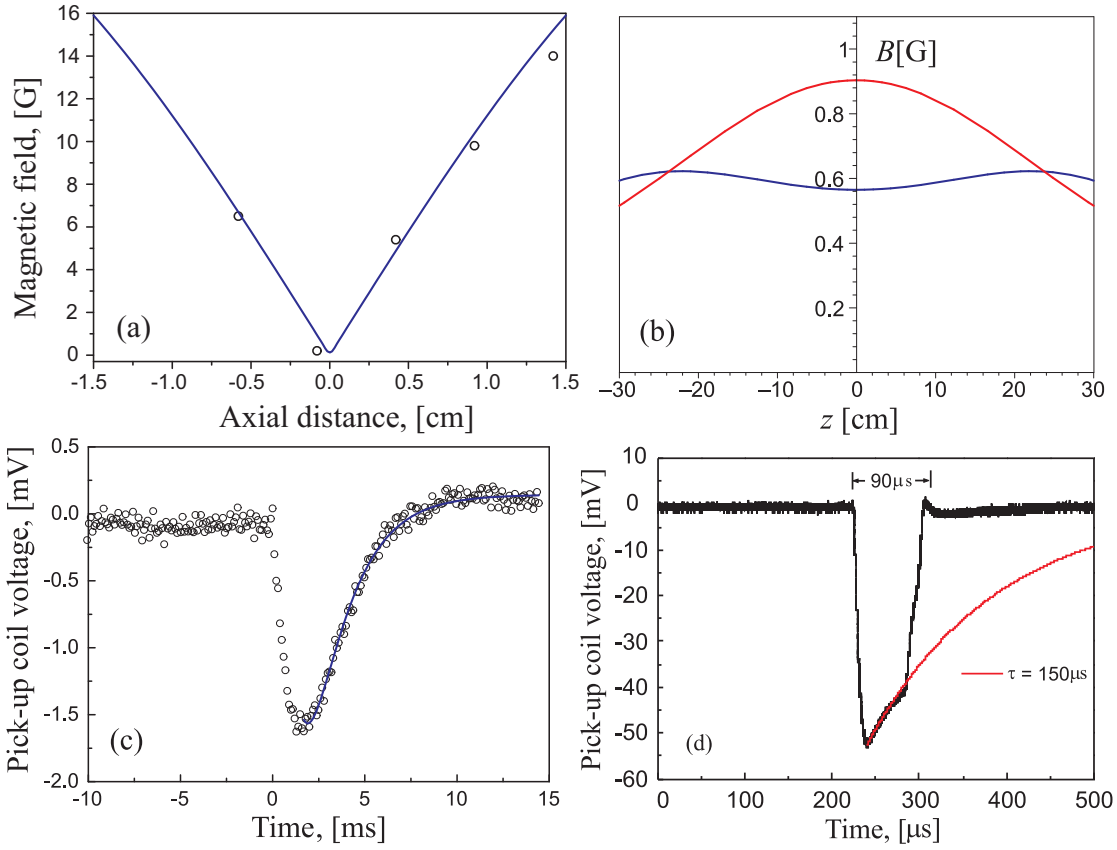

Figure 6.11: *Magnetic fields of the quadrupole trap at NBI: experimental data (○) and a fit shows 11.7 G/cm for a current of 7 A (a). Compensation coils field for the z-pair (b), magnetic field of the coils in Helmholtz configuration (red curve), and in the actual experiment (blue curve). Magnetic field transient (c). Suppression of the magnetic field transients when using the coil driver (d).*

to completely die out. To turn off the current in the coil on a microsecond time scale can be done by using a suppression diode for switching inductive loads [98]. However, bringing down to zero the magnetic field in a MOT is not an easy task since the magnetic flux change induces eddy-current in the metallic parts around the experimental chamber, which on the other hand produces magnetic field. Thus the field cannot be switched off until the eddy-current dies out.

Generally speaking the methods for compensation of the residual magnetic field can be divided to passive and active. Placing the coils inside the MOT chamber seems to be very efficient, but this would greatly complicate the mechanical design. Another passive compensation is to use magnetic shield around the gradient coils. An active stabilization can be achieved by monitoring the magnetic field via a sensor in order to implement an electronic feedback to correct the value of the coils current [99]. A more convenient way to quickly switch the MOT field is to reverse the polarity of the current flowing through the coil. A switching time of the order of 350μs can be achieved with this technique [100].

The magnetic field of NBI MOT is switched off on microsecond timescale by a home-built fast switching current driver which relies on the latter described technique. The full description of the current driver is done in [101] and here only the result will be included.

The switching time constant of the setup is measured using a cryptically damped pick-up coil. The coil is a lot smaller than the gradient coils and has inductance of 7 μH and resistance 0.1 Ω connected in parallel with a capacitor of 2.2 μF and in series with 3.3Ω resistor. The bandwidth of the circuit is limited to 40kHz in order to prevent for high frequency noise pick-up. The voltage drop across the pick-up coil is shown in Fig.6.11(c). The two-exponential fit to the collected data showed exponential decay with time constant of 1.97(17) ms and 0.80(18) ms with a settling time of around 10 ms. This is much slower than the switching time of the supply and therefore attributed to the eddy-currents induced magnetic field transients. When performing the switching of the coils using the driver the duration of the magnetic field transient is reduced to 150 μs (the red curve) and when reducing the settling time due to the Lenz effect we get around 90 μs transient duration (the black curve) as shown in Fig.6.11(d).

At the end of the magnetic field discussion we will dedicate few lines to the compensation coils of the MOT. We use three pairs of square compensation coils which form the six sides of a cube with dimension of approximately 55 cm. If the distance between the coils was roughly equal to half of their dimension, then every coil pair would satisfy the Helmholtz configuration. In Fig.6.11(b) we present theoretical calculation of the field of one pair, taking into account the actual dimensions and number of turns. In the Helmholtz configuration (red curve) we have a constant field along a distance as long as 20 cm, whereas in the actual experimental configuration (blue curve) the field is constant along a distance of 8 cm. However, in the experiment the MOT size is around 3 mm, which is well in the region of the constant bias field.

6.4 Imaging system

In many of the atom cooling experiments the imaging both absorption and fluorescence are primary method of quantitative and qualitative atomic sample characterization. However, in our experiment we use an interferometer as a principal characterization tool and the imaging is only used for determining the cloud size or for qualitative and alignment purposes.

The basic ingredient of an imaging setup is the CCD (charged-couple device) camera. The CCD chip consists of a silicon pixel photo-capacitors array which produces charges when the light impinges on it. The higher the flux is the higher the value of the charge. The charge is collected until the exposure lasts. At the end of the exposure this charge is electronically read out an converted to an analog voltage, which is further digitized by an ADC (Analog-digital converter).

In our experiment the CCD cameras are analog, which means that the video signal is digitized after the camera using a frame-grabber card or other additional electronic equipment which has an ADC. Two types of CCD cameras were used: 60 Hz progressive scan[22] equipped with 1/3-inch frame transfer CCD chip[23] and a standard CCIR interlace[24] mainly used for alignment purposes.

The progressive scan camera allows for taking an image of the atomic cloud on demand. The exposure is controlled by an external voltage and the duration of the trigger pulse sets the exposure time. The analog video signal is converted to digital by a 4-channel 8-

[22] Hitachi KP-F2B

[23] Texas Instruments TC237, 680×500 pixel CCD sensor, 7.4μm pixel size

[24] Philips LDH0701, 1/2-inch interline transfer CCD, 8.2μm pixel size

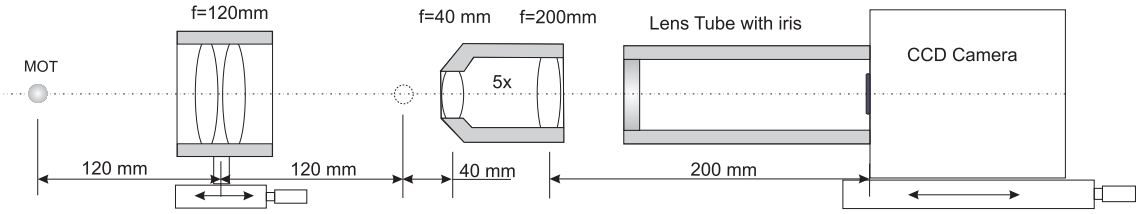

Figure 6.12: *Scheme of the imaging optics of the NBI trap.*

bit monochrome frame-grabber.[25] The frame-grabber is set to external H-lock operation mode, which means that the horizontal and vertical synchronization signals are directly supplied by stripping them of the video signal using an sync-separator.[26] The typical exposure time used is not more than 10 ms and not less than 1 ms. During this relatively short time the level of collected fluorescence is rather low, which results in a very low contrast, especially in the case of very weak photon fluxes. To overcome this problem an average over a sequence of images is taken. A simple home-written software with NI-IMAQ facility in LabView allows for snapping a certain number of images in a consecutive loading cycles and taking their average.

6.4.1 Aarhus imaging setup

Two different imaging schemes are used for the first and second generation magneto-optical traps. The MOT at Aarhus was imaged only by the two interlaced cameras. The cameras have an 80mm TV zoom lens[27] attached. One of the cameras was used in a combination of 100mm lens to produce a 10 times magnification. The second one had a lens system which produces an image of the atomic cloud onto the CCD with an effective pixel size of 30.8μm/pixel. The images with the higher magnification are greatly obscured due to spherical abberations thus preventing for reliable estimation of the cloud size. The high magnification CCD camera was only used to finely adjust the position of the probe beam with respect to the center of the atomic cloud required for the interferometric measurement.

6.4.2 NBI imaging setup

In the NBI MOT imaging in addition to the two interlace cameras we uses the progressive one to take instant images of the dipole trapped atoms. The imaging optics of the second generation experiment at NBI is constructed to be mainly used for observation of the dipole trap. The scheme is shown in Fig.6.12. A pair of achromatic doublet lenses creates 1:1 imaging of the atomic cloud which is then magnified by a 5× infinity corrected objective[28] and focused on the CCD chip of the progressive scan camera by a 200 mm focal distance achromatic doublet lens.[29] The resulting rescaled pixel size after magnification is 1.54μm. We must say that this is not a resolution since the determination of the resolution requires an imaging of an objects spaced on a distance as small as 1.5 μm.

[25] National Instruments PCI frame-grabber, mod. 1409
[26] Elantec Inc., mod. EL4583
[27] Ernitec of Denmark 1:1.4/8-80mm
[28] Infinity Achrovid 5× objective
[29] Thorlabs, AC254-200-B

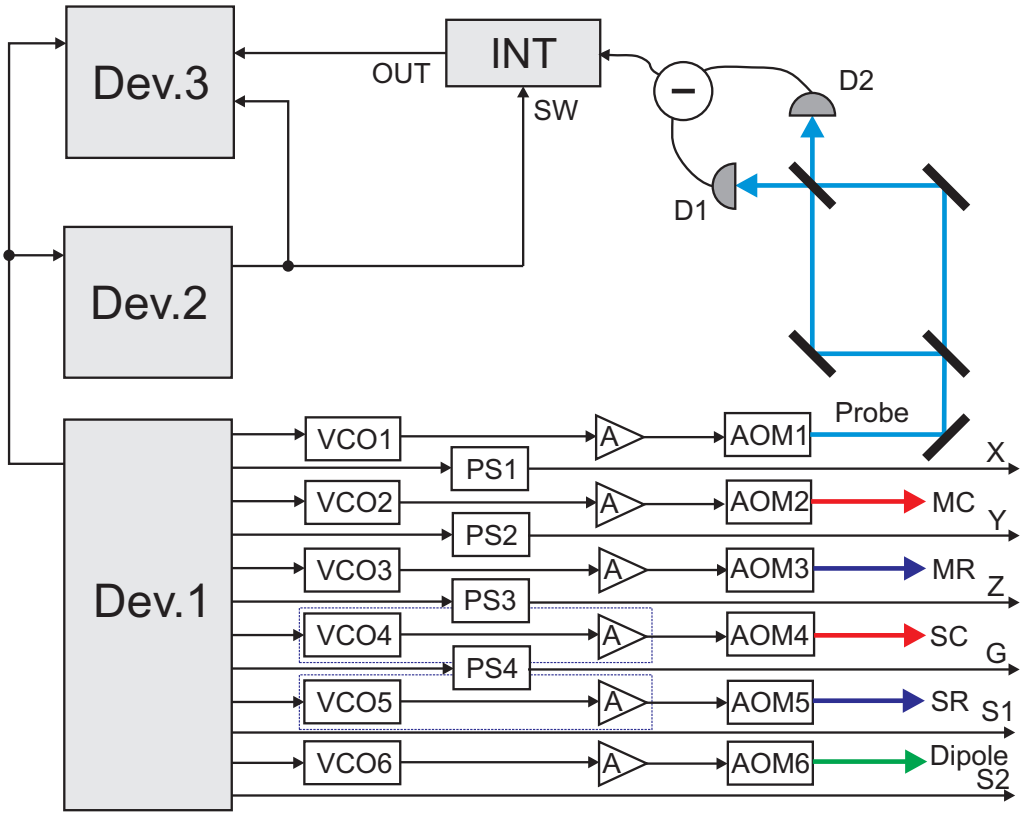

Figure 6.13: *General diagram of the computer control of the experiment: PCI cards (Dev.1,2,3) , voltage-controlled oscillators (VCO1..6), RF amplifiers (A), acousto-optical modulators (AOM1..6), current supplies (PS1..4) for the x-axis (X), y-axis (Y), z-axis (Z) compensation coils and (G) for the gradient coils of the MOT, integrator of the probe pulse area (INT), detectors (D1) and (D2). The colored arrows represent the light of the master cooling and repump lasers (MC) and (MR), respectively, and of the cooling and repump slave lasers (SC) and (SR), respectively, and of the probe and dipole trap laser.*

The CCD camera is mounted on a translation stage to finely adjust the image plane. Due to the high magnification the depth of the focus is limited to 18μm, which does not allow for high degree of adjustability in order to track large fluctuation in the cloud position.

6.5 Computer Control

The section describes the computer control of the experiment. General diagram of the hardware control and data acquisition is shown in Fig.6.13. We use National Instruments cards[30] to produce the transistor-tiristor-logic (TTL) signals for controlling the apparatus that provides signals for changing the light detuning and intensity of the lasers as well as the current of trap and compensation coils.

The Dev.1 card is the main workhorse in the experiment's control. It provides analog voltage signals to control the frequency of the master lasers via the voltage-controlled

[30]National instruments cards PCI-6713 (Dev.1), PCI-MIO-16E-4 (Dev.2), and PCI-6111 (Dev.3)

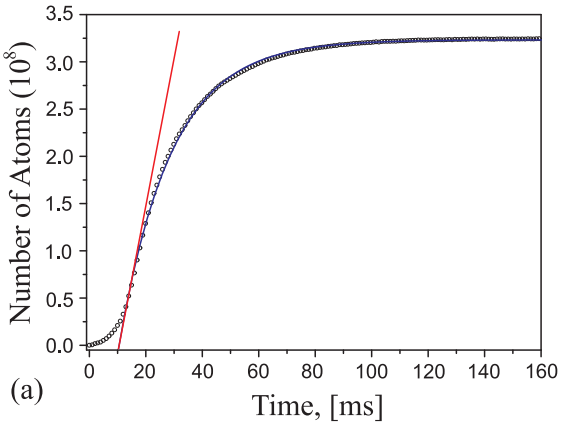

Figure 6.14: *Loading of the MOT.*

oscillators VCO1 and VCO2. The slave laser intensity is controlled by changing the RF power through the intensity AOM's drivers represented with the dashed lines combining the VCO4 and VCO5 with the RF amplifiers, and additionally by the mechanical shutters S1 and S2. The probe laser and dipole laser AOM are also controlled by TTL pulses from Dev.1. In addition to that 4 analog channels of Dev.1 are used to produce triggering signals for the MOT compensation X,Y,Z, and gradient coils G. The Dev.2 and Dev.3 are mutually synchronized to the reset switch (SW) of the integrator INT. The SW signal is produced by Dev.2. The Dev.3 performs the acquisition of already integrated pulse area. The three PCI cards are synchronized by a common clock. The software control of the above described hardware control is provided by home-written program in LabView.[31]

6.6 Diagnostics

This section deals with fluorescence characterization of the first generation magneto-optical trap. As we have mentioned earlier in the characterization of the second generation MOT we have emphasized on the interferometric characterization and especially on the density estimation.

The fluorescence of the MOT is detected by two low noise photodiodes[32] placed in the positions shown in Fig.6.9. The image of the MOT on the photodiode Pd1 is made by a 25mm diameter 63 mm focal distance lens L1, and a 60mm focal distance 50mm diameter lens L2 makes an image of the cloud on a photodiode Pd2. The signal from the photodiodes is amplified by a photo pre-amplifier and send to a low-noise preamplifier[33] and observed on a digital oscilloscope.[34]

6.6.1 Loading and loss

The dynamics of the MOT loading process is investigated in detail [102–105] since its foundation [35]. Along with the MOT filling process there is also a loss mechanism which is proportional to the number of atoms. When the number of atoms loaded in the MOT

[31] CA-MOT program written in LabView 6.1
[32] Hammamatsu Inc.
[33] Stanford Research System, model SR560, low noise voltage preamplifier
[34] LeCroy 9354C, 4-channel, 500MHz bandwidth

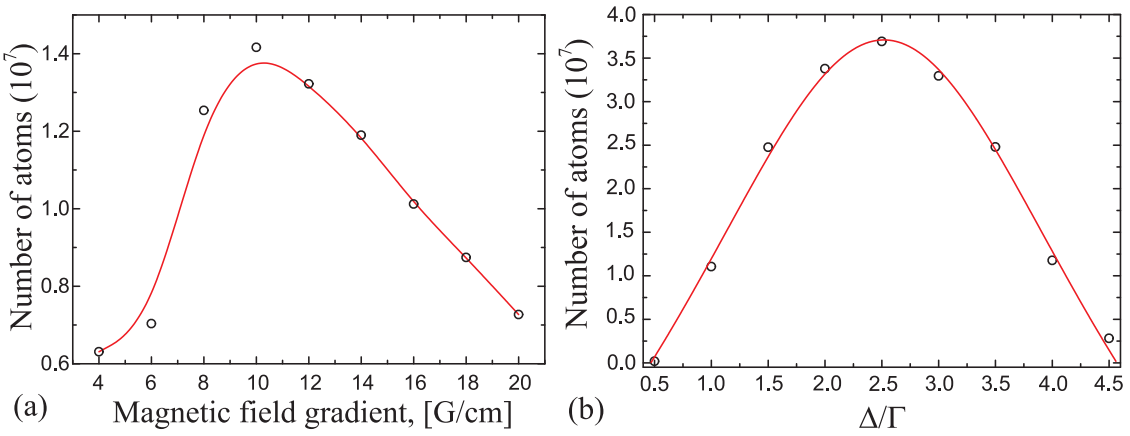

Figure 6.15: *Optimum magnetic field gradient (a) and trap laser detuning (b) for maximum number of atoms. The measurements are taken at* $\Delta = -3\Gamma$ *for (a) and at* $\mathrm{b} = 10\mathrm{G/cm}$. *The solid curves are spline fit (a) and a lorentzian fit (b).*

increases the loss also increases. After some time an equilibrium is reached and the number of atoms in the MOT does not increases any further. The number of atoms in the MOT $N(t)$ as a function of loading time obeys the solution of the following differential equation.

$$\frac{dN(t)}{dt} = R_0 - \gamma_{MOT} N(t), \tag{6.1}$$

where R_0 is the MOT loading rate, and $\gamma_{MOT} = 1/\tau$ is the atomic loss rate with τ being the characteristic loading time. The solution of that equation is:

$$N(t) = \frac{R_0}{\gamma_{MOT}}(1 - e^{-\gamma_{MOT} t}). \tag{6.2}$$

A typical loading trace of the first generation MOT is shown in Fig.6.14(a). The magnetic field gradient is 13.6G/cm. The characteristic loading time is $\tau = 18.6$ ms which gives a loss coefficient of $\gamma_{MOT} = 53.8$ Hz. The experimentally obtained value for the loading rate $R_0 = 17.2\ 10^9$atoms/s agrees well with the one obtained by fitting the initial slope of the loading curve with a straight line i.e. $15.6\ 10^9$atoms/s. The equilibrium number of atoms loaded in the MOT is estimated to be $N_{eq} = 3.2 \times 10^8$. This also is the maximum number of atoms for the setup constructed at the Aarhus University. At the same time the lifetime of the MOT after switching off the magnetic field and the cooling beams is of the order of 10-15ms [see Fig.6.18(b)].

The Cs container was heated up to 85°C. A further increase of the temperature would suggest an increase of the number of atoms, but since the pressure of the Cs vapor becomes higher the loss is also higher which eventually decreases the equilibrium number of atoms in the MOT. The fit in Fig.6.14(a) does not include the first 15 points due to the influence of the magnetic field transients. Thus the initial delay due to eddy-current induced magnetic fields is of the order of 10.7 ms.

The optimum loading parameters for maximizing the number of loaded atoms in the MOT are empirically found. Similar methods of experimental determination has been reported elsewhere [102,106,107]. First a measurement of the number of atoms at different magnetic field gradients fixes the value of the optimum gradient at 10G/cm, and then at

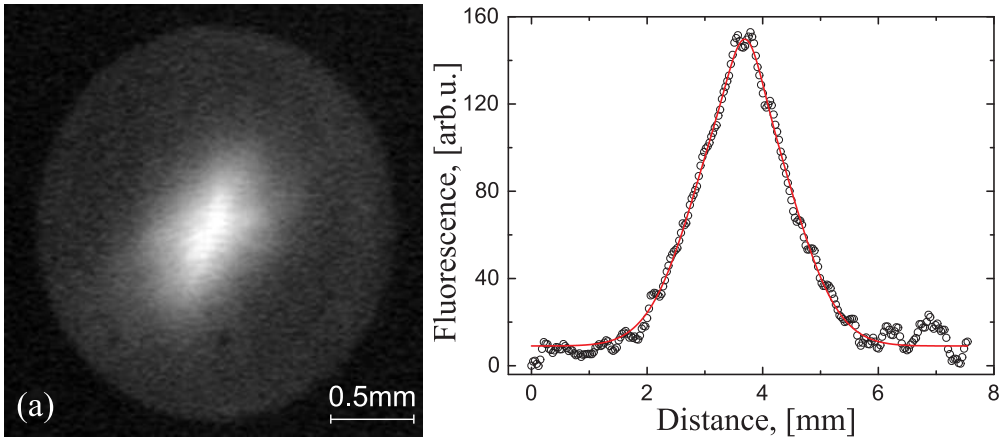

Figure 6.16: *A CCD image of the atomic cloud (a) at detuning* $\Delta = -3\Gamma$ *and gradient* $\mathrm{b} = 10\mathrm{G/cm}$. *A two-component gaussian (b) fit of the stronger confined trap axis for the image from the left.*

this value the number of atoms is measured again but this time as a function of the cooling laser detuning finding an optimum value of 2.5Γ. The results are plotted in Fig.6.15. In frequency units the above would mean that the Zeeman shift at 1 cm away from the trap center is around 14MHz, whereas the detuning is 13MHz.

6.6.2 Density and size

The density of the atomic sample is an important parameter for off-resonant interaction between atoms and light as we saw in the previous chapters.

The number density of atoms in the trap is determined by measuring the cloud diameter i.e. the cloud volume, and the number of atoms in it. The estimation of the density can also be done using the phase shift of the interferometer as it will be explained in Ch.9.

The collection of atoms in the MOT as we have already seen is competed by the loss mechanism and at steady sate there is equilibrium between loading and loss which maintains the number of atoms in the MOT constant with time. The behavior of the trap can be divided to three different regimes [106].

At very low number of trapped atoms i.e. less than 10^4 the cloud diameter depends on the temperature and so the density. This regime is called *temperature limited regime*. The multiple scattering in this regime is insignificant.

When the number of atoms increases further the reabsorption of scattered photons becomes important. The cloud enters in the *multiple scattering regime*. The density is almost independent on the number of atoms.

At still higher number of trapped atoms the central part of the trap, where the confinement is stronger, is filled and then the non-linearity of the spatial dependence of the trapping force becomes important. Further increase of the atom number leads to filling the peripheral regions, where the trapping force is weaker. Thus the cloud enters in the so-called *two component regime*.

The transition between the multiple scattering regime and the two-component regime is characterized with a two component profile of the atomic density distribution. We measure the fluorescence profile of our MOT by a digitized image taken with the Philips camera. We found that a superposition of two gaussian functions fits best the profile along

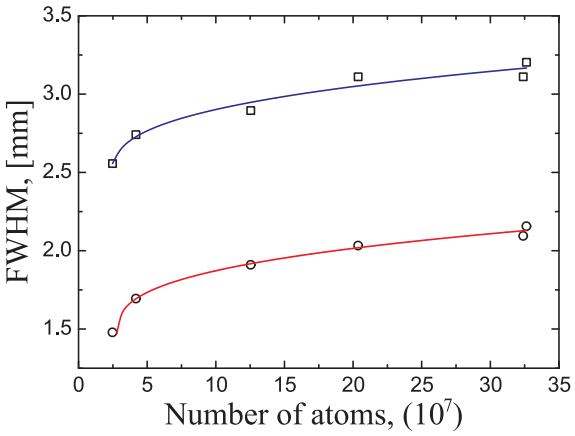

Figure 6.17: *Plot of the two radii of the atomic cloud as a function of the number of atoms. The red curve is a fit to the experimental data for the weaker confined direction and the blue to the stronger one.*

the stronger confined direction. The weaker direction is fitted better to a gaussian. The image and a two-component gaussian fit to it are shown in Fig.6.16.

The cloud has an ellipsoidal shape imparted by the rotational symmetry of the magnetic field due to the different gradients. The circle around the cloud is due to the iris of the camera. We see that there is an appreciable amount of scattered light and background fluorescence. The graph in (b) part of the figure represents a line profile across the direction of the stronger trap confinement. The tilt of the image is due to the 20° inclination of the chamber.

The cloud radii in the multiple scattering regime has been sown to be dictated by the limiting density of the atoms [106]. In both direction the radii are proportional to the $N_{at}^{1/3}$ as:

$$r_{MS} = \frac{1}{\sqrt{2\pi}} \left(\frac{N_{at}}{n_{MS}} \right)^{1/3} \tag{6.3}$$

where n_{MS} is the limiting density in the multiple scattering regime.

In Fig.6.17 we show an Eq(.6.3) fit of the cloud radii in both cloud directions vs the loaded atom number N_{at} for the AU MOT. The density calculated using a gaussian density distribution is $\mathcal{N} = 1.2 \times 10^9 \text{cm}^{-3}$. At the same time the limiting density of the multiple scattering regime in our conditions is estimated from the fit to the data in Fig.6.17 to be around $n_{MS} = 10^{10} \text{cm}^{-3}$. The number of atoms in the MOT is changed by increasing the concentration of Cs vapor in the chamber via increasing the temperature of the Cs container. This also results in increasing the background fluorescence level which can be seen in the image of the trapped cloud. The last point is an indication that the number of atoms collected in the MOT does not rise any further when changing the number of atoms in the reservoir.

We can summarize that our MOT, with number of atoms around 3×10^8, behaves as if it is at the transition between the multiple scattering regime and the two component regime.

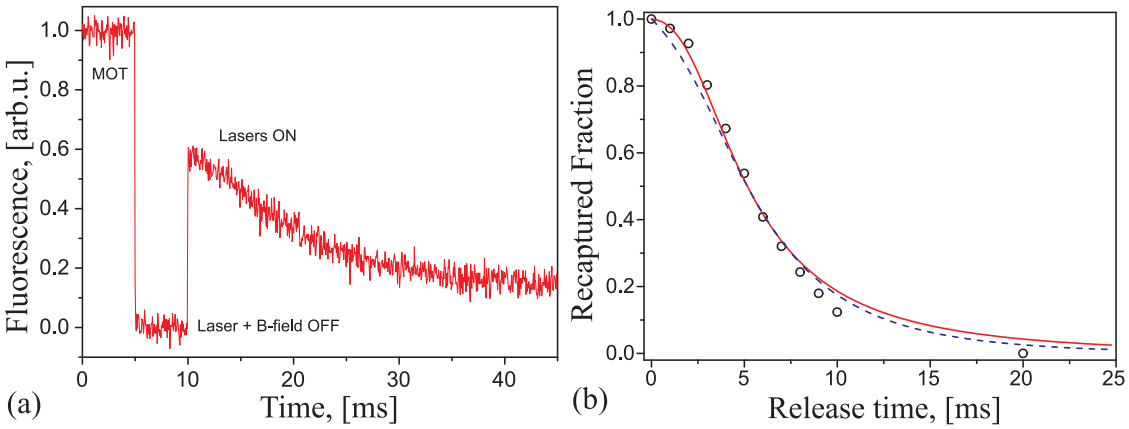

Figure 6.18: *Results from the release R&R measurement: A raw data trace of 5 ms release (a). Recaptured fraction (∘) as a function of release time and a fit (solid line) to it using the result from the theoretical model of cloud ballistic expansion (b). The dashed curve is corrected for background gas collisions.*

6.6.3 Temperature

The laser cooled atomic sample is characterized by a root mean square velocity of the particles which is connected to the temperature. The temperature can be measured in several methods. An extensive analysis of the temperature measurement techniques is done elsewhere [34,38,107–109]. In general, the atoms are released from the trap and then probed during free ballistic expansion.

In the time-of-flight (TOF) technique the atoms fall under gravity and cross a retro-reflected elliptical probe beam at a certain distance below the trap. The fluorescence when interacting with probe beam is detected and plotted as a function of the time which takes for an atom to fall from the molasses region to the probe region.

When the release-recapture method (R&R) method is used the atoms are released for a variable time and then recaptured in the molasses beams. The fluorescence from the recaptured atoms is plotted as a function of the release time. This method is sensitive to all velocity components whereas the TOF only measures the vertical (the gravity influenced) one.

In the AU MOT the temperature of the atoms was measured using the release-recapture method. We tried TOF, but did not succeed. The non-magnetic viewports V1 and V2 30cm below the trap region (see Fig.6.9) were placed with the intention to be used in a TOF measurement, but since the background gas pressure was too high the atoms eventually heat up and collide with the wall of the thin Ti pipe connecting the chamber with the detection region. A simple estimation shows that the time of flight before intersecting the probe region is around 0.25s, which is much longer than the timescale of the background collision losses (10-15ms). Besides, to make the cloud pass through the narrow tube the drift velocity of the atomic sample should be as low as 2.4cm/s, which means that the atom temperature has to be as low as 3.2μK.

The release-recapture method seemed to be experimentally feasible in the "violent" environment in the MOT chamber. In the measurement about 10^6 atoms are collected in the MOT at a detuning of $\Delta = -3\Gamma$ and then released for a variable time (Fig.6.18(a)). At the end of the dark period the light is switched on again and the remaining atoms are

recaptured by the molasses beams. The light is shined for another 500ms until the cloud is completely gone in order to record the background fluorescence level.

The recaptured fraction is calculated as the ratio of the fluorescence signal from the recaptured atoms to the signal from the MOT. The result is plotted against the release time in Fig.6.18(b). After turning the laser back the signal is little delayed of 0.1ms as a result of the low pass filtering to 30kHz. But this does not pose any problems since the subsequent molasses decay is of the order of 10ms. To deduce the temperature the data is fitted to a convenient expression of the ballistic expansion of the atomic cloud shown in Appendix D.

The image of the cloud is magnified 2.2 times and projected onto 5.8×5.8mm photodiode, thus reducing the viewing area to 2.6×2.6mm. Along the line of sight of the detector the integration is performed over the whole trap region.

Under UHV conditions the influence of the background gas collisions over the lifetime of the MOT and respectively the R&R measurement signal is negligible. However, the loss rate due to background gas collisions is quite high $\gamma_{MOT} \sim 50Hz$ corresponding to a characteristic time of 20ms. Thus the contribution of the background collisions to the expansion of the atomic cloud can not be neglected. It could be modeled as an additional exponential decay of the signal of the form $e^{-\gamma_{MOT}t}$.

Finally, the data is fitted to the Eq.(D.6) and plotted in Fig.6.18(b) with a solid line. The estimated temperature is $772 \pm 30\mu K$. When accounting for the background gas collisions we get a value of $417 \pm 49\mu K$ (dashed line). The last result agrees well with the Doppler temperature limit for Cs atoms cooled with light detuned by $\Delta = -3\Gamma$.

Chapter 7

Dipole Trap

The chapter describes the loading of the far-off-resonant optical trap for cesium atoms. We start with the loading scheme of the optical dipole trap. The second and third sections describe the experimental setup of dipole beam coupling optics and some results on imaging of the dipole trap with the triggerable CCD camera described in the previous chapter. Here we must also point out that the loading of the dipole trap is done by using the second generation MOT at the Niels Bohr Institute.

7.1 Loading scheme

The far off resonant optical traps as mentioned earlier are low-scattering rate conservative potentials which are created by focused light beams. The low scattering rate is desired in experiment where the absorption of light is unwanted i.e. in a non-destructive manipulation of atomic samples.

The application of optical trapping in our interferometric measurement is dictated by the possibility to improve the signal-to-noise ratio of the off-resonant interaction. As seen from Eq.(5.10) the interaction strength κ^2 is proportional to the resonant optical density $\alpha_0 = \lambda^2 l\mathcal{N}/2\pi$, which on the other hand is proportional to the atomic density. At the same time the phase shift is linear in the atomic density as shown in Eq.(2.47). Then increasing the density of the atomic sample should allow us to increase the probe light detuning, thus improving the non-destructive character of the interaction or even approaching the regime of QND measurement.

Since the capture rate of a dipole trap is rather low for room temperature atoms then the atoms must be pre-cooled in a MOT and optical molasses. The methods of sub-doppler cooling were discussed in Ch.3, and here we will only describe the current experimental scheme used to load the dipole trap from a MOT.

In our experiment the loading is done in two ways. First, we don't switch the magnetic field during loading. The atomic cloud does not expand during the loading. The second regime is when the magnetic field is adiabatically switched off.

The dipole trap loading scheme is shown in Fig.7.1. Firstly, about $10^8 - 10^9$ atoms are collected in the MOT for 3 sec. Then the cooler detuning is reduced as well as the hyperfine repump intensity in 3 stages with different durations. The overall decrease of the hyperfine repump intensity is about 80 times, and the cooler detuning is increased to -8γ from the typical value of -3γ. At the same time the magnetic field is increased from 10 to 12 G/cm. The initial intention was to compress the MOT, but we found

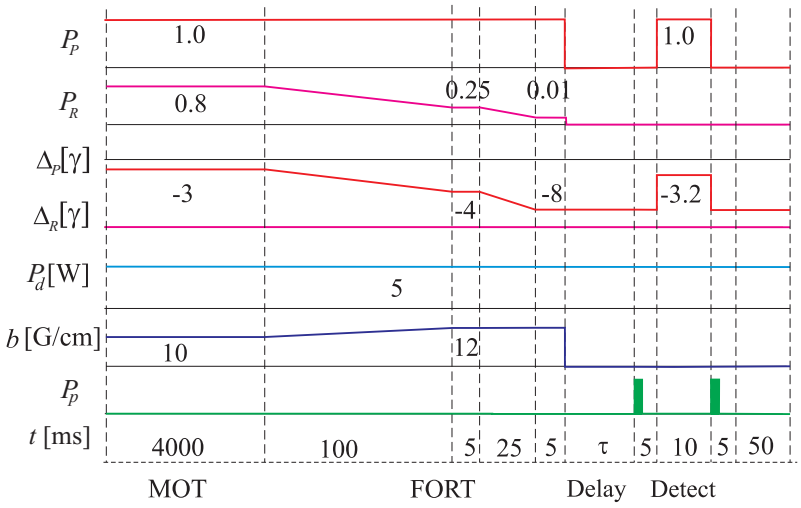

Figure 7.1: Loading sequence of the dipole trap

out that for higher than 12 G/cm settings in the CA-MOT program the driver does not deliver more current and the magnetic field gradient saturates around the above mentioned values. The sub-Doppler cooling stages are followed by a "dark" stage with a duration of 1ms to 1s, to allow for the non-trapped atoms to leave the trapping region or to measure different parameters of the dipole trap. After the dark period a detection stage comes which incorporates either probe laser pulses or molasses beams for detection of atoms in the dipole trap. When a detection is done with the MOT beams an additional triggering pulse is sent to start the exposure of CCD camera.

7.2 Experimental setup

The dipole trap is created by a single focused Gaussian beam. The waist position of the dipole beam coincides approximately with the waist of the interferometer probe beam and the position where the MOT is located as shown in Fig.6.10 from the previous chapter. The optical setup of the dipole trap is shown in Fig.7.2.

The light is provided by an Yb:YAG laser[1], which can emit up to 40W of continuous wave (CW) radiation at 1030nm. The laser is equipped with a Fabry-Perot etalon, which reduces the linewidth of the output light to 5 MHz. The laser spatial mode is approximately gaussian with a beam quality factor of $M^2 = 1.3$. Initially the light is collimated by a single plane-convex lens (L1) with a focal distance of 500mm. Then an s-polarized wave is selected via a PBS and half-wave plate and sent to a mode-matching telescope with a magnification of 0.75 (L2-L3). The first order of the light diffracted by an AOM[2] with a frequency shift of 80MHz is selected and sent to the interferometer table. The AOM driving frequency is provided by an microwave synthesizer which can be gated by an external pulse. The power of the RF wave is 1dBm and the overall diffraction efficiency is around 80%. Further, the beam is reflected off a dichroic mirror (DM) and focused by a 100 mm focal distance double cemented achromatic lens (L4), which also focuses the probe beam. The waist is found to be around $40\mu m$. After being again collimated by the

[1]ELS Versa-Disk Yb:YAG laser
[2]IntraAction Corp. ATM-80A6 AO modulator

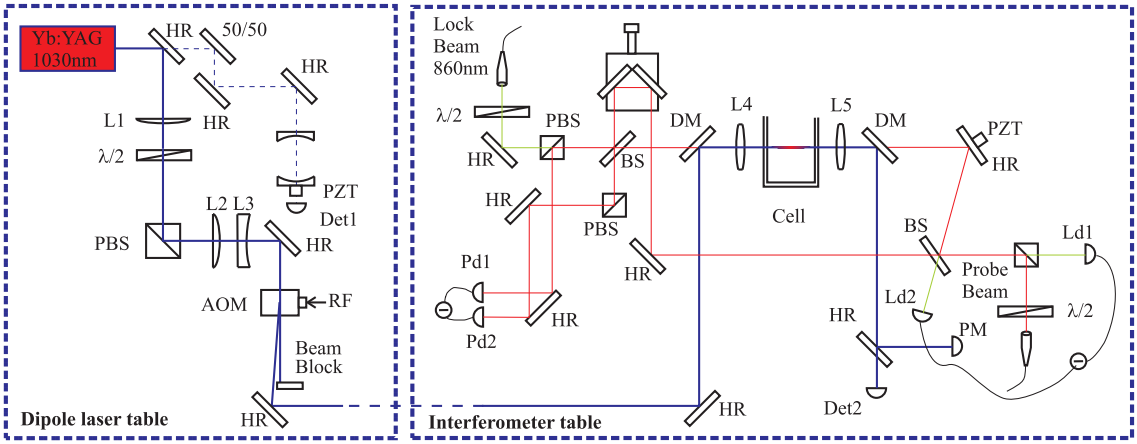

Figure 7.2: *Optical setup of the dipole laser and interferometer.*

second achromatic lens (L5) the beam is reflected off a dichroic mirror and send to a beam dump or to a high-power powermeter.

The alignment of the dipole trap beam with respect to the MOT cloud is done in the following way. First, the power in the interferometer probe arm is increased and the position of the probe beam waist is aligned with respect to the MOT. Second, the visibility of the interference of the probe and locking beams from the probe and reference arm of the interferometer are maximized. If the alignment and mode matching of the two arms is good, it should be possible to couple a reasonable amount of locking laser light back into the probe laser fiber by using a half-wave plate after the first BS before the coupling PBS [see Fig.7.2]. Since the locking beam propagates in the same direction as the dipole trap beam the last is steered out with two high reflection mirrors and overlapped with the locking beam coarsely. Once this is done the power in the dipole beam is increased and by an additional waveplate after the first interferometer BS the weak leakage beam is coupled back into the probe beam fiber. In that way a coupling efficiency of the order of $15-20\%$ can be obtained which ensures the good spatial overlap with the MOT cloud. Further alignment of the dipole trap waist with respect to the MOT is done once the dipole trap is loaded. The fine alignment is done by observing the real time fluorescence image of the dipole trap captured by the CCD camera.

7.3 Imaging of the dipole trap

The optically trapped atomic cloud is observed using the imaging system described in Sec.6.4. The images can be taken at different storage time in the dipole trap using different exposure times from 1 to 10ms. During the exposure of the camera the cloud is illuminated by the MOT cooling and repump beams, thus the influence of the light onto cloud dimensions has to be taken into account. The detuning of the MOT beams during the detection region is set to -3.2γ. A sample image of the dipole trap is shown in Fig.7.3.

The image is taken with an exposure duration of 10 ms and after 50 ms storage time in the trap. It is averaged over 100 frames from 100 loadings of the trap. The background is subtracted using a reference image again averaged over 100 frames. We find the axial and radial profile of the trapped atomic cloud by averaging over the 648 columns of the image pixel array for the axial, and the 243 rows for the radial profile, respectively. The

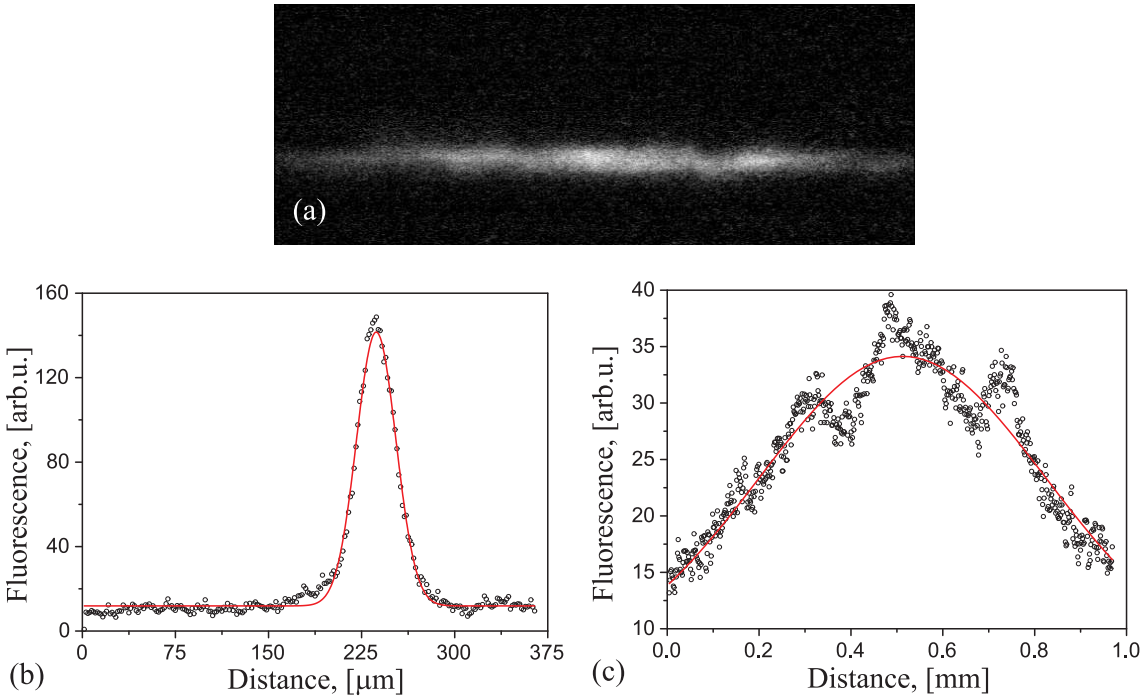

Figure 7.3: *Image of the dipole trap (a) with radial profile (b) and axial profile (c).*

characteristic radii found are $w_r = 31(1)$ μm for the radial direction perpendicular to the direction of propagation and $w_{ax} = 626(29)$ μm for the axial one along the propagation of the dipole beam. A single camera output contains an image with the even or odd lines only. Since we acquire only one output of the camera, the digitized by the framegrabber image contains twice as less horizontal lines. Then the radial cloud dimension in Fig.7.3(a,b) has to be multiplied by a factor of 2. Then the measured characteristic radius in the direction perpendicular to the propagation axis is $w_r = 62$ μm.

The atomic cloud radial size in the dipole trap at conditions of thermal equilibrium is given by the balance between the mean kinetic energy and the potential energy of a single atom [59]. Hence for the w_r we have:

$$w_r = \frac{1}{\omega_r}\sqrt{\frac{k_b T}{M}} \tag{7.1}$$

In Ch.9 we measure the radial oscillation frequency of the trap to be $\omega_r = 2\pi \times 225$ Hz at a power of 3.5 W. The atom temperature, we will see later, is measured to be around 14 μK. Then the radial size of the cloud is calculated, using Eq.(7.1), to be $w_{eq} = 20.8$ μm. The result is three times lower than the one obtained from the fit of the image in Fig.7.3(a,b). We attribute this discrepancy to the excitation of the atoms in the trap due to the light used to image the cloud. In previous section we mentioned that the MOT cooling and repump light is shined with a maximum power so that the on-resonance Rabi frequency per beam is $\Omega = 1.6\gamma$ and saturation parameter s_0 of roughly 5. At a detuning of $\Delta = -3.2\gamma$ the overall scattering rate given by the equation [110]:

$$R_{sc} = \frac{\gamma}{2}\frac{s_0}{1 + s_0 + 4\left(\frac{\Delta}{\gamma}\right)^2}, \tag{7.2}$$

will account to 277 kHz. For the time the exposure lasts (τ_{exp} = 10ms) the atom will scatter on average $N_{sc} = \tau_{exp} R_{sc} = 2.77 \times 10^3$ photons. The energy transferred to a Cs atom for one recoil is calculated using Eq.(3.10). The kinetic energy of an atom will increase with an amount $E_{rec} = \hbar\omega_{rec} = \hbar \times 26$ kHz for each spontaneous emission event. In the last expression ω_{rec} is the recoil frequency. It is obvious, that for 10 ms exposure there will be appreciable heating.

If we assume that the trap is harmonic and the atoms do not interact with each other, we can express the energy of a particle inside the dipole potential in terms of harmonic oscillator states. These states, as we know, are equidistant with a separation of $\hbar\omega_r$. The number of recoils on average needed for an atom to increase its energy such that it can be excited to the next oscillator state is $\frac{\omega_r}{\omega_{rec}} = 18$. Then N_{sc} photons for 10 ms will cause the atom to increase its potential energy to a state with a number $n_r \approx 5 \times 10^4$. The spread of the harmonic oscillator wavefunction for that state is given by the relation:

$$\sigma_{n_r} = \sigma_0 \sqrt{2n_r + 1},\ \sigma_0 = \sqrt{\frac{\hbar}{2M\omega_r}}, \tag{7.3}$$

where σ_0 is the ground state wavefunction width [66](p.505). Then using Eq.(7.3) and the above considerations we find that the spread of the n_r-th excited state is around 126 μm. This result is with a factor of two bigger than the experimentally observed one. Since the imaging is done with all the cooling and repump light in the six beams, it is possible to have molasses cooling which can counteract the expansion due to heating. This would eventually lead to an equilibrium size of the atomic sample which we assume to satisfy the condition 20.8 μm $< w_r <$ 126.8 μm.

Nevertheless, at that high excitation the kinetic energy of the hottest atoms is higher than the trap depth and they are simply ejected from it. We must also note here that we did not include collisions of any kind. As we will see in the next section and in Ch.9, collisions play important role in trap dynamics.

7.4 Loading dynamics

A comprehensive analysis of loading dynamics of FORT is done by Kuppens et al [61]. In this section we discuss the loading dynamics of an optical dipole trap and give some experimental data on atom loss from a dipole trap without presence of MOT light. The data is taken in a fluorescence measurement, which means that the cloud is not sustained after the measurement. A more detailed experimental data will be presented in a later chapter concerning the nondestructive interferometric detection.

The losses from the trap can be caused by heating mechanisms or collisional processes. As heating mechanisms are identified the spontaneous scattering of FORT light photons, background gas collisions [111, 112], intensity fluctuation and the pointing stability of the FORT beam [113]. For large atom numbers the losses are dominated by cold collisional processes [114], including photoassociation, ground state hyperfine changing collisions and radiative escape. Photoassociation collisions can be induced by the FORT light and lead to production of a untrapped molecules. During the ground state hyperfine changing collisions the atoms gain as much kinetic energy as the ground state hyperfine splitting (0.44 K for Cs), which is enough to eject them from the trap. In the radiative escape the characteristic time of a collision between two atoms is longer then the spontaneous decay, which results in a spontaneous emission of a photon during collision. As a result

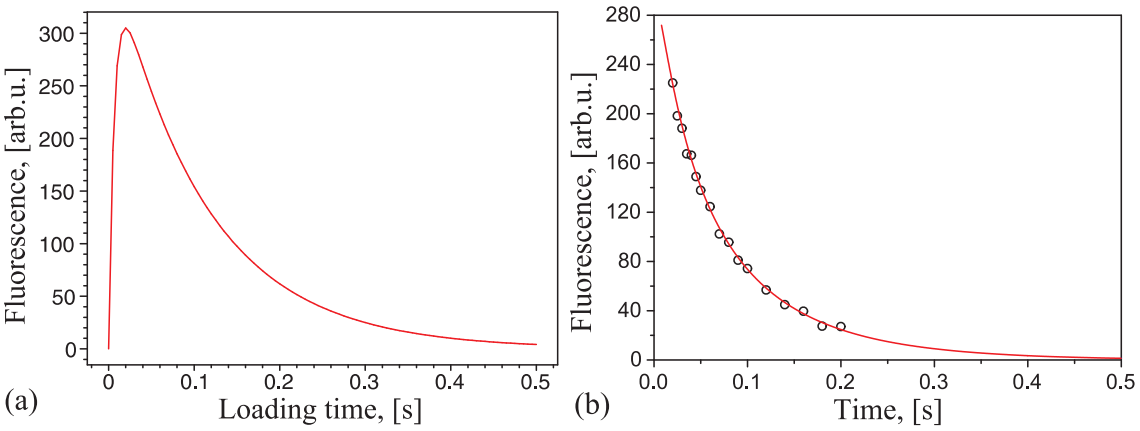

Figure 7.4: *Theoretical loading curve (a) and experimental loss curve of FORT without any MOT light present (b): experimental data* (∘) *and fit (solid curve) to the solution of Eq.(7.5) with parameters* $\Gamma = 9(1)\text{Hz}$, $\beta = 1.3(3) \times 10^{-3}$ Hz.

the energy of the photon is transferred to the colliding atoms, which will obviously eject the atoms from the trap.

In general the dynamics of the loading process is described by the following equation:

$$\frac{dN}{dt} = R_0 \exp\left(-\gamma_{MOT} t\right) - \Gamma_L N - \beta_L N^2, \tag{7.4}$$

where γ_{MOT} is the rate at which the MOT loses atoms, R_0 is the loading rate of the dipole trap, Γ_L is the light assisted loss rate of FORT, β_L is the density dependent light assisted loss rate of dipole trap. We see that the loss processes in Eq.(7.4) can be separated to exponential $-\Gamma_L N$ and collisional $-\beta_L N^2$. The L indexing of the loss parameters denotes their value in presence of light. In general they are different from the losses "in the dark" [115], i.e. where all the light is switched off except the dipole trap light.

It is essential for the investigation of the loss rates to separate the loading process from the loss process. Since we need to apply sub-Doppler cooling to lower the MOT temperature the light will always introduce losses during loading. To separate the loading from the loss one can perform the following measurement. First atoms are loaded in the FORT and after a variable delay the cloud is exposed to a short "flash" of light with the MOT beams [61]. After that the remaining atom number is measured. This way we can omit the first term in Eq.(7.4) and simplify its solution to estimating only the loss parameters. Then the trap atom number obeys the solution of the following differential equation:

$$\frac{dN}{dt} = -\Gamma N - \beta N^2. \tag{7.5}$$

The Eq.(7.5) can be used to study both light-assisted losses and dark losses.

The above described measurement for the case of light-assisted losses is performed non-destructively using interferometric detection and the results of the detection will be presented in Ch.9. For now we restrict ourselves only to fluorescence detection the dark losses of dipole trapped atoms. The result of that measurement is shown in Fig.7.4.

In the fluorescence measurement, after a variable delay period, we shine the MOT

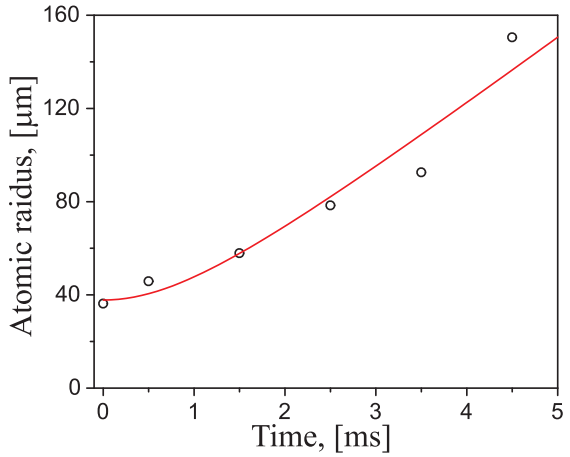

Figure 7.5: *Expansion of the atomic cloud after atoms are released from the trap. Gravity not included.*

light and at the same time start the exposure of the CCD. The exposure lasts for 10 ms and the resulting average fluorescence is detected. The fluorescence signal collected from the atoms is plotted as a function of the delay time. Although, this measurement is not exactly what we aimed for, we can use at as a qualitative example of the lifetime of the FORT. To extract the correct information from the fit one must include the heating effect due to MOT light. The values of Γ and β are listed in the figure caption. More elaborate discussion on them will be done in Ch.9. Here we only state that the values of Γ are mainly determined by the background gas pressure as in the MOT [116], regardless of the presence of light and the values of β are connected with the cross-section for two-body collision and depend on atomic density.

7.5 Temperature

In this section we present results on cloud expansion when atoms are released from the dipole trap. This time the exposure of the camera is set to 0.5ms in order to be able to track a reasonable amount of frames before the density of the cloud drops significantly. The results are shown in Fig.7.5. A fit to Eg.(D.4) gives a temperature value of $T = 14(2)$ μK for an initial atomic radius of $\sigma_0 = 38(8)$ μm. The fit does not take into account the gravity effect on the falling atoms and thus would give lower temperature. However, in our case as we will also see in Ch.9 the contribution of the gravity for the typical measurement times is negligible.

Chapter 8

Mach-Zehnder Interferometer

The chapter describes the main experimental tool for characterizing the atomic sample in this work - the Mach-Zehnder interferometer. Two interferometer setups have been used in the two generation experiments: fibre-optic at Århus University and free-space construction at the Niels Bohr Institute.

The chapter starts with presentation of the optical setup in Sec.8.1. We discuss the generation of the probe light using the diode laser and shortly describe the technique of the frequency lock used to tune the frequency of the probe. Next we continue with the locking laser. In Sec.8.1.3 and Sec.8.1.4 we present the design of the fiber-optic and the free-space interferometers. Further we continue with description of the detection system and the data analysis. We end the section of the interferometer optical setup with presenting the white light alignment. In Sec.8.3 we present the measurements done to characterize the interferometer noise in both amplitude and phase.

8.1 Optical Setup

In this section we describe the part of the optical setup which is responsible for interferometric detection of the phase shift imposed on the light by a dispersive interaction with cold atomic sample. A separate subsection will be dedicated to each of the the three main components of the optical setup i.e. the interferometer, the probe and the locking laser.

8.1.1 Probe laser

The probe laser used in the experiment is a grating stabilized external cavity diode laser. The construction of it has already been discussed in the Sec.6.1. Here we will describe in more detail the tunable frequency offset locking technique used in the experiment performed with the fiber-optic interferometer. according to that scheme two lasers with different frequencies are overlapped on a 50/50 beamsplitter to produce a beat-note at a frequency equal the frequency separation between them [89, 117]. One of the lasers which we refer to as *reference* laser is locked to a Cs atomic resonance in a saturation absorption spectroscopy setup.

Let's assume that two light beams $E_p(t) = \sqrt{2}\mathcal{E}_p \cos(\omega_p t + \phi_p)$ and $E_r(t) = \sqrt{2}\mathcal{E}_r \cos(\omega_r t + \phi_r)$ are overlapped on a beamsplitter. The electric field amplitudes are denoted by $\mathcal{E}_{p,r}$ for the probe and reference lasers with frequency of ω_p, ω_r, and phase ϕ_p ϕ_r, respectively. The resulting interference signal will have the following form:

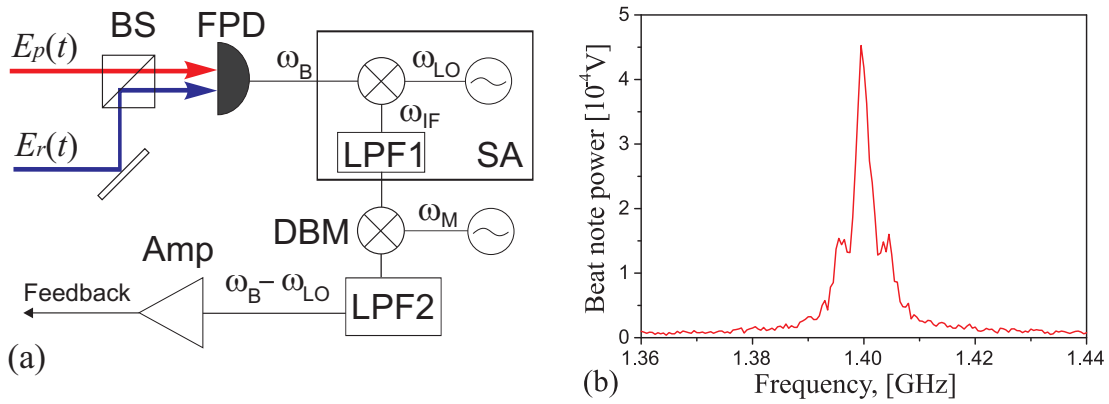

Figure 8.1: *Experimental setup employed to lock the probe beam (a). The elements included in the sketch are: BS - 50/50 beam splitter; FPD - fast photodetector; SA - spectrum analyser; DBM - double balanced mixer; LPF - low pass filter; Amp - amplifier. Frequency diagram of beat-note (b).*

$$|E(t)|^2 = |E_p(t)|^2 + |E_r(t)|^2 + 2\mathcal{E}_p\mathcal{E}_r\{\cos[(\omega_p - \omega_r)t + (\phi_p - \phi_r)] + \\ + \cos[(\omega_p + \omega_r)t + (\phi_p + \phi_r)]\} \tag{8.1}$$

The signal spectrum has a low frequency component at the frequency of the difference between the laser frequencies of the two lasers also called a beat-note and an optical frequency equal to the sum of the two frequencies. The last is not detected by our RF detector[1] with a bandwidth of 15 GHz.

The photodiode signal at RF frequency of ω_B is further mixed with the local oscillator ω_{LO} of the SA analyzer in a zero-span mode as shown in Fig.8.1(a). In zero span mode the frequency of the internal spectrum analyzer local oscillator (LO) is fixed and the fluctuations of the RF power at the ω_{LO} is monitored. A frequency diagram of the beatnote is shown in Fig.8.1(b). The resulting sideband peaks are due to the 4 MHz modulation of the laser diode current resulting in direct modulation of the diode laser phase, in case of low modulation depth. Next, the low frequency component of the intermediate frequency output ω_{IF} of the mixer is selected via low-pass filtering by LPF1. The resulting signal is further mixed on a DBM with the signal used to modulate the laser current for locking purposes at a frequency of $\omega_M = 1$MHz and a modulation depth of 1% or less. After a second low-pass filtering with FPL2 we obtain an error signal at a frequency of $\omega_B - \omega_{LO}$. At the end the signal is amplified and send to a PI circuit to produce a correction for the piezo voltage.

In the following few lines we give the derivation of the error signal following the mixing and filtering performed after the detection as shown in Fig.8.1(a). The light detected by the FPD [see Eq.(8.1)] produces a photocurrent $i_B(t) = i_B \cos(\omega_B t + \phi_B)$, where $\phi_B = \phi_p - \phi_r$. After a phase modulation by modulation of the laser current with a sine wave at a frequency ω_M, we get sidebands as shown in Fig.8.1(b) at the modulation frequency. Mixing further with the local oscillator $i_{LO}(t) = i_{LO} \cos(\omega_{LO} t + \phi_{LO})$ of the

[1] Newport, model 1480-S, GaAs photodetector

spectrum analyzer and low-pass filtering we get for small modulation depths M:

$$i_{IF} = \frac{i_B i_{LO}}{2}\{\cos[(\omega_B - \omega_{LO})t + \phi] - M\cos(\omega_M t)\sin[(\omega_B - \omega_{LO})t + \phi]\} \tag{8.2}$$

where $\phi = \phi_B - \phi_{LO}$. At the DBM the signal is mixed with the modulation signal of the laser current at $i_M(t) = i_M \cos\omega_M t$ and further low pass filtered. The resulting error signal is expressed as:

$$i_{err} = \frac{M i_B i_{LO} i_M}{4}\sin[(\omega_B - \omega_{LO})t + \phi]. \tag{8.3}$$

In the last equation the terms fluctuating with ω_M are filtered by the second LPF2 and only the small difference frequency $\omega_B - \omega_{LO}$ is transmitted. In the locking position the error signal is zero for negligible phase drifts between the local oscillator and the beat note signals. Hence, by changing the frequency of the internal local oscillator of the spectrum analyzer we can tune the relative frequency separation of the two lasers in a very large range given by the range of frequencies of the SA. In this case that range varies from 100 kHz to 23 GHz.[2]. With the above described locking technique and the reference laser locked to the atomic transition $6S_{1/2}(F = 4) \rightarrow 6P_{3/2}(F' = 5)$ by FM saturation spectroscopy, we are able to lock the probe laser by specific detuning Δ variable from a few MHz to a few GHz from the hyperfine transition $6S_{1/2}(F = 4) \rightarrow 6P_{3/2}(F' = 5)$.

The interferometric measurements in this work are performed using a pulsed laser light coupled into a polarization maintaining single mode optical fiber. An AOM is used to produce light pulses of controllable duration. The drive frequency of the modulator can be slightly tuned in a range of 20 MHz.[3] around the center frequency of 80 MHz. This method is used to tune the probe laser frequency in the NBI experiment. Certainly, that kind of tuning leads to a different coupling conditions and diffraction efficiency. To maintain the same power level after changing the frequency in this way, we either change the power of the incoming beam or optimize the fiber coupling efficiency.

In the atomic noise experiments and in the experiments on dipole trap characterization the used probe detuning is fixed to a value of 15, 25 and 100 MHz, thus removing the necessity for a tunable detuning. However for the sake of a QND measurement on the clock transition using only one probe a large value of the detuning is required i.e around 4.5 GHz [see Fig.2.3(a)]. Then a frequency offset locking technique becomes very useful. In the experiment at Aarhus the scheme was also used in a phase shift measurement with atoms on a different excited state hyperfine levels.

8.1.2 Locking Laser

The monitoring of the optical phase in an interferometer is sensitive to acoustic and thermal noise. In the fiber-optic interferometer the change of fiber temperature changes the index of refraction of the silica material thus giving rise to a fluctuations in the optical power transmitted. In the free-space interferometer any mechanical or acoustic vibration leads to fluctuation in the optical path-length difference. To overcome these unwanted effects the interferometer is locked using an additional laser i.e. locking laser. The laser is off-resonant with the atomic transition (the Cs D lines with all hyperfine components). The idea is to use the interference signal of the locking laser as an error signal to lock the

[2] Anritsu, spectrum analyzer, mod. MS2665C
[3] Brimrose Corp. TeO_2 frequency shifter

path length difference of the interferometer. Since the two wavelengths are different the interference fringes from the two lasers would have different width. Then to lock the probe signal at zero crossing, where the sensitivity to phase changes is highest, the locking signal is electronically shifted by adding an offset to the detector photocurrent. The wavelength of the locking laser was 840 nm and 866 nm for the experiments in Aarhus and NBI, respectively.

8.1.3 Fibre-optic interferometer

The interferometer as shown on Fig. 8.2 is a Mach-Zehnder type made of single mode optical fibers with an angle polished connectors to prevent for an etalon effects and optical feedback into the probe and locking laser. The motivation for using fibers instead of free space propagating beams is the enhanced mechanical stability as well as excellent mode overlap of the interfering beams in single mode fibers.

The two laser beams probe and locking are combined on a 50/50 BS and coupled in the input fiber of the interferometer. After splitting by the first fiber-optic beamsplitter C1 the light is directed to the two arms. Each arm along with the input coupling channel is equipped with a polarization controller PC# made up by coiling the fiber to three loops, two $\lambda/4$ and one $\lambda/2$ with a diameter of 25 mm. Part of the fiber in the probe arm is coiled on a PZT element which diameter is changed under applied voltage. This result in stretching the fiber and increasing its length. This way we can adjust the pathlength difference between the interferometer arms. The probe arm is surrounding the Ti chamber where the MOT is formed, having about 20cm free space propagation. The probe light is focused to a waist of 20 μm at the center of the vacuum chamber by a 100 mm achromatic doublet lens[4] L1. Another lens L2 of the same focal distance is used to re-collimate the beam after the chamber. The lenses are mounted in a vertical drive mounts,[5] which give a possibility for fine adjustment of the fiber-air-fiber coupling. The fiber connector in the probe arm is mounted on a z-translation stage[6] to finely adjust the air gap length for the alignment of the white-light operation. The coupling efficiency of the interface fiber-free-space-fiber is preliminary checked to be around 85% before placement at the final experimental position i.e. around the vacuum chamber and without the focusing optics. Unfortunately, due to abberations of the lenses and non-perfect mode overlap after the second focusing lens, the coupling efficiency from fiber to fiber dropped to 35% with chamber in place. The chamber and also the interferometer plate are inclined at 20° with respect to the horizontal plate thus giving a somewhat inconvenient work position. The reference arm contains only the PC2 polarization controller to adjust the reference arm polarization parallel to the polarization of the probe arm. The light from the two arms is again combined on the fiber optic beamsplitter C2 and the two channels are detected using a pair of detectors for the probe and for the locking beams. Since the probe and locking beam propagate in the same direction they are separated using dichroic filters with a peak transmission of 50% at 850 nm and a FWHM of 15nm. Thus the probe laser beams of each arm are transmitted with around 50% loss and the locking beams are reflected. The photocurrents of the two pairs of detectors for probe and locking beams are subtracted for balanced detection.

The chromatic dispersion of the fibers is found to be very sensitive to slow variations

[4]Thorlabs, NIR achromat, mod. AC254-100-B
[5]Thorlabs, mod. VM1/M
[6]Thorlabs, mod. SM1Z

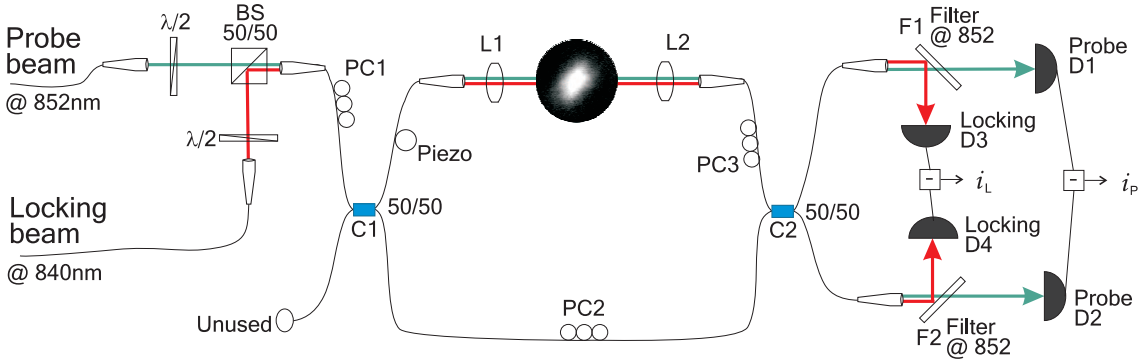

Figure 8.2: *Sketch of the setup of the interferometer with following elements:* BS − 50/50 *beam-splitter;* C1&C2 − 50/50 *fiber couplers;* PC1, PC2&PC3 - *fiber polarization controllers;* L1&L2 - *achromatic lenses;* F1&F2 - *interference filters transmitting @* 852 *nm;* D1&D2 - *Hamamatsu low noise, high gain photodiodes;* D3&D4 - *photodetectors; and several half wave plates* $\lambda/2$ *and collimating lenses for fiber coupling.* i_L *is the locking signal, whereas* $i_- = i_1 - i_2$ *is the probe signal.*

of the temperature, which on the other hand leads to different index of refraction for the the locking and probe beams, thus giving rise to a drift in the lock offset. After all, it was possible to get a stable lock operation on a timescale of about 1s. Further adjustment of the locking position for balanced detection of the probe beam is done by electronically adding a small offset to the subtracted locking detector photocurrent.

After the alignment and taking into account the losses of 30% in the probe arm the obtained visibility of the interference pattern is measured to be $\mathcal{V} = 85\%$.

The final conclusion is that the setup employing single mode fibers is superior in mechanical and acoustic stability, but is lacking of good transmission in the probe arm and is sensitive to polarization drifts and chromatic dispersion of the optical fibers.

8.1.4 Free-space interferometer

After relocation of the experiment at the Niels Bohr Institute the fiber optic interferometer was replaced by a free-space one. This decision was made in favor of minimizing the light losses in the probe arm and eliminating the problem connected with polarization drifts and chromatic dispersion. The only drawback of that design is the susceptibility to acoustic and mechanical vibrations. For that reason the whole construction is closed in an aluminum cage with a sound damping material glued to the plates of the cage.

The interferometer is sketched in Fig. 8.3. It is in a Mach-Zehnder configuration with free space propagating beams. The linearly polarized probe beam hits the interferometer input coupler and is split 50/50 into a reference and a probe arm. The overall power of the probe laser sent through the interferometer is measured using the powermeter PM1 by reflection of a beamsplitter with splitting ratio of $T/R = 40/60$. An additional auxiliary detector (AuxD) is placed after the PBS in order to maximize the power at the interferometer input. The probe arm contains a HR mirror mounted on piezo-electric to adjust finely the pathlength difference. In addition to that the pathlength difference between the two arms is adjusted by an optical delay line made out of two high-reflection mirrors mounted on a micrometer translation stage inserted in the reference arm. As in

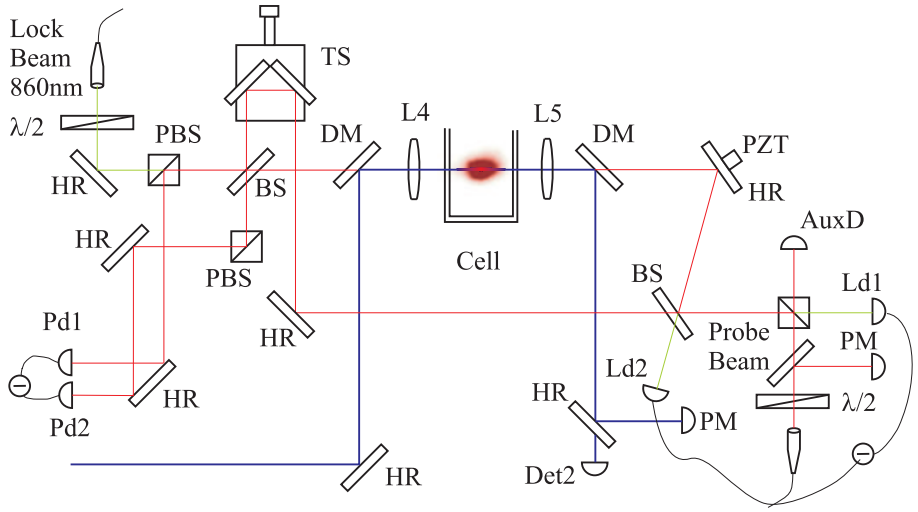

Figure 8.3: *Sketch of the setup of the interferometer with following elements: BS - 50/50 beam-splitter; PBS - polarizing beam-splitter; L4 & L5 - $f = 100mm$ achromatic lenses; DM - dichroic mirrors (HT @ 852nm, HR @ 1030nm); PZT - Piezo electric tube; Pd1 & -2 - Hamamatsu low noise, high gain photodiodes for probe detection; Ld1 & 2 - photodetectors for locking beam detection; and half wave plates $\lambda/2$, PM1&-2 powermeters for the probe and dipole trap beams, AuxD - auxiliary detector, TS -micrometer translation stage.*

the fiber-optic interferometer two lenses are used to create a probe waist of 20μm inside the quartz cell. The reference and probe arm are combined again on the second beamsplitter and detected by the Pd1 and Pd2 in a homodyne scheme. The locking beam in this setup propagates in an opposite direction to the probe beam and its polarization is orthogonal to the probe beam polarization. It is detected in a homodyne detection scheme employing the subtracted photocurrents of Ld1 and Ld2. Two dichroic mirrors DM are placed around the MOT cell to overlap the probe beam with the dipole trap beam. The achieved optimal visibility in the free-space configuration is $\mathcal{V} = 98\%$.

8.1.5 Detection

As we have mentioned earlier the detection of the pulsed laser light is done in a balanced homodyne detection scheme. The light from the two output channels of the Mach-Zehnder is detected with 2 photodiodes which photocurrents are subtracted to give a balanced photocurrent $i_-(t)$. When the detection is balanced the mean value of that current should approach zero. A necessary requirement here is that the detectors electronic noise must not exceed the shot noise of light in order to have shot-noise limited balanced detection. The noise of the detection system is discussed in detail in the following sections. Here we will only introduce the detection scheme.

In the experiment we use a low-noise balanced detector described in [118] incorporating two Hamammatsu photodiodes[7]. The optical probe pulses are generated typically at a rate of 166 kHz and have duration of 2μs. After detection the photodiode current is integrated

[7]Hamammatsu, mod. Si PIN S3883, NEP 6.7×10^{-15}W/$\sqrt{\text{Hz}}$, 20V reverse voltage

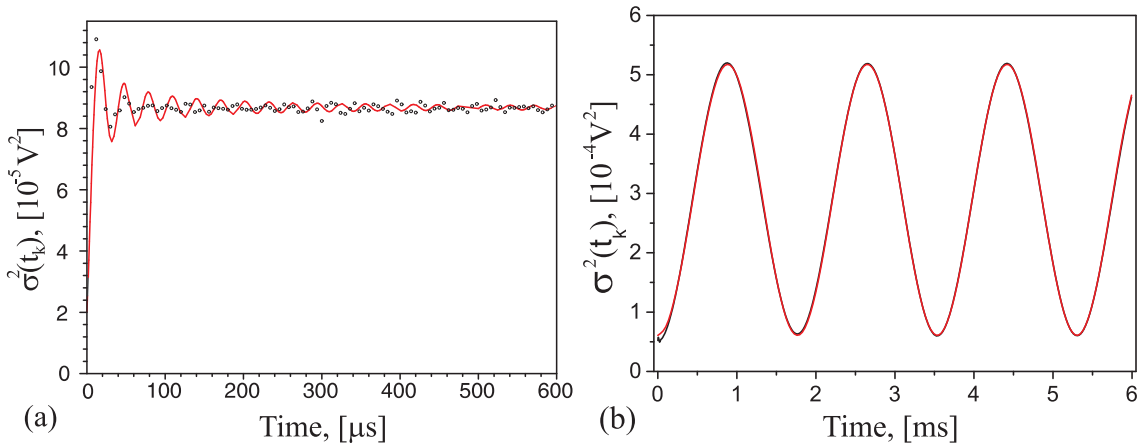

Figure 8.4: *Two-sample variance. Electronic noise of the detection: experimental data (∘) and theoretical simulation (solid curve)(a). Sine wave modulation at 565 Hz: theory (red), experiment (black).*

over the pulse duration τ_p:

$$a_p = G \int_0^{\tau_p} i_-(t)dt \tag{8.4}$$

where G is detection gain, which is a product of the gain of the photodiode preamplifier and the integrator circuit gain. The expectation value of a_p is then obtained as $\langle a_p \rangle = \frac{a_p}{\tau_p} = G\langle i_- \rangle$. The integration circuit[8] is gated by an external pulse which starts the integration. The integration lasts until the gating pulse is high and then after 1μs resets. Since the optical pulse is delayed w.r.t. the VCO drive pulse with about 1μs the integrator has to be gated by a second pulse generated from the PC.

Further, the value of the integrated pulse is acquired by a NI card with a home-written software in Lab-View 6.1.[9] The program is made such it processes the data giving the mean values and the variances in real time so that storing of large amount of data on the PC hard-drive is not necessary. The program also has an option to save the raw data if required.

8.1.6 Data analysis

This section presents the way data is being analyzed i.e which parameters are calculated by the data acquisition program and their connection with the actual parameters of the detected light.

To obtain better statistics we need many pulses. The number of pulses per pulse train depends on the purpose of measurement. Let us consider that the i-th pulse of a pulse train containing M pulses is a_i. Then after the pulse areas are acquired we have an M×1-dimensional array of real numbers which has been further processed using the acquisition program. The program calculates the expectation value $\langle a \rangle$ and the square of the standard

[8] Burr-Brown, mod. IVC102
[9] DO-DAQ-QND 2.6 data acquisition program

deviation i.e. variance $(\delta a)^2$.

$$\langle a \rangle = \frac{1}{M}\sum_{i=1}^{M} a_i, \quad (\delta a)^2 = \frac{1}{M}\sum_{i=1}^{M}(a_i - \langle a \rangle)^2 \tag{8.5}$$

In addition to above quantities the program can also calculate the mean of several pulse trains and the variance of the mean value averaged over the number of trains. This is convenient way of determining shot-to-shot fluctuations especially in the case of characterization of the atomic sample where short pulse trains are used in a multiple loading cycles. The variance over a whole pulse train gives information about the fluctuations in the train itself and is useful for tracking fluctuations of uncorrelated events. To track the fluctuations of correlated events or to describe the stability of the interferometer another statistical quantity is used i.e. the so called 2-sample variance. Let us assume that we have the same pulse train as before but this time we take the i-th element of the array and subtract it from the $(i+k)$-th element so that we get the below expression.

$$\sigma^2(k) = \frac{1}{2(M-k)}\sum_{i=0}^{M-k}(a_{i+k} - a_i)^2 \ , \tag{8.6}$$

As it can be seen the value of k determines which two pulse areas have to be subtracted. In our experiment the pulses have repetition period of τ_0, which would indicate that the above expression can be converted in time units by substituting the value of k with $t_k = k\tau_0$. This would mean that f.ex. the 2-sample variance on $t_k = 12\mu$s time-scale will reflect how different are the pulse areas of pulses separated by 12μs, having that the pulse repetition period is $\tau_0 = 6\mu$s.

Next, we want to give an example of how our analysis will reflect the nature of the real physical process, for example the white noise. It is well known that the white noise should not depend on frequency [70]. Thus its spectral density $W(\omega) = W$ would be constant, and moreover will be constant with time. Then an useful expression for the 2-point variance will be [70]:

$$\sigma^2(t_k) = 2(G\tau)^2 \int_0^\infty W \frac{\sin^2(\omega\tau/2)}{(\omega\tau/2)^2}\sin^2(\omega t_k/2)d\omega. \tag{8.7}$$

The integration is done over the whole frequency space and the result expected should be constant with time for a white noise. However, experimentally the detectors have limited bandwidth B, thus the integration is always done for a given bandwidth. The integration in limited bandwidth should approach the above integral for times $t_k \gg B\tau$.

A good experimental example of a white noise is the electronic noise of detection system. We have measured the electronic noise of our balanced detector for 1000 pulses of $\tau = 6\mu$s duration and $\tau_0 = 6\mu$s repetition period. The result of the experimentally obtained two-sample variance is shown in Fig.8.4(a) along with a theoretical simulation using Eq.8.7. The resemblance of the data with the theoretical curve is obvious for a detection bandwidth of around 200 kHz.

The modulation of the laser frequency results in direct modulation of the 2-sample variance (see Fig.8.4(b)). In this case the integration of Eq.8.7 is done easily since the spectral noise density have one and only component at the modulation frequency Ω i.e. $W(\omega) = \mu\delta(\Omega - \omega)$. This gives a straightforward result for $\sigma^2(t_k)$ as a sine function.

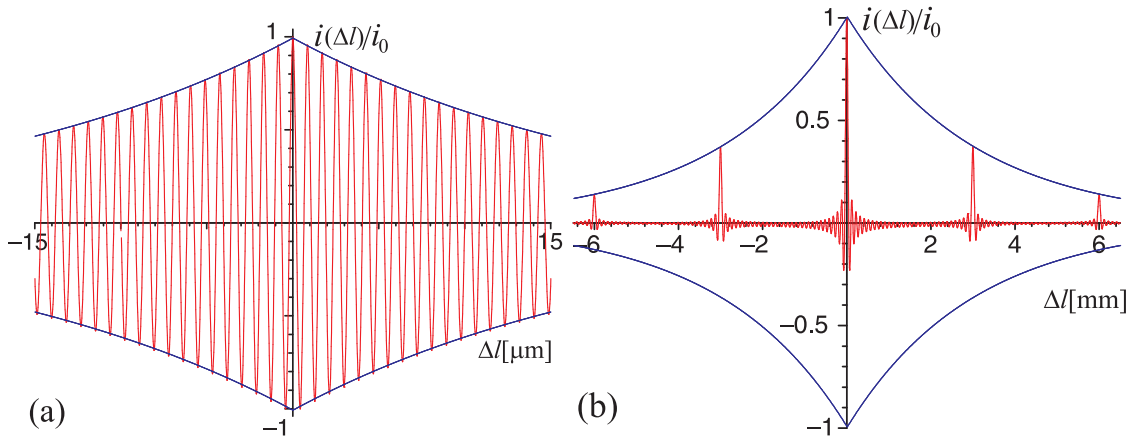

Figure 8.5: *Interferometer signal: broadband LED (a) and multi-mode laser without grating feedback (b).*

8.2 White-light alignment

As we have shown in the theoretical part the white-light alignment of the interferometer would guarantee the cancelation of the classical phase noise. The white-light position corresponds to zero optical path length difference between the probe and reference arm thus raising the requirements for the alignment procedure [119]. First, the alignment is done very coarsely i.e. to within a 1-2 mm, and then is finely adjusted.

It is well known that the interference in a interferometer depends on the pathlength difference between the arms. Two light beams of the same frequency and polarization, propagating in the interferometer arms will interfere if the optical pathlength difference of the arms is smaller then the coherence length of the source emitting them. Thus, if our goal is to make the pathlength difference very small we need to use a light source with sufficiently short coherence length. In any case a single mode laser is not a good source for alignment of the white-light position since it has a coherence length of meters. As an example, a grating stabilized diode laser with a linewidth of $\Delta\nu = 800$ kHz have coherence length of $l_c = c/\Delta\nu = 375\ m$.

In our experiment for the white-light alignment we use a fiber-coupled light-emitting diode (LED),[10] which has a wavelength FWHM bandwidth of $\Delta\lambda$=35 nm centered around 850 nm, thus giving a coherence length of $\lambda = 21$ μm. This would indicate that the two arms of the interferometer can be brought to the same path length with around 21 μm precision.

The alignment is done by monitoring the interference signal obtained from the LED, when scanning the interferometer pathlength difference using the micrometer translation stage in the probe arm of the fiber-optic interferometer or the optical delay line of the free-space one.

It can be shown that when scanning the pathlength difference Δl of the interferometer the subtraction detector photocurrent is given by [70]:

$$i_{-}(\Delta l) = i_0 \exp\left(-\frac{|\Delta l|}{l_c}\right)\cos(2\pi\Delta l/\lambda). \tag{8.8}$$

[10] Fiber-Optic Devices, mod. FOD-3102

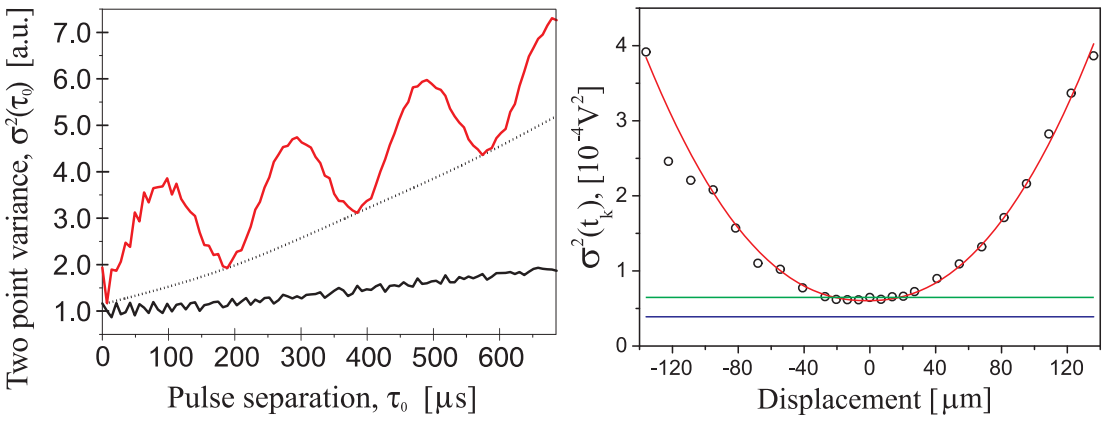

Figure 8.6: *Modulation of the 2-sample variance. (a) 2-sample variance when the laser frequency is modulated (red) , white light position (blue). (b) Mean value of the 2-sample variance as a function of the pathlength difference when the laser frequency is modulated (∘), parabola fit to the data, shot noise level (green), electronic noise (blue). Data (a) is taken with the fiber-optic interferometer and data (b) with the free-space one.*

The exponential factor in front of the cosine describes the coherence of the light source from classical point of view. When we have a highly coherent laser the l_c is very large thus turning the exponent to zero. For an incoherent or "white-light" source as we have already shown above the coherence length is very small thus giving an exponential decay of the interference signal when increasing the optical path length difference [Fig.8.5(a)].

Another option for alignment of the white-light is to use a multimode laser or a diode laser without grating feedback. In that case several modes will contribute to the interference signal. Let's assume that we have a laser diode with cavity length of L and a coherence length for the single mode of l_c. Using the theory presented in [70] we can write for the output photocurrent the following:

$$i_{-}(\Delta l) = i_0 \exp\left(-\frac{|\Delta l|}{l_c}\right) \sum_{n}^{N} \cos(n\pi \Delta l / L). \tag{8.9}$$

The sum is done over the number of generated modes. An example of i_{-} for a laser with $l_c = 3$ mm and $L = 1.5$ mm, generating 30 modes is shown in Fig.8.5(b). It is clear that a broadband light source is more suitable for the fine alignment of the white light position since the characteristic length at which the interference signal from the LED drops is around 10^3 shorter.

The use of the LED ensures equal pathlengths of the two arms in the a range down to a 20 μm, but for our purposes we would like to check whether we are really in that position. The white light position, i.e. the position where an incoherent light would interfere when propagating through interferometer, is also the position where the detection is most insensitive to classical phase noise. For that reason a modulation of the phase of the probe laser should induce modulation in the 2 sample variance as we have seen in Sec.8.1.6. The detected photocurrent is proportional to the optical phase ϕ [see Ch.4] and

the time delay between the two arms $\Delta t = \Delta l/c$. Then for $\sigma^2(\Delta l)$ we get:

$$\sigma^2(\Delta l, t) = \left[\frac{1}{c\tau}\mu g \Delta l \sin\phi \cos(\Omega t/2)\right]^2. \tag{8.10}$$

The amplitude of the induced modulation of the 2-sample variance when vary the interferometer pathlength difference can be used to finely determine the white-light position. An experimental example of that modulation is shown in Fig.8.6(a) for the fiber-optic interferometer. The modulation of the probe laser frequency results in a modulation of the 2-sample variance, when the interferometer is not in the white light position. The modulation disappears when he interferometer is in the white light position.

A more thoroughly done measurement is shown in Fig.8.6(b). The probe laser external grating is swept with a frequency of 355 Hz. The 2-sample variance of 1000 pulses, 2 μs long with a repetition period of 6 μs, is extracted from the balanced detector photocurrent. The measurement is done for different positions of the optical delay line, which translates in scanning the optical pathlength difference of the interferometer (x-axis in Fig.8.6(b)). For every pathlength difference the average value of the 2-sample variance is calculated and plotted in Fig.8.6(b). Changing the position of the delay line in the free-space interferometer, yields different amplitude of the induced 2-sample variance oscillations. The amplitude of the oscillation vanishes at the white light position. The level of the fluctuations at the white light would correspond to the shot noise level for that optical power which is 200 nW. This level is indicated with green line in Fig.8.6(b) along with the electronic noise (blue line).

8.3 Noise properties

In previous section we have emphasized the necessity of having the interferometer in white-light position in order to cancel the classical phase noise. Here we continue the same line of thought, however this time showing the effect of the white-light alignment on the interferometer noise. We would expect that the noise would scale linearly with the optical power i.e. number of photons if the interferometer is shot-noise limited as it has been shown in the theoretical part.

8.3.1 Amplitude noise

The amplitude noise of the detection is a mixture of quantum and classical noise. The last depends quadratically on the optical power and can be overcomed if the detection is balanced. However, the same thing does not apply for the quantum amplitude noise [11]. It scales linearly with the optical power or number of photons. If the scaling becomes quadratic this means that the detection acquires classical amplitude noise.

In general, the diode lasers have very well defined amplitude and thus their output can be considered as almost quantum noise limited in terms of amplitude. Nevertheless, we have to convince ourselves that our detection is shot noise limited in terms of amplitude noise.

The amplitude noise of the detection does not require interferometric operation, which means that the measurement can be done by blocking one interferometer arm and observing the detectors subtracted photocurrent noise at different power levels of the probe laser. For both fiber optic and free-space interferometer we use 1000-2000 pulses 2μs each with a

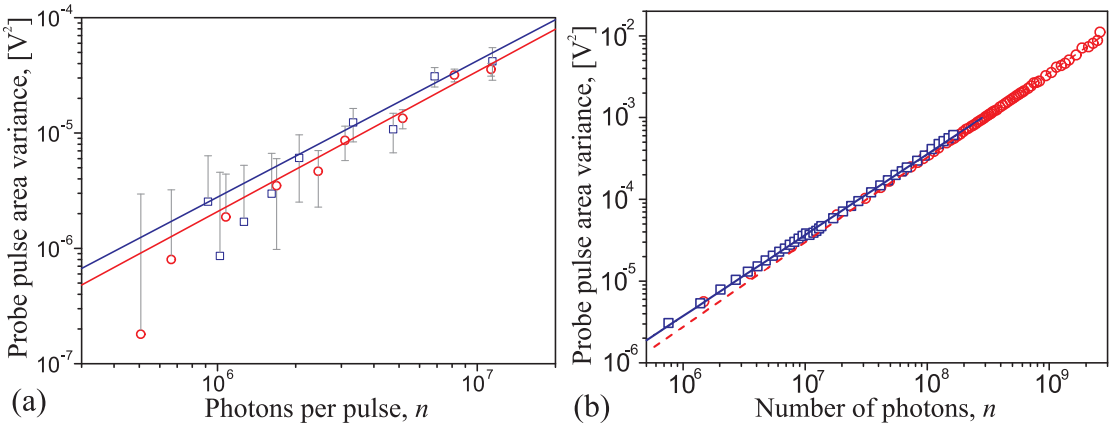

Figure 8.7: *Interferometer noise. (a) Fiber-optic interferometer amplitude* (○) *and phase* (□) *noise as function of number of photons n, fits to the amplitude (red curve, slope: 1.2(2)) and phase (blue, slope: 1.2(3)). (b) Free-space interferometer the same as (a), slopes for amplitude and phase fits 1.036(8) and 0.990(5), respectively.*

repetition period of 6μs. The results from the the measurements are shown in Fig.8.7. The probe pulse area variance is calculated in real time and plotted against the optical power converted into number of photons per pulse using the relation $\langle n \rangle = 4.3\times\ 10^6\ P(\mu\mathrm{W})\tau_p(\mu\mathrm{s})$ for an optical wavelength of 852 nm. The fits to the experimental data show that both interferometer constructions, fiber-optic and free-space, are shot-noise limited in amplitude detection since the log-log scale representation of the noise shows linear dependance with a slope of 1.2(2) and 1.036(8), which in a liner scale would mean linear dependance of the noise as a function of number of photons per pulse. The data taken with free-space interferometer is much less noisy due to the better lock performance eliminating the chromatic dispersion effect in the optical fibers. The detection is shot-noise-limited for up to 10^7 and 3×10^9 photons per single pulse for the fiber-optic and free-space interferometer respectively.

8.3.2 Phase noise

To be able to measure atomic phase shift the interferometer needs to be locked to a half fringe i.e. $\phi + \pi/2$, and the detection to be balanced. However, at that position the susceptibility to acoustic noise and path-length variations, resulting in phase fluctuations is highest. This leads to acquisition of a large amount of classical phase noise during detection leading to a square dependance of the phase noise with the number of photons. When the influence of these disturbances on the interferometer is diminished one would expect a linear dependance of the phase noise as a function of photon number i.e. shot noise limited operation in terms of phase noise.

The interferometer noise characterization experiment is done having both arms unblocked and the homodyne detector photocurrent balanced. The input power in the interferometer is varied and the photocurrent variance is measured for the different power levels. Along with the statistical variance (the square of the standard deviation) we can also produce the 2-sample variance $\sigma^2(t_k)$ as in Eq.(8.6) on a different timescales. The last would tell us how the phase fluctuations due to the above-mentioned phenomena modify the interferometer noise in time. The result from these measurements with the fiber optic

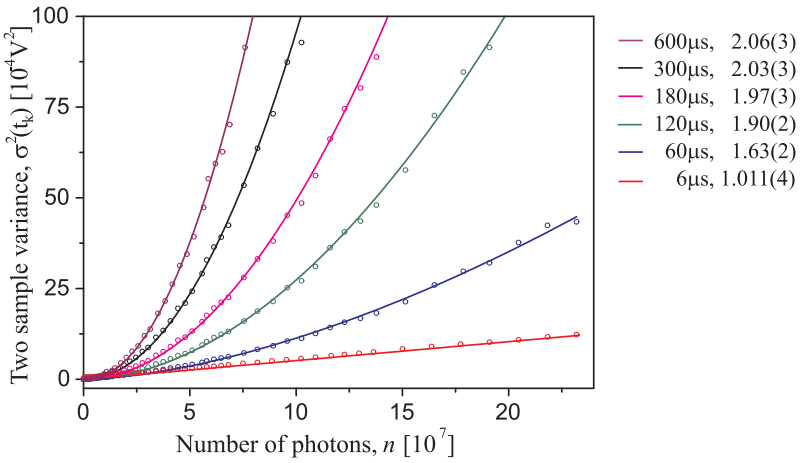

Figure 8.8: *Interferometer noise on a different timescales. Experimental data* (∘) *and a power function fits (solid lines). At the left is shown the value of the power coefficient p.*

interferometer and the free-space one are shown in Fig.8.7(a) and Fig.8.7(b), respectively. Again, the interferometer is shot-noise-limited in terms of phase noise for up to 10^7 and 2×10^8 for the fiber-optic and free-space design. The slopes of the fitting lines are 1.2(3) and 0.990(5) for the two design configurations. It should be noted that the experimental data from the fiber optic interferometer strongly depends on the detectors balance. As it was already mentioned the polarization drift in the fibers and chromatic dispersion due to heating at photon numbers above 10^8 led to difficulties in taking more data.

Additional data can be extracted by measuring the 2-sample variance $\sigma^2(t_k)$. One would expect that with increasing the time interval t_k between the subtracted pulse areas, the variance would grow since more frequency components would contribute to the signal. Thus the longer the timescale t_k the bigger the variance $\sigma^2(t_k)$. The last is expected to rise until it reaches the classical value, which is prone to have quadratic dependance on the number of photons. The data is presented in Fig.8.8 for timescale of 6μs, 60μs, 120μs, 180μs, 300μs, and 600μs together with correspondent fits to the function $\sigma^2(t_k) \simeq \langle n \rangle^p$. The values of p are shown on the right in Fig.8.8. It can be clearly seen that after 60μs the fits tend to be quadratic, thus revealing the classical phase noise influence at low frequencies. However, for relatively low photon number, less then 10^7, the points can be fitted to a straight line. This would indicate that in the low photon number limit, the interferometer is shot-noise-limited even on timescales up to 0.5 ms. The longer the timescale is the lower is the number of photons at which the interferometer is shot-noise-limited. For the atomic phase shift and noise measurements the power chosen is typically not more that 600 nW, which is well in the range of the optical powers where the detection is quantum noise limited.

As a conclusion we can summarize that the interferometer is shot-noise-limited in both phase and amplitude for up to 2×10^8 for the free-space and 10^7 for the fiber-optic design configuration. The noise grows on longer timescales and eventually becomes quadratic i.e. classical for large photon number. For photon numbers below 10^7 the detection is still quantum-noise limited.

An additional care was taken to isolate the free-space interferometer from acoustic noise by shielding it in a box of a sound damping material glued on aluminum sheets. We have also detached the bottom coil from interferometer plate since the fast switching

of the trap field induces an acoustic noise, which eventually couple to the light signal. Detailed analysis of the acoustic noise performance of the setup is done in a master thesis by Daniel Oblak [22].

Chapter 9

Interferometric measurements with cold atoms

In this chapter we present our results on shot-noise limited light interferometry with cold and trapped atoms. In general the interferometric measurements performed in this experiment are divided into two groups: DC or phase shift measurements and noise measurements.

For the first group of measurement the important variable is the mean value of the phase shift of light interacting with atoms. This mean value is proportional to the number of atoms and depend on the detuning of the probe laser from the atomic transition in concern. Then by monitoring the value of the phase shift in different conditions we get a knowledge of important characteristics of the atomic sample.

The second group of measurements are the ones which involve monitoring of the fluctuations of the phase shift in order to get a knowledge of the collective atomic state or simply to determine the accuracy at which the mean value of the phase shift is measured.

The chapter is organized as follows. We start with Sec.9.1 where we describe the transformation of the measured phase shift into the experimentally measured voltage. In Sec.9.2, we present results from nondestructive characterization of atoms during a free expansion from a magneto-optical trap using fiber-optic and free-space interferometer. We perform measurements to estimate the loading time and density of the atomic samples in both AU and NBI MOT's. Then we continue with noise of the atomic ensemble prepared in AU and NBI MOT. The third section of the chapter is devoted to non-destructive characterization of dipole trapped atoms [Sec.9.3]. The characterization includes measurements of both light-assisted and light-independent losses, the loading rate, the radial oscillation frequency, the number of atoms, the density and the temperature of trapped atoms. At the end of Sec.9.3 we present results of the noise measurement of dipole trapped atoms. The chapter ends with a summary of the experiments done on characterization of MOT and FORT.

9.1 Experimental variable

The measurement of atomic phase shift is done via detection of probe light photons. They are detected by detectors which produce a photocurrent. The photocurrent itself is converted to an analog voltage, which is acquired by a computer. The current section is devoted to these transformations of the measured phase shift.

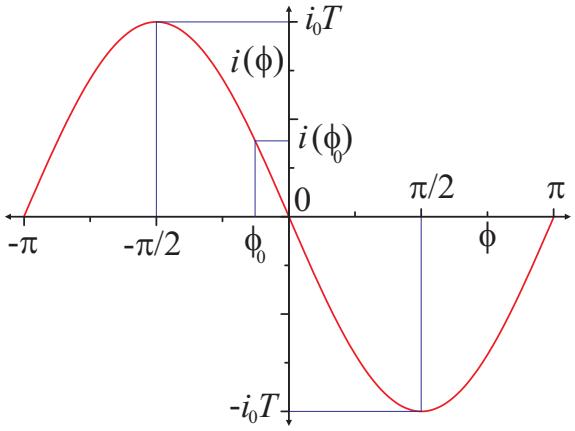

Figure 9.1: *Interferometer fringe*

Let's assume that our interferometer is locked at a half fringe and the homodyne detector is balanced when there are no atoms in the probe arm. The interference fringe of the interferometer is shown in Fig.9.1. The phase shift due to atoms is then calculated as arcsin of the ratio between the measured value of the photocurrent and the fringe amplitude. The fringe amplitude is determined as the half of the difference $2i_0T$ and adjusted for the transmission factor T due to absorption of probe light and losses due to coupling. Finally, the value of ϕ_Δ is found by:

$$\phi_\Delta = \arcsin\left[\frac{\langle i(\phi)\rangle}{i_0 T}\right]. \tag{9.1}$$

The last expression can be used to determine the phase shift from the detector generated photocurrent. One can also approximate the sin function with its argument for small ϕ, which would mean that the phase excursions from the locking point at $\phi = 0$ are very small.

The above equation though very understandable is not much useful since at the end of the detection the generated photocurrent is converted into a voltage and the voltage is acquired by the acquisition card. For that reason we introduce the relationship between the measured voltage at given detuning V_Δ and the atomic phase shift as:

$$\phi_\Delta = \arcsin\left(\frac{V_\Delta}{GP_{DC}}\right) \tag{9.2}$$

where $GP_{DC} = V_0$ is the maximum fringe amplitude as shown in Fig.9.1, but this time in voltage units. The fringe amplitude is calculated as the product of the DC optical power per pulse P_{DC} and the detection gain G.

As we have already mentioned in the introduction the measurements can be divided into two groups: DC phase shift and noise measurements. In the current status of the experiment we are only sensitive to the population of $F = 4$ ground state level, since the probe light is at best 100 MHz away from the $F = 4 \rightarrow F' = 5$ cycling transition. Then the measured mean value and standard deviation of the phase shift concern the atoms residing on $F = 4$ ground hyperfine level. Hence in a DC measurement we can deduce the number of atoms N_4 by the experimentally obtained value of the phase shift via modification of

Eq.(2.42) taking into account only the population of the F=4 ground state:

$$N_4 = \frac{2\pi A}{\lambda^2}\frac{1}{S_{45}}\frac{\Delta_{45}^2 + \left(\frac{\gamma}{2}\right)^2}{\Delta_{45}\frac{\gamma}{2}}\phi_\Delta. \tag{9.3}$$

where Δ_{45} is the detuning from the cycling $F = 4 \rightarrow F' = 5$ transition. The above equation depends on the probe cross-sectional area $A = \pi w_0^2/2$ with gaussian beam waist radius of w_0. The value of $S_{45} = 11/18$ is the relative strength of cycling transition.

So far we have considered a DC measurements. Now we want to add to the above considerations the measurement of the noise, which would indicate how well we know the value of the phase shift. Then the noise of the ϕ_Δ is obtained by differentiating and taking the square of Eq.(9.2)

$$(\delta\phi_\Delta)^2 = \frac{1}{(GP_{DC})^2\cos^2\phi_\Delta}(\delta V_\Delta)^2 \tag{9.4}$$

where ϕ_Δ is given by Eq.(9.2). For an ensemble of uncorrelated particles which obey the poissonian statistics we can write using Eq.(2.44) the following expression for the ratio between the phase shift and its variance

$$\frac{\phi_\Delta^2}{(\delta\phi_\Delta)^2} = \frac{k(\Delta)^2 N_{at}^2}{k(\Delta)^2 N_{at}} = N_{at}. \tag{9.5}$$

The above equation gives an estimate of the atom number in the ensemble which is independent of the probe beam waist. This is an useful relation since the error in the estimation of the waist can be big enough for non-Gaussian beams. The coefficient $k(\Delta)$ denotes the detuning dependent and probe-beam-area dependent coefficient of proportionality.

At the end of that section we want to emphasize that the measured experimental signal in case of the noise characterization contains several noise contributions as also discussed in Sec.4.2, Eq.(4.42). Throughout the discussion so far we have shown that classical amplitude and phase noise are canceled and the only noise contributions we have, are the shot noise of light and the electronic noise of the detection system [see Sec.8.3]. Hence for the noise of the experimental signal we can write:

$$(\delta V)^2 = (\delta V_\Delta)^2 + (\delta V_{SN})^2 + (\delta V_e)^2 \tag{9.6}$$

The shot noise of light $(\delta V_{SN})^2$ depends on the number of photons n_{ph} and has to be subtracted from the overall signal in a reference measurement. The same applies for the electronic noise $(\delta V_e)^2$. Having addressed the issue on how exactly the number of atoms and the phase shift can be determined by the detected experimental signal we can now proceed to presenting the results of the experiments.

9.2 Interferometry with cold atoms in a MOT

The section presents measurements with atoms in a MOT performed with fiber-optic and a free-space interferometers described in the previous chapter. The experimental variable is the phase shift imposed on the coherent probe light by dispersive interaction with the atomic cloud. The section also includes measurement of shot-to-shot atom number fluctuations in the MOT. The physical nature of these fluctuations was already discussed in Ch.4.

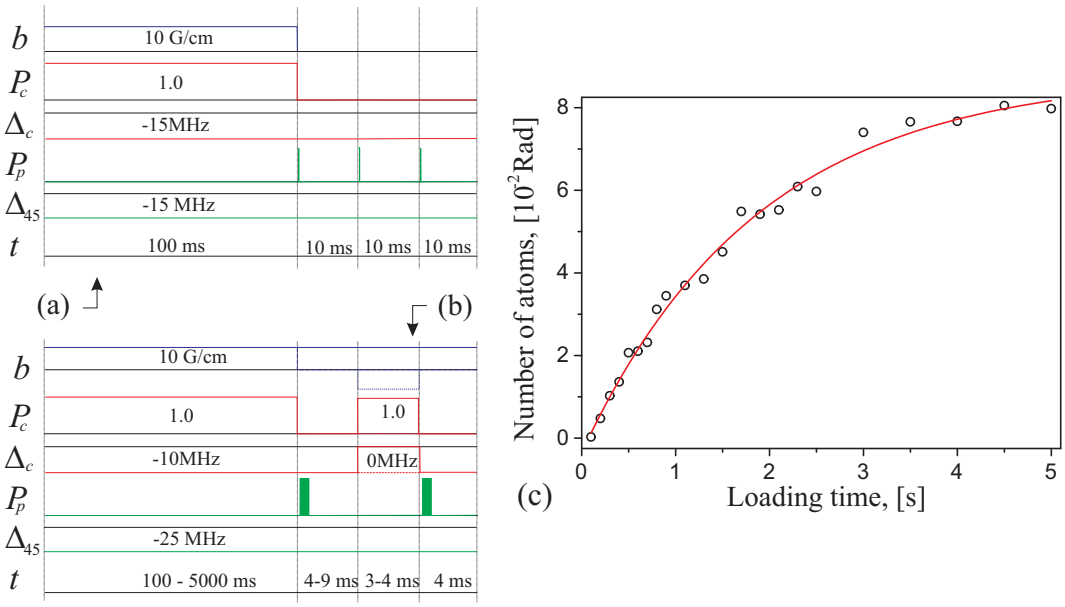

Figure 9.2: *Experimental cycle diagram for fiber-optic (a), and free-space interferometer (b). Loading curve of MOT taken with free-space interferometer (c).*

The measurements include two pulse trains. The first pulse train measures the phase shift due to atoms and the second is a reference measurement with probe light only. The difference of the two would give the necessary information about atomic population. The typical experimental cycles used when performing measurements with fiber-optic and free-space interferometer are shown in Fig.9.2(a,b). Before the reference measurement is performed the atoms has to be removed from the probing volume by applying a resonant light pulse of cooling light.

For the measurements performed on the AU MOT with the fiber-optic interferometer, the application of resonant light pulse was not necessary since the MOT has decayed at the arrival of the second pulse after 10 ms. In this case the second and the third pulse merely take the reference measurement.

For the measurements done on the NBI MOT with the free-space interferometer, due to the long decay of the NBI MOT (about 0.5 s), a resonant pulse of MOT light or a negative-gradient magnetic field "kick" has to be applied in order to "clean" the probing volume for the sake of the reference measurement.

9.2.1 Loading dynamics

This measurement is done with the free-space interferometer to estimate the loading time, loading and loss rates of the MOT. The light phase shift depends on the number of atoms residing in the atomic level of concern. In our experiment the probed atomic level is the F=4 ground hyperfine state of Cs atoms. Since the atoms are mainly distributed over the magnetic sublevels of that state after the cooling process the choice to probe that level is reasonable.

The atoms are loaded in the MOT for variable time from 100 ms to 5 s. Then the MOT light fields are switched off for 4 ms. In the beginning of that stage 100 probe pulses of 2 μs duration and 6 μs repetition period are sent to the released atomic sample. The

probe light is detuned by $\Delta_{45} = -25$MHz from the $6S_{1/2}(F = 4) \rightarrow 6P_{3/2}(F' = 5)$ cycling transition. The influence of the magnetic field results in a Zeeman shift of the probed atomic transition of about 1 MHz. A second pulse train of 100 pulses takes a reference measurement with no atoms present 4 ms after the atom probing. The result is shown in Fig.9.2(c).

The characteristic loading time of the MOT is found to be around 1.88(15) s, which indicates a loss rate of 0.53(0.04) Hz. The idea behind this measurement, except determining the loading time, is to find a a method of changing the number of atoms for the sake of the noise measurement described later. However, we have found out that the values of the phase shift have very large uncertainties (not shown in the graph). When we plot the square of the standard deviation we see a clear quadratic dependance, which is an evidence for an excess classical noise over the measured signal. Hence there is a classical noise mechanism that couples to the system. Later we have found a different method to change the number of atoms by changing the dispenser current. The dependance of the equilibrium number of atoms on the dispenser current is almost linear for low currents up to 3.4 A.

9.2.2 Density in the MOT

The strength of the off-resonant interaction depends on the optical density, which on the other hand is proportional to the number density of the atomic sample [see Eq.(5.26)]. To determine the number density of the atomic sample we can use its relation to the measured phase shift [see Eq.(2.47)]. The phase shift as we have shown is a function of the detuning of the probe laser with respect to the atomic resonance in our case the cycling $6S_{1/2}(F = 4) \rightarrow 6P_{3/2}(F' = 5)$ transition. By scanning the detuning of the probe laser across the excited state hyperfine manifold we can observe the characteristic dispersive curve as the one shown in Fig.2.3(a), but for atoms on $F = 4$ ground hyperfine state.

The experiment is done with the fiber-optic interferometer by using the experimental cycle shown in Fig9.2(a). The frequency is varied using the advantages of the tunable frequency offset locking described in Ch.8.

About 10^8 caesium atoms are collected in the MOT for 100 ms at a detuning of -3γ and magnetic field gradient of 10 G/cm. Then the light and magnetic field are switched off for 10 ms. Since the switching of the magnetic field is at the millisecond level, the atomic transition frequency is Zeeman shifted during the measurement of about 1 MHz. During that stage the first probe pulse of duration 2 μs and power of 1 μW interacts with atoms. At the end of that stage the atoms have already left the probing region and second pulse is applied for a reference.

The frequency of the probe laser is scanned in the range of -550 to 600 MHz, with respect to the cycling transition frequency and the corresponding phase shift is measured. The result is plotted in Fig.9.3.

The dispersive curve is similar to the $F = 4 \rightarrow F' = 3, 4, 5$ part of the one presented in Fig.2.3(a). The relative amplitudes of the linewidth functions near the hyperfine transitions have to be equal to the relative hyperfine transitions strengths. For example $\phi_{45}/\phi_{44} = S_{45}/S_{44} = 2.1$ and $\phi_{44}/\phi_{43} = S_{44}/S_{43} = 3$. However, the experimental results do not agree with the above. The values obtained from a linewidth function fit are 4.55 and 2.13. The transition $F = 4 \rightarrow F' = 5$ is cycling and the decay of the excited state $F' = 5$ to the ground hyperfine component $F = 3$ is dipole forbidden. However the two lower hyperfine states of the excited $6P_{3/2}(F' = 3, 4)$ manifold are coupled to the $F = 3$ state

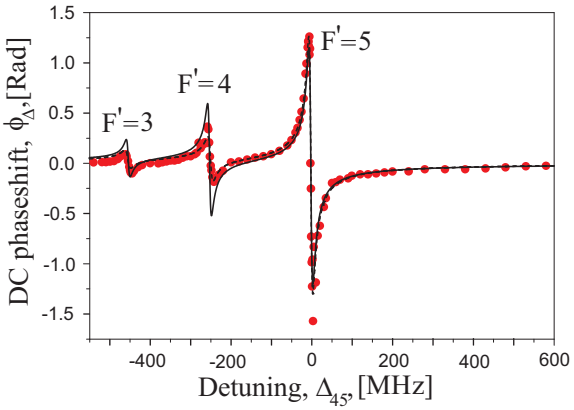

Figure 9.3: *Atomic phase shift as a function of probe laser detuning (b), fit with a fixed values of the lineshape amplitudes (solid line); fit with the amplitudes varied and corrected for depumping by the probe light (dashed line).*

via dipole allowed transition, allowing for depumping of the $F = 4$. This indicates that the probe does redistribution of atomic population among the ground hyperfine states. When correcting for the depumping using the rate equation analysis the fit to the data agrees well with the experiment as shown in Fig.9.3.

The value obtained for the natural linewidth is $\gamma_{exp} = 9$ MHz, which is about 1.7 times higher than the actual one of $\gamma = 5.2$ MHz. At a temperature of the probed atoms of around $T = 417$ μK the value of the Doppler broadening γ_D can be found using the expression [120]:

$$\gamma_D = 2\nu\sqrt{\frac{2k_BT}{Mc^2}\ln 2},$$

where $\nu = 350$ THz is the value of the atomic transition frequency. The calculated Doppler broadening is about 0.44 MHz, which tells us that there is additional broadening mechanisms that contribute to the observed linewidth.

Broadening can arise due to collisions wit the background gas inside the apparatus. The collisions with nitrogen N_2 molecules are dominant. In that case the induced linewidth broadening is of the order of 22 MHz/Torr as measured by [121]. In our experiment the background pressure is 2×10^{-7} Torr, which amounts to a pressure broadening due to background molecule collisions of 0.44Hz, which is obviously negligible. The transit-time broadening is connected with the time it takes for an atom to traverse the probe beam i.e. $\tau_{tr} = 2w_0/v$. Then the associated linewidth broadening would be $\gamma_{tr} = 1/(2\pi\tau_{tr})$. For our experimental parameters $w_0 = 20\mu$m, $v = 16$cm/s the transit time broadening is calculated to be 0.6 kHz, which obviously does not contribute much to the line broadening.

Then the last possible broadening mechanism, which can contribute to the wide linewidth is the power broadening. The power broadened linewidth γ' is calculated from Eq.(9.8) in the next section. Since the beam has a waist inside the cloud the intensity varies along the cloud diameter. For that reason we can use an average beam radius to calculate the probe light intensity. For 150 nW probe laser power used in the measurement and a waist of 20 μm the expected power-broadened linewidth is 21.4 MHz, which is about two times higher from the one deduced by the measurement. We aware that the probe beam waist could be off-centered w.r.t the atomic cloud. Then the atoms will see lower

intensity due to the bigger beam diameter. Since the cloud has a gaussian diameter of around 3 mm and the probe is directed along its longer diameter it is possible that the waist of the probe beam is positioned before or after the cloud center.

The number density of the probed atomic sample is estimated from the fit in Fig.9.3, using the experimentally obtained value for the total phase shift and the Eq.(2.47). The length of the atomic sample is taken to be 3 mm and the probe gaussian radius of 20 μm. The result obtained is $\mathcal{N} = 2.2 \times 10^9$ cm^{-3}, which agrees well with the value 1.2×10^9cm^{-3} obtained by fluorescence measurement in Ch.6.

9.2.3 Stark shift measurement

In the experiments performed with the MOT the only light field, which is on during probing stage, is the probe laser filed. The presence of MOT light during probing could introduce wave mixing effects [122], which could give a wrong estimate of the phase shift at given detuning, thus resulting in wrong estimate for the number of atoms. For that reason we have installed shutters to block the light completely during probing stage. However, in some cases we would like to have MOT cooling light during probing in order to determine important parameters such as the Stark shift induced by this light.

In this section we present an interferometric measurement of the Stark shift of the atomic transition caused by the presence of strong light field during probing. Let's assume that in addition to the probing field there is one more optical field which causes a Stark shift of the atomic transition frequency depending on its power and spatial distribution. The detuning of the probe field is denoted by Δ, and the MOT detuning is Δ_{MOT}. Then Δ is modified by the induced Stark shift as:

$$\Delta' = \Delta + \frac{\gamma^2}{4|\Delta_{MOT}|}\frac{I}{I_s} \tag{9.7}$$

where I_s is the saturation intensity, and I is the intensity of the trapping beams with gaussian beam radius of 1.25 cm. The atomic transition linewidth also becomes power dependent through the power broadened linewidth [123]:

$$\gamma' = \gamma\sqrt{1 + \frac{I}{I_s}}. \tag{9.8}$$

In the case of interferometric measurement the detected phase shift would change due to the Stark shift, which is equivalent to change of the probe detuning as seen below. Then the atomic phase shift becomes function of a new set of parameters Δ', γ' the modified detuning and the power broadened transition linewidth.

$$\phi(\Delta') = \frac{\phi_0}{2}\frac{\gamma'\Delta'}{\Delta'^2 + \left(\frac{\gamma'}{2}\right)^2} \tag{9.9}$$

The measurement is done with the free-space interferometer in the NBI MOT. The trap fills for 1 s at detuning of the cooling laser $\Delta_{MOT} = -2\gamma$ and magnetic field gradient $b = 12$G/cm. Next, the light beams are switched off for 1 ms and again applied for 1 ms more, but this time with different power. The power of the cooling light at the second 1 ms long stage is varied from 35% to 100% of the maximum power P_{max}=18 mW available for that measurement. During the whole 2 ms long period a long probe pulse train of 200

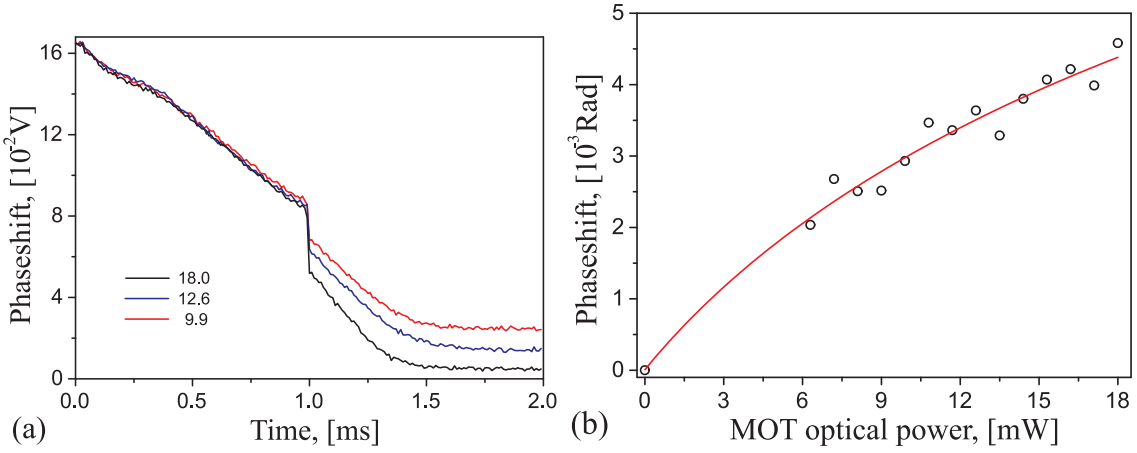

Figure 9.4: *Stark shift experiment. Raw data traces for three different power level of MOT light (a). Lorentzian fit of the atomic lineshape function in terms of phase shift of interferometer (b).*

pulses with the usual duration and repetition period of 10 μs is sent through the sample and the dynamics of the phase shift is recorded. The probe light detuning is fixed to $\Delta = -25$ MHz from the cycling transition, and the power is 0.6μW.

We anticipate that the phase shift, right at the border of switching on the MOT light again will undergo a fast change due to Stark shift as long as the number of atoms does not change much for 10 μs. Thus, at the end we expect to have MOT-light-power-dependent phase shift difference between the 100-th and 101-st pulses. The raw experimental data traces for three different power levels are plotted in Fig.9.4(a) along with the difference of the phase shifts between 100-th and 101-st pulses for all the powers in the range of $0.35P_{max}$ to P_{max} [Fig.9.4(b)]. The fit is directed through zero as a physically feasible result when there is not any MOT light. Unfortunately, the current experimental conditions did not allow to take points below 6.3 mW since the hyperfine repump laser did not have stable lock. Nevertheless, the fit to 15 data points showed a Stark shift per milliwatt optical power of 0.21 MHz/mW, which agrees with the theoretically calculated one 0.24 MHz/mW from Eq.(9.7). The maximum value obtained for the phase shift is $\phi_0 = 0.047(1)$Rad, which can also be used to determine the density in the MOT using the following equation:

$$\mathcal{N} = \frac{2\pi\phi_0}{S_{45}\lambda^2 l} \tag{9.10}$$

where $l = 0.05$ cm is the radius of the atomic sample. The result obtained show that the density is around $\mathcal{N} = 1.32 \times 10^9$ cm^{-3}, which can also be compared to the density of the Ti chamber MOT from the previous chapter. The density has almost the same value for the two MOT setups in Aarhus and Copenhagen, as anticipated. The only difference appears in the loading times. The lifetime of the NBI MOT is far longer than the one of the AU MOT, owing to the lower background gas pressure in the quartz cell.

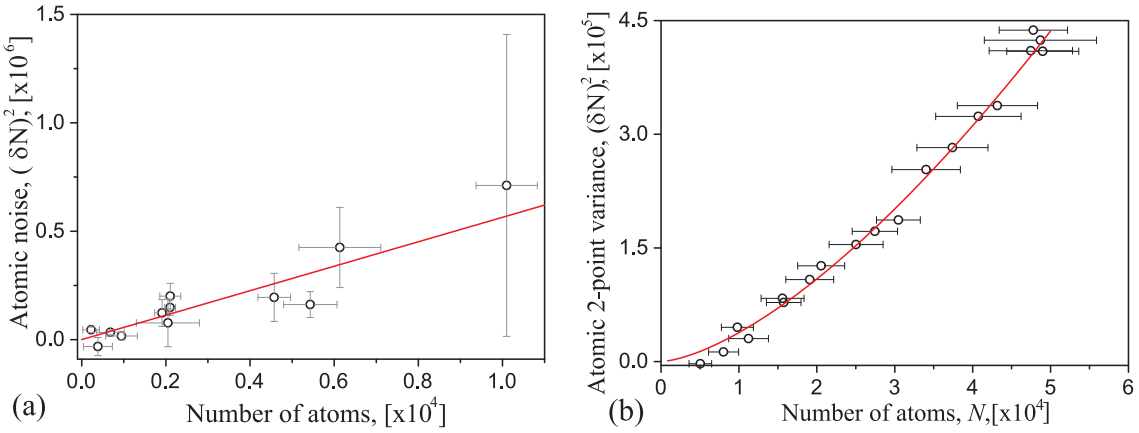

Figure 9.5: *Atomic noise measurements. Fiber-optic interferometer data (a)and a linear fit through* 0. *Free-space interferometer (b) and a fit to the equation* $(\delta N)^2 = p_1 N^{p_2}$, $p_2 = 1.51(5)$.

9.2.4 Atomic noise

The section is devoted to atomic noise measurements performed on a cold atomic sample prepared in a MOT. The noise measured is not the spin noise, which will be discussed in the scope of the QND measurement, but rather the population fluctuations of a specific hyperfine level. The data presented here is obtained in measurements done with both AU MOT using the fiber-optic interferometer and NBI MOT using the free-space one.

The noise of the atomic population on the F=4 ground state hyperfine level is poissonian when multiple loading of the MOT are considered [see Ch.4, Sec.4.2]. This means that the noise has linear dependance on the number of atoms. In this section we show that our apparatus is capable of detecting the population noise, indicating that the setup has the sensitivity to detect atomic fluctuations at the projection noise level.

The experimental sequence for measuring the atomic noise in the AU MOT is described in Fig.9.2(a). The three pulses are detuned by $\Delta = -15$ MHz from the cycling transition. The power in each pulse is $P_{DC} = 0.6\mu$W, and with duration of 2 μs gives a total number of photons per pulse of 5.2×10^6. The number of atoms is varied by changing the temperature of the Cs container.

Let's denote the areas of the pulses as a_i, $i = 1..3$. The first pulse obtains information about atomic noise and the second detects the shot noise, since the cloud has already decayed for about 10 ms. An additional reference pulse is sent through the sample another 10 ms after to account for locking point drifts. The difference between the first and second $d_{12} = a_1 - a_2$, and the second and the third $d_{23} = a_2 - a_3$ pulses as well as their variances $(\delta d_{12})^2$ and $(\delta d_{23})^2$ are calculated. The latter are further expressed as $(\delta d_{12})^2 = (\delta a_{at})^2 + 2(\delta a_{SN})^2$ and $(\delta d_{23})^2 = 2(\delta a_{SN})^2$, where $(\delta a_{at})^2$ and $(\delta a_{SN})^2$ denote the atomic and shot-noise contribution to the noise, respectively. The atomic variance is then expressed as $(\delta a_{at})^2 = (\delta d_{12})^2 - (\delta d_{23})^2$, using the above relations. The data acquisition program has given us the values of a_i and the atomic noise contribution was calculated. The number of atoms and noise are transformed from voltage units by use of the analysis presented in Sec.9.1. The result is plotted in Fig.9.5(a).

Fitting the data to a straight line would compare how well the noise can be approx-

imated to poissonian. The fit shows the anticipated linear dependency of the noise with the atomic number as discussed in Sec.4.2. This would mean that the built interferometer has the required sensitivity to detect the projection noise.

The NBI MOT setup contains Cs dispenser as a source of atoms, and the number of atoms in the background can be changed by varying the dispenser current. The current is firstly increased to about 3.5 A for a short time and then gradually decreased by steps of 0.5 A down to 2.5 A. After every current change a short delay period of 5 min enables system equilibrium before the next measurement is taken.

For this measurement we send two pulse trains, both containing 100 pulses, through the atomic sample prepared in the MOT using the scheme shown in Fig.9.2(b) with magnetic field switched off during measurement. The atoms are collected in the MOT at a detuning of $\Delta = -2\Gamma$ and trap magnetic field gradient of 10G/cm for 1 s. Then they are released and probed by the light for total of 0.6 ms. After the typical "cleaning" of 9ms we take a reference measurement, which lasts for another 0.6 ms. After the end of the cycle a blank period of 4 ms separates the next loading cycle. The number of cycles or equivalently the number of averages is 200, which means that every point on Fig.9.5(b) is a result of the 200 averages.

The fit of the data to a power function gives a parameter of $p_2 = 1.51(5)$, which means that the atomic noise has some classical noise influence, but is not dominated by classical noise since $p_2 < 2$. At the same time the measured noise is not poissonian since in these units the power parameter must be one. It has to be mentioned that the uncertainty in the x-axis i.e. the number of atoms or DC phase shift is large. The result indicates that the equilibrium number of atoms is not reached for 5 min delay before every measurement. An evidence for that are the points at highest atom numbers, which are taken first in the measurement.

9.3 Nondestructive characterization of dipole trap

There are different techniques to measure various parameters of trapped samples. The conventional ones rely on a destructive measurement i.e. absorption imaging or collection of atomic fluorescence. When applying these techniques the atomic sample is destroyed after the measurement. However, if one wants to track dynamical processes happening in the atomic sample, the probe light must not introduce heating or even loss of atoms from the cloud. It has been shown that in the above case for optically thick samples, the nondestructive techniques are superior [124,125]. The dark-ground imaging [126], the phase-contrast imaging [124] and the phase shift measurement [127] has been implemented for a BEC and the spatial heterodyne imaging for a dark-spot MOT [128]. A recent paper introduces the diffraction-contrast imaging as a non-destructive measurement technique [129] of cold atoms. However, most of these experiments consider imaging with a CCD camera and off-resonant light. In this section we will present a novel method of shot-noise limited interferometric nondestructive characterization of dipole trapped atomic sample.

The dipole trap is loaded using the sequence described in Ch.7. Then after a variable storage time, but not shorter than 10 ms, the atoms in the dipole trap are probed by light pulses with duration of typically 2 μs and repetition period between 6 μs and 100 μs, depending on the current measurement. The number of pulses is chosen upon the purpose of the measurement, but it usually varies from 10 to 100. The probe light is 100MHz from the cycling $6S_{1/2}(F = 4) \rightarrow 6S_{3/2}(F' = 5)$ transition in caesium. The power is varied from 150 to 300nW. After the probing, a resonant light pulse with the MOT beams is

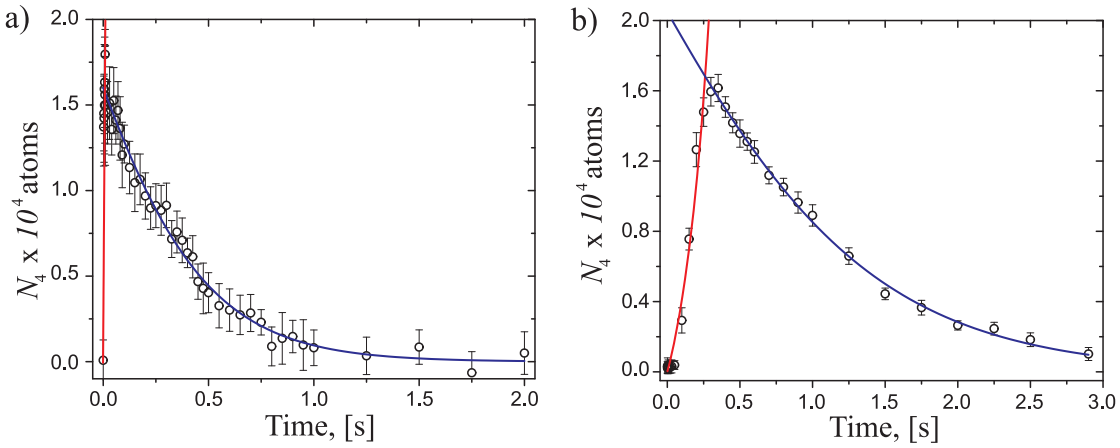

Figure 9.6: *Loading curves of FORT: compression (a) and molasses (b).The data is fitted to the loading and loss terms in Eg.7.4. The parameters deduced from the fits are stated in Table 9.1.*

applied in order to remove the atoms from the probing volume and consecutive reference measurement is taken using the same probe light characteristics.

9.3.1 Loading dynamics

In this section we present our nondestructive measurement method to determine the loading and loss parameters of the dipole trapped atomic sample. The dynamics of the loading process is described by the Eq.(7.4) from Ch.7. However, we only consider the population of the $F = 4$ hyperfine ground state, since the probe laser is closer to it. The nature of the losses during loading was discussed earlier and here we only show the results obtained via nondestructive population measurement.

The measurement is done in two regimes of loading the dipole trap from the MOT. First, atoms from the MOT are loaded in the FORT by increasing the magnetic field as shown in Fig.7.1. We will refer to this regime as compression regime. Second atoms are loaded in the FORT using molasses cooling. This means that the magnetic field is switched off during the loading stage. This way the density of the atomic sample is reduced due to expansion of the cloud during the molasses. We will refer to this regime of loading as molasses regime. The corresponding results from these two loading schemes are presented in Fig.9.6, where the number of atoms is plotted against the loading stage duration. The conditions at which the two measurements are done are described below.

For the first measurement, presented in Fig.9.6(a), the magnetic field gradient is increased from 10 to 12 G/cm, during the dipole trap loading stages as also shown in Ch.7, Fig.7.1, and is rapidly decreased to zero for 100 μs [101] at the end of the loading stages. Next, after a delay stage of 100 ms the atomic sample is probed by 10 light pulses, 2 μs long and with 40 μs repetition period. The power per pulse is 300 nW, and the detuning of the probe light is $\Delta_{45} = 100$ MHz with respect to the cycling transition. The reference measurement is taken 25 ms after with the same probe pulse parameters.

The second measurement referred to as a molasses regime [Fig.9.6(b)] is performed as follows. The loading is done as shown in Ch.7, Fig.7.1, but this time the field gradient is adiabatically reduced to zero during the entire first loading stage and the cooler detuning

Parameter	Compression	Molasses regime	With light	Without light
R_0 [Hz]	1.34×10^7	$3.2(6) \times 10^4$	-	-
γ_{MOT} [Hz]	831	5	-	-
Γ_L [Hz]	3.5	1.2	47(20)	-
β_L [Hz]	1.1×10^{-4}	$3(1) \times 10^{-5}$	$1.1(1) \times 10^{-2}$	-
Γ [Hz]	-	-	-	21(1)
β [Hz]	-	-	-	$2.3(2) \times 10^{-4}$

Table 9.1: Loading and loss parameters of the dipole trap

is only decreased to -6.5γ. Again, after a storage time in the dipole trap for 100 ms the atoms are probed by 10 light pulses with 2 μs duration and in this case 10 μs repetition period. The power and detuning are the same as in the compression regime and the reference measurement comes after 25 ms, with the same probe light parameters.

For each point in Fig.9.6 we have repeated the loading cycle 20 times, and taken the average over the obtained values for the number of atoms.

Since the general solution of Eq.(7.4) is expressed with Bessel functions, which makes very difficult and time consuming the fitting of the experimental data on an ordinary PC, we have adopted the method of separating the loading process to two parts: initial loading during which the MOT loses atoms exponentially and subsequent loss mechanism caused by collisions and decay due to cooling light. In this way for short times we fit to a solution of the differential equation which includes only the first term on the right-hand-side of Eq.(7.4), and for longer times we fit to a solution of the Eq.(7.5). We must emphasize here that in this case Eq.(7.5) will actually give the value of light dependent losses. The results from the two measurements are compared in the following Table.9.1

We see that in the case of compression loading is faster due to the magnetic field gradient, or in other words the MOT does not expand, which helps atoms to be transferred to the FORT faster. However the density dependent loss-mechanism is a main trap loss source compared to the molasses regime where the β_L coefficient is around 30 times lower. The difference between the Γ_L loss coefficients in both cases is not significant since they do not depend on the atomic density, but mainly on the background gas pressure.

As it was discussed earlier in the Ch.7 the losses during loading are different in presence of MOT light. To study the light induced losses independently from the loading rate we use the method suggested in [61] and described in Ch.7. After a 10 ms storage in the dipole trap we switch on the MOT beams with total intensity of the cooling laser of 4.6 mW/cm^2, detuning of -8γ and repump laser intensity of 1.1 mW/cm^2 on resonance for a certain time. Next, the MOT light is switched off again and 10 probe light pulses of 2μs duration and repetition period of 40μs are applied. In Fig.9.7 we plot the average number of atoms over 30 loading cycles as a function of the delay time i.e. the time for which the MOT light is applied.

The losses in presence of light are compared to the losses without any MOT light in Table 9.1. It can be clearly seen that the light induced density dependent loss increases by factor of roughly 50 in the case of large detuning -8γ, which tells us that the FORT undergoes severe loss through multiple scattering. At the same time the linear loss coefficient stays almost the same as expected since it depends on the background pressure. We must also note that the values of Γ in the third and fourth columns are measured at a higher background gas pressure.

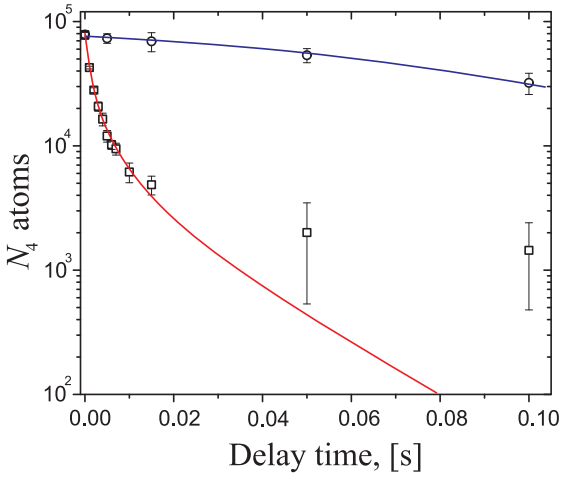

Figure 9.7: *Loss curves of FORT. With MOT light on:* (□). *Without any MOT light* (○).

9.3.2 Oscillation frequency

In this section we present a non-destructive measurement of the trap radial oscillation frequency. We adopt a different measurement technique and demonstrate that the interferometric characterization can give information about important parameters of FORT in an measurement procedure which is significantly less time consuming than the conventional methods [59, 68]. The nondestructive monitoring of the atomic sample under different perturbations allows to explore phenomena which take place on a microsecond timescale.

We induce radial oscillation in the FORT by switching off the Yb:YAG laser for 500μs. Then the atoms in the trap start to oscillate with a frequency which is twice the radial oscillation frequency. These oscillations are damped following an exponential law. We track the radial "breathing" mode of the FORT cloud by sending a long pulse train of 100 pulses with 2μs duration, 100μs repetition period and power of 150 nW.

The result is shown in Fig.9.8(a). We must emphasize here that the measurement can be done in only one measurement cycle since the atomic sample is not destroyed after the measurement. The curve in the upper graph in Fig.9.8(a) is a result of a single measurement cycle and every point represents the phaseshift obtain by the interaction of the oscillating atoms with each probe pulse from the pulse train. The lower graph is an average of the 50 cycles and is less influenced by the shot-to-shot fluctuations. For the two graphs we also take a reference measurement without inducing radial oscillations in order to account for the possible depumping due to probe light. The deduced oscillation frequencies from the damped sinusoidal fits are 454(5) Hz and 453(3)Hz for the single and averaged traces, respectively. The exponential damping time constant of the oscillations is 1.76(9) ms and 1.87(7) ms for the upper and lower traces respectively. We see that the fit values are similar which indicates that the single run measurement is little influenced by the shot-to-shot fluctuations.

The above measurement was also performed for several different values of the dipole beam power. The result is plotted in Fig.9.8(b), for a single run measurements (upper graph) and for multiple cycles measurement. The estimated dipole beam waist radius, using Eq.(3.36), is almost 2.25 times bigger as expected one of 40μm, and is similar for both measurement cases. The expected dipole beam radius 40μm is calculated taking into

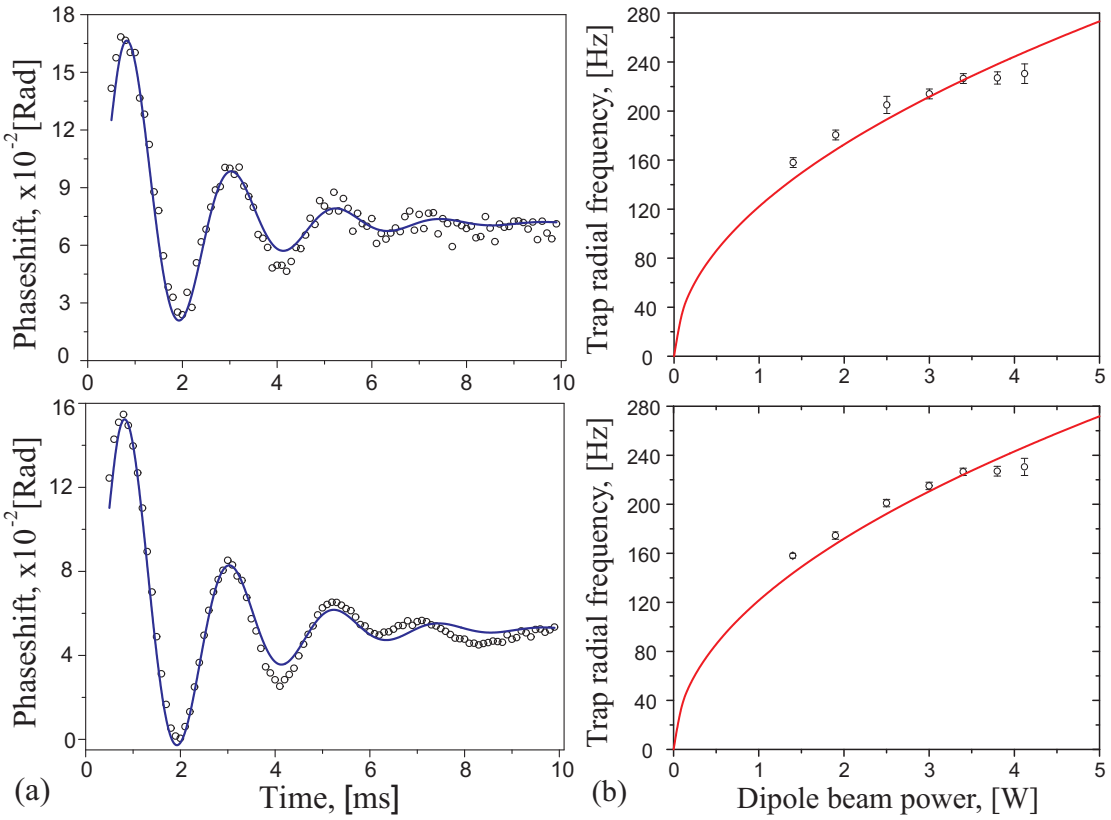

Figure 9.8: *(a). Oscillation in the trap after its revival by switching the dipole trap laser again after 500 μs release. The period of the damped oscillations corresponds to oscillation frequency of* 453(3) Hz. *The upper curve is a single experimental trace from one measurement, the lower curve represents a 50 times average from 50 independent loading cycles. Dipole beam power of* 1.4W. *The damping constant of the oscillation is* 536(20)Hz. *(b). Trap radial oscillation frequency as a function of dipole beam power for a single run case (upper) and 50 times averaged (lower). The estimated from this fit waist of dipole trap beam is* 90(1)μm.

account the experimentally obtained divergency of the incoming beam and beam quality factor of $M^2 = 1.34$. Then the experimentally obtained value for the dipole potential depth is reduced by a factor of 2.25^2 for a dipole power of 3.5 W. The rescaled value of the potential becomes $U_{exp} = 75$ μK.

For cold enough atoms the induced oscillation are of the center of mass motion, which in fact will give the right scaling. However, for an initial atomic temperature of the order of $14\mu K$ the ballistic expansion of the cloud for 500μs is roughly $14\mu m$ in horizontal, and about $15\mu m$ in the vertical direction. This indicates that the gravity has a little influence on the measured frequency. Since the gravity is the only way the cloud can acquire velocity component of the center of mass motion, it is evident that the observed oscillations cannot be attributed to the "sloshing" mode.

The observed discrepancy of a factor of two is probably due to the wrong estimate of the dipole beam waist since the laser beam is not entirely gaussian.

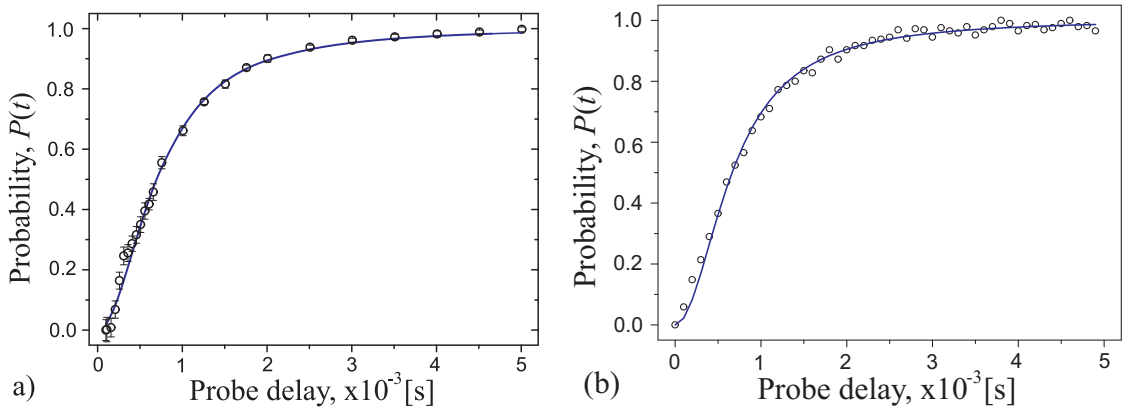

Figure 9.9: *Ballistic expansion of the released atomic cloud. Data from multiple measurement runs gives* T = 14.5(2) μK, *and* $\nu_r = 259(4)$ Hz *for temperature and radial oscillation frequency at probe power of* 300 nW *(a). Data from single run and continuous pulse train of 50 pulses* 100μs *apart with probe power of* 150 nW *gives* T = 15(2) μK, *and* $\nu_r = 275(4)$ Hz, *respectively (b).*

9.3.3 Temperature

This subsection is devoted to our measurement of atoms temperature using the interferometer phase shift. Initially the atoms are stored in the dipole trap having all MOT light and magnetic fields switched off. Then they are released by switching off the dipole laser. The atomic cloud starts to expand ballistically under gravity influence and the atoms will acquire velocity proportional to their temperature. Then after a variable time delay the cloud is probed during free expansion using optical pulses.

The measured atomic phase shift can be used to find out how great is the fraction of atoms that have left the probe beam volume after a given time. In other words, we can measure the probability $P(t)$ of an atom initially inside the probe volume, to be outside it after a certain time t. We derive a simple model for estimation of the temperature using the ballistic expansion of the atomic cloud [see Appendix E]. The model describes the evolution of $P(t)$ as a function of the time of flight and is similar to already known time-of-flight technique [38, 109].

After 50 ms storage the atoms are released and two pulse trains are applied. The first pulse train is delayed by time t from the atom release. The reference pulse train is applied 25 ms after the probing. Each pulse train consists of 10 probe pulses with repetition period of 10μs. The results are plotted in Fig.9.9(a) along with the fits to the experimental data. The fit to the data is done by using an approximate expression for the probability function which has the following form:

$$P(t) = 1 - \frac{w_0^2 + 4\sigma_{r,0}^2}{w_0^2 + 4\sigma_r(t)^2} \exp\left\{-\frac{(gt^2)^2}{2[w_0^2 + 4\sigma_r(t)^2]}\right\}, \tag{9.11}$$

where $w_0 = 20\mu$m is the probe beam waist radius, $\sigma_r(t) = \sqrt{\sigma_{r,0}^2 + \sigma_v^2 t^2}$ is the radius of atomic sample as a function of time with $\sigma_{r,0} = \sqrt{k_B T/(M\omega_r^2)}$ and $\sigma_v = \sqrt{k_B T/M}$ being the initial radial extension of the atomic cloud and the initial atom velocity, respec-

	$T[\mu\text{K}]$	ν_r[Hz]	P_p[nW]	Δ_{45}[MHz]	$\tau_p[\mu\text{s}]$	$T_{rep}[\mu\text{s}]$	Pulses	Averages
(a)	14.5(2)	259(4)	300	100	2	10	10	20
(b)	15(2)	275(4)	150	100	2	50	100	1

Table 9.2: Temperature of dipole trapped atoms

tively, which depend on the temperature T, Boltzman's constant k_B, angular radial trap frequency ω_r and atomic mass of ^{133}Cs.

The data for short delay times of the probe pulses is scattered and has some oscillation behavior. The model function Eq.(9.11) fits better in the wing of the ballistic expansion and the obtained parameters from the fit give temperature of T = 14.5(2) μK for an oscillation frequency of $\nu_{\text{r}} = 259(4)$ Hz. The estimated value of the radial oscillation frequency is in a good agreement with the previously obtained value of 244 Hz [Fig.9.8(b)] for a power of dipole laser of approximately 4 W. Each point in Fig.9.9(a) is a result of 20 averages and the error bars come from the shot-to-shot fluctuations in the loaded atom number in the dipole trap.

In another measurement we send a long pulse train through the atomic sample once the atoms are released from the FORT. The pulse train contains 50 pulses with duration of 2μs and repetition period of 100μs. The probe power is 150 nW. Hence, each point on the graph in Fig.9.9(b) is a result of the phase shift recorded by a single pulse.

A single measurement trace of that kind represents a ballistic expansion besides free from shot-to-shot fluctuations in the atom number. We also take a reference measurement while the dipole trap operates and subtract it from the ballistic data in order to correct for eventual decay due to probe light depumping. The estimated relative decay of the detected signal due to probe light depumping is found to be around 3.5%. A more detailed analysis of the depumping mechanism will be presented in the next section.

We see that the obtained results for temperature T = 15(2) μK and oscillation frequency $\nu_{\text{r}} = 275(4)$ Hz are also in reasonable agreement with the ones obtained by the multiple runs method. The data from the to measurements is listed in Table 9.2. The (a) and (b) rows of the table concern the graphs in Fig.9.9(a) and (b), respectively. The obtained values compared with the temperature estimated from the fluorescence measurement in Ch.7, Fig.7.5 of T = 14(2) μK shows a very good agreement. The fit of the fluorescence measurement does not take into account the gravity influence and agrees well with the non-destructive measurements which do include the gravity. This is another confirmation that the gravity does not play a significant role on a timescale similar to the the traverse time i.e. the time it takes for an atom to cross the probe beam.

9.3.4 Density and number of atoms

In this section we give an estimation of the maximum number of atoms in the dipole trap and the corresponding density at conditions of thermal equilibrium.

At thermal equilibrium the radius of the dipole trapped sample is estimated from the measurement of the oscillation frequencies to be around $w_{eq} = 20.8$ μm [see Ch.7, Sec.7.3]. In the dipole trap interferometric measurements presented in this thesis, the probing of the atoms is done after several tens of milliseconds storage in the dipole trap (except the loading rate measurements), which ensures that the sample is at thermal equilibrium. Then its radial extent $w_a = w_{eq}$, matches the probe beam size of 20 μm. In that way the geometrical factors defined in Ch.5, Eq.(5.23,5.24) are calculated to be $g_L = 0.76$ and

$g_T = 0.5$ for the longitudinal and transverse factors, respectively. The last two modify the coherently scattered power by a factor of $g_L g_T = 0.38$. In the following lines we will use the above considerations to estimate the density and number of atoms in the trap.

As we have already shown in Ch.2.3 and Ch.5 the atomic phaseshift ϕ_0 and interaction strength κ^2 depend on the atomic density. In the case of a MOT the estimated density is of the order of 10^9 cm^{-3}. Loading the atoms in the dipole trap increases the density and improves the matching to the focused probe due to the elongated geometry of the atomic sample. The typical maximum phaseshift measured on a daily bases at a detuning of 100 MHz from the cycling transition is around 1 Rad. Then using the Eq.(2.51) for the case when we measure only the population of $F = 4$ ground state, we calculate the maximum phaseshift ϕ_0 and then insert it in Eq.(2.47). For a sample length of 1.25 mm as deduced form the fit in Fig.7.3, and correcting for $g_L g_T$ we get a number density of $\mathcal{N} = 3 \times 10^{11}$ cm^{-3}. The last result is almost 100 times higher than the density in the MOT.

For the number of atoms we need to calculate the volume of the atomic cloud using the equilibrium sample size w_{eq} and sample length l. The volume is $V = \frac{\pi w_{eq}^2}{2} l = 8 \times 10^{-6}$ cm^{-3} and the number of atoms $N_4 = 2.4 \times 10^5$.

9.3.5 Rate of real transitions

The last issue that we want to address is the problem of depumping due to absorption of probe light photons. The absorption is a process working parallel to the dispersive interaction. Absorption of photons induces heating of the atoms in the trap and can lead to atom loss. This on the other hand reduces the atomic phase shift. When we claim to perform a nondestructive measurement we must estimate the probability of atom to undergo a real transition due to absorption of photon.

We have already introduced the pulse-integrated rate of spontaneous emission η_Δ [see Ch.5.1] as a relevant parameter to describe the depumping due to probe excitations in the off-resonant case. However, in the experiment the probe light detuning is only 100 MHz with respect to the cycling transition. Thus, an excitation to the weakly coupled $F' = 4$ excited state would pump the atoms to the lower hyperfine ground state level via spontaneous emission. For the η parameter we can write [11]:

$$\eta_\Delta = \frac{\lambda^2}{3\pi A} \mathcal{L}_\Delta n_{ph} \tag{9.12}$$

where $\mathcal{L}_\Delta$ is a linewidth function which can be derived using Eq.(2.43). The linewidth function has the usual $1/\Delta^2$ dependance of the absorption in Eq.(2.43) on the probe beam detuning. For a probe light near to the cycling transition the value of this function is:

$$\mathcal{L}_\Delta = \sum_{F'=3}^{5} S_{4F'} \frac{\left(\frac{\gamma}{2}\right)^2}{\Delta_{4F'}^2 + \left(\frac{\gamma}{2}\right)^2} \tag{9.13}$$

The pulse integrated rate of excitations is independent on the atom number but is a function of the number of photons in the probe beam n_{ph}. The next few paragraphs we present an experimental method for estimation of η_Δ when the probe light is 100 MHz detuned from the cycling $6S_{1/2}(F = 4) \rightarrow 6P_{3/2}(F' = 5)$ transition. Since the depumping parameter is proportional to the number of photons we would naturally expect that it will change in accordance with the power of our probing beam. Hence, we choose to monitor

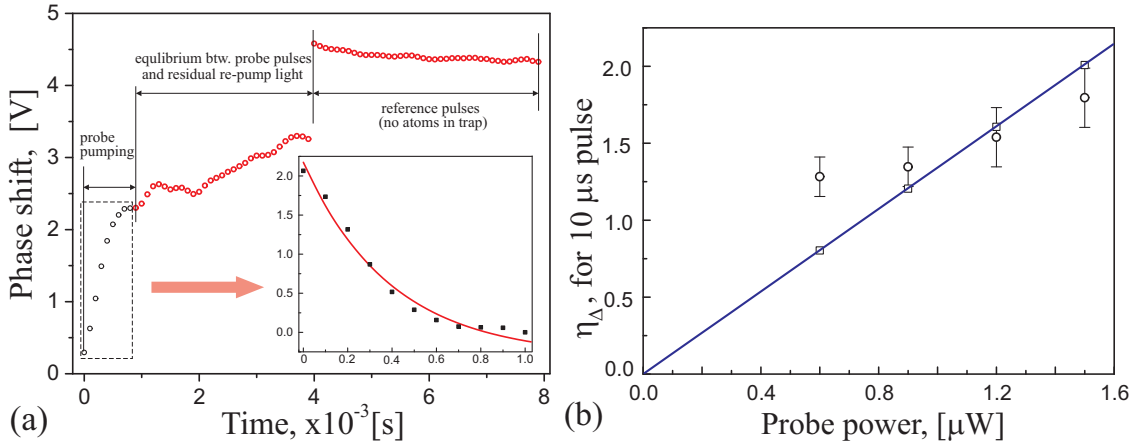

Figure 9.10: *Pulse integrated rate of spontaneous emission. Raw data for probe power of* 1.2μW *and a fit to the selected depumping part (the inset)(a), and experimentally obtained value for the* p_e *parameter as a function of the probe power for a* 10μs *long probe pulses: values of* η_Δ *for different power obtained from the fit of the phase shift decay (*$\circ$*), theoretically calculated values for a probe beam waist radius of* 21.2μm *(*$\square$*), and a linear fit to the data (solid line) (b).*

the decay of the interferometer phase shift as a function of the probe power. The direct experimental parameter is the characteristic time constant of that decay and we expect that it will increase linearly with the probe power.

We send a long pulse train consisting of 40 pulses of 10μs duration and 100μs repetition period through the atomic sample along with the usual reference pulse train. The measurement is done at four different power levels of the probe beam. The blue detuning is set to 100 MHz.

An example measurement trace for probe power of 1.2μW is shown in Fig.9.10(a). The initial decay during a period of 1 ms is caused by the probe light depumping. It is then followed by an approximately flat region which is a result from an equilibrium between probe depumping and repumping process due to residual light of the MOT repump laser. The last 4 ms from the raw data presented is a reference level without atoms in the dipole trap.

The interesting for us part of the trace is the first one since it contains the depumping due to probe light. The inset in Fig.9.10 shows a fit to the solution of the rate equations described in Appendix F. The value of η_Δ for a given power of the probe is obtained by fitting the initial decay of the phase shift to an expression obtained from integration of the rate equations for the levels of concern taking into account two optical fields: probe and repump laser [see Appendix F]. Then the values of the η_Δ are plotted against the probe power and fitted to a straight line Fig.9.10(b). An additional theoretically calculated values of η_Δ using Eq.(9.12) and Eq.(9.13) for a probe waist radius of 21.2 μm agrees well with the experimentally measured waist radius of 20 μm. We see that for very low probe power the pulse integrated rate of spontaneous emission per atom is less than one. The lowest power used in our experiment is 150 nW, in a pulse with duration of 2 μs. This would mean that the lowest photon scattering rate per atom in our experiment is of the order of $\eta_\Delta = 0.038$.

9.3.6 Noise of dipole trapped atoms

In this section we present measurements of the atomic population noise done with atoms prepared in a dipole trap. To study the nature of atomic noise we need to find how the latter is changing as a function of the atom number. For the MOT measurements described in Sec.9.2.4 we change the number of atoms by changing the dispenser current. The same procedure can also be applied in the case of dipole trap which in fact uses the MOT as an atomic reservoir. However, it turned out that after a several months of operation of the MOT the above described method was no longer a reliable one due to the formation of low pressure Cs background vapor. Then a different technique was adopted. The number of atoms was changed by varying the time delay before they are probed.

In the experiment the probe laser is close to the $F = 4 \rightarrow F = 5$ transition at a blue detuning of 100 MHz. Using 2 μs long pulses of 0.6 μW power, this yields, according to Eq.(9.12) a pulse integrated rate of atomic transitions of $\eta = 0.4$. This number has been verified experimentally by monitoring the de-pumping of the $F = 4$ to the $F = 3$ ground state through the weakly coupled[1] $F = 4 \rightarrow F' = 4$ transition in a measurement described in the previous section. The value deduced is $\eta = 0.33$. With the photon flux of 2.5×10^6, every atom performs about 43 absorption cycles on resonance in the center of the probing volume, whereby the largest possible recoil velocity of an atom will be approximately 15cm/s. In this extreme case the atom would move 1.5μm during 10μs, which is well in the range of the probing beam waist radius of approximately 20μm.

The measurement of the atomic population fluctuations can be performed on an independently prepared atomic samples or on a single atomic sample. We refer to independent samples the ones prepared in consecutive loading cycles when the loading and probing conditions are the same. The number of atoms in samples prepared in consecutive loading cycles are uncorrelated, and so the fluctuation of this number. Then population noise will scale linearly with the number of atoms as already discussed in Sec.4.2. Since our probe light is closer to the cycling transition, as in the case of MOT measurements, the atom number fluctuations are expected to scale linearly with the population of $F = 4$ ground state level, namely N_4.

When the noise measurement is performed on a single atomic sample we expect that the phase shift measured by consecutive pulses would contain both uncorrelated and correlated fluctuations. We will get back to it further in the discussion.

Let us start with the first type of measurement. The procedure is as follows: We send a probe pulse through the atomic sample and obtain a pulse area a_1, then after 10ms a reference measurement a_2 is taken. The reason to take a reference phase measurement in each loading cycle, is that over the 3-4s of a full cycle the interferometer may drift significantly, or in other words the light noise could no longer be white noise. The atomic phase shift is then computed as $\phi_\Delta = arcsin(a_1 - a_2)/a_+$, where a_+ is the pulse area corresponding to a $\pi/2$ phase shift (i.e. the fringe amplitude in units of integrated photocurrent). The calculation of the phase shift is basically done using the expressions Eq.(9.1) for the difference between the two pulse areas $a_1 - a_2$ in voltage units.

The areas of the two pulses are uncorrelated, hence in a sequence of many repeated measurements the variance of their difference is the sum of the variances of each pulse. The variance of the first pulse $(\delta a_1)^2$ contains noise of dipole trapped atoms and shot noise. In Sec.4.2 we saw how the classical phase and amplitude noise can be overcomed, hence the only noise contributions to the atomic signal are the photon shot noise and

[1] the probe is detuned by 351MHz from this transition.

electronic noise. The variance of the second pulse only consists of a shot and electronic noise. Then the variance of their difference is expressed as

$$(\delta\{a_1 - a_2\})^2 = 2(\delta i)^2_{SN} + \left(2\frac{\varepsilon e}{\tau_p} T\langle\hat{n}\rangle \cos\phi_\Delta\right)^2 (\delta\phi_\Delta)^2. \tag{9.14}$$

In the last equation the second term is the atomic noise given by Eq.(4.35) with the $\sin\phi$ simplified as $\sin(\phi_N + \phi_\Delta) = \sin(\pi/2 + \phi_\Delta) = \cos\phi_\Delta$ by the use of the phaseshift ϕ in Eq.(4.13). To extract the atomic contribution to the noise, we need to measure the shot noise independently, which is done by taking a measurement without atoms in any of the pulses. Then the noise of this reference measurement becomes $(\delta\{a_1 - a_2\})^2_{SN} = 2(\delta i)^2_{SN}$. Further the atomic noise is calculated by subtracting the last from from Eq.(9.14):

$$(\delta\phi_\Delta)^2 = \frac{(\delta\{a_1 - a_2\})^2 - (\delta\{a_1 - a_2\})^2_{SN}}{\left(2\frac{\varepsilon e}{\tau_p} T\langle\hat{n}\rangle\right)^2 \cos^2(\phi_\Delta)} \ , \tag{9.15}$$

The result of the measurement on independent samples is shown in Fig.9.11(a). The number of atoms is varied by changing the storage time in the dipole trap. The atomic contribution to the phase noise of the interferometer $(\delta\phi_\Delta)^2$ is translated into population fluctuations and is plotted as a function of the number of atoms extracted from the DC-phase shift ϕ_Δ. The linear fit within the uncertainty shows that the variance of the atomic fluctuations scales as N_{at}. Thus the white light interferometry is capable of achieving the sensitivity approaching the level of projection noise fluctuations.

The second measurement type, as mentioned above, is to make consecutive measurements of the same dipole trapped sample to see how the population of $F = 4$ fluctuates from pulse to pulse. This would mean that the noise is characterized by the 2-sample variance on a different timescales. The two point variance in Eq.(8.6) is essentially the mean value of the squared pulse differences i.e. $\sigma_{2p} = \langle(a_{i+k} - a_i)^2\rangle$ [2]. Assuming that there is no average difference between the pulses involved i.e. $\langle a_{i+1} - a_i\rangle = 0$, which is true if the fluctuations are truly randomly distributed around zero, then we can re-write

$$\sigma_{2p} = \langle(a_{i+1} - a_i - \langle a_{i+1} - a_i\rangle)^2\rangle = (\delta a_i)^2 + (\delta a_{i+1})^2 - 2(\delta a_i a_{i+1}) \tag{9.16}$$

In this form it becomes simpler to identify the contributions to the noise. The pulse variances in the two first terms are the same since the number of atom does not change much in 10μs. The term $(\delta a_i a_{i+1}) = \langle a_i a_{i+1}\rangle - \langle a_i\rangle\langle a_{i+1}\rangle$ is the covariance of the two pulses and measures the correlation between them. If there is no correlation then the covariance will be zero. However, if the pulses are correlated the last term would have positive or negative value.

The measurement consists of two pulse trains 20ms apart and each containing 10 pulses, which are 2μs long and separated by 10μs. The first pulse train probes the dipole trapped atoms, then and the second pulse train is taken as a reference, to extract the atomic phase shift and thus the number of atoms. A special feature is that the dipole trap laser is switched off right before probing the atoms. Hence, during the first pulse train the atomic sample begins to expand.

As for the first type of measurement, the contributions to the variance are given by the non-vanishing terms of Eq.(4.42). Hence by subtracting the 2-point variance of the

[2]The index in the mean value is to be understood as $\langle a_{i+k}\rangle = \sum_{i=0}^{M-k} a_i \approx \sum_{i=k}^{M} a_i$.

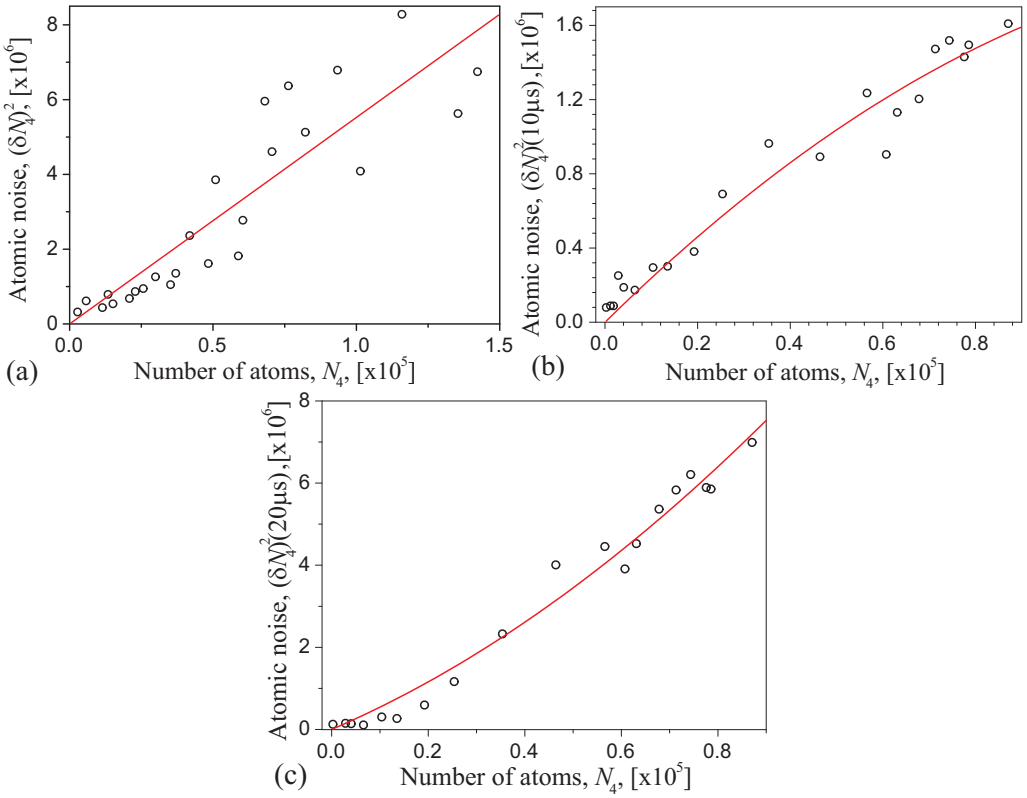

Figure 9.11: *Phase noise induced in the probe light from the interaction with cold atoms. The density is derived from the dc phase-shift. (a) The linear fit (—) of the experimental data (○), shows poissonian statistics of the loading process. (b), (c) Atomic two point variance on 10 μs and 20 μs timescale, respectively. The fit (—) of the experimental data (○) to* $(\delta N_4)^2 = a_i N_4 + b_i N_4^2,\ i = 10, 20,\ a_{10} = 25 \pm 3$ and $b_{10} = -(8 \pm 4) \times 10^{-5}$, and $a_{20} = 51 \pm 9$ and $b_{20} = -(4 \pm 1) \times 10^{-4}$, *for the case of (b) and (c), respectively, shows correlations between consecutive pulses.*

reference pulse train from that of the first "atom probing" pulse train we get the 2-point variance caused by atomic population fluctuations. As for the correlations, the pulses of reference train are uncorrelated since they are affected purely by quantum light noise. In the presence of atoms it is natural to expect that if the pulses are not far separated, then the number of atoms will not have changed much between them. In essence, the probe pulses interact with the same atoms. This way the measured fraction of atoms does not contribute to the noise but only to the phaseshift since after the interaction with the first pulse their state will be well known. As a result only the fraction of atoms which have not been measured will contribute to the noise.

The experimental results in Fig. 9.11(b), shows the two point variance for pulses separated by 10μs. The points for different number of atoms are obtained by varying the probe light delay while atoms are released from the trap. We see that the 2-point variance does not grow linearly with the atom number N_4. Fitting a second order polynomial with no 0'th order term, we extract the linear and the quadratic term of the scaling. Given the quality of the fit we conclude that we see the signature of correlations between the pulses.

We can also plot the 2-point variance for 20μs pulse separation [Fig.9.11(c)], where we see that the correlation term becomes negative, so that the 2-point variance grows faster

than a linear curve. This is not surprising since the atoms are being released from the dipole trap, and thus the density is decaying rather fast. Therefore, given the pulse area a_i it is most likely that the pulse area a_{i+1} will be smaller, i.e. the two areas are anti-correlated or the covariance $\delta a_i a_{i+1}$ becomes negative. Strictly speaking, the assumption that $\langle a_{i+1} - a_i \rangle = 0$ breaks down, but the considerations still help illustrate what happens.

From the above we conclude that our apparatus has measured the statistical trapping fluctuations, and has been able to detect correlations in the atomic number density from one pulse to the other.

9.4 Conclusion

With the above described measurements the experimental part of the current thesis comes to its end. It can be summarized in the following lines.

First, a shot noise limited Mach-Zehnder interferometer was built and characterized using a balanced homodyne detection technique. The white light alignment of the interferometer allows for efficient laser phase noise cancelation. The interferometer is locked to an off-resonant interference fringe in order to avoid thermal and acoustic drifts. The fiber optic interferometer showed better performance in terms of resistivity to acoustic and mechanical vibrations, whereas the free-space one is shot noise limited for a photon number as high as 2×10^8 for the phase and 2×10^9 amplitude quadrature.

We have also demonstrated a method for nondestructive characterization of cold atomic samples prepared in an optical dipole trap and MOT. The atomic sample is placed in one of the arms of the Mach-Zehnder interferometer. The phase shift of the light imposed by dispersive interaction with atoms is detected via a pulsed balanced homodyne detection scheme. This phase shift is proportional to the population of the level in concern.

The measured parameters of the MOT are in reasonable agreement with the ones performed using fluorescence detection. The MOT at Aarhus and NBI experiment are found to have almost the same atom number density which is expected since the trap geometry was preserved. The loading time of the second generation MOT is longer owing to the lower background pressure achieved.

The dipole trap is loaded from a MOT through a molasses cooling stage. The number of atoms trapped is around 10^5 which corresponds to around a 1 Rad of phase shift and a number density of the order of $10^{11}\mathrm{cm}^{-3}$. We have measured several parameters of the dipole trap characterizing its loading and loss dynamics. The radial oscillation frequencies and temperature measurements were done in a single loading run, thus enabling us for fast characterization of atomic sample. The temperature estimated from both single and multiple runs nondestructive measurements agrees with the one obtained in the fluorescence measurement. The trap radial oscillation frequency is measured directly by the release-recapture method, and indirectly by estimation from temperature measurements data. Both values are in a good agreement. Furthermore an estimation of the nondestructive character of the measurement was done by measuring the pulse integrated rate of real transitions tracking the decay of the phase shift of dipole trapped atoms at different probe power levels. The estimated rate of real transitions induced by a single probe pulse is found to be as low as $\eta_\Delta = 0.038$.

The real time monitoring of the phase shift in a Mach-Zehnder interferometer allows for fast and nondestructive characterization of atomic samples. The method is applied to a dipole trapped atomic sample but with the same success it can be expanded to Bose-Einstein condensates, where the optical density is much higher and the absorption imaging

does not give the necessary contrast [124]. Moreover, our pulsed detection scheme allows for microsecond timescale monitoring of processes and phenomena taking place in the atomic cloud, which in other cases as absorption or fluorescence imaging are not visible due to the requirement of long exposure time of the CCD cameras.

Chapter 10

Summary and Outlook

At the end of this thesis we will summarize the experimental work done on characterization of atomic samples using a shot noise limited interferometer. In the second part of the chapter we briefly discuss the concept of QND measurement via off-resonant interaction - the near future application of the built interferometric setup. The feature of the QND measurement to act as a quantum state preparation device is pointed out as a tool to produce a squeezed state of the population number difference in the Cs microwave clock.

10.1 Summary

In this work we have built an experimental setup that is able to characterize non-destructively various parameters of an cold atomic sample prepared in a MOT and subsequently trapped in a far-off-resonant optical dipole trap. The measurement is done via monitoring of the phase of a weak light probe interacting with the atomic sample placed in one of the arms of a Mach-Zehnder interferometer. The light is detuned by several tens of natural linewidths from the cycling atomic transition $6S_{1/2}(F = 4) \rightarrow 6P_{3/2}(F' = 5)$ in Caesium and detected in a pulsed homodyne detection scheme involving the two output ports of the interferometer.

The different noise contributions to the obtained homodyne signal are investigated. The main contribution are divided in two: quantum noise and classical noise. The first is the shot-noise of the probe light. The second is the classical noise, which consists of amplitude noise of the detection and classical phase noise that comes from the excess phase noise of diode lasers. The quantum noise of the probe is a fundamental noise limit in our interferometric measurement. The classical amplitude noise, although very small in the case of semiconductor laser, is canceled by the balanced detection. The phase noise of diode laser is found to depend on the optical path-length difference between the interferometer arms. Thus aligning the interferometer in the white-light position, overcomes the influence of the excess phase noise over the experimental signal. In practice the white light alignment is limited in the coherence length of the white light source. To keep the the interferometer in white-light position and to be sensitive to small phase shifts the interferometer is locked in a quadrature, using the interference of an additional off-resonant laser, and a piezo actuator.

Two different interferometric designs have been used. The fiber-optic and free-space construction. The first one showed better mechanical and acoustic stability, as well as good mode overlap in the fibers, but difficulties in balancing the photocurrents from the

two arms has appeared due to the temperature dependent chromatic dispersion of the single mode fibers. Moreover an additional losses in fiber-free-space-fiber coupling interface reduced the photon flux to about 30% of its initial value in the air gap of the probe arm. The free space interferometric setup showed much better balance and losses from the coupling were greatly reduced. However, the free-space interferometer had poor stability to acoustic and mechanical vibration, which forced us to use shielding of the interferometer using a construction with sound damping material.

The noise properties of both free-space and fiber-optic interferometer were checked, making a measurement of the fluctuations in the detected homodyne photocurrent, at different input photon fluxes and found linear dependance of the former with the photon number - a signature of shot-noise limited operation. The interferometers were found to be shot noise limited in amplitude and phase up to 4×10^8 photons for the free-space and 10^7 for the fiber-optic construction.

In this work we used two different constructions of magneto-optical trap for initial preparation of the atomic sample. The first generation trap, the AU MOT, was loaded in a titanium chamber, and the second one, the NBI MOT in a quartz cell. The AU MOT had better aligned beams, however the problems with home-made Ti-viewports did not allow for better than 10^{-7}mbar vacuum. An additional difficulty was connected with the low efficiency transport of Cs atoms from their container to the experimental chamber. The NBI MOT is loaded in a quartz cell and has very compact design allowing for lower gas load, due to the smaller inner surface of the vacuum apparatus. The lowest pressure achieved is of the order of 10^{-9}Torr reflecting in longer lifetime.

The first generation MOT was investigated using destructive fluorescence collection method and non-destructive interferometric measurement of the atomic population, taking advantage on the cycling transition in Cs. The number of atoms collected in the MOT was of the order of 10^8 with a number density of 10^9cm^{-3}. The performed interferometric measurement of the population noise of $F = 4$ in a multiple loading cycles scaled linearly with the population itself as expected from the stochastic nature of the loading process. A release and recapture measurement, done by fluorescence detection of the remained fraction of the atoms in the MOT after free flight of variable time, showed temperature of 417 ± 49 μK. The nondestructive measurement of the loading-to-loading population fluctuations showed linear dependence with the number of atoms as theoretically predicted.

The second generation MOT was non-destructively characterized using the free-space interferometer. The density of the MOT was extracted by measuring the Stark-Shift induced by the MOT light during the probing of the atomic cloud. The noise of the atomic population of $F = 4$ was also measured in consecutive loading cycles and is found to have a power dependance on the atom number with a coefficient of 1.5. The linear scaling of the atomic noise with the number of atoms is a signature of population noise.

The atoms prepared in the second generation MOT were loaded in a far-off-resonant dipole trap made by a single focused gaussian laser beam. The trap was loaded through an optical molasses stage in two ways - with magnetic field on to maintain the MOT density during loading and with a magnetic field adiabatically switched off.

The loading dynamics in these two cases was monitored by measuring the phase shift of weak light beam imposed by interaction with the atomic sample at a detuning of 100 MHz. The loading and loss coefficients are experimentally obtained for two cases: in presence of MOT light i.e. light induced losses and without any light i.e. light independent losses. We found that the density dependent light losses are dependent on the MOT light parameters as expected. The linear losses are mainly determined by the background gas pressure.

A measurement of the radial oscillation frequency was done by releasing the atoms from the dipole trap for a short time and probing the induced density oscillation using a long train of weak light pulses. The measurement is much faster than the standard oscillation frequency measurement, since it is done in a single loading cycle in contrast with the fluorescence collection and absorption imaging techniques.

We have also performed a measurement of the trapped atoms temperature by probing the density of the expanding atomic cloud when released from the dipole trap for a variable delay of the probe light pulses. The measurement was done in two ways, for a multiple loading cycles and for a single cycle. The two methods showed reasonable agreement with a similar fluorescence measurement and the temperature found was of the order of 14μK. The single run measurement allows for fast and non-destructive determination of the atom temperature as an advantage over the common destructive fluorescence and absorption techniques.

The non-destructive nature of the off-resonant probing was independently checked by performing a measurement of the pulse integrated rate of spontaneous emission. The last was estimated to be as low as 0.038 for a single probe pulse. This rate of real transitions allows for detection of a phase change as small as 0.002 Rad.

The measurement, presented in this thesis, to our knowledge, is the first implementation of interferometric non-destructive characterization of cold and trapped atomic samples with a sensitivity limited only by the fundamental quantum noise of the optical probe. We have also shown that the described interferometric technique has the necessary sensitivity to measure atomic projection noise. The last is known to scale linearly with the atom number.

10.2 Outlook

In this chapter we discuss the two main experimental directions in which the current experimental setup will be involved. These are the implementation of a QND measurement and subsequent generation of a spin squeezed state.

10.2.1 QND measurement

When performing a measurement on a quantum system we gain a knowledge about the system, but in the same time the system is also changed and its internal state is not the same after the measurement. Then it is natural to ask whether it is possible to find a way to measure a variable of the system without disturbing it. The answer is yes, this can be done by performing the so-called quantum non-demolition measurement.

The concept of QND measurement is the following. A quantum mechanical variable $\hat{A}$ is a QND (or signal) variable if it is a constant of motion i.e. $\hat{A}$ commutes with the free Hamiltonian of the system or $[\hat{A}, \hat{H}_0] = 0$ (in the case of atom-light system it is the unperturbed part of the Hamiltonian). The QND variable has to remain unchanged after the interaction, which constitutes that it must commute with the interaction Hamiltonian $\hat{H}_{int}$ or $[\hat{A}, \hat{H}_{int}] = 0$. To gain a knowledge of $\hat{A}$ one has to find a meter variable $\hat{B}$ which does not commute with the interaction Hamiltonian $\hat{H}_{int}$ [130], or in other words it does not conserve during the interaction. The variable $\hat{A}$ is coupled to $\hat{B}$ via the appropriately chosen QND interaction Hamiltonian $\hat{H}_{int}$. During a certain interaction time an information about the quantum state of the signal variable $\hat{A}$ is transferred to the meter variable $\hat{B}$. Then a conventional destructive measurement on $\hat{B}$ reads out that

information. Aside to the unchanged by the interaction quantum state of $\hat{A}$, a strong back-action is exerted into a variable conjugate to $\hat{A}$ namely $\hat{C}$. Thus by making a destructive measurement on $\hat{B}$ one obtains an information of $\hat{A}$ without disturbing it via hiding the measurement back-action noise into a conjugate variable $\hat{C}$.

In the off-resonant case the interaction hamiltonian is given by Eq.(2.49). The $\hat{J}_z$ projection of the collective atomic spin is a QND variable, and $\hat{S}_z$ is the meter variable. Dropping out the constant term in Eq.(2.49) we get that that the part of the Hamiltonian responsible for the evolution of the atomic and light variables is

$$\hat{H}_i = 4\hbar\tilde{\kappa}\hat{S}_z\hat{J}_z \tag{10.1}$$

Then after integration over the interaction τ of the Heisenberg equations of motion for the different component of $\mathbf{J}$ and $\mathbf{S}$ we get the following input output relations:

$$\hat{S}_y^{out} = \hat{S}_y^{in} + 4\tilde{\kappa}\tau\hat{S}_x^{in}\hat{J}_z^{in}, \quad \hat{S}_z^{in} = \hat{S}_z^{out} \tag{10.2}$$

$$\hat{J}_y^{out} = \hat{J}_y^{in} + 4\tilde{\kappa}\tau\hat{J}_x^{in}\hat{S}_z^{in}, \quad \hat{J}_z^{in} = \hat{J}_z^{out} \tag{10.3}$$

The information about the atomic system $\hat{J}_z$ is encoded in the light variable $\hat{S}_y$, and the value of the QND variable $\hat{J}_z$ is conserved throughout the measurement process. Thus making a destructive measurement on $\hat{S}_y$ a knowledge about the quantum state of $\hat{J}_z$ is obtained, with the back-action transferred to variable conjugate to $\hat{J}_z$, namely $\hat{J}_y$. In our experiment the destructive measurement is done by detecting the light from the two outputs of the interferometer via the homodyne detection. The subtracted photocurrent is proportional to the phase shift of the light.

The quantum mechanical variance of the measured variable is expressed, as it was already mentioned in Sec.5.1, by

$$\left(\delta S_y^{out}\right)^2 = \left(\delta S_y^{in}\right)^2 + (2\tau\tilde{\kappa})^2\langle\hat{n}\rangle^2\left(\delta J_z^{in}\right)^2 \tag{10.4}$$

In the above equation the $\hat{J}_z^{in}$ variance scales with the number of atoms N_{at} as shown in Eq.(2.12) for a coherent input atomic state or $\left(\delta J_z^{in}\right)^2 = N_{at}/4$. Then inserting this in the above equation we can separate a parameter κ^2 the same as the one defined in Sec.5.1

$$\kappa^2 = (\tau\tilde{\kappa})^2\langle\hat{n}\rangle\langle\hat{N}\rangle \tag{10.5}$$

The last equation is only valid if the variance is limited from below by the shot noise of light or in other words the above equation assumes that the initial light state is coherent. Substituting the value for $\tilde{\kappa}$ in the above equation and taking into account that $\tau = l/c$ - the time it takes the light to travel through the atomic sample we get:

$$\kappa^2 = \left(\frac{\lambda^2 D_-(\Delta)}{4\pi A}\right)^2 n_{ph}N_{at} \tag{10.6}$$

where $D_-(\Delta)$ is the detuning function given by Eq.(4.36). The last formula does not account for a possible atomic decoherence. The figure of merit of the interaction κ^2 depends on the atom N_{at} and photon n_{ph} number and can be increased by increasing the column number density $l\mathcal{N} = N_{at}/A$, or by having higher photon numbers. The column density can be increased by increasing the atom number density. The increase of the photon number is limited by the requirement for shot-noise operation of our interferometer.

10.2.2 Spin-squeezing

In that section we discuss how a possible QND measurement can be used for production of a squeezed atomic state as it has been predicted by Kuzmich et al. [5]. In the pervious section attention was brought to the light variable $\hat{S}_y$, which carries information about the atomic state. Now the emphasis is on the atomic variable $\hat{J}_y$, with an input-output relation for the variances given by

$$(\delta\hat{J}_y^{out})^2 = (\delta\hat{J}_y^{in})^2 + (2\tilde{\kappa})^2\tau N_{at}^2(\delta\hat{S}_z^{in})^2 = \frac{N_{at}}{4}\left(1+4\kappa^2\right), \tag{10.7}$$

where we have substituted the noise of the $(\delta S_z^{in})^2 = n_{ph}/4$ of a coherent light state in terms of angular momentum operators. Since the QND variable J_z is a conjugate to the J_y their variances obey the Heisenberg uncertainty principle, as mentioned in Ch.2. Hence, we can write that:

$$(\delta\hat{J}_z^{out})^2 = \frac{N_{at}}{4}\frac{1}{1+4\kappa^2} \tag{10.8}$$

The two expressions contain a common factor $N_{at}/4$, and a comparison with Eq.(2.12), valid for a coherent superposition state, reveals that the $(\delta J_z)^2_{coh} = N_{at}/4$. The noise of the coherent state defines the standard quantum limit and comparing the noise of $\hat{J}_y$ and $\hat{J}_z$ after the measurement one can find that the noise of $\hat{J}_y$ is increased by a factor of $1+4\kappa^2$ and the noise of the $\hat{J}_z$ is reduced by the same factor, whereas the uncertainty principle is not violated. Thus, by performing a QND measurement of the $\hat{J}_z$ we have prepared it in a state with noise reduced below the standard quantum limit, or in other words the $\hat{J}_z$ is in a *squeezed spin state* [2, 4]. The conjugate variable $\hat{J}_y$ is *anti-squeezed* according to Eq.(10.7).

The squeezed state is characterized by the squeezing parameter ξ. The definition used here is taken from [2]:

$$\xi = \frac{(\delta\hat{J}_z)^2}{\langle\hat{J}\rangle^2}N_{at} \tag{10.9}$$

Inserting the value of $\langle\hat{J}\rangle = N_{at}$ we get that $(\delta J_z)^2_{sq} = \xi(\delta J_z)^2_{coh}$ with the squeezing parameter defined as:

$$\xi = \frac{1}{1+4\kappa^2}. \tag{10.10}$$

The value of ξ is 1 for a coherent state and $\xi < 1$ for a squeezed state. The degree of spin squeezing as seen from above equation is related to κ^2. In Sec.5.1 we have shown that the figure of merit of the interaction is proportional to the optical depth α_0 and the decoherence parameter η_Δ. To obtain a large spin-squeezing one need to increase the optical column density α_0, while in the same time keep small the rate of real transitions or decoherence η_Δ.

10.2.3 Spin-squeezing on the Cs clock transition

The caesium microwave transition between the two hyperfine levels of the ground state $6S_{1/2}(F=3, m_F=0) \rightarrow 6S_{1/2}(F=4, m_F=0)$ is chosen worldwide for a frequency and time standard. The idea behind the atomic clock consists of isolating the transition frequency from external disturbances and stabilizing an oscillator to it. The atomic frequency standards is a vast field, and nowadays also a brunch of the commercial scientific technology. The quantum physics of the atomic clocks and their construction are extensively

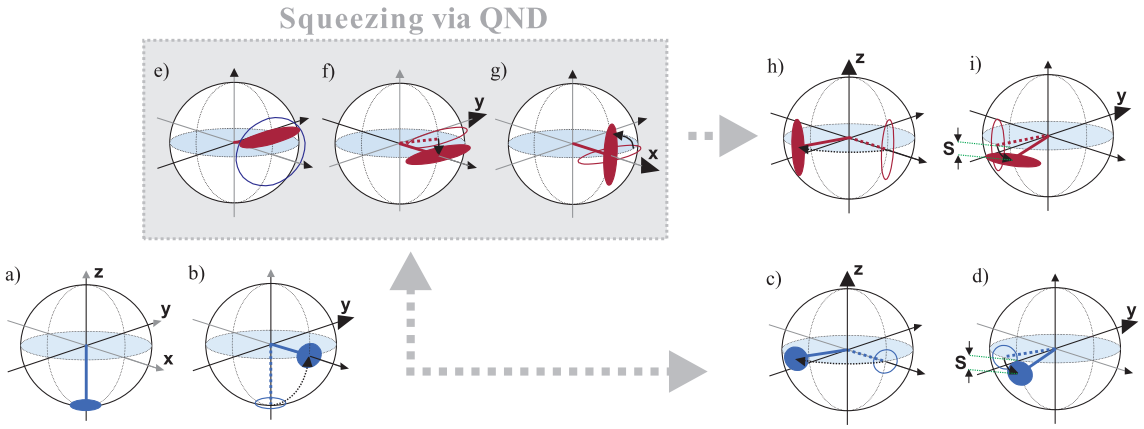

Figure 10.1: *Bloch-sphere representation of the clock operation*

discussed in [131,132] for both beam and cold atomic fountain standards. Experimentally, the atomic clocks rely on the Ramsey method of the separated oscillatory fields [133]. This method is briefly presented in Fig.10.1 using the angular momentum formalism with Bloch-spheres pictorial representation.

The atoms are initially prepared in a coherent spin state with $m_F = 0$ in one of the hyperfine states of the ground electronic state of Cs atom. Here we choose to use the $F = 3$ hyperfine state as represented by the spin vector pointing to the south pole of the Bloch sphere [Fig.10.1(a)]. Then a microwave pulse with duration $\tau_{\pi/2}$, Rabi frequency Ω_μ and detuning Δ_μ from the atomic resonance ω_0 interacts with the atoms while they pass a region of microwave radiation i.e. the microwave cavity. In the literature this pulse is called a $\pi/2$ pulse. The $\pi/2$ pulse creates a superposition state of the kind introduced in Eq.(2.11). In the language of the Bloch spheres this translates to rotation of the collective spin vector to the equatorial plane around the y axis [Fig.10.1(b)]. Then the microwave radiation is switched off and the system freely evolves for a time T, which corresponds to a rotation of the macroscopic spin around the z-axis on an angle defined by the time T and the detuning Δ_μ i.e. $\phi_{rot} = \Delta_\mu T$ [Fig.10.1(c)]. After the free precession another $\pi/2$ pulse is applied which translates in a rotation along y-axis Fig.10.1(d). At the end of that period the population of the levels $|3\rangle$ and $|4\rangle$ is measured destructively.

The method of the oscillatory fields can also be explained using the formalism of SU(2) interferometers described by Yurke et al [28]. The two regions of microwave interaction in the beam clocks or the two passes through the microwave cavity in the atomic fountains are represented by the two 50/50 beamsplitters of the Mach-Zehnder interferometer, and the accumulated phase during the free precession ϕ_{rot} by the phase difference between the two interferometer arms ϕ.

The today state of the art clocks are limited by the quantum projection noise of an ensemble of uncorrelated particles [1]. The noise scales linearly with the number of atoms and the uncertainty of the frequency offsets has been sown to be dominated by $1/\sqrt{N_{at}}$ [1]. However increasing the atom number, to improve the accuracy, increases the probability of collisions between particles, and thus the collision shift [134] could become a dominant factor for the standard. To overcome the projection noise, when the cold collision shift does not dominate, on needs to create a spin squeezed state.

Our proposal for generation of a squeezed state on the Cs clock transition involves off-resonant QND interaction with light in an interferometer as it is described extensively

in [11]. Here only a short pictorial representation is shown as a natural continuation of the presented in this thesis experiment.

The sequence of rotations in the Bloch space are more or less the same but this time we start from the second step of the Ramsey cycle. Right after the first $\pi/2$ pulse has created the coherent superposition an off resonant light pulse is applied at a detuning Δ_0 [see Ch.2.3]. After the QND measurement the $\hat{J}_z$ component of the collective spin is left in a state with reduced noise of the population number difference i.e. a squeezed state of $\hat{J}_z$ is created [Fig.10.1(e)]. Since $\langle J_z \rangle = 0$ then the result of the measurement will have a certain outcome $(J_z)_1 \neq 0$ which has to be corrected for as shown in Fig.10.1(f). At the same time as explained in the previous section the conjugate to $\hat{J}_z$ variable i.e. is anti-squeezed as shown in Fig.10.1(e). Before letting the system to freely evolve we must apply an additional $\pi/2$ pulse to convert the population squeezing into phase squeezing [Fig.10.1(g)]. After a free evolution during time $T = \pi/(2\Omega_\mu)$ [see Fig.10.1(h)] the second $\pi/2$ pulse from the Ramsey sequence transfers the phase squeezing again into population squeezing [Fig.10.1(i)]. At the end the uncertainty in the population number difference is reduced by a factor defined by Eq.(10.10) compared to that of an uncorrelated state.

Appendix A

The Electro-Magnetic Field

A.1 Classical field

The classical electric $\mathbf{E}(\mathbf{r},t)$ and magnetic fields $\mathbf{B}(\mathbf{r},t)$ obey Maxwell's equations:

$$\nabla \cdot \mathbf{E}(\mathbf{r},t) = \frac{1}{\epsilon_0}\rho(\mathbf{r},t) \tag{A.1}$$

$$\nabla \times \mathbf{E}(\mathbf{r},t) = -\frac{\partial \mathbf{B}(\mathbf{r},t)}{\partial t} \tag{A.2}$$

$$\nabla \cdot \mathbf{B}(\mathbf{r},t) = 0 \tag{A.3}$$

$$\nabla \times \mathbf{B}(\mathbf{r},t) = \mu_0 \mathbf{J}(\mathbf{r},t) + \mu_0\epsilon_0\frac{\partial \mathbf{E}(\mathbf{r},t)}{\partial t} \tag{A.4}$$

where $\rho(\mathbf{r},t)$ and $J(\mathbf{r},t)$ are the charge and current densities, μ_0 and ε_0 are the magnetic and electric constants of vacuum. In free space, or in a space, which does not contain any charges or currents i.e. $\rho, J = 0$ the equations can reduce to the two famous wave equations:

$$\nabla^2\mathbf{E}(\mathbf{r},t) = \mu_0\epsilon_0\frac{\partial \mathbf{E}^2(\mathbf{r},t)}{\partial^2 t} \tag{A.5}$$

$$\nabla^2\mathbf{B}(\mathbf{r},t) = \mu_0\epsilon_0\frac{\partial \mathbf{B}^2(\mathbf{r},t)}{\partial^2 t} \tag{A.6}$$

where $c = 1/\sqrt{\mu_0\varepsilon_0}$ is the velocity of light in vacuum. The solution of the wave equation for $\mathbf{E}$ is:

$$\mathbf{E}(\mathbf{r},t) = \frac{1}{\sqrt{2}}(\epsilon\mathcal{E}(t)e^{i(\mathbf{k}\cdot\mathbf{r}-\omega t)} + \epsilon^*\mathcal{E}(t)^*e^{-i(\mathbf{k}\cdot\mathbf{r}-\omega t)}) \tag{A.7}$$

where $\omega = |\mathbf{k}|c$ is the frequency of a single mode electromagnetic (EM) field, with k being the wave-vector along which the EM wave propagates. The amplitude of the wave is given by $\mathcal{E}(t)$ and in general is a function of time. The intensity of the EM field is defined as:

$$I(r,t) = \frac{1}{2}c\epsilon_0|\mathbf{E}(\mathbf{r},t)|^2 = \frac{1}{2}c\epsilon_0|\mathcal{E}(t)|^2 \tag{A.8}$$

Another representation of the classical EM field arises from the introduction of the vector potential $\mathbf{A}(\mathbf{r},\mathrm{t})$ [12]:

$$\mathbf{E}(\mathbf{r},t) = -\frac{\partial \mathbf{A}(\mathbf{r},t)}{\partial t} \tag{A.9}$$

$$\mathbf{B}(\mathbf{r},t) = \nabla \times \mathbf{A}(\mathbf{r},t). \tag{A.10}$$

Substituting the above into the Maxwell's equations and applying the Coulomb gauge where $\nabla \cdot \mathbf{A}(\mathbf{r},t) = 0$ we arrive at a wave equation for the vector potential $\mathbf{A}$:

$$\nabla^2 \mathbf{A}(\mathbf{r},t) = \frac{1}{c^2}\frac{\partial \mathbf{A}^2(\mathbf{r},t)}{\partial^2 t} \tag{A.11}$$

In a cubic space with dimension L and periodic boundary conditions the vector field is expanded as a sum of contributions from the different modes:

$$\mathbf{A}(\mathbf{r},t) = \sum_{k,p} \epsilon_{kp} A_{kp}(t) e^{i\mathbf{k}\cdot\mathbf{r}} + c.c. \tag{A.12}$$

where $\mathbf{k}$ is the wave vector, which values are restricted by the boundary conditions, ϵ is the polarization vector, and $A_{kp}(t)$ is the mode function. Then in the Coulomb gauge they must satisfy $\mathbf{k} \cdot \epsilon_{\mathbf{k}} = 0$, or the polarization of light is orthogonal to its propagation vector. Another condition arises from the orthogonality of the polarization vectors $\epsilon_{kp} \cdot \epsilon_{kp'} = \delta_{p,p'}$. Further, inserting Eq.(A.12) into the wave equation we get an equation for the mode function with a solution $A_{kp}(t) = A_{kp}\exp(-i\omega_k t)$, with ω_k being the frequency of the k-th mode. Finally, inserting the above in Eq.(A.12) we get:

$$\mathbf{A}(\mathbf{r},t) = \sum_{k,p} \epsilon_{kp} A_{kp} e^{i(\mathbf{k}\cdot\mathbf{r}-\omega_k t)} + c.c. \tag{A.13}$$

To express the $\mathbf{E}$ and $\mathbf{B}$ we need to solve Eq.(A.9). Then for the energy of the classical field $H_c = \frac{1}{2}\int_V dV[\epsilon_0|\mathbf{E}|^2 + \mu_0^{-1}|\mathbf{B}|^2]$ we obtain:

$$H_c = \sum_{k,p} \varepsilon_0 V \omega_k^2 (A_{kp}A_{kp}^* + A_{kp}^* A_{kp}) \tag{A.14}$$

where $V = L^3$ is the quantization volume.

A.2 Field Quantization

The quantization of the electromagnetic field is done by association of a quantum mechanical harmonic oscillator to each mode of the classical field [12]. The conversion from the classical to quantum description we do by making the following substitutions:

$$A_{kp} \to \sqrt{\frac{\hbar}{2\varepsilon_0 V \omega_k}}\hat{a}_{kp} \tag{A.15}$$

$$A_{kp}^* \to \sqrt{\frac{\hbar}{2\varepsilon_0 V \omega_k}}\hat{a}_{kp}^\dagger \tag{A.16}$$

The relations Eq.(A.15) when inserted in Eq.(A.13) give the quantized vector potential of the EM field as:

$$\hat{\mathbf{A}}(\mathbf{r},t) = \sum_{k,p} \sqrt{\frac{\hbar}{2\epsilon_0 V \omega_k}} (\epsilon_{kp} \hat{a}_{kp} e^{i(\mathbf{k}\cdot\mathbf{r}-\omega_k t)} + \epsilon^*_{kp} \hat{a}^\dagger_{kp} e^{-i(\mathbf{k}\cdot\mathbf{r}-\omega_k t)}) \tag{A.17}$$

The field operators $\hat{a}_{kp}$ and $\hat{a}^\dagger_{kp}$ fulfill the commutation relations:

$$[\hat{a}_{kp}, \hat{a}^\dagger_{k'p'}] = \delta_{kk'}\delta_{pp'} \tag{A.18}$$

$$[\hat{a}_{kp}, \hat{a}_{k'p'}] = [\hat{a}^\dagger_{kp}, \hat{a}^\dagger_{k'p'}] = 0 \tag{A.19}$$

The electric and magnetic field can be found from Eq.(A.9). We will only write the expression for the electric field vector of a single mode quantum field:

$$\hat{\mathbf{E}}(\mathbf{r},t) = \sqrt{\frac{\hbar\omega}{2\epsilon_0 V}} (\epsilon \hat{a} e^{i(\mathbf{k}\cdot\mathbf{r}-\omega t)} + \epsilon^* \hat{a}^\dagger e^{-i(\mathbf{k}\cdot\mathbf{r}-\omega t)}) \tag{A.20}$$

The energy or the Hamiltonian of the EM field can be found by substituting into the classical formula Eq.(A.14).

$$\hat{H}_q = \frac{1}{2} \int_V \left[\epsilon_0 \hat{\mathbf{E}}^2(\mathbf{r},t) + \frac{1}{\mu_0} \hat{\mathbf{B}}^2(\mathbf{r},t) \right] d^3r \tag{A.21}$$

$$= \frac{1}{2} \sum_{k,p} \hbar\omega \left[\hat{a}_{kp}(t) \hat{a}^\dagger_{kp}(t) + \hat{a}^\dagger_{kp}(t) \hat{a}_{kp}(t) \right] \tag{A.22}$$

$$= \sum_{k,p} \hbar\omega \left[\hat{a}^\dagger_{kp}(t) \hat{a}_{kp}(t) + \frac{1}{2} \right] \tag{A.23}$$

The integration is done over the quantization volume V introduced earlier. In most cases we can neglect the $\frac{1}{2}\hbar\omega_{kp}$ zero point energy. The operators $\hat{n}_{\mathbf{k}p} = \hat{a}^\dagger_{\mathbf{k}p} \hat{a}_{\mathbf{k}p}$ give the photon number in each mode and the summation in Eq.(A.21) gives the total number of photons in the field multiplied by $\hbar\omega$.

Appendix B

Dipole Transition Strengths

The discussion in this appendix is based on the data provided by D. Steck [110]. In the theoretical part Sec.2.3 we have given the formula for the coupling constant g in Eq.(2.27).

$$g = \frac{i\omega_{ge}\epsilon \cdot \hat{d}_{ge}}{\sqrt{2\hbar V \omega \epsilon_0}} \tag{B.1}$$

It includes the dipole matrix element $\hat{d}_{eg}$, the volume overlap of the probe beam with the atomic sample V, the atomic transition frequency ω_{ge}, EM field frequency ω, and polarization vector ϵ, which is parallel to the quantization axis.

In this appendix we will derive an expression to help us calculate the dipole matrix element $\hat{\mathbf{d}}_{ge}$ for a specific transition. Since the dipole matrix element is a characteristic of an atomic transition between two levels $|g\rangle$ and $|e\rangle$ in the dipole approximation, we can write that:

$$\hat{\mathbf{d}}_{ge} = \langle F_g m_{F_g} | e\mathbf{r} | F_e m_{F_e} \rangle \tag{B.2}$$

where F and m_F are the quantum number for the total atomic spin and its projection respectively. The indices g and e as usual denote ground and excited state. The probability of transition to happen between these two levels is proportional to the square of the modulus of the dipole matrix element. considering a spherical symmetry we can write that $|\hat{\mathbf{d}}_{ge}|^2 = 3|\hat{d}_q|^2$. Then using the Wigner-Eckart theorem [13], we factor out the angular dependance and write the matrix element $\hat{d}_q$ as a product of the Clebsch-Gordon coefficient and the reduced matrix element:

$$|\hat{d}_q|^2 = |\langle F_g m_{F_g} | e r_q | F_e m_{F_e} \rangle|^2 = |\langle F_g || e\mathbf{r} || F_e \rangle|^2 |\langle F_g m_{F_g} | F_e 1 m_{F_e} q \rangle|^2 \tag{B.3}$$

where the Clebsch-Gordan coefficient $\langle F_g m_{F_g} | F_e 1 m_{F_e} q \rangle$ will vanish unless $m_{F_e} = m_{F_g} - q$. For linearly polarized light we only have $q = 0$ transitions. Moreover, the field interacts with all magnetic sublevels m_{F_g}, so the dipole operator becomes:

$$\sum_{m_{F_g}, m_{F_e}} |\hat{d}_q|^2 = \sum_{m_{F_g}, m_{F_e}} |\langle F_g || e\mathbf{r} | F_e \rangle|^2 |\langle F_g m_{F_g} | F_e 1 m_{F_e} 0 \rangle|^2 = \frac{1}{3} |\langle F_g || e\mathbf{r} || F_e \rangle|^2. \tag{B.4}$$

The reduced matrix element in the basis of the F_g, F_e states can be expressed as a product of the hyperfine transition strength factors $S_{F_g F_e}$ and the reduced matrix element in the

basis of J_g, J_e. Then the dipole matrix element becomes:

$$|\hat{d}_q|^2 = \frac{1}{3} S_{F_g F_e} |\langle J_g || e\mathbf{r} || J_e \rangle|^2. \tag{B.5}$$

$$S_{F_g F_e} = (2F_e + 1)(2F_g + 1) \begin{pmatrix} J_g & F_g & I \\ F_e & J_g & 1 \end{pmatrix}^2 \tag{B.6}$$

The transition strength satisfy the following condition $\sum_{F_e} S_{F_g F_e} = 1$. In other words the values of S sum up to unity for transitions to the same ground state. The values of $S_{F_g F_e}$ are given in [110]. The connection of the matrix element $|\langle J_g || e\mathbf{r} || J_e \rangle|^2$ with the emission linewidth γ is given by [23]:

$$|\langle J_g || e\mathbf{r} || J_e \rangle|^2 = (2J_g + 1) \frac{3\hbar\epsilon_0 \lambda^3 \gamma}{8\pi^2} \tag{B.7}$$

Then at the end for the square of the coupling constant $|g|^2$, assuming that $\omega \approx \omega_{ge}$ and the volume is $V = Al$, where A is cross-section of probe beam and l is the length of the atomic sample, we get:

$$|g|^2 = (2F_e + 1)(2F_g + 1)(2J_g + 1) \begin{pmatrix} J_g & F_g & I \\ F_e & J_g & 1 \end{pmatrix}^2 \frac{\lambda^2 c}{4\pi A l} \frac{\gamma}{2} \tag{B.8}$$

$$= (2J + 1) S_{F_g F_e} \frac{\lambda^2 c}{4\pi A l} \frac{\gamma}{2} \tag{B.9}$$

Appendix C

Eigenvalues of the dressed states Hamiltonian

In the full quantum treatment of light interaction with a two-level atom we have the following Hamiltonian:

$$\hat{H}_{tot} = \hbar\omega_0|e\rangle\langle e| + \hbar\omega\left(\hat{a}^\dagger\hat{a} + \frac{1}{2}\right) + \frac{\hbar\Omega}{2}\left(|e\rangle\langle g|\hat{a}e^{-i\omega t} + |g\rangle\langle e|\hat{a}^\dagger e^{i\omega t}\right) \tag{C.1}$$

where the first term is the atomic Hamiltonian with an energy referenced to the ground state $|g\rangle$, the second term is the light field Hamiltonian, and the third is the dipole interaction Hamiltonian. The three terms are also given in Sec.3.3.2, Eq.(3.19). The above Eq.(C.1) is another expression for the total system Hamiltonian given in Eq.(2.29).

The combined state of atom-light system is expressed as direct tensor product of the atom and light state $|g\ n\rangle = |g\rangle \otimes |n\rangle$ as shown in Sec.3.3.2. The matrix representation of the $\hat{H}_{tot}$ in the basis of these combined states is:

$$\mathbf{H} = \begin{pmatrix} \langle g\ n|\hat{H}|g\ n\rangle & \langle g\ n|\hat{H}|e\ n-1\rangle \\ \langle e\ n-1|\hat{H}|g\ n\rangle & \langle e\ n-1|\hat{H}|e\ n-1\rangle \end{pmatrix}. \tag{C.2}$$

By the use of the annihilation and creation operations in Eq.(2.20), and taking into account the orthogonality conditions $\langle m|n\rangle = \delta_{mn},\ m = g, e$ we arrive at the following matrix form:

$$\mathbf{H} = \hbar\begin{pmatrix} \omega n & \frac{1}{2}\Omega\sqrt{n}e^{i\omega t} \\ \frac{1}{2}\Omega\sqrt{n}e^{-i\omega t} & \omega_0 + \omega(n-1) \end{pmatrix} + \frac{\hbar\omega}{2}\mathbf{1}. \tag{C.3}$$

In the field rotating frame $\mathbf{H}$ transforms by the law $\tilde{\mathbf{H}} = \mathbf{S}^\dagger\mathbf{H}\mathbf{S}$, where $\mathbf{S}$ is given by

$$\mathbf{S} = \hbar\begin{pmatrix} e^{i\omega t} & 0 \\ 0 & e^{-i\omega t} \end{pmatrix}. \tag{C.4}$$

After this transformation we to the following form of the Hamiltonian:

$$\tilde{\mathbf{H}} = \hbar\begin{pmatrix} \omega n & \frac{1}{2}\Omega\sqrt{n} \\ \frac{1}{2}\Omega\sqrt{n} & \omega_0 + \omega(n-1) \end{pmatrix} + \frac{\hbar\omega}{2}\mathbf{1}. \tag{C.5}$$

Now we can proceed to calculate the eigenvalues of $\tilde{\mathbf{H}}$. The result obtained is the energy

levels of combined light-atom system in a multiplicity of n photons as in Eq.(3.22).

$$E_{\pm}(n) = \hbar\left(-\frac{\Delta}{2} + \omega n \pm \frac{1}{2}\sqrt{\Delta^2 + \Omega^2 n}\right). \tag{C.6}$$

The eigenstates depend on the photon number n and the detuning of the EM field from the resonance Δ. The states $|e\ n-1\rangle$ and $|g\ n\rangle$ in the far-off-resonant case are separated by an amount δE which depends on the detuning Δ:

$$\delta E = E_{\pm}(n) - E(n-1)_{\pm} = \frac{\hbar\Omega^2}{4\Delta}. \tag{C.7}$$

For red detuning ($\Delta < 0$) the ground state shifts down and for blue detuning ($\Delta > 0$) shifts up.

Appendix D

Numerical model for R&R temperature measurement

Lets assume for initial conditions that we have a Gaussian density profile. This is not entirely true as refereing to the Fig.6.16(b), but we found out that the only difference from the Gaussian density distribution is at the very top of the profile. Next, let us consider a Maxwell-Boltzman initial velocity distribution corresponding to temperature T. Hence the initial phase-space density distribution is described by:

$$\Phi(\mathbf{r}_0, \mathbf{v}_0, 0) = \frac{1}{(2\pi\sigma_0^2)^{3/2}} \exp\left(-\frac{r_0^2}{2\sigma_0^2}\right) \frac{1}{(2\pi\sigma_v^2)^{3/2}} \exp\left(-\frac{v_0^2}{2\sigma_v^2}\right) \;\; \sigma_v = \sqrt{\frac{k_B T}{M}} \tag{D.1}$$

where σ_0 is the initial cloud radius, and σ_{v} the rms velocity spread. The transformation of the coordinates with time is given by:

$$\mathbf{r} = \mathbf{r}_0 + \mathbf{v}_0 t + \frac{1}{2} g t^2 \hat{z}, \;\; \mathbf{v} = \mathbf{v}_0 + g t \hat{z} \tag{D.2}$$

Then the density profile as a function of the release time t is obtained by integration over the velocity distribution:

$$n(\mathbf{r}, t) = \int \Phi(\mathbf{r}_0, \mathbf{v}_0, 0) d\mathbf{v} = \frac{1}{(2\pi\sigma(t)^2)^{3/2}} \exp\left[-\frac{x^2 + y^2 + (z - \frac{1}{2}gt^2)}{2\sigma(t)^2}\right] \tag{D.3}$$

$$\sigma(t) = \sqrt{\sigma_0^2 + \sigma_v^2 t^2} \tag{D.4}$$

The signal from the recaptured atoms is proportional to the convolution of the density profile and the trapping beam profile. The last can be expressed as:

$$I(r) = \frac{2P}{\pi w^2} \exp\left(-\frac{2r^2}{w^2}\right) \tag{D.5}$$

Finally the R&R signal is obtained by integration over the volume V seen by detector [109] and a subsequent normalization to the value of that signal for $t = 0$.

$$S(t) = \frac{1}{S(0)} \int d^3\mathbf{r} n(\mathbf{r}, t) I(\mathbf{r}) \tag{D.6}$$

Appendix E

Model of dipole trap phase-shift temperature measurement

In this appendix we present a theoretical model for fitting the data obtained from the temperature measurement described in Sec.9.3.3. The atoms are held in a dipole trap for a certain time and then released. During the time of flight the atomic expand ballistically, and the density in the probing volume drops as a function of time of flight.

Lets assume that at time $t_0 = 0$ the atoms are released from the dipole trap and start to expand. The atomic radii can be expressed as in Appendix D:

$$\sigma(t) = \sqrt{\sigma_{0i}^2 + \sigma_v^2 t^2},\ i = r, a \tag{E.1}$$

where r and a stands for radial and axial directions, respectively, and t is the time of flight. In our case for the measurements on multiple loading cycles this time translates into delay time of the probe pulses. In the case of a measurement in a single loading cycle this time is just the delay of the i-th pulse with respect to the release of the atoms. The first term is the initial radius of the cloud and is expressed with the help of the trap frequencies ω_i as:

$$\sigma_i(0) = \sqrt{\frac{k_B T}{M\omega_i^2}} \tag{E.2}$$

The density distribution of the atomic sample falling under gravity we express as:

$$n(x, y, z, t) = \frac{1}{8\pi^{3/2}\sqrt{\sigma_r^2\sigma_r^2\sigma_a^2}} \exp\left[-\frac{(x - \frac{gt^2}{2})^2 + y^2}{2\sigma_r^2} - \frac{z^2}{2\sigma_a^2}\right] \tag{E.3}$$

The probe beam intensity $I(x, y, z)$ is given by the intensity of the gaussian beam as shown in Eq.(3.30), with w_0 being the probe beam waist radius. We assume that the propagation direction is along the z-axis. Then the overlap function between the cloud and the laser beam is:

$$n(x, y, z, t) = n(x, y, z, t)I(x, y, z) \tag{E.4}$$

The probability $p(t)$ of an atom to be inside the probing volume after a time t is given by the integration of the overlap function over the whole space:

$$
\begin{aligned}
p(t) &= \int_{-\infty}^{\infty}\int_{-\infty}^{\infty}\int_{-\infty}^{\infty} N(x,y,z,t)dxdydz \qquad \text{(E.5)}\\
&= 2P\exp\left[-\frac{g^2t^4}{8\sigma_r(t)^2}\right]\frac{1}{\sqrt{(2\pi)^3\sigma_a^2(t)}}\times\int_{-\infty}^{\infty}dz\frac{\exp\left[\frac{\sigma_a^2g^2t^4w^2(z)-4\sigma_r^2(w^2(z)+4\sigma_r^2)z^2}{8\sigma_r^2(w^2(z)+4\sigma_r^2(t))\sigma_a^2}\right]}{w^2(z)+4\sigma_r^2(t)}
\end{aligned}
$$

The above equation integral cannot be solved analytically. The Rayleigh range of the probe beam $\pi w_0^2/\lambda = 1.5$ mm. That compared to the cloud half-length of $l/2 = 0.625$ mm is almost to times longer, which means that at a distance of $l/2$ the probe beam radius increases with only 10%. Than we can assume that the atoms see the probe beam almost collimated i.e. $w(z) = w_0$. Then the above equation simplifies to:

$$p(t) = \frac{\mathcal{P}}{\pi(w_0^2+4\sigma_r^2(t))}\exp\left[-\frac{g^2t^4}{2(w_0^2+4\sigma_r^2(t))}\right], \qquad \text{(E.6)}$$

where $\mathcal{P}$ is the probe power. Then for the fitting expression in Eq.(9.11) we need to normalize $p(t)$ to its initial value and subtract it from unity in order to get the probability of atom initially in the probing volume to be outside it at a given time t.

$$P(t) = 1 - \frac{p(t)}{p(0)} \qquad \text{(E.7)}$$

Appendix F

Estimation of the rate of real transitions

In this appendix we treat the problem of real transition due to probe light. As we mentioned in Sec.9.3 the blue detuning of the probe laser from the cycling transition is $\Delta_1 = 100$ MHz. However, there is a certain probability the probe light to excite atoms on the $F' = 4$ state, which is 351 MHz detuned. An additional complication comes from the weak residual repump power present at the time of performing the experiment. To estimate the depumping due to probe light we build a rate equation model of the depopulation dynamics of $F = 4$ state to $F = 3$ via the weakly coupled $F = 4 \rightarrow F' = 4$ (the probe light is 351 MHz detuned from that transition) state in a presence of additional light field, i.e. the repump laser. The scheme of the analysis is shown in Fig.F.1 below. Considering the excitations and levels as depicted in the figure, the evolution equations will be as follows

$$\begin{aligned}
\frac{dN_3(t)}{dt} &= \Gamma_3 N_4'(t) + \frac{\eta_r}{\tau_r}(N_4'(t) - N_3(t)) \\
\frac{dN_4(t)}{dt} &= \Gamma_2 N_4'(t) + \frac{\eta_p}{\tau_p}(N_4'(t) - N_4(t)) \\
\frac{dN_4'(t)}{dt} &= -(\Gamma_2 + \Gamma_3) N_4'(t) + \frac{\eta_r}{\tau_r}(N_4'(t) - N_3(t)) - \frac{\eta_p}{\tau_p}(N_4'(t) - N_4(t))
\end{aligned} \tag{F.1}$$

where we can consider the excitation by two lasers of the atomic populations of the ground states. The populations of $F = 3,\ F = 4,$ and $F' = 4$ are denoted with $N_3,\ N_4$ and N_4', respectively. The values of $\Gamma_1 = \frac{44}{144}\gamma,\ \Gamma_2 = \frac{21}{144}\gamma,$ and $\Gamma_2 = \frac{15}{112}\gamma$ are the decay rates as shown in Fig.F.1. The depumping parameter due to probe and repump light are η_p, and η_r, respectively, with τ_p and τ_r being the probe pulse duration, and the duration of the repump light exposure. The last is equivalent to the duration of the probe pulse train. Solving the above system of equations for the population of the $F = 4$ ground state, namely N_4, would allow us to fit the data obtained in the measurement described in Sec.9.3.5 and extract from this fit the value of η_p. We search for solutions in the form:

$$N_3(t) = Ae^{\lambda t}, N_4(t) = Be^{\lambda t}, N_4(t) = Ce^{\lambda t} \tag{F.2}$$

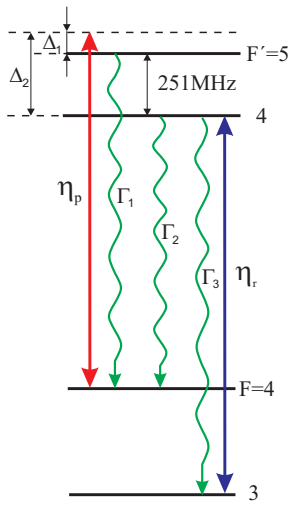

Figure F.1: *Scheme of the relevant levels included in the rate equation analysis*

we get the following characteristics roots ($P_{e1} = \frac{\eta_r}{\tau_r}, P_{e2} = \frac{\eta_p}{\tau_p}$)

$$\begin{aligned}
\lambda_1 &= 0 \\
\lambda_2 &= -\frac{1}{2}(\Gamma_2 + \Gamma_3 + 2P_{e1} + 2P_{e2}) + \\
&+ \frac{1}{2}\sqrt{(\Gamma_3 + 2P_{e1})^2 + (\Gamma_2 + 2P_{e2})^2 + 2(\Gamma_2\Gamma_3 + 2P_{e1}P_{e2})} \\
\lambda_3 &= -(\Gamma_2 + \Gamma_3 + 2P_{e1} + 2P_{e2}) - \\
&- \frac{1}{2}\sqrt{(\Gamma_3 + 2P_{e1})^2 + (\Gamma_2 + 2P_{e2})^2 + 2(\Gamma_2\Gamma_3 + 2P_{e1}P_{e2})}
\end{aligned} \tag{F.3}$$

and the solutions for initial conditions $N_3(0) = N_4'(0) = 0,$ and, $N_4(0) = N_{04}$ are

$$\begin{aligned}
N_3(t) &= \sum_{i=3}^{3} A_i e^{\lambda_i t} \\
N_4(t) &= \sum_{i=3}^{3} \frac{\lambda_i + P_{e1}}{\lambda_i + P_{e2}} \frac{\Gamma_2 + P_{e2}}{\Gamma_3 + P_{e1}} A_i e^{\lambda_i t} \\
N_4'(t) &= \sum_{i=3}^{3} \frac{\lambda_i + P_{e1}}{\Gamma_3 + P_{e1}} A_i e^{\lambda_i t}
\end{aligned} \tag{F.4}$$

where

$$\begin{aligned}
A_1(t) &= \frac{e-f}{D} N_{04},\ A_2(t) = \frac{f-d}{D} N_{04},\ A_3(t) = \frac{d-e}{D} N_{04} \\
e - f &= \frac{\lambda_2 - \lambda_3}{P_{e1} + \Gamma_3},\ d - e = -\frac{\lambda_2}{P_{e1} + \Gamma_3},\ f - d = \frac{\lambda_3}{P_{e1} + \Gamma_3} \\
D &= c(d-e) + a(e-f) + b(f-d) \\
a &= \frac{P_{e1}}{P_{e2}} \frac{P_{e2} + \Gamma_2}{P_{e1} + \Gamma_3},\ b = \frac{\lambda_2 + P_{e1}}{\lambda_2 + P_{e2}} \frac{P_{e2} + \Gamma_2}{P_{e1} + \Gamma_3},\ c = \frac{\lambda_3 + P_{e1}}{\lambda_3 + P_{e2}} \frac{P_{e2} + \Gamma_2}{P_{e1} + \Gamma_3}
\end{aligned} \tag{F.5}$$

The obtained expression for the $N_4(t)$ is used to fit the data in Fig.9.10.

List of Figures

List of Tables

Bibliography

[1] G. Santarelli, Ph. Laurent, P. Lemonde, A. Clairon, A. G. Mann, S. Chang, A. N. Luiten, and C. Salomon. Quantum projection noise in an atomic fountain: A high stability cesium frequency standard. *Phys. Rev. Lett.*, **82**:4619, (1999).

[2] D. J. Wineland, J. J. Bollinger, W. M. Itano, and D. J. Heinzen. Squeezed atomic states and projection noise in spectroscopy. *Phys. Rev. A*, **50**:67, (1994).

[3] A. Einstein, B. Podolsky, and N. Rosen. *Phys. Rev.*, **47**:777, (1935).

[4] M. Kitagawa and M. Ueda. Squeezed spin states. *Phys. Rev. A*, **47**:5138, (1993).

[5] A. Kuzmich, N. P. Bigelow, and L. Mandel. Atomic quantum non-demolition measurements and squeezing. *Europhys. Lett.*, **42**:481, (1998).

[6] A. Kuzmich, L. Mandel, J. Janis, Y. E. Young, R. Ejnisman, and N. P. Bigelow. Quantum nondemolition measurements of collective atomic spin. *Phys. Rev. A*, **60**:2346, (1999).

[7] J. Hald, J. L. Sorensen, C. Schori, and E. S. Polzik. Spin squeezed atoms: A macroscopic entangled ensemble created by light. *Phys. Rev. Lett.*, **83**:1319, (1999).

[8] L. K. Thomsen, S. Mancini, and H. M. Wiseman. Spin squeezing via quantum feedback. *Phys. Rev. A*, **65**:061801, (2002).

[9] J.M. Geremia, J.K. Stockton, and H. Mabuchi. Real-time quantum feedback control of atomic spin-squeezing. *Science*, **304**:270, (2004).

[10] J.F. Roch, K. Vigneron, Ph. Grelu, A. Sinatra, J.Ph. Poizat, and Ph. Grangier. Quantum nondemolition measurements with cold trapped atoms. *Phys. Rev. Lett.*, **78**:634, (1997).

[11] D. Oblak, P.G. Petrov, C.L. Alzar, W. Tittel, A.K. Vershovski, J.K. Mikkelsen, J.L. Sørensen, and E.S. Polzik. Quantum-noise-limited interferometric measurements of atomic noise: Towards spin squeezing on the cs clock transition. *Phys. Rev. A*, **71**:045504, (2005).

[12] R. Loudon. *The quantum theory of light.* Oxford University Press, New York, 3rd edition, 2000.

[13] J.J. Sakurai. *Modern Quantum Mechanics.* Addison-Wesley, rev. ed. edition, 1994.

[14] J. M. Radcliffe. Some properties of coherent spin states. *J. Phys. A*, **4**:313, (1971).

[15] F. T. Arecchi, E. Courtens, R. Gilmore, and H. Thomas. Atomic coherent states in quantum optics. *Phys. Rev. A*, **6**:2211, (1972).

[16] R. P. Feynman, F.L. Vernon, and R.E. Hellwarth. Geometrical representation of schrödinger equation for solving maser problems. *J. Appl. Phys.*, **28**:49, (1957).

[17] W. M. Itano, J. C. Bergquist, J. J. Bollinger, J. M. Gilligan, D. J. Heinzen, F. L. Moore, M. G. Raizen, and D. J. Wineland. Quantum projection noise: Population fluctuations in two-level systems.

[18] J.D. Jackson. *Classical Electrodynamics*. Wiley, 3th. ed edition, 1998.

[19] V.A. Fock. *Zs. f. Phys.*, **49**:339, (1928).

[20] R.J. Glauber. Coherent and incoherent state of radiation field. *Phys. Rev.*, **131**:2766, (1963).

[21] D.F. Walls and G.J. Milburn. *Quantum Optics*. Springer-Verlag, 1994.

[22] D. Oblak. Non-destructive quantum noise limited interferometric measurements on cold cs atoms. Master's thesis, Århus University, (2004).

[23] I. I. Sobelman. *Atomic spectra and radiative transitions*. Springer, Berlin, 2nd edition, 1992.

[24] A.E. Siegman. *Lasers*. University Science Books, 2nd edition, 1986.

[25] J.H. Müller, P. Petrov, D. Oblak, C. L-G. Alzar, S. R. de Echaniz, and E.S. Polzik. Diffraction effects on light-atomic ensemble quantum interface. *Phys. Rev. A.*, **71**:033803, (2005).

[26] J. L. Sorensen, J. Hald, and E. S. Polzik. Quantum noise of an atomic spin polarization measurement. *Phys. Rev. Lett.*, **80**:3487, (1998).

[27] B. Julsgaard, A. Kozhekin, and E. S. Polzik. Experimental long-lived entanglement of two macroscopic objects. *Nature*, **413**:400, (2001).

[28] B. Yurke, S.L. McCall, and J.R. Klauder. `SU(2)` and `SU(1,1)` interferometers. *Phys. Rev. A*, **33**:4033, (1986).

[29] R. Frisch. *Z. Phys.*, **86**:42, (1933).

[30] A. Ashkin. *Phys. Rev. Lett.*, **25**:1321, (1970).

[31] A. Ashkin. *Phys. Rev. Lett.*, **24**:156–159, (1970).

[32] T. Hänsch and A. Schalwow. *Opt. Commun*, **13**:68, (1975).

[33] W.D. Phillips and H. Metcalf. *Phys. Rev. Lett.*, **48**:596, (1982).

[34] S. Chu, L. Hollberg, J. E. Bjorkholm, A. Cable, and A. Ashkin. Three-dimensional viscous confinement and cooling of atoms by radiation pressure. *Phys. Rev. Lett.*, **55**:48–51, (1985).

[35] E.L. Raab, M. Prentiss, A. Cable, S. Chu, and D.E. Pritchard. Trapping of neutral sodium atoms with radiation pressure. *Phys. Rev. Lett.*

[36] H. Metcalf and P. van Straten. *Laser cooling and trapping.* Springer-Verlag, 2001.

[37] C.S. Adams and E. Riis. Laser cooling and trapping of neutral atoms. *Prog. Quant. Electr.*, **21**:1–79, (1997).

[38] P. D. Lett, R. N. Watts, C. I. Westbrook, W. D. Phillips, P. L. Gould, and H. J. Metcalf. Observation of atom laser cooled below doppler limit. *Phys. Rev. Lett.*, **61**:169–172, (1988).

[39] C. Cohen-Tannoudji J. Dalibard. Laser cooling below doppler limit by polarization gradients: simple theoretical models. *JOSA B*, **6**:2023, (1989).

[40] P.J. Ungar, D.S. Weiss, S. Chu, and E. Riis. Optical molasses and multilevel atoms - theory. *JOSA B*, **6**:2058, (1989).

[41] G. Alzette, A. Gozzini, L. Moi, and G. Orriols. *Nuovo Cimento B*, **36**:5, (1976).

[42] S.E. Harris, J.E. Field, and A. Imamoğlu. Nonlinear optical processes using electromagnetically induced transparency. *Nuovo Cimento B*, **64**:1107, (1990).

[43] B.M Garraway and V.G Minogin. Theory of an optical dipole trap. *Phys. Rev. A*, **62**:043406, (2000).

[44] S. Chu, J. E. Bjorkholm, A. Ashkin, and A. Cable. Experimental observation of optically trapped atoms. *Phys. Rev. Lett.*, **57**:314, (1986).

[45] M.D. Barett, J.A. Sauer, and M.S. Chapman. All-optical formation of an atomic bose-einstein condensate. *Phys. Rev. Lett.*, **87**:010404, (2001).

[46] T. Weber, J. Herbig, M. Mark, H.-C. Nägerl, and R. Grimm. Bose-einstein condensation of cesium. *Science*, **299**:232, (2003).

[47] S. Jochim, M. Bartenstein, A. Altmeyer, G. Hendl, S. Riedl, C. Chin, J.H. Denschlag, and R. Grimm. Bose-einstein condensation of molecules. *Science*, **302**:2101, (2003).

[48] N. Schlosser, G. Reymond, I.E. Protsenko, and P. Grangier. Sub-poissonian loading of single atoms in a microscopic dipole trap. *Nature*, **411**:1024, (2001).

[49] D. Frese, B. Ueberholz, S. Kuhr, W. Alt, D. Schrader, V. Gomer, and D. Meschede. Single atoms in an optical dipole trap: Towards a deterministic source of cold atoms. *Phys. Rev. Lett.*, **85**:3777, (2000).

[50] D. Schrader M. Mller V.Gomer S. Kuhr, W. Alt and D. Meschede. Deterministic delivery of a single atom. *Science*, **293**:278, (2000).

[51] I. Dotsenko, W. Alt, M. Khudaverdyan, S. Kuhr, D. Meschede, Y. Miroshnychenko, D. Schrader, and A. Rauschenbeutel. Submicrometer position control of single trapped neutral atoms. *Phys. Rev. Lett.*, **95**:033002, (2005).

[52] D. Schrader, S. Kuhr, W. Alt, M. Müller, V. Gomer, and D. Meschede. An optical conveyor belt for single neutral atoms. *Appl. Phys. B*, **73**:819, (2001).

[53] D. Schrader, I. Dotsenko, M. Khudaverdyan, Y. Miroshnychenko, A. Rauschenbeutel, and D. Meschede. Neutral atom quantum register. *Phys. Rev. Lett.*, **93**:150501, (2004).

[54] V.S. Lethokov. Narrowing of the doppler width in a standing light wave. *JETP*, **7**:272, (1968).

[55] C. Salomon, J. Dalibard, A. Aspect, H. Metcalf, and C. Cohen-Tannoudji. Channeling atoms in a laser standing wave. *Phys. Rev. Lett.*, **59**:1659, (1987).

[56] M. Greiner, O. Mandel, T. Esslinger, T.W. Hänsch, and I. Bloch. Quantum phase transition from a superfluid to a mott insulator in a gas of ultracold atoms. *Nature*, **415**:39, (2002).

[57] T. Ido and H. Katori. Recoil-free spectroscopy of neutral sr atoms in the lamb-dicke regime. *Phys. Rev. Lett.*, **91**:053001, (2003).

[58] M. Takamoto, F.L. Hong, R. Higashi, and H. Katori. An optical lattice clock. *Nature*, **435**:321, (2005).

[59] D. Boiron, A. Michaud, J.-M. Fournier, L. Simard, M. Sprenger, G. Grynberg, and C. Salomon. Cold and dense cesium clouds in far detuned dipole traps. *Phys. Rev. A*, **57**:R4106, (1998).

[60] D.J Han and D.S. Weiss M.T DePue, and. Loading and compressing cs atoms in a very far-off-resonant trap. *Phys. Rev. A*, **63**:023405, (2001).

[61] S.J.M. Kuppens, K.L. Corwin, K.W. Miller, T.E. Chupp, and C.E. Wieman. Loading an optical dipole trap. *Phys. Rev. A*, **62**:013406, (2000).

[62] R. Grimm, M Weidemüller, and Y. B. Ovchinnikov. Optical dipole traps for neutral atoms. *Adv. in Atom., Mol. & Opt. Phys.*, **42**:95, (2000).

[63] S.A. Webster, G. Hechenblaikner, S.A. Hopkins, J. Arlt, and C.J. Foot. Dipole force trapping of caesium atoms. *J. Phys. B*, **33**:1449, (2000).

[64] N. Davidson, H.J. Lee, C.S. Adams, M. Kasevich, and S. Chu. Long coherence times in an optical dipole trap. *Phys. Rev. Lett.*, **74**:1311, (1995).

[65] N. Friedman, L. Khaykovich, R. Ozeri, and N. Davidson. Compression of cold atoms to very high densities in a rotating-beam blue-detuned optical trap. *Phys. Rev. A*, **74**:R031403, (2000).

[66] C. Cohen-Tannoudji, B. Diu, and F. Laloë. *Quantum Machanics*. Wiley, New York, 1977.

[67] B. Brandsen and C. Joachain. *Physics of Atoms and Molecules*. Longman Group Limited, 1 edition, 1983.

[68] A. Mosk, S. Kraft, M. Mudrich, K. Singer, W. Wohlleben, R. Grimm, and M. Weidemüller. Mixture of ultracold lithium and cesium atoms in an optical dipole trap. *Appl. Phys. B*, **73**:791, (2001).

[69] H.A. Bachor and T.C. Ralph. *A guide to experiments in quantum optics*. Wiley, 2nd edition, 2004.

[70] K. Petermann. *Laser diode modulation and noise*. Klüwer academic press, 1991.

[71] C. L. Alzar. Sample reshufling due to atomic motion. *Internal work note*, (2004).

[72] T.M. Brzozowski, M. Maczynska, M. Zawada, J. Zachorowski, and W. Gawlik. *J. Opt. B*, **35**:62, (2002).

[73] A. Kuzmich, K. Mølmer, and E.S. Polzik. *Phys. Rev. Lett.*, **79**:4782, (1997).

[74] L. M. Duan, J. I. Cirac, P. Zoller, and E. S. Polzik. Quantum communication between atomic ensembles using coherent light. *Phys. Rev. Lett.*, **85**:5643, (2000).

[75] A. Kuzmich and E.S. Polzik. *Phys. Rev. Lett.*, **85**:5639, (2000).

[76] A.E. Kozhekin, K. Mølmer, and E.S. Polzik. *Phys. Rev. A*, **62**:033809, (2000).

[77] B. Kraus, K. Hammerer, G. Giedke, and J.I Cirac. *Phys. Rev. A*, **67**:042314, (2003).

[78] J. Fiurášek. *Phys. Rev. A*, **68**:022304, (2003).

[79] B. Nagorny, T. Elsässer, and A. Hemmerich. *Phys. Rev. Lett.*, **91**:153003, (2003).

[80] A. K. Pati and S. L. Braunstein, editors. *in Quantum Information Processing with Continuous Variables*, chapter by A. Kuzmich and E.S. Polzik, pages 231–265. Kluwer Academic Publishers, Dordrecht, 2003.

[81] M. Born and E. Wolf. *Principles of optics*. Cambridge University Press, Cambridge, England, 7th edition, 1999.

[82] K. Szymaniec, S. Ghezali, L. Cognet, and A. Clairon. Injection locking of diode lasers to frequency modulated source. *Opt. Commun.*, **144**:50, (1997).

[83] C. Wieman and L. Hollberg. Using diode lasers for atomic physics. *Rev. Sci. Inst.*, **62**:1, (1991).

[84] L. Ricci, M. Weidemüller, T. Esslinger, A. Hemmerich, C. Zimmermann, V. Vuletic, W. König, and T.W. Hänsch. A compact grating-stabilized diode laser system for atomic physics. *Opt. Commun.*, **117**:541, (1995).

[85] O. Schmidt, K.-M. Knaak, R. Wynands, and D. Meschede. Cesium saturation spectroscopy revisited: how to reverse peaks and observe narrow resonances. *Appl. Phys. B*, **59**:167, (1994).

[86] K.B. MacAdam, A. Steinbach, and C. Wieman. A narrow-band tunable diode laser system with grating feedback and a saturated absorption spectrometer for cs and rb. *Am. J. Phys.*, **60**:1098, (1992).

[87] H.R. Telle. Stabilization and modulation schemes of laser diodes for applied spectroscopy. *Spectrchimica Acta Rev.*, **15**:301, (1993).

[88] R.W.P. Drever, J.L. Hall, F.V. Kowalski, J. Hough, G. M. Ford, A.J. Munley, and H. Ward. Laser phase and frequency stabilization using an optical resonator. *Appl. Phys. B*, **31**:97, (1983).

[89] G. Santarelli, A. Clairon, S.N. Lea, and G.M. Tino. Heterodyne optical phase loacking of extended-cavity semiconductor lasers at 9 ghz. *Opt. Commun.*, **104**:339, (1994).

[90] G.C. Bjorklund. Frequency-modulation spectroscopy: a new method for measuring weak absorptions and dispersions. *Opt. Lett*, **5**:15, (1980).

[91] G.C. Bjorklund, M.D. Levenson, W. Lenth, and C. Ortiz. Frequency modulation (FM) spectroscopy. theory of lineshapes and signal-to-noise analysis. *Appl. Phys. B*, **32**:145, (1983).

[92] M. Gehrtz, G.C. Bjorklund, and E.A. Whittaker. Quantum-limited laser frequency-modulation spectroscopy. *J. Opt. Soc. Am. B*, **2**:1510, (1985).

[93] B.C. Young, F.C. Cruz, W.M. Itano, and J.C. Bergquist. Visible lasers with subhertz linewidths. *Phys. Rev. Lett*, **82**:3799, (1999).

[94] L. Hollberg, V.L Velichansky, C.S. Weimer, and R.W. Fox. High-accuracy spectroscopy with semiconductor lasers: Application to laser frequency stabilization. *Frequency control of semiconductor lasers, edited by: Motoichi Ohtsu*, page 73, (1996).

[95] R.W. Fox, H.G. Robinson, A.S. Zibrov, N. Mackie, J. Marquardt, J. Magyar, and L.W. Hollberg. High-sensitivity spectroscopy with diode lasers. *SPIE Conference on frequency lasers and their applications*, **1837**:360–365, (1992).

[96] M. Minato and Y. Itoh. Vacuum charcteristics of titanium. *J. Vac. Sci. Technol. A*, **13**:540, (1995).

[97] T. Bergeman, G. Erez, and H.J. Metcalf. Magnetostatic trapping fields for neutral atoms. *Phys. Rev. A*, **35**:1535, (1987).

[98] P. Horowitz and W. Hill. *The Art of the Electronics*. Cambridge University Press, 2 edition, 2001.

[99] V. Senaj, G. Guillot, and L. Darrasse. *Rev. Sci. Instr.*, **69**:2400, (1998).

[100] C.J. Dedman, K.G.H. Baldwin, and M. Colla. *Rev. Sci. Instr.*, **72**:4055, (2001).

[101] D. Oblak J. H. Müler C. L. Alzar, P. G. Petrov and E. S. Polzik. Compensation of eddy-currents induced magnetic field trancients in a mot. *Internal report*, (2004).

[102] K. Lindquist, M. Stephens, and C. Wieman. Experimental and theoretical study of the vapor-cell zeeman optical trap. *Phys. Rev. A*, **46**:4082–4090, (1992).

[103] M. Stephens and C. Wieman. High collection efficiency in a laser trap. *Phys. Rev. Lett.*, **7**:3783–3790, (1973).

[104] C. Monroe, W. Swann, H. Roninson, and C. Wieman. Very cold trapped atoms in a vapor cell. *Phys. Rev. Lett.*

[105] C.D. Wallace, T.P. Dinneen, Kit-Jan N. Tan, and T.T. Grove. Isotopic difference in trap loss collisions of laser cooled rubidium atoms. *Phys. Rev. Lett.*

[106] C.J. Townsend, N.H. Edwards, C.J. Cooper, K.P. Zetie, C.J. Foot, A.M. Steane, P. Szriftgiser, H. Perrin, and J. Dallibard. Phase-space density in a magneto-optical trap. *Phys. Rev. A*, **52**:1423–1440, (1995).

[107] M. Drewsen, Ph. Laurent, A. Nadir, G. Santarelli, A. Clairon, Y. Castin, D. Grison, and C. Salomon. Investigation of sub-doppler cooling effects in a cesium magneto-optical trap. *Appl. Phys. B*, **59**:283, (1994).

[108] D. Sesko, C. G. Fan, and C. E. Wieman. Production of a cold atomic vapor using diode-laser cooling. *J. Opt. Soc. Am. B*, **5**:1225–1227, (1988).

[109] D. Weiss, E. Riis, J. Shevy, P.J. Ungar, and S. Chu. Optical molasses and multilvel atoms: experiment. *J. Opt. Soc. Am. B*, **6**:2072, (1989).

[110] Daniel A. Steck. Caesium d line data. *http://george.ph.utexas.edu/ dsteck/alkalidata*, (2002).

[111] S. Bali, K.M. O'Hara, M.E. Gehm, S.R. Granade, and J.E. Thomas. Quantum-diffractive background gas collisions in atom-trap heating and loss. *Phys. Rev. A*, **60**:R29, (1999).

[112] H.C.W. Beijerinck. Rigorous calculation of heating in alkali-metal traps by background gas collisions. *Phys. Rev. A*, **61**:033606, (2000).

[113] M.E. Gehm, K.M. O'Hara, T.A. Savard, and J.E. Thomas. Dynamics of noise-induced heating in atom traps. *Phys. Rev. A*, **58**:3914, (1998).

[114] T. Walker and P. Feng. *Adv. At. Mol. Opt. Phys.*, **34**:125, (1997).

[115] D. Sesko, T. Walker, C. Monroe, A. Gallagher, and C. Wieman. Collisional losses from a light force atom trap. *Phys. Rev. Lett.*

[116] J.E Bjorkholm. Collision limited lifetimes of atom traps. *Phys. Rev. A*, **38**:1599, (1988).

[117] U. Schünemann, H. Engler, R. Grimm, M. Weidemüller, and M. Zielonkowski. Simple scheme for tunable frequency offset locking of two lasers. *Rev. Sci. Instrum.*, **70**:242, (1999).

[118] H. Hansen, T. Aichele, C. Hettich, P. Lodahl, A. I. Lvovsky, J. Mlynek, and S. Schiller. Ultrasensitive pulsed, balanced homodyne detector: application to time-domain quantum measurements. *Opt. Lett.*, **26**:1714, (2001).

[119] A. Dandridge. Zero path-length difference in fiber-optic interferometers. *J. Lightwave Technol.*, **3**:514, (1983).

[120] N.V. Karlov. *Lectures on Quantum Electronics*. CRC Press, 2 edition, 1993.

[121] A. Andalkar and R.B. Warrington. High-resolution measurement of the pressure broadening and shift of the `Cs` `D1` and `D2` lines by `N2` and `He` buffer gases. *Phys. Rev. A*, **54**:032708, (2002).

[122] J.W.R. Tabosa, G. Chen, Z. Hu, R.B. Lee, and H. J. Kimble. Nonlinear spectroscopy of cold atoms in a spontaneous-force optical trap. *Phys. Rev. Lett.*, **66**:3245, (1991).

[123] P.W. Milloni and J.H. Eberly. *Lasers*. John Wiley and Sons, 1988.

[124] M.R. Andrews, M.-O. Mewes, N.J. van Druten, D.S. Durfee, D.M. Kurn, and W. Ketterle. Direct, nondestructive observation of a bose condensate. *Science*, **84**:1996, (1996).

[125] J.E. Lye, J.J. Hope, and J.D. Close. Nondestructive dynamic detectors for bose-einstein condesates. *Phys. Rev. A*, **67**:043609, (2003).

[126] M.R. Andrews, C.G. Townsend, H.-J. Meisner, D.S. Durfee, D.M. Kurn, and W. Ketterle. Observation of interference between two bose condensates. *Science*, **275**:637, (1997).

[127] M. R. Matthews, B. P. Anderson, P. C. Haljan, D. S. Hall, M. J. Holland, J. E. Williams, C. E. Wieman, and E. A. Cornell. Watching a superfluid untwist itself: Recurrence of rabi oscillations in a bose-einstein condensate. *Phys. Rev. Lett.*, **83**:3358, (1999).

[128] S. Kadlecek, J. Sebby, R. Newell, and T.G. Walker. Nondestructive spatial heterodyne imaging of cold atoms. *Opt. Lett.*, **26**:137, (2001).

[129] L.D. Turner, K.F.E.M. Domen, and R. E. Scholten. Diffraction-contrast imaging of cold atoms. *Phys. Rev. A*, **72**:031403(R), (2005).

[130] V.B. Braginsky and F.Y. Khalili. *Quantum Measurements*. Cambridge University Press, 1992.

[131] J. Vanier and C. Audion. *Quantum Physics of atomic frequancy standards*. Insitute of Physics Publishing, 1989.

[132] C. Audion and B. Guinot. *The measurement of time*. Cambridge University Press, 2001.

[133] N.F. Ramsey. *Molecular beams*. Oxford University Press, 1963.

[134] S. Chu, V. Vuletic, A. J. Kerman, and C. Cheng, editors. *Atomic Clocks and Cold Atom Scattering*. ICOLS XV, 2001. chapt. by K. Gibble.